

**High Power Microwave Generation Using an
Active Metamaterial Powered by an Electron
Beam**

by

Jason Samuel Hummelt

B.S. (NE and Physics), University of Wisconsin-Madison (2010)

M.S. (NEEP), University of Wisconsin-Madison (2010)

Submitted to the Department of Nuclear Science and Engineering

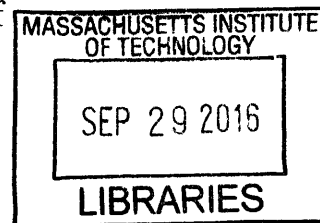
in partial fulfillment of the requirements for the degree of

Doctor of Philosophy

at the

MASSACHUSETTS INSTITUTE OF TECHNOLOGY

June 2016



ARCHIVES

©Massachusetts Institute of Technology 2016. All rights reserved.

Signature redacted

Author

.....

Department of Nuclear Science and Engineering

April 15, 2016

Signature redacted

Certified by

.....

Richard J. Temkin

Senior Research Scientist, Department of Physics

Thesis Supervisor

Signature redacted

Certified by

.....

Anne White

Associate Professor, Nuclear Science and Engineering

Thesis Reader

Signature redacted

Accepted by

.....

Ju Li

Professor, Nuclear Science and Engineering

Chair, Department Committee on Graduate Students

High Power Microwave Generation Using an Active Metamaterial Powered by an Electron Beam

by

Jason Samuel Hummelt

Submitted to the Department of Nuclear Science and Engineering
on April 15, 2016, in partial fulfillment of the
requirements for the degree of
Doctor of Philosophy

Abstract

This thesis presents the theory, design, and experimental demonstration of coherent microwave generation at 2.4 GHz in a metamaterial loaded waveguide using a 490 keV, 84 A, one microsecond pulse length electron beam that produced more than 5 MW of microwave power. Three different metamaterial structure designs named MTM1, MTM2, and MTM3 were tested with design frequencies of 2.8, 2.4, and 3.7 GHz, respectively. The waveguides were loaded with two metamaterial plates that were machined with complementary split ring resonators with periods ranging from 5 to 10 mm. The metamaterial waveguides supported two distinct modes: a symmetric mode that occurs when the two metamaterial plates were excited in phase, and an antisymmetric mode that occurs when the metamaterial plates were excited out of phase. The electron beam propagated on axis between the metamaterial plates. The output radiation was studied for solenoid magnetic field values in the range 350 to 1600 G and for beam voltages from 350 to 500 kV. The best results were found in a 370 mm long structure using the MTM2 design, where output power levels of up to 5 MW were obtained at 400 G in the antisymmetric mode at a frequency near 2.39 GHz. The frequency tuning vs. magnetic field for operation at a power level exceeding 1 MW was consistent with that predicted by an anomalous Doppler shifted resonance condition, $\omega = k_z v_z - \Omega_c / \gamma$. At magnetic fields above 750 G, the microwave output switched to the symmetric mode at a frequency near 2.44 GHz, but the power level dropped drastically to below 100 W. In contrast to the antisymmetric mode, the frequency tuning of the symmetric mode was consistent with that predicted by a normal Cherenkov resonance, $\omega = k_z v_z$. CST PIC simulations predict the observed output frequencies and the switch between modes at 750 G. However, the CST simulations also predict multi-megawatt power levels in both modes, which was observed in the antisymmetric mode, but not the symmetric mode. The discrepancy between the symmetric mode output power of the simulations and experiment is unexplained. To the authors knowledge, these are the first reported experimental results of high power (> 1 MW) microwave generation from an electron beam interacting with a metamaterial structure. The results are important for the development of new microwave

sources and novel devices which utilize active metamaterials.

Thesis Supervisor: Richard J. Temkin

Title: Senior Research Scientist, Department of Physics

Acknowledgments

I want to thank my professional collaborators to whom much of the scientific success of this thesis is owed. First, my supervisor Richard Temkin was always available and interested in the project. His dedication to perfection has stretched me, and from him I've learned much. Michael Shapiro is a brilliant and patient mentor who would always take the time to listen to my ideas and answer my questions, even the silly ones. Ivan Mastovsky was always there to help fix things when everything went wrong (which seemed all too frequent!) and knew how to keep the lab running. To Emilio Nanni, David Tax, Elizabeth Kowalski, Brian Munroe, Haoran Xu, Xueying Lu, JieXi Zang, Sam Schaub, and Sergey Arsenyev I owe a significant amount of gratitude for not only helping with this project, but for their friendship during my time at MIT. Specifically, I thank Sasha Soane who was a great friend and a constant source of postcards. Thanks to Sudheer Jawla, Guy Rosenzweig, and Jacob Stevens for their help. Thanks to Jake Haimson for his help in keeping the electron gun operational. Finally a big thanks to the MIT central machine shop, particularly Andrew Gallant and Michael Abruzzese, who were kind enough to work through all of the different iterations of the project.

I also want to thank my family who supported me through the journey. My dad was an inspiration to me that it is cool to be curious about science. My mom was incredibly loving and supported and encouraged me to strive to achieve. My sister, on whom I was able to carry out my very first science experiments, put up with me even though I teased her too much. And then there is Melissa, who certainly deserves a Ph.D. as much as I do for all she had to go through in order for me to successfully finish mine. Unfortunately, all she'll get instead is my love.

Contents

1	Introduction	23
1.1	Background	23
1.2	Metamaterials	27
1.2.1	Metamaterial Physics	28
1.2.2	Metamaterial Engineering	34
1.3	Microwave Generation Using Electron Beams	38
1.3.1	Cherenkov Radiation	39
1.3.2	Transition Radiation	44
1.3.3	Radiation by Accelerating Charges	47
1.4	An Electron-Beam Powered Metamaterial	52
1.5	Summary of Thesis Contributions	54
2	Metamaterial Circuit Design	59
2.1	Theory of A Metamaterial Filled Waveguide	59
2.1.1	For $\epsilon_{xx} = \epsilon_{yy} = \epsilon_{zz} = 1$	61
2.1.2	For a Lorentzian $\epsilon_{xx} = \epsilon_{yy}$ and $\epsilon_{zz} = 1$	62
2.1.3	A Uniform Metamaterial Slab with an Electric and Magnetic Response	65
2.2	Electromagnetic Design	66
2.2.1	Metamaterial Element Choice	68
2.2.2	MTM1 Design	69
2.2.3	MTM2 Design	76
2.2.4	MTM3 Design	81

2.3	Theory of an Electron Beam Interacting with a Metamaterial Waveguide	83
2.4	PIC Simulations	90
2.4.1	MTM1 PIC Simulations	92
2.4.2	MTM2 PIC Simulations	97
2.4.3	MTM3 PIC Simulations	103
2.4.4	Effective Medium PIC Simulations	104
2.5	Cold Tests	108
2.6	Summary of Design	113
3	High Power Test Experimental Setup	115
3.1	Magnetic Lens and Solenoid	115
3.2	500 keV Electron Beam and Transport	118
3.3	High Power Modulator and Test Facility in NW21	126
3.4	Vacuum System	129
3.4.1	RF Components	131
3.4.2	Structure Assembly and Installation	136
4	Experimental Results	143
4.1	Experimental Diagnostics	143
4.2	Experiments Using the MTM1 Design	145
4.2.1	Unbrazed MTM1 Structure Results	145
4.2.2	Unbrazed MTM1 Structure with Indium Foil Results	150
4.2.3	Brazed MTM1 Structure Results	157
4.3	Experiments Using the MTM2 Design	160
4.3.1	370 mm Unbrazed MTM2 Structure Results	160
4.3.2	370 mm Brazed MTM2 Structure Results	161
4.3.3	420 mm Brazed MTM2 Structure Results	170
4.4	Experiments Using the MTM3 Design	178
4.5	Summary of Results	183

5	Conclusions	187
5.1	Summary of Accomplishments and Relevance	187
5.2	Discussion of Discrepancies Between the Results and Simulation/Theory	189
5.2.1	Structure Fabrication Errors	190
5.2.2	Numerical Issues	191
5.2.3	Voltage and Current Pulse	191
5.3	Potential Future Work	192
A	CST PIC Code Documentation	195

List of Figures

1-1	Average power limit of commonly used solid-state (blue) and vacuum-electron (red) microwave devices.	24
1-2	Schematic of the U.S. E-18G Growler jet.	26
1-3	Photographs of current active denial systems mounted on vehicles for remote deployment.	26
1-4	Simple diagram which classifies materials by their constitutive parameters.	30
1-5	Graphical depiction of Snell's law, a 'perfect lens', and a Negative index metamaterial lens designed at MIT.	33
1-6	Graphical depiction of Cherenkov shock waves in a material with a positive and a negative index	34
1-7	Original magnetic material proposed by Pendry.	36
1-8	Real and Imaginary μ_{eff} for a Drude-like magnetic response, with $\omega_c = 1$, and $\gamma = 0$	38
1-9	John R. Pierce (left) and Rudolph Kompfner (right) shown with some of their earliest TWT tubes.	41
1-10	Simplified illustration that shows the bunching of electrons as they travel with the electric field of an electromagnetic wave.	42
1-11	Illustration of the TWT amplifier and BWO interaction in a rippled wall waveguide	43
1-12	Photograph of the Varian brothers with one of their klystron tubes [28].	45
1-13	Schematic of a simplified two-cavity klystron design.	46

1-14	Applegate diagram shows how modulated electron velocities from a bunching cavity result in current modulation at a catcher cavity. . . .	47
1-15	Schematic of a simplified gyrotron oscillator.	49
1-16	Diagram of the gyro-BWO interaction and gyro-TWT interaction. . .	50
1-17	Diagram of the anomalous Doppler interaction with a slow wave mode. The doppler shifted beam line is drawn in blue, and the Cherenkov resonance is drawn in red for reference.	51
1-18	Photograph of a VGT-8110 Gyrotron Oscillator gyrotron which was designed and built by CPI.	52
1-19	For the 370 mm MTM2 structure, microwave power (black curve), electron gun voltage (blue curve) and measured collector current (red curve) for an applied magnetic field of 375 G.	55
1-20	Microwave frequency tuning for the 370 mm MTM2 structure. . . .	57
2-1	Graphical illustration of the metallic waveguide that is filled with a theoretical dielectric of permittivity $\hat{\epsilon}$ and permeability $\hat{\mu}$	60
2-2	Dispersion curve for the lowest order TM_{11} mode in a vacuum filled rectangular waveguide for $(\pi/a)^2 = (\pi/(2b))^2 = 1$	63
2-3	Dispersion curve for the lowest order TM_{11} mode in a dielectric filled rectangular waveguide that has a Lorentz response.	65
2-4	Dispersion curve for the lowest order TM_{11} mode in a dielectric slab with a Lorentz permittivity and Drude permeability response. . . .	67
2-5	CAD rendering of the MTM1 structure and one of the two identical metamaterial plates it uses.	70
2-6	Dispersion relation for the six lowest order modes solved with the eigenmode solver of HFSS for one period of the MTM1 waveguide. . . .	72
2-7	Field profiles of the three symmetric modes of MTM1.	73
2-8	Field profiles of the three antisymmetric modes of MTM1.	74
2-9	CAD rendering of the MTM2 structure and one of the two identical metamaterial plates it uses.	76

2-10	Dispersion relation for the four lowest order modes solved with the eigenmode solver of HFSS for one period of the MTM2 waveguide. . .	78
2-11	Field profiles of the three symmetric modes of the MTM2 waveguide.	79
2-12	Field profiles of the three antisymmetric modes of the MTM2 waveguide.	80
2-13	CAD rendering of the MTM3 structure and one of the two identical metamaterial plates it uses.	82
2-14	Dispersion relation for the four lowest order modes of the MTM3 waveguide.	84
2-15	Field profiles of the three symmetric modes of the MTM3 waveguide.	85
2-16	Field profiles of the three antisymmetric modes of the MTM3 waveguide.	86
2-17	Start current of MTM1, MTM2, and MTM3.	90
2-18	PIC simulation structure schematics.	91
2-19	Beam radius used in PIC simulations.	92
2-20	Output power of a 352 mm long metamaterial waveguide with the design of MTM1 calculated by the PIC simulation	93
2-21	Fields of the MTM1 structure for 1500 G.	94
2-22	Electron energies of the MTM1 structure for 1500 G.	95
2-23	Fields of the of the MTM1 structure for 700 G.	96
2-24	Electron energies of the MTM1 structure for 700 G.	97
2-25	Output power, saturation time, output frequency, and beam interception calculated for the 352 mm MTM1 device for eight different simulations performed at different magnetic field values. The red line in each plot is drawn between the two simulations where the beam is observed to transition from purely axial bunching to bunching while spiraling between 800 and 900 G to indicate the transition between modes. . .	98
2-26	Output power of a 370 mm long metamaterial waveguide with the design of MTM2 calculated by the CST PIC simulation along with the Fourier Transform of the output signal.	99
2-27	Fields of the MTM2 structure at 1500 G.	100
2-28	Fields of the MTM2 structure at 700 G.	101

2-29	Output power, saturation time, output frequency, and beam interception calculated for the 370 mm MTM2 device for simulations performed at seven different magnetic field values	102
2-30	Output power of a 420 mm long metamaterial waveguide with the design of MTM3 calculated by the PIC simulation along with the Fourier Transform of the output signal.	103
2-31	Output power, saturation time, output frequency, and beam interception calculated for the 420 mm MTM3 device for simulations performed at seven different magnetic field values.	105
2-32	Dispersion relation for the upper negative group velocity mode of the MTM1 metamaterial structure compared with the effective medium structure.	106
2-33	Output power of the Lorentz dielectric filled waveguide calculated by the PIC simulation along with the Fourier Transform of the output signal.	107
2-34	Fields of the effective medium structure.	108
2-35	CAD rendering, photograph of the MTM1a metamaterial test structure based on a slightly modified version of the MTM1 design, and photograph of the metamaterial brass plate.	110
2-36	Transmission measurement of the test MTM1a structure (blue) compared with CST Microwave Studio simulation (red).	111
2-37	Photographs of the MTM1b metamaterial test structure based on a slightly modified version of the MTM1 design. The device has two input ports and two output ports.	112
2-38	Transmission measurement of the test MTMBWO structure (blue) compared with CST Microwave Studio simulation (red).	113
3-1	Magnetic field profile provided by Haimson Research Corporation measured at 3 different radial positions. Also shown is the longitudinal field integrated along the axis at different radial positions.	116

3-2	Magnetic field profile of the solenoid and steel pole pieces calculated with the code Poisson for a current of 175 A through each of the solenoid magnets. The field profile is shown in blue, and the location of the pole pieces is given in gray. The four pancake magnets are sandwiched between the pole pieces.	117
3-3	Simplified schematic of the high power metamaterial experiment. . . .	119
3-4	Photograph of the cathode opened up to air for installation. The anode is centered on the inside of the flange on the right. The gun vacuum isolation valve is also shown attached to the beam tunnel (not visible).	120
3-5	Gun voltage (black) and measured current at the collector (blue) of the electron gun before the cathode was replaced.	121
3-6	Gun voltage (black) and measured current at the collector (blue) of the electron gun after the cathode was replaced.	122
3-7	Measured secondary heater current and voltage applied to the heater element as the power in the primary power supply is increased from 0 to its full operational value.	123
3-8	Beam envelope for the Haimson Research Corporation 500 keV gun.	124
3-9	Beam envelope of a 500 keV, 80 A electron beam starting from a focused 7.5 mm width spot size calculated with MICHELLE and the 1D code developed at MIT.	125
3-10	Beam envelopes of a 500 keV, 80 A electron beam starting from a focused 7.5 mm width spot size calculated by the 1D beam envelope code for three different magnetic field profiles.	127
3-11	Photograph of the 500 kV electron gun mounted to the high power modulator. This photograph was taken before installation of the metamaterial experiment and magnets, and some of the magnets used in the choppertron experiment are visible on the lower right side of the picture.	128

3-12	Photograph taken looking in to the modulator tank. The photo was taken just prior to operation of the metamaterial experiment gun. Because the klystron and linac use the same modulator, some of the connections in the tank are different when running those experiments.	129
3-13	CAD rendering of one of the RF arms which labels the RF load, Bethe-hole coupler, external waveguide bend, waveguide to conflat mating port, and internal bend.	132
3-14	Simulated S_{11} and S_{21} of the internal waveguide bend, waveguide to conflat flange mating port, and external waveguide bend showing good transmission over a wide frequency range. The assembly connects the output coupler of the device to the Bethe-hole coupler.	133
3-15	Measured coupling of the two Bethe-Hole couplers used in the experiment.	134
3-16	Mode content of microwaves entering the Bethe-hole coupler as launched from the metamaterial structure. Almost all of the power is in the TE_{10} and TM_{10} modes.	135
3-17	Plot of the simulated output coupling of microwaves in the TE_{10} and TM_{11} modes in coupler A and B.	136
3-18	Plot of the calculated coupling for the metamaterial experiment for coupler A and coupler B.	137
3-19	Perspective view and cut perspective view of the high power metamaterial experiment. All of the major components are labeled. The electron beam is generated on the left by the 500 kV gun (not shown).	138
3-20	From left to right, ceramic standoff, collector piece 1 that bolts to the ceramic standoff, collector piece 2 that bolts on to the end of collector piece 1, collector fingers that bolt to the end of collector piece 2 that provide a ground plane for the beam after it exits the structure. . . .	139
3-21	Photographs of the MTM1 structure.	140

3-22	Photograph of the experiment under vacuum after bakeout. This photo was taken before the experiment was installed on the gun. To install on the gun, the tube was inserted into the magnet (just visible in the bottom left of the photo) and the vacuum was opened. Dry nitrogen could be pumped through the structure so that it never saw atmospheric air after bakeout.	141
4-1	Summary of the metamaterial design and frequency of the MTM1, MTM2, and MTM3 structures.	144
4-2	Photograph of the 352 mm unbrazed MTM1 structure taken on October 17, 2014 before high power testing.	145
4-3	Microwave power for the bolted MTM1 structure at 1500 G.	146
4-4	Normalized microwave signal and Fourier transform.	148
4-5	Power and frequency of the MTM1 structure vs. magnetic field.	149
4-6	Frequency tuning of the 352 mm unbrazed MTM1 structure as the voltage of the electron beam is varied from 520 kV to 380 kV.	150
4-7	Transmission of the 352 mm metamaterial structure with (blue) and without (red) indium foil put into the structure joints before the structure was bolted together.	151
4-8	Microwave power in two different modes in the 352 mm MTM1 structure assembled with indium foil.	152
4-9	Microwave power measured at 2.83 GHz (red) and 2.35 GHz (blue) as the solenoid field is varied from 300 to 400 G.	153
4-10	Frequency tuning of the 2.35 GHz microwave signal as the voltage (and current) of the electron beam is varied from 520 kV to 380 kV.	154
4-11	Photograph of the partially unassembled 352 mm unbrazed MTM1 structure that had indium foil put in structure joints before the structure was clamped together.	155
4-12	Simplified schematic of the MTM1 metamaterial structure with a 0.5 mm gap around the metamaterial plate.	156

4-13	Transmission of the brazed 352 mm metamaterial structure (blue) compared with a CST MWS simulation of the transmission (red).	158
4-14	For the brazed MTM1 structure, microwave power (black curve), electron gun voltage (blue curve) and measured collector current (red curve) for an applied magnetic field of 1285 G.	159
4-15	For the brazed MTM1 structure, microwave power (black curve), electron gun voltage (blue curve) and measured collector current (red curve) for an applied magnetic field of 265 G.	159
4-16	Microwave power measured at 2.83 GHz as the solenoid field is varied from 260 to 350 G.	160
4-17	Photograph of the brazed 370 mm MTM2 structure taken on January 1, 2015 after high power testing.	161
4-18	Transmission of the 370 mm unbrazed MTM2 structure (blue) compared with a CST MWS simulation of the transmission (red).	162
4-19	For the 370 mm MTM2 structure, microwave power (black curve), electron gun voltage (blue curve) and measured collector current (red curve) for an applied magnetic field of 1500 G.	162
4-20	Transmission of the 370 mm brazed MTM2 metamaterial structure (blue) compared with a CST MWS simulation of the transmission (red). The measurement (and associated simulation) were performed using SMA coax to WR284 couplers to excite the antisymmetric mode of the structure.	163
4-21	For the 370 mm MTM2 structure, microwave power (black curve), electron gun voltage (blue curve) and measured collector current (red curve) for an applied magnetic field of 375 G.	164
4-22	For the 370 mm MTM2 structure, microwave power (black curve), electron gun voltage (blue curve) and measured collector current (red curve) for an applied magnetic field of 431 G.	165
4-23	Measured starting voltage of the 370 mm brazed MTM2 structure. . .	167

4-24	Variation of the frequency of the high power microwave pulses with the gun voltage for the 370 mm brazed MTM2 structure at a fixed magnetic field of 410 G	168
4-25	Microwave power and frequency for the 370 mm MTM2 structure. . .	169
4-26	Transmission of the 420 mm brazed MTM2 metamaterial structure (blue) compared with a CST MWS simulation of the transmission (red). The measurement (and associated simulation) were performed using SMA coax to WR284 couplers to excite the antisymmetric mode of the structure.	171
4-27	For the 420 mm MTM2 structure, microwave power (black curve), electron gun voltage (blue curve) and measured collector current (red curve) for an applied magnetic field of 1550 G.	172
4-28	For the 420 mm MTM2 structure, microwave power (black curve), electron gun voltage (blue curve) and measured collector current (red curve) for an applied magnetic field of 790 G.	173
4-29	For the 420 mm MTM2 structure, microwave power (black curve), electron gun voltage (blue curve) and measured collector current (red curve) for an applied magnetic field of 640 G.	174
4-30	Variation of the frequency and microwave power of the positive group velocity mode of the 420 mm MTM2 structure as a function of the magnetic field. The power is averaged over FWHM of the RF pulse. The gun voltage and current were fixed at 480 kV and 81 A. The lens current was 10.8 A.	175
4-31	Variation of the frequency of the symmetric positive group velocity mode with the gun voltage for the 420 mm brazed MTM2 structure at a fixed magnetic field of 1550 G.	176
4-32	Variation of the 5.95 GHz microwave power as a function of the gun voltage for 640 G (red), 790 G (blue) and 1550 G (black). The power is averaged over the FWHM of the RF pulse.	176

4-33	For the 420 mm MTM2 structure, microwave power in the 2.4 GHz mode (black curve), electron gun voltage (blue curve), and measured collector current (red curve) for an applied magnetic field of 514 G.	177
4-34	For the 420 mm MTM2 structure, microwave power (black curve), electron gun voltage (blue curve) and measured collector current (red curve) for an applied magnetic field of 470 G.	177
4-35	Transmission of the 420 mm brazed MTM3 metamaterial structure (blue) compared with a CST MWS simulation of the transmission (red).	179
4-36	For the 420 mm MTM3 structure, microwave power (black curve), electron gun voltage (blue curve) and measured collector current (red curve) for an applied magnetic field of 1550 G.	180
4-37	For the 420 mm MTM3 structure, microwave power (black curve), electron gun voltage (blue curve) and measured collector current (red curve) for an applied magnetic field of 450 G.	181
4-38	Frequency tuning of the structure as the voltage (and current) of the electron beam is varied from 390 kV to 365 kV.	181
4-39	Microwave power and frequency of the MTM3 structure.	182
4-40	Summary of the metamaterial design and frequency of the MTM1, MTM2, and MTM3 structures.	184

List of Tables

2.1	Dimensions of the MTM1 structure shown in Fig. 2-5 that were used in high power microwave testing.	71
2.2	Dimensions of the MTM2 structure shown in Fig. 2-9 that were used in high power microwave testing.	77
2.3	Dimensions of the MTM3 structure shown in Fig. 2-9 that were used in high power microwave testing.	83
2.4	Coupling impedances and group velocities of the six lowest order modes of the MTM1 device. The coupling impedances and group velocities were calculated at the point of synchronism with a 500 keV beam. . .	88
2.5	Coupling impedances and group velocities of the four lowest order modes of the MTM2 device. The coupling impedances and group velocities were calculated at the point of synchronism with a 500 keV beam.	88
2.6	Coupling impedances and group velocities of the four lowest order modes of the MTM3 device. The coupling impedances and group velocities were calculated at the point of synchronism with a 500 keV beam.	88
4.1	Summary of the experimental results obtained for all four brazed metamaterial structure tests.	185
5.1	High power experimental results from the metamaterial structures that were tested.	188

A.1 Simulations presented in Fig. 2-20, pg. 93; Fig. 2-21, pg. 94; Fig. 2-22, pg. 95	197
A.2 Simulations presented on pg. 93	198
A.3 Simulations presented in Fig. 2-23, pg. 96; Fig. 2-24, pg. 97	198
A.4 Simulations presented in Fig. 2-25, pg. 98	199
A.5 Simulations presented in Fig. 2-26, pg. 99; Fig. 2-27, pg. 100	199
A.6 Simulations presented on pg. 99	200
A.7 Simulations presented in Fig. 2-28, pg. 101	200
A.8 Simulations presented in Fig. 2-28, pg. 101	201
A.9 Simulations presented in Fig. 2-30, pg. 103	201
A.10 Simulations presented in Fig. 2-31, pg. 105	202
A.11 Simulations presented in Fig. 2-33, pg. 107	202
A.12 Simulations presented in Fig. 4-25, pg. 169	203
A.13 Simulations presented in Fig. 4-39, pg. 182	203

Chapter 1

Introduction

1.1 Background

Microwave radiation occupies the part of the electromagnetic spectrum defined by the frequency and free space wavelength range of 300 MHz to 300 GHz and 1 m to 1 mm, respectively. Partly due to the characteristic wavelength size of microwaves, it has been relatively straightforward to build microwave based devices compared to devices in other frequency ranges, and microwaves are now utilized in a wide variety of applications. Most people are familiar with the microwave oven in their homes, which uses a magnetron to produce microwave power at 2.45 GHz in order to heat food. This is an example of microwaves being used as a means to transport energy. By far the biggest economic and societal impact that microwaves have had is not in their ability to carry electromagnetic energy, but as a means to transport *information* either in the amplitude or frequency of the microwave signal. The most obvious examples of this are the wired transmission of microwave signals within a computer and the wireless transmission of information that enables the modern cellular phone. In fact, the majority of microwave devices used today are found in radar and communications systems. However, in addition to these two giant fields, microwaves are also used in a variety of other fields including various remote-sensing applications (which span multiple diverse disciplines), weather monitoring systems, GPS, imaging, spectroscopy, medicine, and a large number of other specialized areas. Since microwave

technology is the enabling factor in so many different applications which are important to both industry and defense, there is a huge incentive to advance the existing field of microwave technology and discover new applications along the way.

An obvious component of all active microwave technology is a microwave source. Since there are so many different applications the required performance of microwave sources is highly application dependent. Nevertheless, generally speaking the most important parameters of merit that distinguish between the available sources include peak and average output power, frequency, bandwidth, stability, efficiency, cost, and size. Further, microwave sources can generally be divided into two different camps, those that rely on solid-state technology and those that rely on electron beams or ‘vacuum electronic’ devices. Due to their ability to produce very high power, vacuum electronic sources have remained the only microwave source available for many

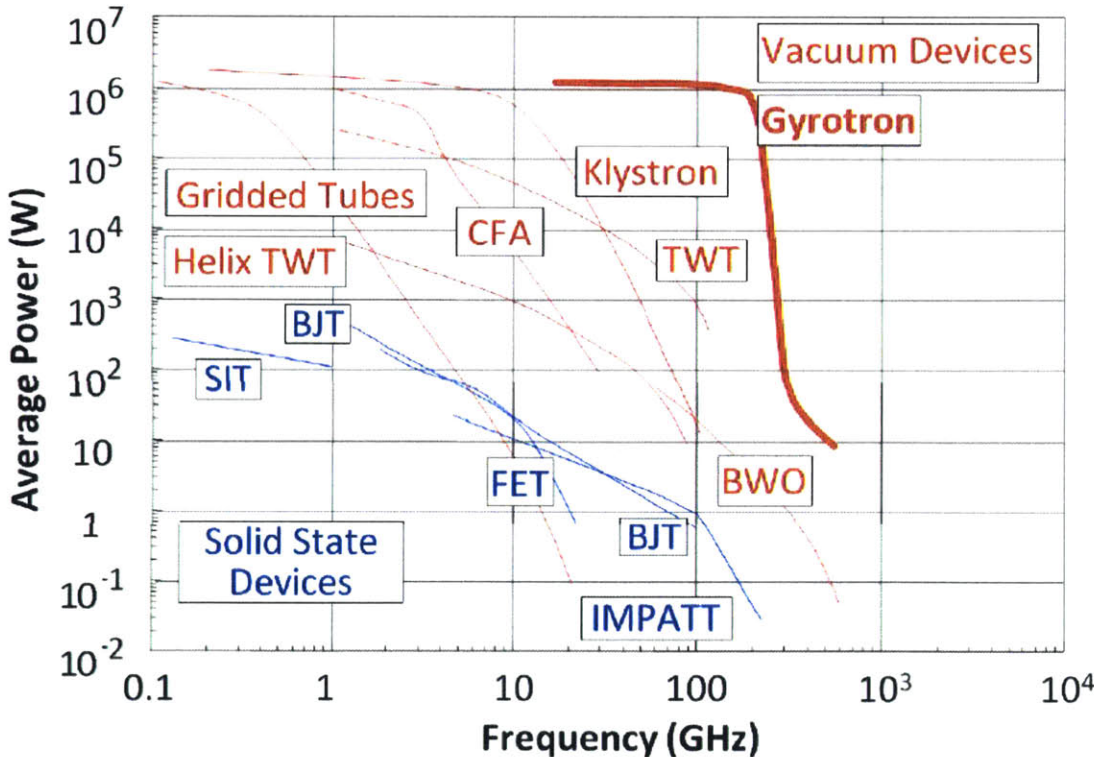


Figure 1-1: Average power limit of commonly used solid-state (blue) and vacuum-electron (red) microwave devices which is adapted from Ref [1].

applications requiring very high power (and some other application specific qualities) despite the major advances in reducing the size and cost of solid state microwave sources over the past few decades. A comparison between the maximum average output power as a function of frequency for some of the most common microwave sources is shown in Fig. 1-1. The vacuum electronic devices (red curves) are in general able to achieve a much higher power for a given frequency than the solid state devices (blue curves).

The research presented in this thesis has been funded by the Air Force Office of Scientific Research as part of a five university MURI grant administered by the University of New Mexico. The Air Force has a significant interest in microwave technology and future applications. Some major areas of research in microwave technology include directed energy, defense and civilian radar, communications, particle accelerators, and other interests in the fundamental understanding of microwave science. One particular area of research is in the generation, amplification, and control of high-power microwaves (HPMs). While the HPM criteria has only been loosely defined, it includes microwave sources from 10's or 100's of MW to as high as 15 GW in power [2]. At these power levels and even significantly below them, electric fields are strong enough that certain nonlinear field effects can be important, such as vacuum or gas breakdown, evolution of plasmas on surfaces, multipactor, material and dielectric damage, and for continuous wave sources, heating and potentially long term damage of microwave components. These particular issues present a significant challenge in the overall performance of HPM sources and components and thus have a substantial influence on their design and engineering.

One area of HPM research has been in the application of HPMs in electronic warfare. The general concept is that a HPM device mounted to an aerial or ground vehicle can fry the sensitive electronics of an enemy vehicle in order to immobilize them. In theory it is also possible to fry electronics without injuring a human on board (or nearby civilians in the case of enemy ground vehicles in heavily populated areas). In Fig. 1-2 a schematic of the US EA-18G Growler jet is shown which makes use of electronic warfare components. HPMs can also be used to immobilize human



Figure 1-2: Schematic of the U.S. E-18G Growler jet, showing its armaments; a modified F/A-18, the Growler uses electronic warfare in place of bombs and missiles [3].

targets without injuring them. Use of microwaves in this fashion is usually referred to as directed energy or active denial technology. In active denial systems a microwave beam (usually in the millimeter band) is launched from a vehicle to a person or group of persons. Because the high-frequency microwaves attenuate in the top layer of skin the radiation can be very painful, but cause very little or no long term damage to the



Figure 1-3: Photographs of current active denial systems mounted on vehicles for remote deployment that are in development by the US military [4].

individual. In Fig. 1-3 a photograph of two different active denials systems is shown where the beam forming microwave antenna is on top of both vehicles. In both of these particular applications there is a large effort to develop novel ways to generate and control HPMs.

1.2 Metamaterials

A new area of research in microwave and optical technology is in the development of artificially engineered materials that have unique electromagnetic behavior. In electromagnetics these artificially engineered materials have been given the name metamaterials, where the prefix meta- implies the exciting ability to extend 'beyond' the limitations of natural electromagnetic materials. Natural materials such as a metal or a dielectric are composed of atoms and molecules that are generally on the order of Angstroms in size. While the way microwave radiation propagates through the material is ultimately determined at the atomic level, the individual building blocks of normal materials are so small compared to the microwave wavelength that individual photon-atom interactions aren't consequential to wave propagation. In many substances this is also true of optical radiation as well (i.e. most crystals), and it isn't really until the ultraviolet region of the electromagnetic spectrum that individual photon-atom interactions become important and it is necessary to use quantum instead of classical electrodynamics to describe how electromagnetic radiation interacts with matter. Simply put, metamaterials are the new 'atoms' of electromagnetic design, but now because we have the ability to build these atoms from scratch we can engineer them in such a way as to make bulk materials that have properties that normal materials do not.

Metamaterials are composed of an assembly of a (usually) periodic, repeating element (the unit cell) that is composed of conventional electromagnetic materials (metals and dielectrics). What makes a metamaterial unique is that the bulk metamaterial derives its unique electromagnetic behavior from the magnetic or electric responses that occur within the unit cell, which is much smaller than the wavelength,

and not the bulk properties of the materials that make up the individual parts of the unit cell. Practically, this is accomplished by engineering the geometries associated with the components of the unit cell in order to give them electric or magnetic resonances. These discrete resonances affect the overall propagation of the wave. In a general sense this separates them from the class of electromagnetic materials known as photonic crystals, which may also be composed of sub-wavelength periodic structures. Photonic crystals instead rely on internal reflections resulting in wave cancellation to give them their unique properties and do not necessarily use resonant elements [5]. However it should be stated that the term metamaterial has become somewhat ubiquitous, so it sometimes may be used interchangeably to describe a material that is not resonant or sub-wavelength and so not in the strict sense a metamaterial.

Because of their unique properties, metamaterials have the potential to significantly impact the current methods for generating and manipulating electromagnetic radiation. In addition, they have been proposed to create completely new and exotic applications including cloaking at optical and microwave frequencies, perfect lensing for microwave and optical beams, advanced antennas for microwave signals, as well as many additional passive and active electromagnetic devices. Some of these applications are briefly discussed below after an introduction to the general physical concepts underlying metamaterial design is given.

1.2.1 Metamaterial Physics

Even though many metamaterials have fairly complex geometries that make purely analytical analysis of their electromagnetic behavior difficult, it is important to gain an intuitive understanding of the physics that underlie the truly unique ways they can influence electromagnetic waves. The differential form of Maxwell's equations in a medium absent of both charge and current sources can be written as [6]

$$\begin{aligned}
\nabla \cdot \vec{E} &= 0 \\
\nabla \cdot \vec{B} &= 0 \\
\nabla \times \vec{E} &= -\mu \frac{\partial \vec{H}}{\partial t} \\
\nabla \times \vec{H} &= \epsilon \frac{\partial \vec{E}}{\partial t}
\end{aligned} \tag{1.2.1}$$

In addition, the constitutive equations that relate the electric and magnetic fields to the electric and magnetic fluxes can be written as

$$\begin{aligned}
\vec{D} &= \epsilon \vec{E} \\
\vec{B} &= \mu \vec{H}
\end{aligned} \tag{1.2.2}$$

where ϵ is the permittivity and μ is the permeability of the medium. Maxwell's equations are a set of coupled first-order partial differential equations which relate the electric and magnetic fields. In most circumstances it is easier to solve second-order equations by introducing the scalar electric potential ϕ and the vector magnetic potential \vec{A} defined by

$$\begin{aligned}
\vec{B} &= \nabla \times \vec{A} \\
\vec{E} &= -\nabla \phi - \frac{\partial \vec{A}}{\partial t}
\end{aligned} \tag{1.2.3}$$

Using these definitions it is straightforward to obtain the wave equations which are given by

$$\begin{aligned}
\nabla^2 \phi - \epsilon \mu \frac{\partial^2 \phi}{\partial t^2} &= 0 \\
\nabla^2 \vec{A} - \epsilon \mu \frac{\partial^2 \vec{A}}{\partial t^2} &= 0
\end{aligned} \tag{1.2.4}$$

There are real and propagating solutions to these wave equations when the material's index n is real (where $n = \sqrt{\epsilon \mu}$), which occurs when both ϵ and μ are both

positive or both negative. Waves will decay (become evanescent) in materials where n is imaginary and ϵ or μ is independently positive. Materials can thus be classified according to the simple diagram shown in Fig. 1-4 which highlight the materials that exhibit wave propagation and evanescence according to their constitutive parameters.

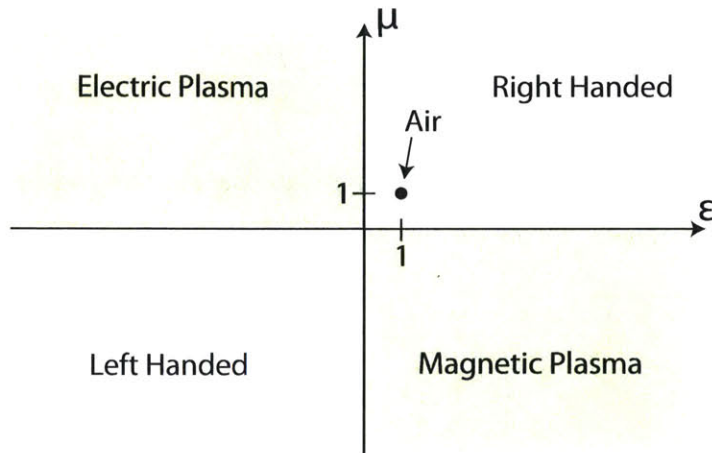


Figure 1-4: Simple diagram which classifies materials by their constitutive parameters ϵ and μ and highlights the regions of wave propagation and evanescence. Materials with real n may have propagating waves, while materials with imaginary n have decaying waves.

The most familiar type of materials belong to the quadrant where both ϵ and μ are positive. These types of materials include dielectrics and represent many of the materials on the earth's surface (glasses, many rocks, biological material, etc.) A material where $\epsilon < 0$ and $\mu > 0$ is called an electric plasma. For this type of material microwaves are evanescent and do not propagate. Materials that fall into this category are actually fairly abundant in the universe and include many types of low-loss plasmas, metals, and semiconductors at optical and infrared frequencies. For $\epsilon > 0$ and $\mu < 0$ the material is a magnetic plasma and the wave is again evanescent. Materials of this kind are not common due to the weak magnetic interactions in most solid-state materials, though ferrites fall into this category and are very important in many microwave components. Veselago is credited with first describing the situation where both parameters are negative, and he is considered by many to first envision the significance of the 'left-handed' material that results [7].

We again turn our attention to Eq. 1.2.4 and consider a plane wave in vacuum of the form $\vec{E} = \vec{E}_0 \exp(-i\vec{k} \cdot \vec{r} + i\omega t)$ and $\vec{H} = \vec{H}_0 \exp(-i\vec{k} \cdot \vec{r} + i\omega t)$ to be incident on a hypothetical infinite block of material with $\epsilon < 0$ and $\mu < 0$. We know from the above discussion that there is a solution for a propagating wave in this material and so there will be some transmission of the plane wave into it. To get a qualitative understanding of the wave we reduce the first-order Maxwell's equations to

$$\begin{aligned}\vec{k} \times \vec{E} &= \mu\omega\vec{H} \\ \vec{k} \times \vec{H} &= -\epsilon\omega\vec{E}\end{aligned}\tag{1.2.5}$$

From Eqs. 1.2.5 we see that a change in sign of ϵ and μ does affect the plane wave solutions just described. For $\epsilon > 0$ and $\mu > 0$ the wave is a right-handed orthogonal system of vectors. However, for $\epsilon < 0$ and $\mu < 0$ the wave is a left-handed orthogonal set. This is why negative index media are commonly referred to as 'left-handed.' Interestingly, the sign of the Poynting vector $\vec{S} = \frac{1}{2}\vec{E} \times \vec{H}^*$ does not change for a change in the sign of the index. Therefore, wavefronts in a left-handed medium move in the opposite direction as energy [8]. Physically, this means that the group velocity $\vec{v}_g = \frac{\partial\omega}{\partial\vec{k}}$ and phase velocity $\vec{v}_\phi = \frac{\omega}{\vec{k}}$ have opposite sign, and as a result left-handed metamaterials are sometimes called 'backward-wave' materials. The significance of backward-wave propagation applied to some well known physical phenomena is investigated below.

Negative Refraction

One of the most exciting areas of application in metamaterials research has been in utilizing the property of negative refraction. For a TE or TM wave propagating in a positive index medium with Poynting and wavevectors \vec{S}_i and \vec{k}_i that is incident on a slab of negative index media, Snell's law still holds the same as it does for a positive index medium [9]. Snell's law is given by the equation

$$n_1 \sin(\theta_i) = n_2 \sin(\theta_t)\tag{1.2.6}$$

where θ_i and θ_t are the angles of the incident and transmitted wave, and n_1 and n_2 are the indices of the two materials. For a negative index medium Snell's law is depicted in Fig. 1-5a. Because of the sign change of the index between the two media and the fact that the wavevectors must be parallel to the Poynting vectors, the component of the transmitted Poynting vector (and hence the energy) traveling in the direction parallel to the interface will have the opposite sign of what it would be for an interface between two positive index media. This has important ramifications for geometrical optics. First, concave and convex lenses made from a negative index material have the opposite focusing effect from their positive index counterparts, namely, they become convergent and divergent, respectively. Second, even flat lenses made from negative index media can have a focusing effect. Finally, for a lossless flat lens of index $n = -1$ it can be shown that all light rays coming from a source are focused at two points, one inside and one outside the lens. This type of lens has been called a 'perfect lens' for its ability to focus electromagnetic energy to much smaller than the conventional limit of $\lambda/2$ for a gaussian beam. This type of lens is illustrated in Fig. 1-5b. Much of the research on metamaterials has been on trying to achieve perfect lensing like the one shown in 1-5c which was built at MIT and uses a copper mesh-like metamaterial to focus microwaves near 10 GHz [10]. Unfortunately losses and other issues have so far limited the performance of perfect lenses, but it has been shown experimentally that resolutions much smaller than the classical limit of $\lambda/2$ and as small as $\lambda/20$ can be achieved [11].

Inverse Doppler Effect

The Doppler effect is a well known physical phenomenon whereby a relative velocity between a source and receiver of radiation can shift the frequency of the radiation detected by the receiver [6]. In the non-relativistic case the formula for the frequency shift detected by the receiver is given by the formula [8]

$$df = f_0 \frac{nv}{c} \tag{1.2.7}$$

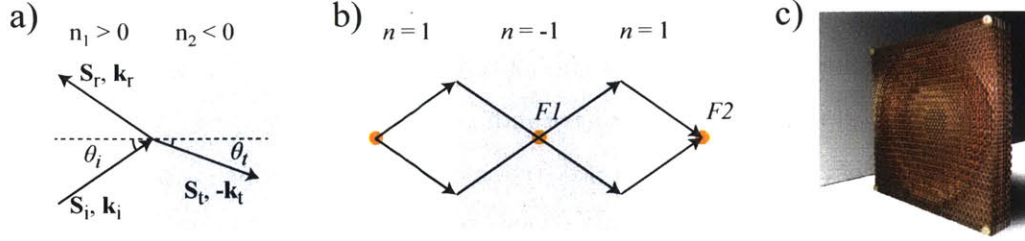


Figure 1-5: a) Graphical depiction of Snell's law for a negative index medium. The incident wave is from the left, and the normalized Poynting and wavevectors are shown. b) An illustration of a 'perfect lens', where rays from the source are perfectly focused within and outside the lens. c) Negative index metamaterial lens designed at MIT for operation at 10 GHz [10].

where f_0 is the original frequency of the source, v is the component of the receiver velocity moving towards the source in the frame of reference where the source is stationary (and may be positive or negative), n is the index of the media, and c is the speed of light in free space. From the above formula it is easy to see that as n changes sign so does the frequency shift. Thus radiation that would normally be blue-shifted in a positive index medium is red-shifted in a negative index one, and vice versa. This effect has been observed in negative index media in experiment [12, 13].

Backward Cherenkov Radiation

Another well known physical phenomenon that is significantly affected by the introduction of negative index materials occurs for radiation from relativistic moving charges in a dielectric medium. Cherenkov radiation is a well known phenomena whereby charged particles moving faster than the speed of light in the medium they are traveling in will radiate. The spherical wavefronts radiated by the relativistic particle will create a forward propagating shock wave or 'Cherenkov cone' [6]. The angle between the shock wave and the particle velocity is given by the formula

$$\cos(\theta) = \frac{c}{nv} \quad (1.2.8)$$

where θ is the angle between the radiation wavevector and the velocity of the particle, c is the speed of light in vacuum, n is the material index, and v is the particle velocity. This concept is illustrated for a positive index medium in Fig. 1-6a. However, from Eq. 1.2.12 it is easy to see that for a negative index the wave propagation is backward. This effect, which is called backward Cherenkov radiation and is illustrated in Fig. 1-6b, has also been observed in experiment [14].

Fig. 1-6a depicts the formation of Cherenkov shock waves in a positive or normal index medium travelling faster than the speed of light in the medium. Spherical wavefronts move away from the source at a speed $c/|n|$. The spherical wavefronts are therefore delayed with regard to the particle motion which results in the shock wave or Cherenkov cone which is depicted in the figure. The axial direction of the shock wave is in the same direction as the particle motion. In 1-6b the Cherenkov shock wave is shown for a negative index medium. In this case, the axial direction of the shock wave is in the direction opposite to the electron motion.

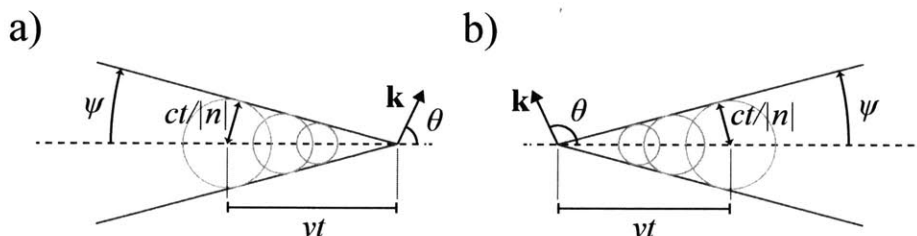


Figure 1-6: Graphical depiction of Cherenkov shock waves in a material with a) a positive index and b) a negative index. For the positive index media wavefronts propagate from the source at a speed $c/|n|$ and for the negative index media wavefronts propagate towards the source at a speed $c/|n|$. This figure has been adapted from Ref. [8].

1.2.2 Metamaterial Engineering

It has already been mentioned that left-handed materials as a concept, and hence the very interesting applications associated with them, long preceded experimental demonstration of such materials. The lack of a doubly negative natural material

was overcome with several systematic attempts at simulating and understanding the permittivity of ionosphere plasmas, which have a negative permittivity. It was realized that certain simple systems composed of periodic unit cells (namely hollow metal waveguides and metal wire meshes) behave like plasmas for a particular range of frequencies [15, 16]. This work resided on the premise that ‘effective permittivities’ can be obtained which describe the overall interaction of a wave with a composite material if the size of the components that the composite is constructed from is small enough to permit accurate field averaging over the unit cell. The next step was to create composite materials where both the permittivity and permeability were individually controlled parameters. The composite materials would be described by the effective parameters, which are defined by the relations [17]

$$\begin{aligned}\vec{B}_{ave} &= \mu_{eff}\mu_0\vec{H}_{ave} \\ \vec{D}_{ave} &= \epsilon_{eff}\epsilon_0\vec{E}_{ave}\end{aligned}\tag{1.2.9}$$

where the subscript ‘ave’ refers to the averaged field over the unit cell. For a square unit cell the x component may be calculated from the following equations

$$\begin{aligned}(\vec{H}_{ave})_x &= \frac{1}{a} \int_{r=(0,0,0)}^{r=(a,0,0)} \vec{H} \cdot d\vec{r} \\ (\vec{B}_{ave})_x &= \frac{1}{a^2} \int_{S_x} \vec{B} \cdot d\vec{S} \\ (\vec{E}_{ave})_x &= \frac{1}{a} \int_{r=(0,0,0)}^{r=(a,0,0)} \vec{E} \cdot d\vec{r} \\ (\vec{D}_{ave})_x &= \frac{1}{a^2} \int_{S_x} \vec{D} \cdot d\vec{S}\end{aligned}\tag{1.2.10}$$

Finally the effective parameters are defined by the relations

$$\begin{aligned}\mu_{eff} &= \frac{(\vec{B}_{ave})_x}{\mu_0(\vec{H}_{ave})_x} \\ \epsilon_{eff} &= \frac{(\vec{D}_{ave})_x}{\epsilon_0(\vec{E}_{ave})_x}\end{aligned}\tag{1.2.11}$$

where averaging must be performed over each spatial dimension to obtain the total effective parameter. A major advancement came in 1999 when Pendry et. al. demonstrated that edge coupled split-ring resonators (edge-coupled SRRs) could be used to create an artificial negative permeability in 3 spatial dimensions. Various experiments verified this effect [17, 18, 19]. In Fig. 1-7a is the unit cell of Pendry's original design for his negative permeability material, which consists two thin rings printed on a dielectric. Each ring is split in order to introduce a small capacitance into the

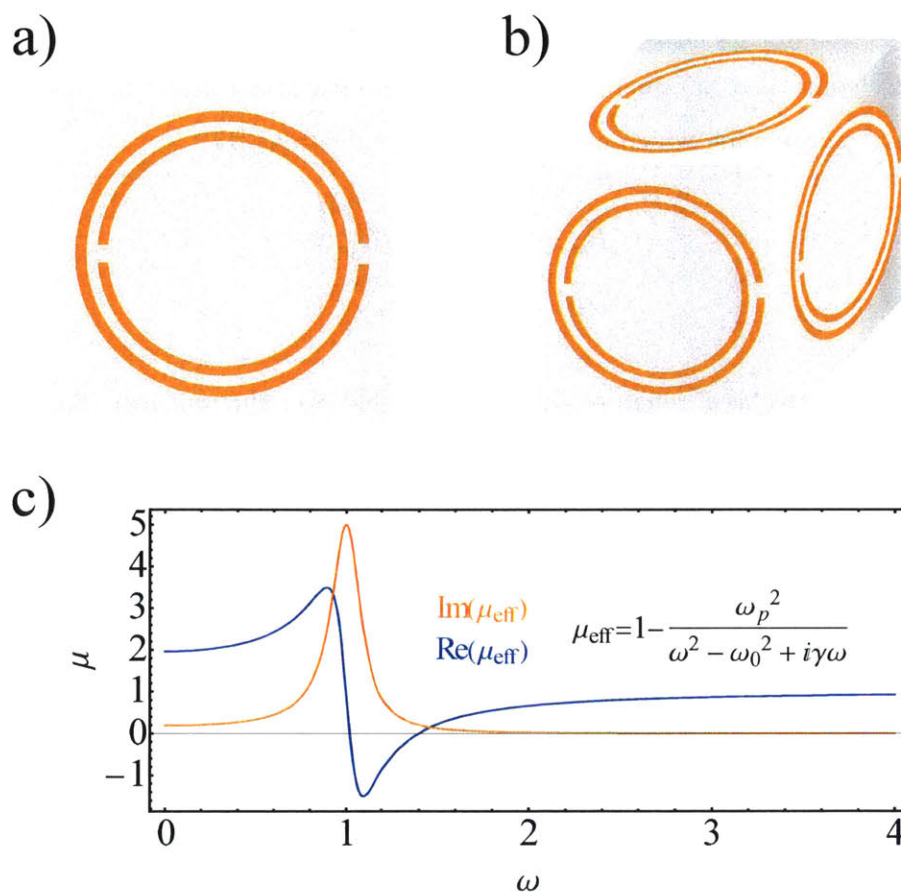


Figure 1-7: Original magnetic material proposed by Pendry et. al. [17] a) a single metallic split ring resonator pair which is printed on a dielectric substrate of permittivity ϵ_d has a magnetic resonance at frequency ω_0 . b) A unit cell of a 3D arrangement of the split ring resonators shown in Fig 1-7a. The unit cell has a resonance in all three spatial dimensions. c) Real and Imaginary μ_{eff} for the 3D magnetic material proposed for $\omega_0 = 1$, $\omega_p = 1$, and $\gamma = 0.2$.

loop which serves to enhance the loop's magnetic response near a particular resonance frequency. When the system is excited by a time-varying external magnetic field just above the resonance frequency, ω_0 , the effective permeability of the ring is negative. A 1D array of identical SRRs can create a negative effective permeability just above the resonance frequency, and arranging the rings as shown in Fig. 1-7b can create a negative effective permeability in 3 spatial dimensions. The resonance frequency of the SRR can be estimated analytically by using an equivalent circuit analysis. Then ω_0 is given by the expression

$$\omega_0 = \sqrt{\frac{1}{LC}} \quad (1.2.12)$$

Where L is the inductance of the SRR system and C is the capacitance. For simple geometries (such as a single edge-coupled SRR) this can be estimated analytically, but in practice this is calculated numerically. Generally the effective parameters usually exhibit a 'Drude-like' response or a 'Lorentz-like' response, where the mathematical form of each is given by the equations

$$f_{Drude} = 1 - \frac{\omega_c^2}{\omega^2 + i\gamma\omega} \quad (1.2.13)$$

$$f_{Lorentz} = 1 - \frac{\omega_p^2}{\omega^2 - \omega_0^2 + i\gamma\omega} \quad (1.2.14)$$

where ω_0 is the resonant frequency, γ is the damping coefficient that accounts for ohmic and dielectric loss, and ω_p and ω_c are the plasma and cyclotron frequencies and are determined by the geometry of the unit cell (here the cyclotron frequency has no direct relation to the cyclotron frequency of a plasma, which depends on the background magnetic field, but is so named to be consistent with the nomenclature of Pendry). As an example, the split rings presented by Pendry et. al. have a Lorentz-like response, which is graphically illustrated in Fig 1-7c. A below-cutoff waveguide or a wire mesh has a Drude-like response, which is shown graphically in Fig. 1-8.

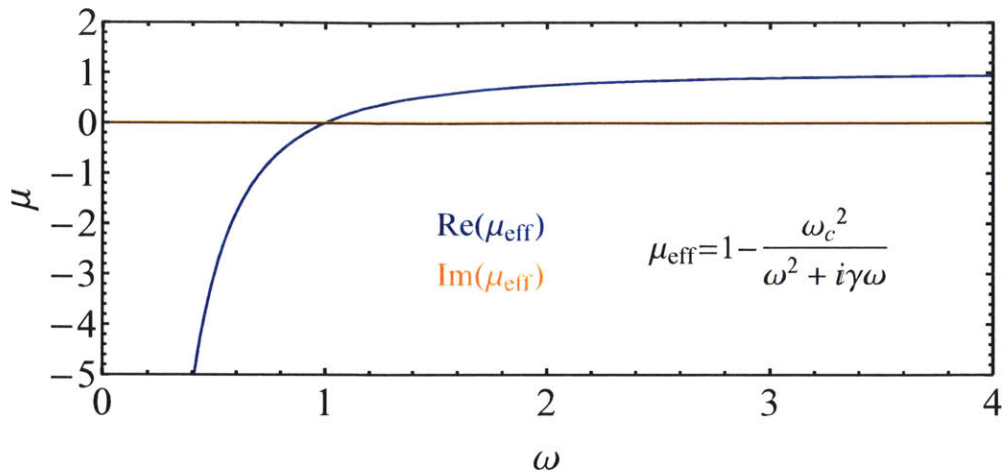


Figure 1-8: Real and Imaginary μ_{eff} for a Drude-like magnetic response, with $\omega_c = 1$, and $\gamma = 0$.

1.3 Microwave Generation Using Electron Beams

The use of high power electron beams to produce or amplify coherent microwave radiation is a well-established area of research that is commonly referred to as vacuum electronics [20]. All vacuum electron microwave devices rely on the use of electron beams to generate electromagnetic radiation. Moving electrons, electron bunches, and electron beams all have the ability to radiate photons. There are a wide variety of vacuum electron devices that make use of different physical radiation mechanisms (Cherenkov, Transition, Bremsstrahlung, Cyclotron, Synchrotron, etc.) in order to generate electromagnetic waves that cover the electromagnetic spectrum from RF all the way to X-Rays. In general the frequency and power of the electromagnetic radiation is the most important factor in determining the radiation mechanism (and the device) that is most useful. The most common vacuum electron devices, and of greatest interest to this work, occur in the microwave range. In the following sections the three most important radiation mechanisms for vacuum electronics at microwave frequencies are discussed, along with some examples of microwave amplifiers and generators that rely on each of the mechanisms presented.

1.3.1 Cherenkov Radiation

A relativistic electron with velocity v that is moving in a medium of relative permittivity $\epsilon(\omega)$ and permeability $\mu(\omega)$ will emit Cherenkov radiation when $v > c/\sqrt{\epsilon(\omega)\mu(\omega)}$, where c is the speed of light in vacuum [6, 21]. This type of radiation was first produced in experiment by Cherenkov in 1934 and later explained mathematically in 1937 by Tamm and Frank. The Frank-Tamm equation that they derived, which describes the energy radiated per unit length by an electron, is given by the expression

$$\frac{dE}{dx} = \frac{e^2}{4\pi} \int_{v > c/n(\omega)} \mu(\omega)\omega \left(1 - \frac{1}{\beta^2 n^2(\omega)}\right) d\omega \quad (1.3.1)$$

From the above equation it is evident that Cherenkov radiation is not continuous, but only occurs for frequencies that satisfy the condition $v > c/n(\omega)$. In a dielectric, this puts a requirement on either the minimum permittivity or the minimum electron energy required to observe radiation at a given frequency. Cherenkov radiation is responsible for the eerie ‘blue glow’ that is observed from spent nuclear fuel assemblies that are usually stored in water. Highly relativistic beta particles emitted from the nuclear fuel travel much faster than the speed of light in the water and so radiate. It should be noted that Cherenkov radiation is emitted by individual electrons. For an electron beam traveling through a dielectric the radiation from individual electrons is incoherent. For coherent radiation it is necessary to first form electron bunches.

An analogous radiation mechanism that occurs in periodic structures and can be thought of as a type of Cherenkov radiation is called Smith-Purcell radiation. In Smith-Purcell radiation the phase velocity of the electromagnetic wave is modified by the periodicity of the waveguide. This type of radiation was first discovered in 1953 by sending an electron beam over a periodic grating [22]. The radiation is due to the fact that in a periodic structure slow waves may exist where the phase velocity is less than the velocities of the electrons. From Floquet’s theorem the electric field E of an electromagnetic mode with frequency ω in a periodic structure with periodicity d can be represented as an infinite sum of spatial harmonics over harmonic number l

and axial wave number k_{zl} . This can be expressed mathematically as

$$E = e^{-i\omega t} \sum_{l=-\infty}^{+\infty} A_l e^{ik_{zl}z} \quad (1.3.2)$$

$$k_{zl} = k_{z0} + \frac{2\pi l}{d} \quad (1.3.3)$$

where k_{z0} is the zeroth order spatial harmonic and A_l is determined by the geometry of the periodic waveguide. The spatial harmonics have a wavelength $\lambda_l = 2\pi/k_{zl}$, phase velocity $v_{\phi l} = \omega/k_{zl}$ and group velocity $v_g = \partial\omega/\partial k_{z0}$.

Slow-Wave Devices

A common microwave device that relies on Smith-Purcell radiation is the slow-wave structure, which can be used as a backward-wave oscillator (BWO) or as a traveling-wave tube (TWT) amplifier. The first TWT amplifier was first conceived and built by Rudolph Kompfner in 1943 [23]. This first device was a metal helix structure which is still used today for its impressively large bandwidth. Approximately 10 years later Kompfner also discovered that his TWT could be used to generate microwaves and used it as a BWO. The full detailed linear theory of these devices was developed shortly after by John Pierce while working with Kompfner [24]. A photograph of both Pierce and Kompfner along with some of their early tube designs is shown in Fig. 1-9.

In a slow-wave device a DC electron beam that is guided by a magnetic field interacts with a traveling TM polarized electromagnetic wave with a phase velocity approximately equal to the electron beam velocity. It was discussed in the previous section that Cherenkov radiation from individual electrons is by nature incoherent and bunches must be formed in order to generate coherent radiation. This is accomplished in a slow-wave device by using a synchronous wave, or by using an electron beam and an electromagnetic mode where the difference between the beam velocity and the phase velocity $v_z - v_\phi$ is small. This bunching is forced and the radiation that is emitted is induced, and so it is most accurate to say that the slow-wave device makes



Figure 1-9: John R. Pierce (left) and Rudolph Kompfner (right) shown with some of their earliest TWT tubes. These tubes utilized a metal helix structure to slow down the electromagnetic wave in order to interact with the electron beam. These early tubes were enclosed in glass tubes in order to provide the vacuum necessary for the emitter of the electron gun to work. This photo was taken at Bell labs in the 1950's [25].

use of stimulated Cherenkov radiation [26].

The bunching interaction of a slow-wave device is most easily understood when examined from the frame of reference where the DC electron beam and wave are both stationary. As the electrons enter the device they are uniformly distributed in phase, but as they co-propagate with the wave they experience an accelerating or decelerating field from the AC field which in turn results in an AC modulation of the electron beam. This is illustrated graphically in Fig. 1-10.

The electron bunches are formed on the zero field point, but there is a phase slippage putting the bunches in the retarding field of the electromagnetic wave which allows energy transfer between the bunches and the wave. Once the bunches have lost a significant amount of energy to the wave they may fall into the accelerating part

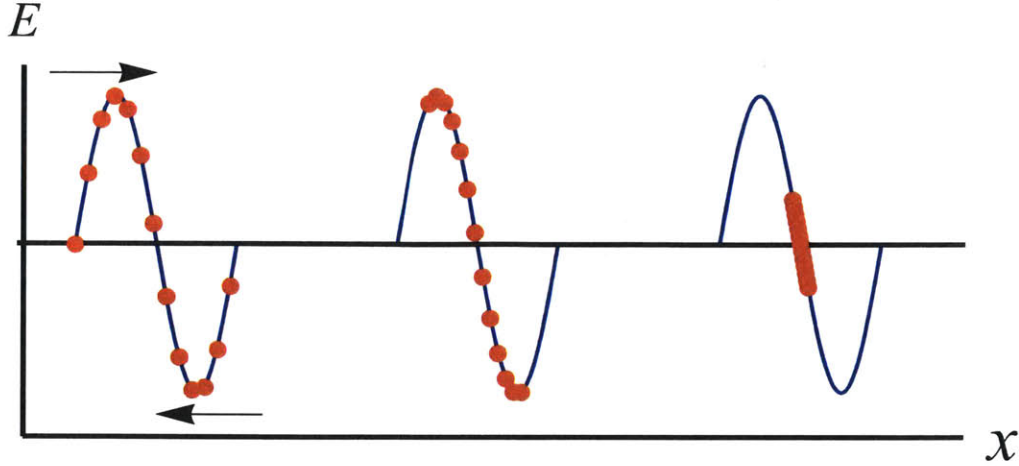


Figure 1-10: Simplified illustration that shows the bunching of electrons (red dots) as they travel with the electric field of an electromagnetic wave (blue curve) that has a phase velocity equal to the electron beam velocity. As the electrons travel with the wave they are bunched due to the electric field of the wave.

of the electric field and take energy back from the wave. Therefore it is necessary to build the device short enough so that the interaction stops after electrons have had enough time to bunch and dump energy to the wave, but also not so long that the efficiency of the device is reduced.

The coupling impedance K , a measure of how strongly the electron beam couples to a mode in a slow-wave structure, is given by the formula

$$K = \frac{E_w^2}{2k_z^2 P} \quad (1.3.4)$$

where P is the power flux through the structure and the electric field that couples to the electron beam E_w is given by the formula

$$E_w = \frac{1}{P} \int_0^P E_z(z) e^{ik_z z} \quad (1.3.5)$$

In addition to coupling to and amplifying a wave with positive group velocity, a TWT can be used as a backward-wave oscillator to generate microwaves. Oscillation in the device comes from noise in the electron beam, where the frequency spectrum of the noise is very wide. Because there is a mechanism for feedback for a backward

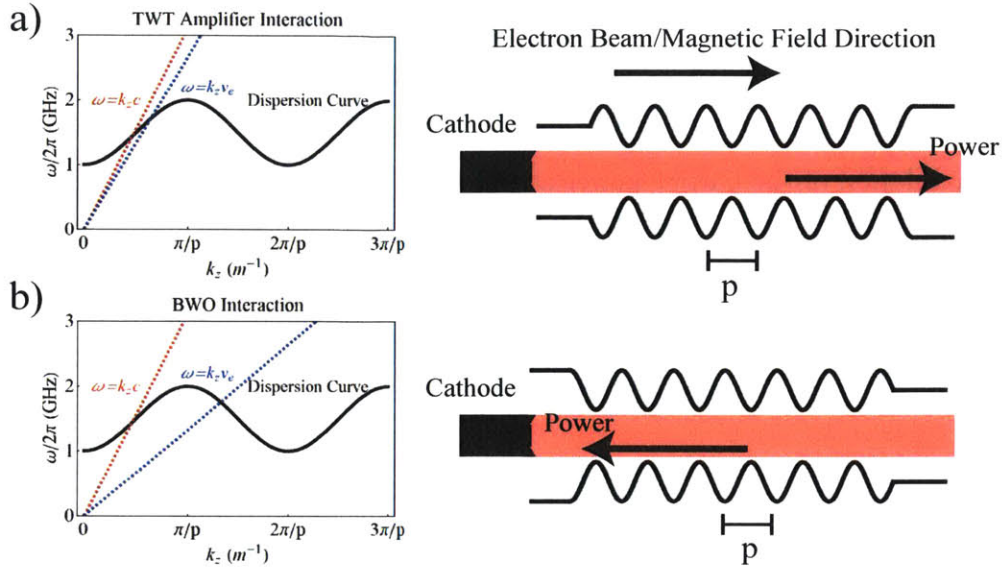


Figure 1-11: a) Illustration of the TWT amplifier interaction in a rippled wall waveguide. A simplified schematic of the device is shown which shows the power flowing in the same direction as the electron beam. b) Illustration of the BWO interaction in a rippled wall waveguide. A simplified schematic of the device is shown which shows the power flowing in the opposite direction as the electron beam.

wave when the right conditions are met (namely that the current is above the start current for the structure geometry and beam voltage) the beam will bunch and amplify the microwave noise until saturation is reached or the interaction is terminated. The BWO interaction is an absolute instability, which means that it is an instability that will start simply from the microwave noise that exists in the system and doesn't require any input microwave signal. This has an important physical consequence in that the phase of the generated microwaves cannot be controlled, which is disadvantageous for several microwave applications (especially in communications). Another interesting point about BWOs is that by inspection of the dispersion relation in Fig. 1-11 it's clear that the group velocity and phase velocity are of the opposite sign, which is the same physical result obtained in the analysis of a left-handed material. This observation will be further discussed in this thesis.

As was already mentioned, a BWO has a start current for oscillation, I_{st} , above which the device will oscillate and generate microwaves with zero input signal. The

start current depends on the device geometry, mode of interaction, and beam parameters. Traditionally BWOs are operated when the current is $\sim 3\times$ the start current. Increasing the current well beyond the start current ($> 7\times$) can result in auto-modulation of the output power as the device enters a stochastic regime. This type of behavior has been observed in both theory and experiment as shown, for example, in Ref. [27]. In order to estimate I_{st} for any microwave waveguide one can follow the method similar to that outlined by Pierce and discussed in detail in Ref. [26], where I_{st} is given by the equation

$$I_{st} = 4U_0 \frac{(CN)_{st}^3 \lambda_z^3}{KL^3} \quad (1.3.6)$$

where U_0 is the beam energy, K is once again the coupling impedance, $\lambda_z = \frac{2\pi}{k_z}$ is the longitudinal wavelength, L is the total length of the structure, $(CN)_{st}$ is the start condition parameter, $N = L/\lambda_z$ is the number of longitudinal wavelengths, and C is the Pierce parameter. The Pierce parameter is an important normalized parameter in microwave tube analysis, and is given by the equation

$$C^3 = \frac{I_0 K}{4U_0} \quad (1.3.7)$$

Here I_0 is the beam current. Loss, space charge, and the spatial harmonic that the device is operating in will determine the value of $(CN)_{st}$. For the simple lossless case with no space charge and operating in the zeroth harmonic $l = 0$ the start condition $(CN)_{st}$ is calculated to be 0.314 [26]. In order to accurately include the effects of space charge, loss, and other losses due to coupling etc., a nonlinear calculation of the fields or a PIC simulation is needed to calculate the start current.

1.3.2 Transition Radiation

Transition radiation occurs when electrons pass through a discontinuous media, either as a discontinuity in the index of refraction or through regions with grids, plates, and cavities. Moving, negatively charged electrons induce positive charges on the metal

or dielectric through which it passes. At a discontinuity the dipole moment between the moving charge and the induced charge changes in time and thus will radiate [26]. Several microwave devices are based on this type of radiation mechanism.

Klystron Devices

The klystron tube was first proposed by the Varian brothers Russel and Sigurd in 1935 and the first successful test was carried out in 1937 [28]. While the tube was

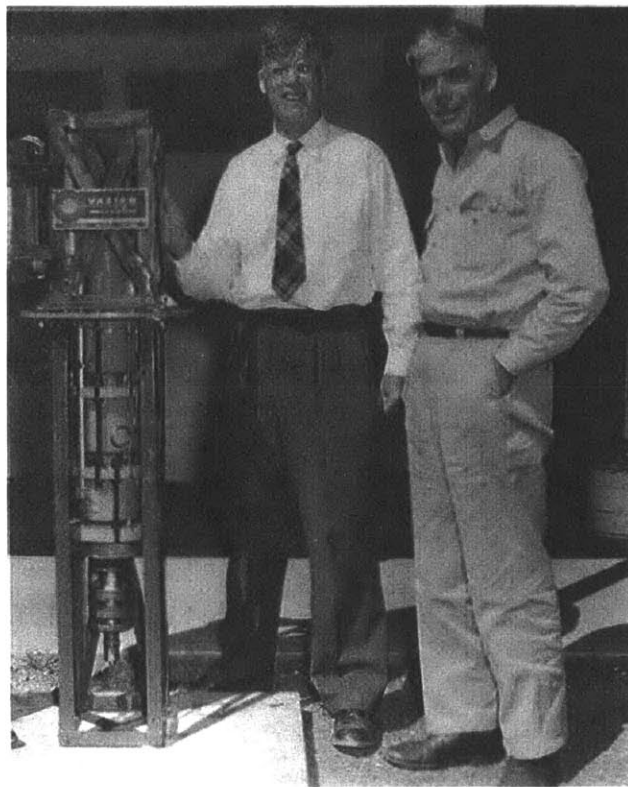


Figure 1-12: Photograph of the Varian brothers with one of their klystron tubes [28].

developed at Stanford University and has become synonymous with the Stanford Linear Accelerator Center (now SLAC National Accelerator Laboratory), Stanford originally only provided the Varian brothers with \$100 to carry out their work [26]. A photograph of the Varian brothers with their klystron invention is shown in Fig. 1-12. A simplified schematic of the klystron tube is shown in Fig. 1-13.

The klystron uses a velocity modulated electron beam and electromagnetic cavities

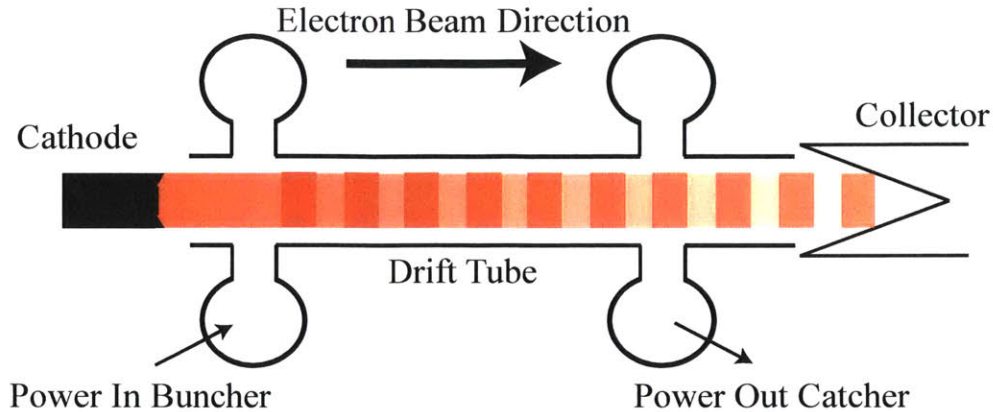


Figure 1-13: Schematic of a simplified two-cavity klystron design. The design shows a DC electron beam formed by an electron gun (the cathode) that is bunched by a buncher cavity. A drift tube separates the buncher from the catcher cavity where the amplified microwave signal is coupled out.

to amplify coherent microwave radiation. Cavities with very high quality factors that utilize TM modes (an electromagnetic mode with an electric field parallel to the velocity of the electrons) are used to bunch an electron beam. The bunches in the electron beam grow as they travel through a drift section that is below-cutoff for the microwave signal. A magnetic field of moderate strength ($\approx 0.5T$) is used to confine and guide the electron beam through the cavities and down the drift tube, usually produced from several different solenoids. A catcher cavity is used to rapidly generate a microwave signal by decelerating the bunched electron beam where the AC current is maximum. A common way to display how velocity modulation is used to amplify microwaves in a klystron is with the so called ‘Applegate Diagram,’ which is shown in Fig. 1-14.

The Applegate Diagram illustrates how a sinusoidal velocity modulation in time (on the x-axis) results in a time varying AC current at the catcher cavity a particular distance away from the buncher cavity (the y-axis). In the figure the blue lines represent the electron trajectories, and the slope of a line is the velocity of the electrons. The transit angle of the electron bunches in the catcher cavity $\theta_{catcher} = \omega L_{catcher}/v_z$ cannot exceed π to maintain optimal phasing between the electron bunches and the

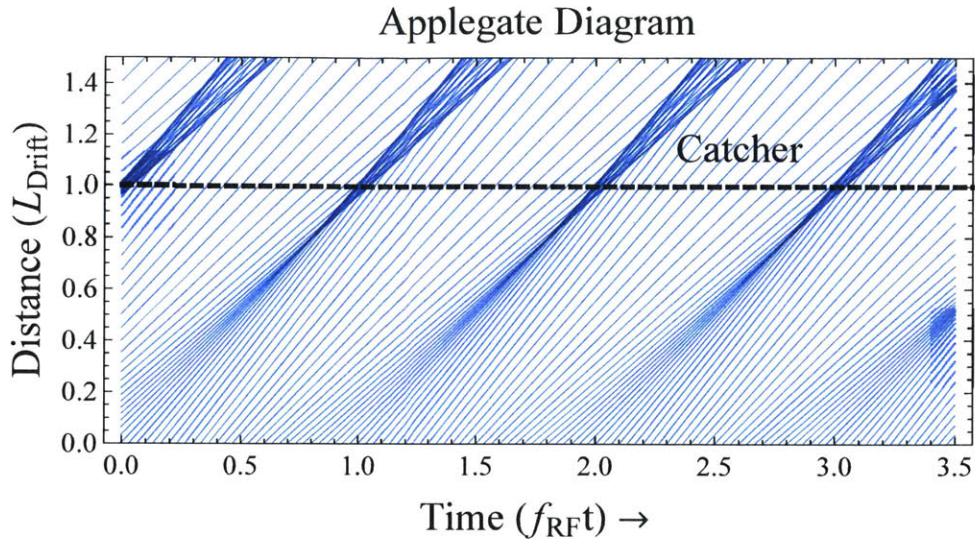


Figure 1-14: Applegate diagram shows how modulated electron velocities from a bunching cavity result in current modulation at a catcher cavity. Electrons velocities are modulated by a time-varying microwave signal in the bunching cavity at $y = 0$ and excite an electromagnetic mode in a catcher cavity at $y = L_{Drift}$ where L_{Drift} is the distance between the catcher and buncher cavities.

microwave field. This requires a short cavity length relative to the wavelength of operation. Both this condition and the requirement that the drift tube between the buncher and catcher cavities be below-cutoff limits the maximum power achievable as the frequency is increased beyond X-band. In some klystrons many cavities or electron beams may be used in order to overcome problems associated with microwave breakdown or reduced beam-wave interaction.

1.3.3 Radiation by Accelerating Charges

Charges that undergo acceleration due to a magnetic or electric field will radiate. Bremsstrahlung describes the radiation from charged particle collisions and is commonly observed in nature. Positrons and electrons emitted during beta decay undergo Bremsstrahlung as they are rapidly accelerated in the parent nucleus [6]. Bremsstrahlung also occurs plasmas, in which Coulomb collisions between charged particles results in radiation due to their acceleration. In general the radiation produced by these natural processes has a very wide spectrum and is not coherent. Some X-ray tubes

also rely on Bremsstrahlung, where electrons which are accelerated to high energy collide with a metallic anode in order to generate X-rays.

Charges can also be accelerated by an externally applied, static magnetic field. This kind of radiation is the basis for many types of vacuum electron devices such as synchrotrons, free electron lasers, and gyrotrons. Electrons moving perpendicular to a spatially uniform magnetic field will orbit around the field lines due to the Lorentz force. The acceleration from the curved orbit results in radiation. At very high energies, the radiation is called synchrotron radiation, while for moderate electron energy the radiation is generally referred to as cyclotron radiation [29]. Both of these radiation mechanisms will in general produce incoherent radiation.

Gyrotron Devices

The gyrotron oscillator is a microwave tube that relies on induced cyclotron radiation to produce coherent narrow band microwave radiation. Gyrotrons are the highest power sources of microwave radiation in the millimeter-wave region where klystrons and TWT structures are impractical to build due to the difficulty in fabricating interaction structures which must be on the order of the wavelength. In this respect, what makes the gyrotron so successful from a practical point of view is the ability to use overmoded cavities to produce microwaves. This means the dimensions of the cavities they use can be fairly large compared to their operation wavelength. Also, unlike klystrons and TWTs, which extract energy from the velocity component parallel to both the beam direction and magnetic field, gyrotrons extract energy from the energy associated with the components of the electron velocity that are perpendicular to the beam direction and magnetic field. A simplified schematic of a gyrotron oscillator is shown in Fig. 1-15.

Electrons in a strong magnetic field will gyrate in Larmor orbits of radius $r_L = v_{\perp}/\omega$, where r_L is the Larmor radius, $\Omega = eB_z/m_e\gamma$ is the relativistic cyclotron frequency, γ is the beam energy, and v_{\perp} is the electron velocity component perpendicular to the magnetic field. For a ring of electrons interacting with an electromagnetic wave with frequency $\omega \approx s\Omega$, where s is the cyclotron harmonic, the electrons will tend to

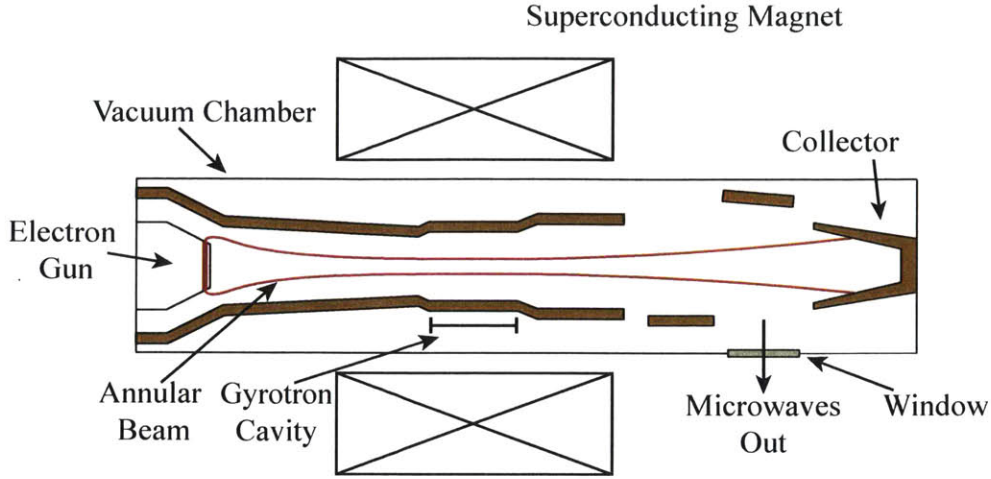


Figure 1-15: Schematic of a simplified gyrotron oscillator. The electron gun is on the left and produces an annular electron beam with a large transverse velocity. The large superconducting magnet compresses the beam, and microwaves are generated in the small gyrotron cavity in the flat-top portion of the magnetic field.

form electron bunches which can then transfer their kinetic energy to the electromagnetic wave [30]. In a gyrotron device, however, an annular electron beam (traveling at slightly relativistic velocities where $\gamma \approx 1.25$) is used to interact with a fast $TE_{m,n}$ mode. Therefore the condition for energy transfer between the electrons and the $TE_{m,n}$ mode is given by the Doppler shifted cyclotron resonance condition, which is given by the equation

$$\omega = k_z v_z + \frac{s\omega}{\gamma} \quad (1.3.8)$$

For an electron that loses energy to a co-propagating wave, both the axial component of velocity will change as well as the cyclotron frequency Ω . One special case that is interesting is when these two changes nearly cancel, which causes an electron initially in resonance to stay in resonance. This effect is called ‘autoresonance.’

Gyrotrons may also be used as microwave amplifiers, sometimes called Gyro-TWTs or Gyroklystrons. The dispersion curve for a gyrotron oscillator and Gyro-TWT is shown in Fig. 1-16.

While gyrotrons are normally designed to interact with the normal Doppler shifted

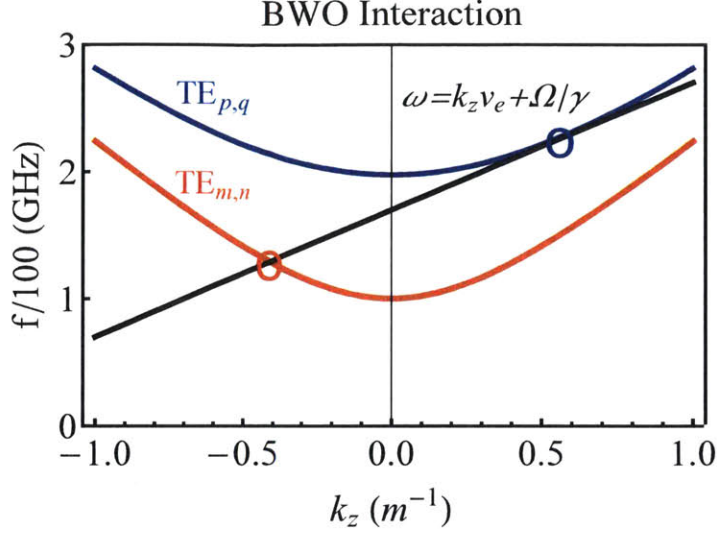


Figure 1-16: Diagram of the gyro-BWO interaction with the $TE_{m,n}$ mode at 125 GHz (red circle) and gyro-TWT interaction with the $TE_{p,q}$ mode at 225 GHz (blue circle). The interaction uses the first ($s = 1$) cyclotron harmonic.

cyclotron resonance condition and therefore use a fast wave ($v_\phi > c$), there is also the possibility for an interaction at the anomalous Doppler shifted resonance when an electron beam interacts with a slow wave ($v_\phi < c$) [31, 32, 33]. Obviously this requires a different type of interaction structure than most gyrotrons, which generally interact with one of the fast waves of a cylindrical metal cavity. Mathematically, the anomalous doppler interaction relies on the resonance condition given by the equation

$$\omega = k_z v_z - \frac{s\omega}{\gamma} \quad (1.3.9)$$

In Ref. [30], the author points out that in terms of the quantum theory often used to describe gyro-devices, electrons simultaneously radiate photons and transition to higher perpendicular energy levels, where the energy for this transition is taken from the axial motion of the electrons. Therefore, in devices that make use of the anomalous Doppler effect, an electron beam with zero initial perpendicular velocity can be used. Gyro-devices that make use of the ‘normal’ doppler effect must use an electron beam which has a significant amount of perpendicular energy, usually provided by a magnetron injection gun (MIG). Despite not needing a MIG, building a slow-wave

structure adds to the complexity of the device and so there are a relatively small number of experimental devices that make use of the anomalous doppler effect [34]. The dispersion curve for the anomalous Doppler interaction is shown in Fig. 1-17.

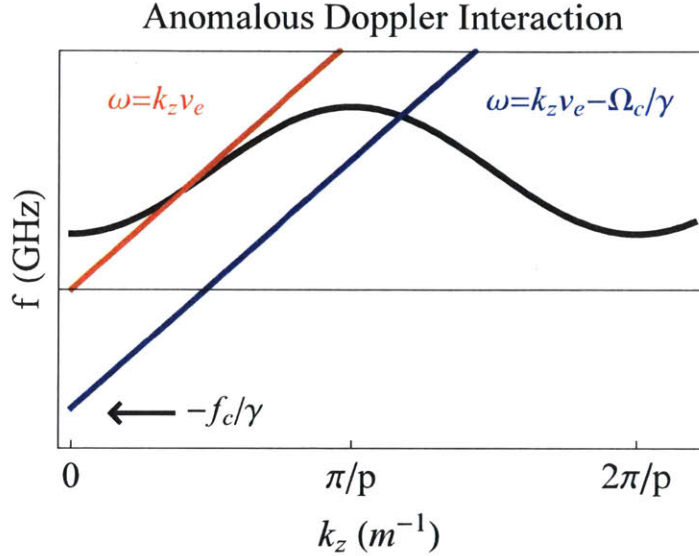


Figure 1-17: Diagram of the anomalous Doppler interaction with a slow wave mode. The doppler shifted beam line is drawn in blue, and the Cherenkov resonance is drawn in red for reference.

Because gyrotrons are the only source of high power microwaves in the millimeter-wave regime they have a wide variety of different applications. Very high power (greater than 1 MW) continuous-wave gyrotrons at 110 and 170 GHz have been developed for fusion research in electron-cyclotron heating (ECH) for tokamak plasmas. In addition, gyrotrons are used for some niche materials processing applications where the use of microwave heating is advantageous, but the low loss tangent of the material to be heated (such as in glasses or ceramics) does not allow the use of lower frequency microwave devices which in general are usually less expensive to build. An exciting new application area is in NMR spectroscopy, where a gyrotron is used in order to increase nuclear spectroscopic signals by factors greater than 100 [35]. A photograph of a Communication and Power Industries (CPI) gyrotron developed for fusion research is shown in Fig. 1-18.

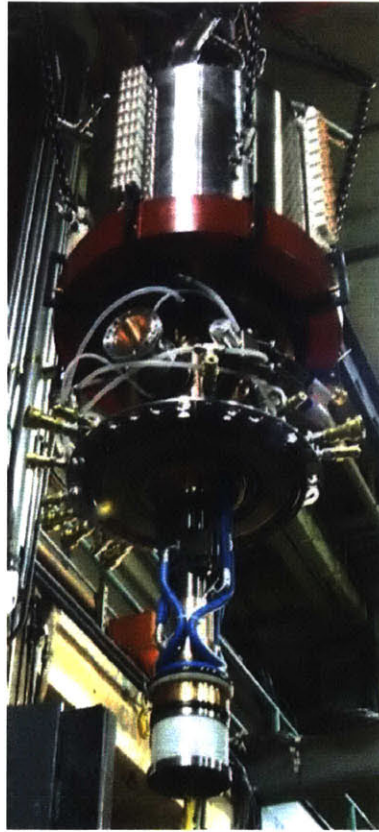


Figure 1-18: Photograph of a VGT-8110 Gyrotron Oscillator gyrotron which was designed and built by CPI. The electron gun is in the very bottom of the photo and the very large water cooled collector, which is designed to handle all of the power from the spent beam, is on the top of the photograph [36].

1.4 An Electron-Beam Powered Metamaterial

While research on electromagnetic metamaterials is a decade-old field of study, there are still many unexplored new applications. One such area is in the design of active metamaterials [37, 38]. As the name implies this field makes use of passive metamaterial components in conjunction with active elements—solid state devices, plasmas, and electron beams. The theory of the electron beam powered metamaterial was first developed by Shapiro et. al. in 2012, where it was shown that the dispersion of a negative index material powered by an electron beam is analogous to the linear theory of the TWT [39]. From the discussion of slow-wave devices above, it has been established that electron beams can be used to generate microwaves when they have a

high enough current to interact with a spatial harmonic of a periodic structure. Here noise from the electron beam is amplified at the frequency where feedback is met, or where the resonance condition is established. Several attempts to theoretically investigate metamaterial devices that use electron beams for microwave generation [40, 41, 42, 43, 44] and particle acceleration [45, 46] have previously been made. In addition, some experiments have been performed where incoherent microwave generation from electron bunches and metamaterial structures was observed [47]. However, coherent microwave generation from a metamaterial loaded waveguide with an electron beam, where the metamaterial is composed of subwavelength *and* resonant periodic structures, has yet to be experimentally demonstrated. This was the primary aim of this thesis, and this goal was achieved and the results are presented in detail in Chapter 4. A 370 mm long metamaterial structure with a particular design (MTM2-see Chapter 2) that uses periodically spaced CSRRs with a 10 mm period was used in order to generate over 5 MW of microwave power at 2.4 GHz.

In addition to the first experimental demonstration of microwave generation from a device that uses a metamaterial-based interaction circuit and an electron beam, this work also has several additional research ambitions. First, and most obvious, is the characterization of the performance of metamaterial based vacuum electron devices. In particular it is important to understand what specific advantages metamaterial devices have over conventional slow-wave vacuum electron devices, if any. The metamaterial structure investigated is a planar structure formed from metal plates. Large scale manufacturing of a device with planar (2D) elements is inherently simpler and easier to fabricate than a structure that has a 3D interaction slow-wave structure, as is the case with a rippled-wall or coupled-cavity device. It is also important to investigate the potential advantages of using a waveguide below cutoff, which allows the transverse dimensions of the structure to be much smaller than a wavelength. This is important in the miniaturization of low frequency (<10 GHz) microwave generators and amplifiers where structure size can be important. In addition, it is essential to understand some of the nonlinear effects of the unique HPM environment that affect the design and performance of metamaterials at high power. In the chapters that

follow we present the design, simulation, low-power test, and high-power test of a metamaterial loaded waveguide.

1.5 Summary of Thesis Contributions

This thesis presents the first experimental demonstration of coherent, high power microwave generation from a metamaterial interacting with an electron beam. Three different metamaterial designs are presented: MTM1, MTM2, and MTM3 with design frequencies of 2.8, 2.4, and 3.7 GHz, respectively. The most significant results came from a structure that was built with the MTM2 design (see section 2.2.3 and 4.3.2) that was 370 mm long, which is summarized here. Multi-megawatt output power levels were achieved at a frequency near 2.39 GHz using a 490 keV, 84 A electron beam. In Fig. 1-19 an example trace is shown which has a peak power of 2.3 MW and uses a gun voltage of 400 keV and 60 A. This particular trace is shown because it had an efficiency of approximately 10%. For a more detailed description of the figure and the operating conditions in which it was taken, see Fig. 4-21 and the surrounding discussion. The result shown in Fig. 1-19 is the first experimental demonstration that a metamaterial and an electron beam can be used to generate coherent, high power microwaves.

The possibility of generating microwave radiation from an electron beam and a metamaterial via a reverse Cherenkov interaction has been extensively studied in the literature [39, 40, 41, 42, 43, 45, 46, 47]. However, to the author's knowledge, microwave generation from an electron beam interacting with a cyclotron mode of a metamaterial has not been discussed. The MTM2 structure supports two different modes, a symmetric mode that is observed to have a Cherenkov interaction, and an antisymmetric mode that is observed to have an anomalous Doppler or cyclotron-Cherenkov interaction. A significant discovery of this thesis was that multi-megawatt operation was observed with the anomalous Doppler interaction and not the Cherenkov interaction, especially given the previous theoretical work. This discovery was confirmed in experiment by the frequency tuning of the device, which followed the

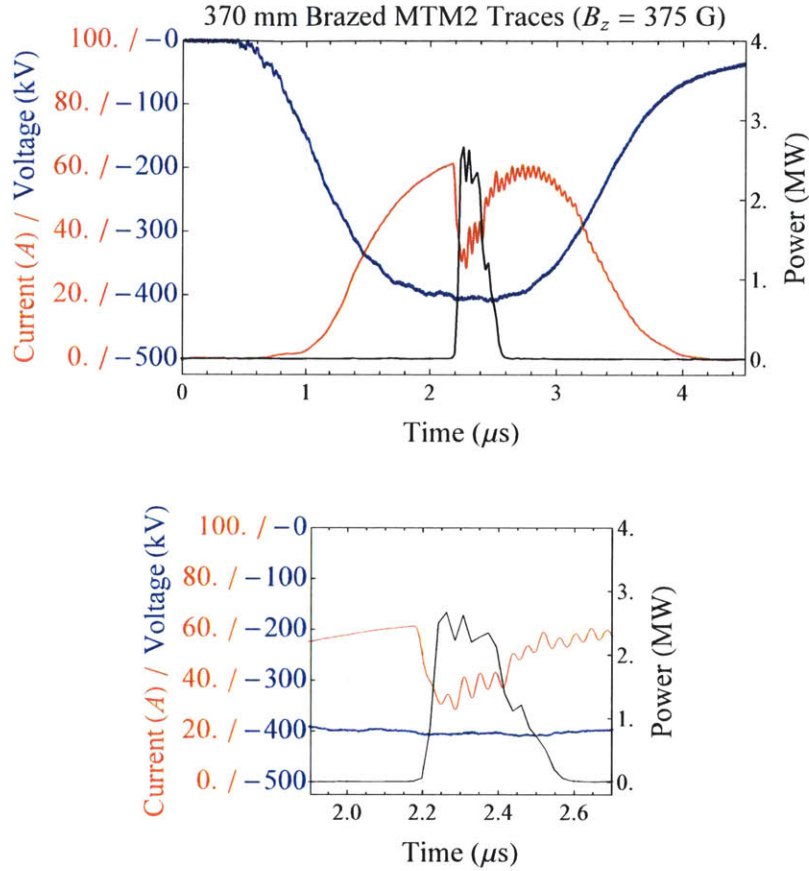


Figure 1-19: Microwave power (black curve), electron gun voltage (blue curve) and measured collector current (red curve) for an applied magnetic field of 375 G. The scale for the current (voltage) is given on the left in red (blue) and the scale for the microwave power is given on the right in black. The lens current was set at 10.1 A. A blow up of the high power trace is also shown below.

anomalous Doppler resonance condition. A plot of the experimental frequency, PIC simulation frequency, and theoretical frequency predicted by the anomalous Doppler interaction are shown in Fig. 1-20. For a more detailed description of the results shown in Fig. 1-20 see Fig. 4-25 and the surrounding discussion. Despite the good agreement between theory, simulation, and experiment for the anomalous Doppler interaction with the antisymmetric mode, poor agreement between simulation and experiment was achieved with regard to the output power of the metamaterial structure for the Cherenkov interaction with the symmetric mode. This highlights an important area

for future research to develop better a better theory and/or simulations that match the experimental results obtained in this thesis.

In addition to the novel physical results that were just discussed, the research presented in this thesis was done in a structure that is undersized (smaller transverse dimensions-63 mm by 43 mm) than conventional microwave tubes (which generally are on the order of the wavelength, which at 2.4 GHz is 125 mm). This may have practical benefits for device miniaturization for some microwave device applications.

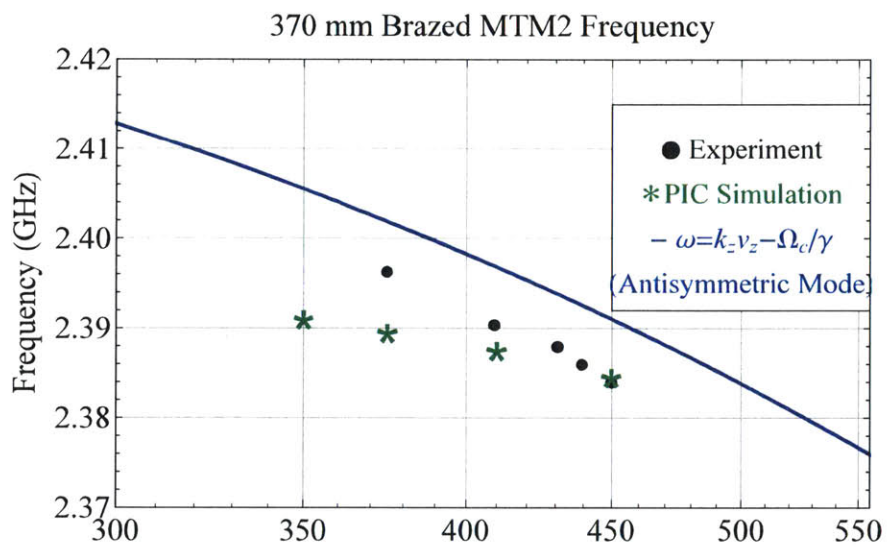


Figure 1-20: Frequency tuning of the 370 mm MTM2 structure. All of the green star data points are those obtained from PIC simulations, and the black data points are the experimentally measured values. The power plot shows a distinct transition at about 430 G where the device starts to produce high power in the antisymmetric mode, and a transition at about 750 G where the device switches from antisymmetric to symmetric mode excitation.

Chapter 2

Metamaterial Circuit Design

In this chapter we outline the general theory and specific simulation tools that went into the design of a beam-powered, metamaterial waveguide. First the general electromagnetic description of a metamaterial filled waveguide is presented. Following this, eigenmode and PIC simulations are discussed which were used to characterize the performance of the metamaterial BWO design. Finally low-power measurements are shown to benchmark the simulation tools vs. experiment.

2.1 Theory of A Metamaterial Filled Waveguide

We wish to solve for the lowest order TM modes in a rectangular metallic waveguide, where $H_z = 0$. The waveguide extends from one of its corners at $x = 0, y = 0$ to its other corner at $x = a, y = b$, is perfectly conducting, and is filled with a dielectric. The general model of the waveguide is shown in Fig. 2-1. The dielectric completely

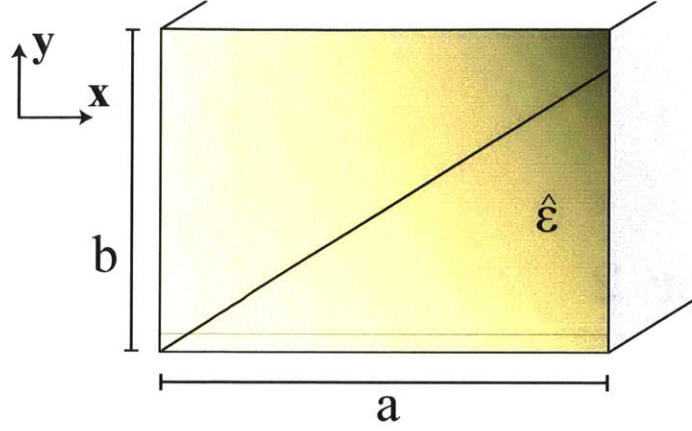


Figure 2-1: Graphical illustration of the metallic waveguide that is filled with a theoretical dielectric of permittivity $\hat{\epsilon}$ and permeability $\hat{\mu}$.

fills the waveguide, and has a permittivity and permeability

$$\hat{\epsilon} = \epsilon_0 \begin{bmatrix} \epsilon_{xx} & 0 & 0 \\ 0 & \epsilon_{yy} & 0 \\ 0 & 0 & \epsilon_{zz} \end{bmatrix} \quad (2.1.1)$$

$$\hat{\mu} = \mu_0 \begin{bmatrix} 1 & 0 & 0 \\ 0 & 1 & 0 \\ 0 & 0 & 1 \end{bmatrix}$$

To solve for the propagating waves in the waveguide we assume time-harmonic fields that depend on time as $e^{-i\omega t}$. We can then write Maxwell's Equations as [48]

$$\begin{aligned} \nabla \times \vec{E} &= -i\omega\hat{\mu}\vec{H} \\ \nabla \times \vec{H} &= i\omega\hat{\epsilon}\vec{E} \end{aligned} \quad (2.1.2)$$

The waveguide is also uniform in the z direction and so we can assume that the fields also depend on z as $e^{ik_z z}$. After expanding out Eq. 2.1.2 we obtain the following set

of equations which are valid for TM waveguide modes.

$$\begin{aligned}
\frac{\partial E_z}{\partial y} + ik_z E_y &= -i\mu_0\omega H_x \\
-ik_z E_x + \frac{\partial E_z}{\partial x} &= -i\mu_0\omega H_y \\
\frac{\partial E_y}{\partial x} - \frac{\partial E_x}{\partial y} &= 0 \\
ik_z H_y &= i\omega\epsilon_0\epsilon_{xx}E_x \\
-ik_z H_x &= i\omega\epsilon_0\epsilon_{yy}E_y \\
\frac{\partial H_y}{\partial x} - \frac{\partial H_x}{\partial y} &= i\omega\epsilon_0\epsilon_{zz}E_z
\end{aligned} \tag{2.1.3}$$

Combining Eqns. 2.1.3 we arrive at the ‘wave equations’ (which have now been reduced to the form of Helmholtz’s equation after a change of variables is made) for E_y and E_x

$$\begin{aligned}
\epsilon_{xx} \frac{\partial^2 E_y}{\partial x^2} + \epsilon_{yy} \frac{\partial^2 E_y}{\partial y^2} + \epsilon_{zz} \left[\left(\frac{\omega}{c} \right)^2 \epsilon_{yy} - k_z^2 \right] E_y &= 0 \\
\epsilon_{xx} \frac{\partial^2 E_x}{\partial x^2} + \epsilon_{yy} \frac{\partial^2 E_x}{\partial y^2} + \epsilon_{zz} \left[\left(\frac{\omega}{c} \right)^2 \epsilon_{xx} - k_z^2 \right] E_x &= 0
\end{aligned} \tag{2.1.4}$$

After finding a solution for E_y and E_x it is straightforward to find the various field components and solve for the dispersion relation in the waveguide for the lowest order TM mode (e.g. analogous to the TM_{11} mode of a rectangular waveguide and the TM_{01} mode of a circular waveguide) from Eqns. 2.1.3. We now consider the solution to these equations for two different cases of $\hat{\epsilon}$.

2.1.1 For $\epsilon_{xx} = \epsilon_{yy} = \epsilon_{zz} = 1$

This is the case of a vacuum filled rectangular waveguide. Eqns. 2.1.4 can be solved by assuming a separated solution of the form $E_y(x, y, z, t) = A_0\chi(x)\psi(y)e^{ik_z z - i\omega t}$ and then solving for $\chi(x)$ and $\psi(y)$. All of the field components can then be readily obtained from Eqns. 2.1.3. Using the boundary condition on the metal walls, we can

readily solve to obtain the following fields for the lowest order mode

$$\begin{aligned}
E_z &= E_0 \operatorname{Sin}\left(\frac{\pi y}{b}\right) \operatorname{Sin}\left(\frac{\pi x}{a}\right) \\
E_x &= \frac{-ik_z\pi}{ak_c^2} E_0 \operatorname{Sin}\left(\frac{\pi y}{b}\right) \operatorname{Cos}\left(\frac{\pi x}{a}\right) \\
E_y &= \frac{-ik_z\pi}{bk_c^2} E_0 \operatorname{Cos}\left(\frac{\pi y}{b}\right) \operatorname{Sin}\left(\frac{\pi x}{a}\right) \\
H_x &= \frac{i\omega\pi\epsilon_0}{bk_c^2} E_0 \operatorname{Cos}\left(\frac{\pi y}{b}\right) \operatorname{Sin}\left(\frac{\pi x}{a}\right) \\
H_y &= -\frac{i\omega\pi\epsilon_0}{ak_c^2} E_0 \operatorname{Sin}\left(\frac{\pi y}{b}\right) \operatorname{Cos}\left(\frac{\pi x}{a}\right)
\end{aligned} \tag{2.1.5}$$

Here we have defined the cutoff wavenumber and the propagation constant by

$$\begin{aligned}
k_c &= \sqrt{\left(\frac{\pi}{a}\right)^2 + \left(\frac{\pi}{b}\right)^2} \\
k_z &= \sqrt{\left(\frac{\omega}{c}\right)^2 - k_c^2}
\end{aligned} \tag{2.1.6}$$

The cutoff frequency is given by the equation

$$\omega_c = c\sqrt{\left(\frac{\pi}{a}\right)^2 + \left(\frac{\pi}{b}\right)^2} \tag{2.1.7}$$

Eq. 2.1.6 defines the dispersion relation for the lowest order TM mode of this waveguide which is well known [48]. The dispersion of this mode is shown in Fig. 2-2 for $\pi/a = \pi/(2b)$ along with the dispersion curve of a free space electromagnetic wave which is given by $\omega = k_z c$. The dispersion of Eq. 2.1.6 is positive and the mode is a fast wave, which means it cannot interact with an electron beam.

2.1.2 For a Lorentzian $\epsilon_{xx} = \epsilon_{yy}$ and $\epsilon_{zz} = 1$

To model an anisotropic metamaterial with an electric response in the direction perpendicular to wave propagation we set $\epsilon_{zz} = 1$ and $\epsilon_{xx} = \epsilon_{yy} = \epsilon_L$, where

$$\epsilon_L = (1 - F) \frac{\omega^2 - \frac{\omega_0^2}{1-F}}{\omega^2 - \omega_0^2} \tag{2.1.8}$$

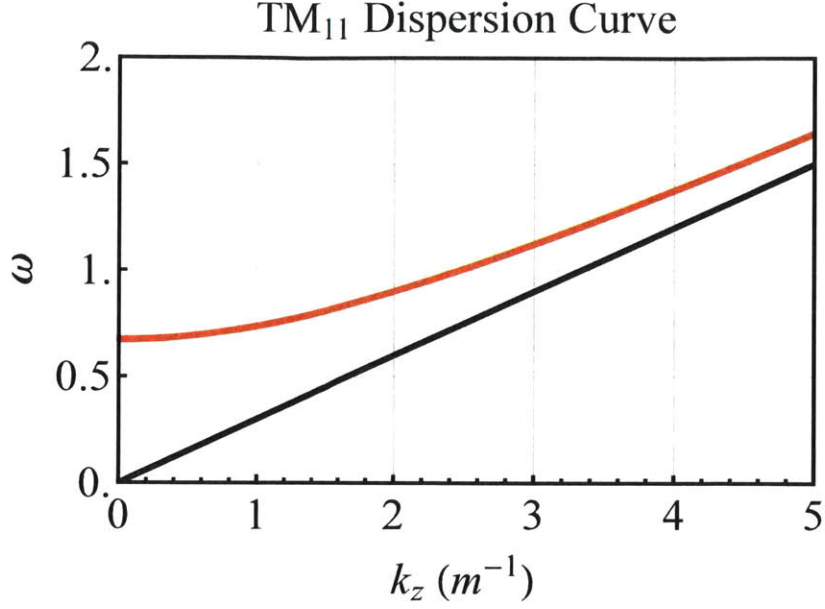


Figure 2-2: Dispersion curve for the lowest order TM_{11} mode in a vacuum filled rectangular waveguide for $(\pi/a)^2 = (\pi/(2b))^2 = 1$. Also shown is the dispersion curve of a wave in free space $\omega = k_z c$.

where F is the filling factor (typical value ~ 0.9) and is determined by the geometry of the metamaterial unit cell and ω_0 is the resonant frequency. Then the fields can be solved in the same manner as before

$$\begin{aligned}
 E_z &= E_0 \sin\left(\frac{\pi y}{b}\right) \sin\left(\frac{\pi x}{a}\right) \\
 E_x &= \frac{-ik_z \pi}{ak_c^2 \epsilon_L} E_0 \sin\left(\frac{\pi y}{b}\right) \cos\left(\frac{\pi x}{a}\right) \\
 E_y &= \frac{-ik_z \pi}{bk_c^2 \epsilon_L} E_0 \cos\left(\frac{\pi y}{b}\right) \sin\left(\frac{\pi x}{a}\right) \\
 H_x &= \frac{i\omega \pi \epsilon_0}{bk_c^2} E_0 \cos\left(\frac{\pi y}{b}\right) \sin\left(\frac{\pi x}{a}\right) \\
 H_y &= -\frac{i\omega \pi \epsilon_0}{ak_c^2} E_0 \sin\left(\frac{\pi y}{b}\right) \cos\left(\frac{\pi x}{a}\right)
 \end{aligned} \tag{2.1.9}$$

where the propagation constant k_z and the cutoff wavenumber k_c are defined by the expressions

$$\begin{aligned} k_c &= \sqrt{\left(\frac{\pi}{a}\right)^2 + \left(\frac{\pi}{b}\right)^2} \\ k_z &= \sqrt{\epsilon_L \left(\frac{\omega}{c}\right)^2 - \epsilon_L k_c^2} \end{aligned} \quad (2.1.10)$$

Eq. 2.1.10 defines the dispersion relation for the lowest order TM mode of this waveguide. Interestingly, because of the addition of the Lorentz response in the dispersion relation, the dispersion relation now depends on the values of a , b , ω_0 , and F . Depending on the relative values of these parameters, the dispersion can either be positive or negative. For purposes of illustration we now define the transition frequency ω_t by

$$\omega_t = c \sqrt{(1 - F) \left(\left(\frac{\pi}{a}\right)^2 + \left(\frac{\pi}{b}\right)^2 \right)} \quad (2.1.11)$$

The dispersion is sensitive to the relative value of ω_0 and ω_t . When $\omega_0 > \omega_t$, the resonance is well above the cutoff of the equivalent vacuum filled waveguide and modifies the dispersion curve defined by Eq. 2.1.6 as $\omega \rightarrow \omega_0$. The lowest order *TM* mode is no longer a fast-wave, but intersects the light line with positive group velocity. This type of dispersion curve is analogous to one used in a TWT amplifier [26]. For $\omega_0 < \omega_t$, the resonance of the dielectric is below the cutoff frequency of the equivalent vacuum filled waveguide and allows for a new mode with negative dispersion (negative group velocity). This type of dispersion curve is analogous to one used in a BWO [26]. However, this mode may exist in a uniform waveguide that can be well below-cutoff, or where the dimension of the waveguide is much smaller than the wavelength. For $\omega_0 \approx \omega_t$ the dispersion curve is nearly flat due to the strong resonance near the cutoff of the vacuum equivalent waveguide. The dispersion curve for the lowest order *TM* mode with $\omega_0 > \omega_t$, $\omega_0 = \omega_t$, and $\omega_0 < \omega_t$ is shown in Fig. 2-3 along with the dispersion curve of free space $\omega = k_z c$.

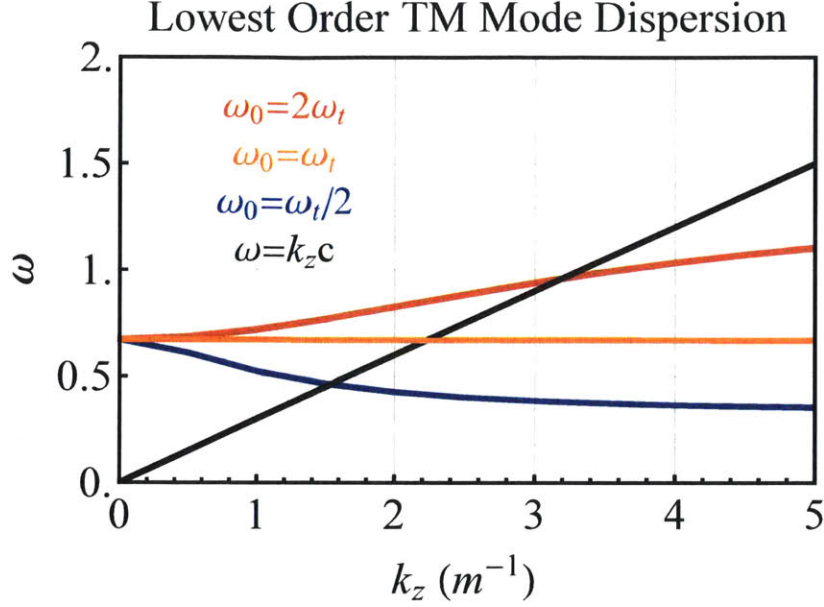


Figure 2-3: Dispersion curve for the lowest order TM_{11} mode in a dielectric filled rectangular waveguide where ϵ_{xx} and ϵ_{yy} are defined by Eq. 2.1.8. For the red curve $(\pi/a)^2 = (\pi/(2b))^2 = 1$, $F = 0.9$ and $\omega_0 = 2\omega_t$. Because the resonance is above ω_t the dispersion is positive. For the orange curve $(\pi/a)^2 = (\pi/(2b))^2 = 1$, $F = 0.9$ and $\omega_0 = \omega_t$. Because the resonance is equal to ω_t the dispersion is nearly flat. For the blue curve $(\pi/a)^2 = (\pi/(2b))^2 = 1$, $F = 0.9$ and $\omega_0 = 0.5\omega_t$. Because the resonance is below ω_t the dispersion is negative. Also shown is the dispersion curve $\omega = k_z c$ in black.

2.1.3 A Uniform Metamaterial Slab with an Electric and Magnetic Response

The effect that the waveguide has on the dispersion of the lowest order TM mode becomes more clear when we compare wave propagation in the waveguide in subsection 2.1.2 to an even simpler case where a wave is incident on a slab of isotropic material with both a magnetic and electric response defined by

$$\begin{aligned} \epsilon &= (1 - F) \frac{\omega^2 - \frac{\omega_0^2}{1-F}}{\omega^2 - \omega_0^2} \\ \mu &= 1 - \frac{\omega_c^2}{\omega^2} \end{aligned} \quad (2.1.12)$$

Where ω_c is the cutoff frequency of the material. Now the dispersion relation in the slab is found by relating the index to the constitutive parameters as $n = \sqrt{\epsilon\mu}$ in order to obtain

$$k_z = \frac{\omega}{c} \sqrt{(1-F) \frac{\omega^2 - \frac{\omega_0^2}{1-F}}{\omega^2 - \omega_0^2} \left(1 - \frac{\omega_c^2}{\omega^2}\right)} \quad (2.1.13)$$

For the appropriate choice of ω_c this is identical to the expression encountered earlier in Eqn. 2.1.10. Therefore, the cutoff frequency of the rectangular waveguide (which is indirectly proportional to its dimensions) influences the dispersion in an equivalent way as to how the cutoff frequency influences the dispersion of the theoretical metamaterial slab. In the slab example, the resonant frequency of the permittivity must fall below the cutoff frequency in order to have negative dispersion, which is analogous to the waveguide example where the Lorentz resonance of the theoretical dielectric had to occur below the cutoff of the waveguide in subsection 2.1.2. Therefore, the size of the waveguide and the type of metamaterial that fills it affects the dispersion of a metamaterial filled waveguide. By tuning the parameters of the metamaterial and the waveguide we are able to tune the dispersion curve. The dispersion curve for the lowest order *TM* mode of the slab model with $\omega_0 = 0.33$, $\omega_c = 0.67$, and $F = 0.9$ is shown in Fig. 2-4 along with the dispersion curve of free space $\omega = k_z c$. The curve is identical to the curve of Fig. 2-3 when $\omega_0 = 0.5\omega_t$.

2.2 Electromagnetic Design

It is clear from the above discussion that a resonant metamaterial can significantly affect the dispersion of a waveguide. Thoughtful engineering of the metamaterial can result in a carefully controlled beam-wave interaction and mode dispersion. The ability to have precise control over waveguide dispersion is an attractive potential benefit of using metamaterials in vacuum electronics. With very precise manipulation of the dispersive properties of microwave generators and amplifiers there may be ways to demonstrate physical or practical advancements.

In a mode with negative dispersion, power flows anti-parallel to the electron

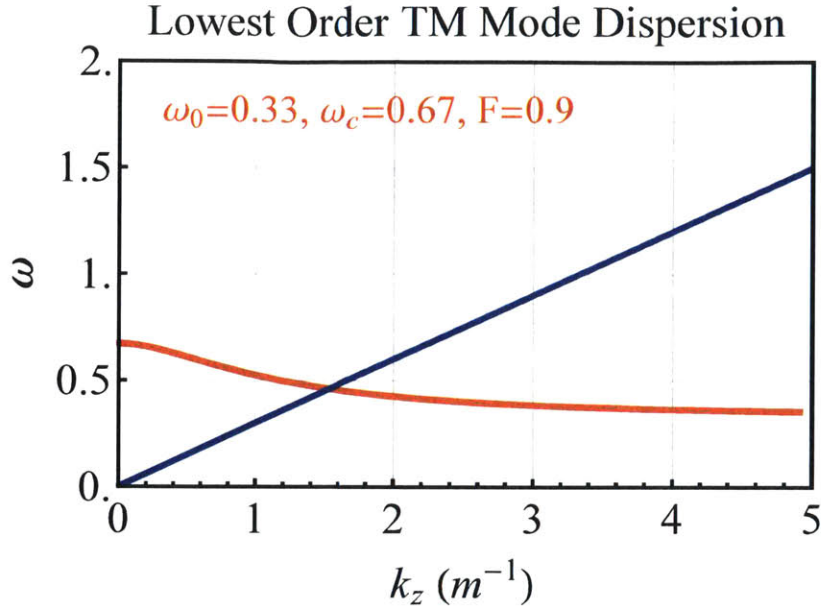


Figure 2-4: Dispersion curve for the lowest order TM_{11} mode in a dielectric slab with permittivity and permeability given by equations Eq. 2.1.12 with $\omega_0 = 0.33$ and $\omega_c = 0.67$, and $F = 0.9$.

beam's motion. While the interaction is similar in nature to a traditional BWO, it is unique in that a conventional BWO relies upon the interaction of an electron beam with spatial harmonics of a slow wave structure. In a negative index guide, a mode with negative group velocity is supported by the simultaneous negative permittivity and permeability of the guide. A related approach in creating structures that support modes with negative group velocity makes use of plasmonic waveguides [49, 50, 51, 52, 53, 54]. In contrast, the use of metamaterials in a waveguide provides a means to artificially duplicate the dispersive effect of the plasma without introducing the tricky engineering problem of producing and sustaining a plasma in a microwave tube while simultaneously sending a beam through it.

The above discussion of a waveguide filled with a theoretical negative permittivity resonant dielectric is only illustrative in nature. However, we now wish to extend the discussion to a waveguide filled with an actual metamaterial and show that the treatment of a metamaterial as a dielectric is accurate in some cases. Two different metamaterial based waveguides suitable for microwave generation will be introduced

after a motivation for the choice of metamaterials used is given.

2.2.1 Metamaterial Element Choice

It has already been stated that arrays of split-ring resonators (SRRs) can be used to produce an effective negative permeability in a bulk material [17]. When used in conjunction with a carefully designed array of metallic posts or a below-cutoff waveguide, SRRs can also be used to create a negative index medium with a simultaneous negative permeability and permittivity [18]. Unfortunately, the structures investigated in these early metamaterials are unsuitable for vacuum electronics for several reasons. First, these structures make use of SRRs, which must be printed on a dielectric. Even though there are vacuum-compatible dielectrics, they are not commonly used in many vacuum electronics applications because they can create problems with beam charging and decrease the breakdown threshold, which is of major concern for a high-power device.

Second, similar to our analysis in the above section, we wish to construct a waveguide that supports a negative group velocity TM mode in order to interact with a rectilinear electron beam. This means, as in the theoretical example, we wish to use a metamaterial that demonstrates a negative effective permittivity that may either have a Drude or Lorentz like response. Unfortunately, SRRs have a magnetic response and thus cannot be used.

Therefore, for our structure design we use the electric analog of the SRR, the complementary-SRR (CSRR) [55]. The CSRR was first proposed as a result of the theory of diffraction and the Babinet principle and was shown to possess a negative effective permittivity over a small frequency band due to its Lorentz-like electric response. The CSRR is particularly attractive to vacuum electronics applications because it is all metallic, robust, and eliminates the need to use lossy dielectrics which can limit microwave tube performance due to breakdown and charging. Moreover, because CSRRs can be machined from thin metal plates and inserted into prefabricated rectangular metallic waveguides they can allow for simple structure fabrication that only relies on 2D machining methods using a CNC. As long as the CSRRs are

designed to have a resonance below the cutoff of the waveguide for the TM mode, the waveguide should in theory behave like the dielectric filled waveguide investigated earlier.

In the following subsection, the particular design for the metamaterial plates of three different metamaterial structures, named MTM1, MTM2 and MTM3, is presented. The MTM1 and MTM2 metamaterial structures consist of an identical rectangular waveguide with metamaterial plates that are loaded with CSRRs. The metamaterial plates of MTM1 and MTM2 are slightly different, which affects their dispersive qualities. In addition, MTM3 is nearly identical to MTM2 except that it is scaled to operate at a higher frequency. In order to make the fields in the rectangular waveguides symmetric (with respect to the beam) two metamaterial plates are all the structure. Consequentially two different general types of modes exist in both structures, which are called antisymmetric and symmetric modes and are discussed in more detail in the subsection that follows (2.2.2). In the theoretical analysis of metamaterial structures it was also found that the geometrical arrangement of the metamaterial layers is shown to affect the types of modes they support [56].

2.2.2 MTM1 Design

The MTM1 structure is constructed by placing two periodic metamaterial plates into a rectangular waveguide. A CAD rendering of the MTM1 structure and metamaterial plate that it utilizes is shown in Fig. 2-5. In this figure the structure dimensions are labeled with corresponding variable names. Different values of the waveguide variables in Fig. 2-5 were investigated in simulation and experiment, however the values used for the high power microwave test are shown in Table 2.1. These particular dimensions and also the machining tolerances that went into the structure fabrication were chosen after numerous eigenmode simulations were performed to calculate the condition for beam-wave synchronism at S-Band frequencies. Consideration was made to align with other standard components purchased for the experiment, and after discussion with the MIT central machine shop where all structures were fabricated. The device can be easily scaled in order to be used at different frequencies.

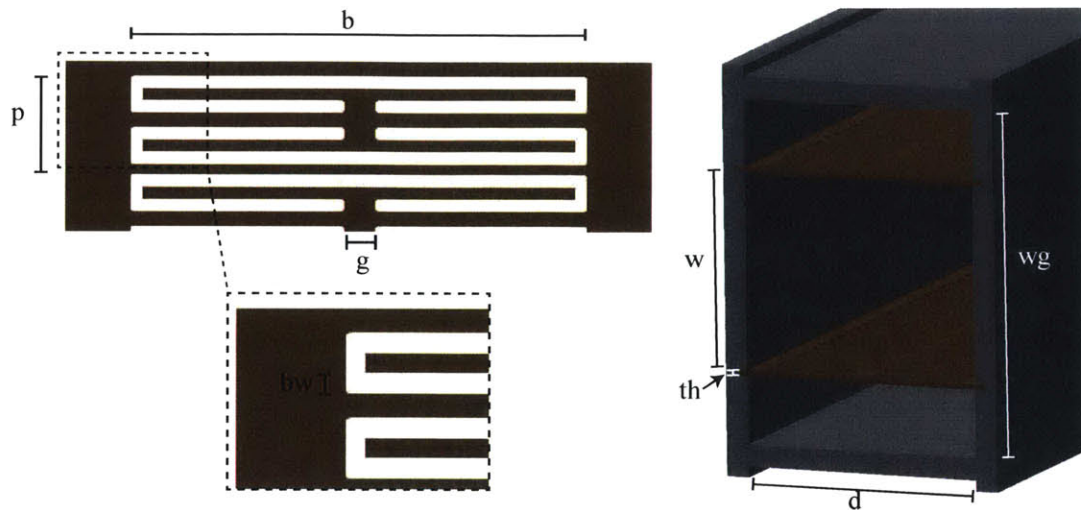


Figure 2-5: CAD rendering of the MTM1 structure on the right and one of the two identical metamaterial plates it uses on the left. Variable names for important dimensions are given, and values used for microwave testing are given in Table 2.1.

This metamaterial plate design makes use of dual CSRRs which are oriented parallel to each other. The resonant frequency of the CSRRs is designed to be below-cutoff for TM modes in the waveguide. The metamaterial plates are created by machining CSRRs with period $p = 8$ mm and width $b = 37$ mm along two metal plates of thickness $th = 1$ mm. The resonators have a slot width of $g = 2.5$ mm. These plates are then placed with a separation of $w = 36$ mm in a rectangular waveguide with inner dimensions $wg = 63$ mm by $d = 43$ mm.

The eigenmode solver of the ANSYS High Frequency Structure Simulator (HFSS) code and CST Microwave Studio (MWS) were used to simulate the eigenmodes of one period of the total structure, and the codes were found to be in agreement [57, 58]. Both codes are 3-D finite element electromagnetic field solvers. The eigenmodes are solved while enforcing a particular phase advance across the structure period in the direction of wave propagation. These simulations were repeated at different phase advances in order to find the dispersion of the waveguide modes (frequency vs. wavenumber). The eigenmode simulations also generate 3D E and H field vectors in the structure. These fields are important to visualize, but also can be used to estimate the beam-wave coupling and peak electric fields in the device.

Table 2.1: Dimensions of the MTM1 structure shown in Fig. 2-5 that were used in high power microwave testing.

Variable	Dimension (mm)
w	36
wg	63
d	43
b	37
g	2.5
bw	1
th	1
p	8

In general two types of modes were found in this structure, antisymmetric modes ($E_{z,axis}=0$) and symmetric modes ($E_{y,axis}=0$). The names ‘symmetric’ and ‘antisymmetric’ are used because they describe the symmetry of the electric field components across the imaginary plane lying in the center of the waveguide and parallel to both metamaterial plates. Antisymmetric modes can be found by enforcing an ‘E-wall’ boundary along the y axis symmetry plane between the two metamaterial plates, and the symmetric modes could be found by enforcing an ‘H-wall’ boundary condition along the same plane. The ‘E wall’ boundary represents a perfect electrical conductor and restricts the simulation to find modes where the electric field is perpendicular to the boundary, and the ‘H-wall’ boundary represents a perfect magnetic conductor and forces the tangential component of the H-field to be the same on both sides of the boundary.

The dispersion curves of the six lowest order modes calculated by the eigenmode solver are shown in Fig. 2-6. Also shown is the beam line $2\pi f = k_z v_0$ for a 500 keV electron beam, where $2\pi f$ is the angular frequency, c is the speed of light, k_z is the wavenumber, and $v_0 = 0.86 c$. The mode structure of the waveguide is clearly more complex than the waveguide investigated in the analysis of Section 2.1. The eigenmode solver calculates negative group velocity modes ($v_{gr} \equiv \frac{\partial\omega}{\partial k} < 0$) below the cutoff frequency of the TM_{11} mode in the empty rectangular waveguide ($f_c \approx 4.2$ GHz) as well as positive group velocity ($v_{gr} \equiv \frac{\partial\omega}{\partial k} > 0$) modes. In total there are

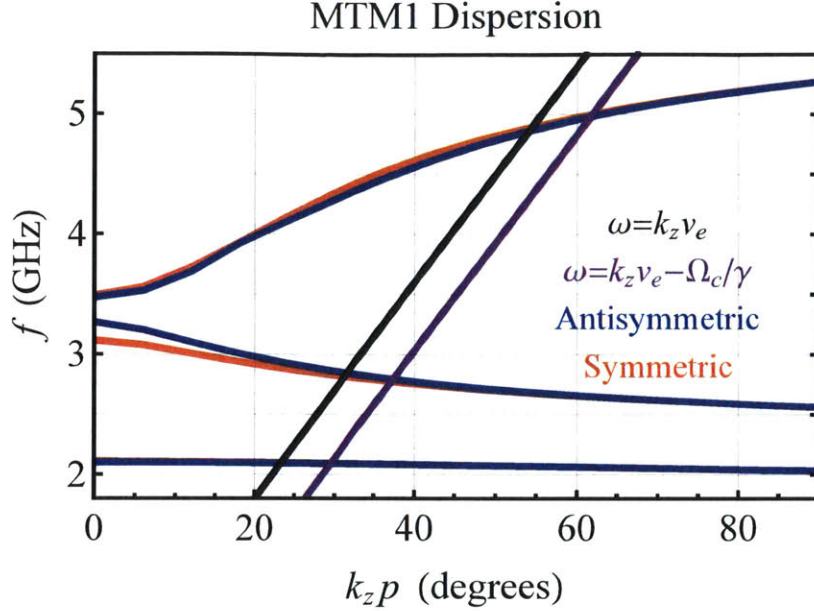


Figure 2-6: Dispersion relation for the six lowest order modes solved with the eigenmode solver of HFSS for one period of the MTM1 described by Fig. 2-5 and Table 2.1. The antisymmetric modes are in blue and the symmetric modes in red. There are four negative group velocity modes and two positive group velocity modes shown. Also shown is the beam line for a 500 keV electron beam (black) and the beam line corresponding to the anomalous Doppler shift in a magnetic field of 400 G (purple).

four negative group velocity modes in this waveguide that result from the insertion of the metamaterial plates. These four modes are analogous to the negative group velocity mode that was discovered in the waveguide filled with a dielectric possessing a Lorentz-like electric response, however due to both the symmetry in the metamaterial and the symmetry of the waveguide the singular negative group velocity mode has become four distinct modes.

To understand the differences between these modes it is instructive to look at the field profiles generated by the eigenmode solver. In Fig. 2-7 and Fig. 2-8 the field profiles of the three symmetric and three antisymmetric modes are shown, respectively. The fields are plotted for a phase advance of 24 (lower negative group velocity modes), 32 (upper negative group velocity modes), and 54 degrees (positive group velocity modes), which is the approximate phase advance of each of the modes corresponding to synchronism with a 500 keV beam. For each mode the vector field

MTM1 Field Patterns - Symmetric Modes ($E_{\text{axis}} \sim E_z$)

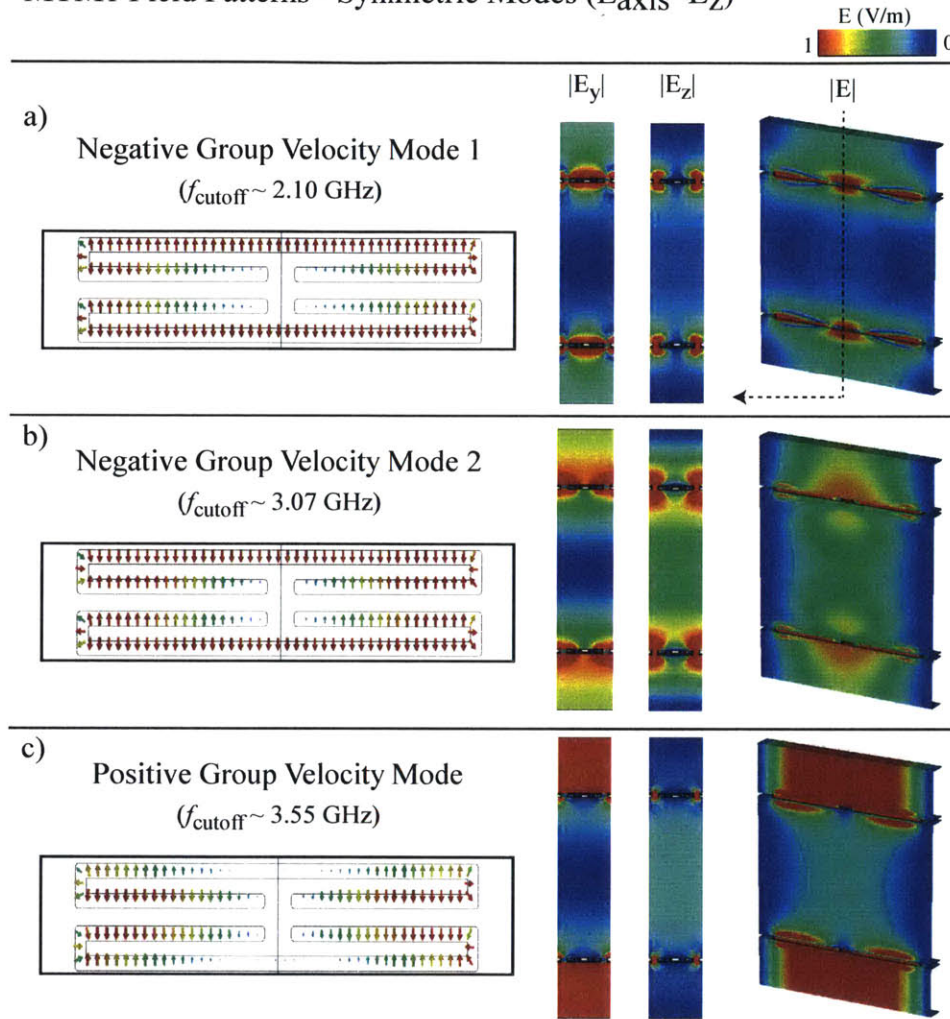


Figure 2-7: Field profiles of the three symmetric modes (red curves of Fig. 2-6) of MTM1. Shown are the vector field distributions within the CSRRs on the far left, the $|E_y|$ and $|E_z|$ fields on the symmetry plane that intersects the CSRRs along the center of the waveguide, and $|E|$ plotted on the plane that is normal to the electron beam direction. Note the difference between the vector fields of the two negative group velocity modes, and the difference between the $|E_y|$ and $|E_z|$ fields of these symmetric modes and antisymmetric modes of Fig. 2-8.

MTM1 Field Patterns - Antisymmetric Modes ($E_{\text{axis}} \sim E_y$)

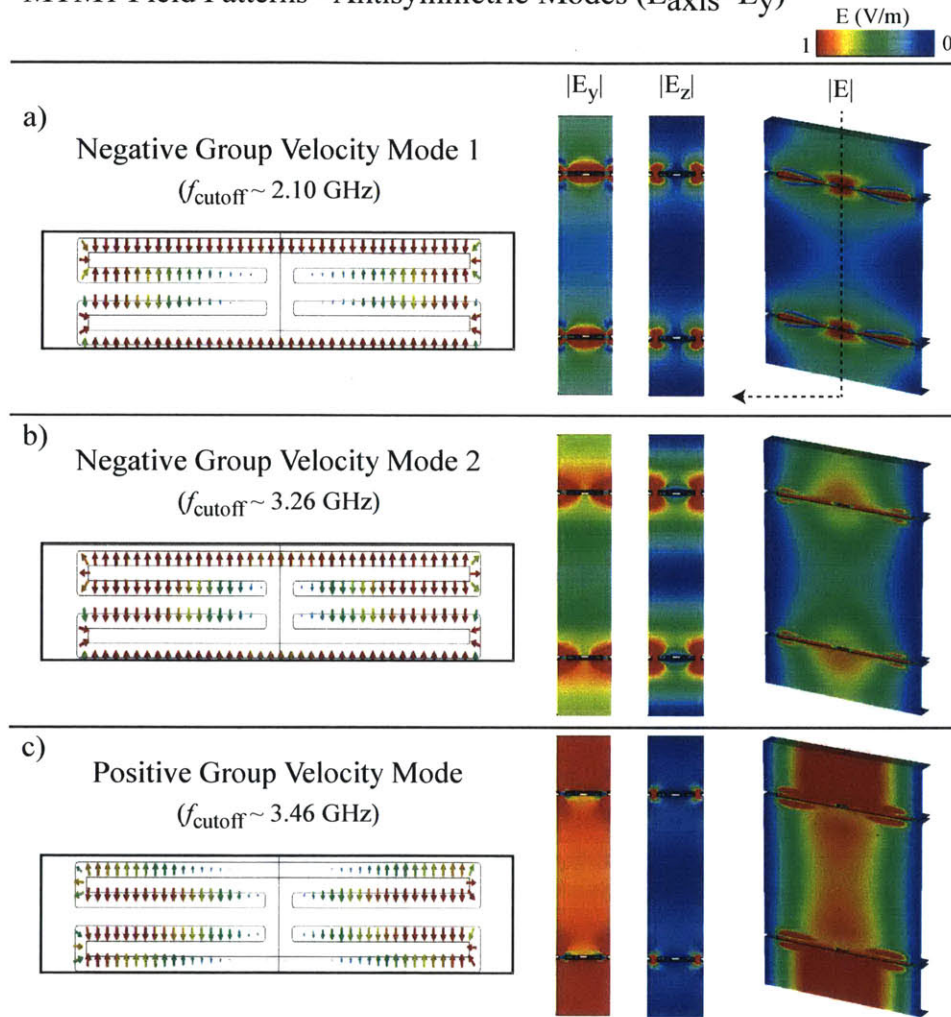


Figure 2-8: Field profiles of the three antisymmetric modes (blue curves of Fig. 2-6) of MTM1. Shown are the vector field distributions within the CSRRs on the far left, the $|E_y|$ and $|E_z|$ fields on the symmetry plane that intersects the CSRRs along the center of the waveguide, and $|E|$ plotted on the plane that is normal to the electron beam direction. Note the difference between the vector fields of the two negative group velocity modes, and the difference between the $|E_y|$ and $|E_z|$ fields of these antisymmetric modes and symmetric modes of Fig. 2-7.

distribution within the CSRRs is shown on the far left. In the center the $|E_y|$ and $|E_z|$ fields are shown in the full structure on the plane of symmetry that intersects the CSRRs along the center of the waveguide (the x plane). On the far right $|E|$ is plotted on the plane normal to the beam to show the distribution of fields in the waveguide.

The qualitative differences between the symmetric and antisymmetric modes are best understood when each is considered as the superposition of two surface modes of each metamaterial plate. Because there are two plates there is the possibility for a phase difference between the two metamaterial plate surface waves. The symmetric mode occurs when two surface waves are in phase, and the antisymmetric occurs when they are 180 degrees out of phase. Looking at the $|E_y|$ and $|E_z|$ components of the electric field in Fig. 2-8 and Fig. 2-7, it is evident that the electric field that the electron beam sees (which is generally 6-15 mm in diameter in size depending on the applied magnetic field, and is located on the axis of the device) is essentially perpendicular or *TE*-like in the case of the antisymmetric mode and longitudinal or *TM*-like mode in the case of the symmetric. For the upper negative group velocity modes, the frequency of the antisymmetric mode is slightly higher than the frequency of the symmetric mode.

In addition to splitting into antisymmetric and symmetric modes due to the use of two metamaterial plates, there are also two different types of negative group velocity modes (lower and upper) due to the fact that dual CSRRs are used. The lower frequency modes (cutoff just above 2 GHz) have essentially a flat dispersion and have a very small field on axis. The higher frequency upper negative group velocity modes (cutoff above 3 GHz) have much greater dispersion and have a stronger electric field on axis. When the vector fields of the lower and upper negative group velocity modes are compared in Fig. 2-8 the difference between the two modes becomes quite obvious in that the fields of one CSRR relative to the other CSRR are in phase in the lower negative group velocity mode, whereas in the upper modes the fields are 180 degrees out of phase. This causes two different unique resonances for the metamaterial (the dual CSRR) as a whole unit. Intuitively speaking, since the CSRRs are oriented

in opposing directions, when the fields in the individual CSRRs are in phase they actually tend to cancel out. That is why the fields of the lower modes are much weaker on axis than the upper modes. Also, changing the phase advance of the structure has much less of a change on the eigenfrequencies of the lower modes and these modes have a much flatter dispersion curve.

2.2.3 MTM2 Design

The MTM2 structure is constructed by placing two periodic metamaterial plates into a rectangular waveguide. A CAD rendering of the MTM2 structure and metamaterial plate it utilizes is shown in Fig. 2-9. In this figure the structure dimensions are labeled with corresponding variable names. Different values of the variables that describe the

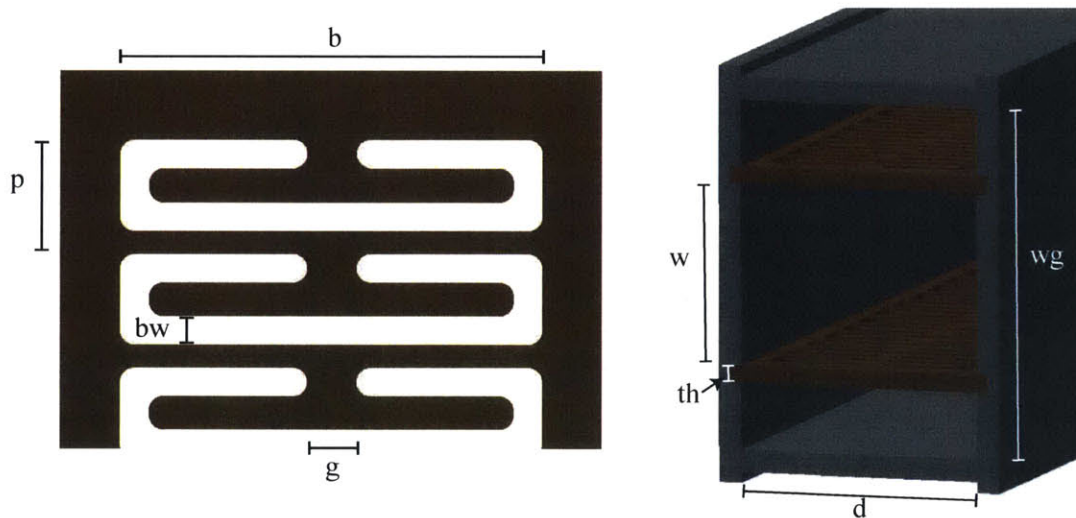


Figure 2-9: CAD rendering of the MTM2 structure on the right and one of the two identical metamaterial plates it uses on the left. Variable names for important dimensions are given, and values used for microwave testing are given in Table 2.2.

waveguide in Fig. 2-9 were investigated in simulation and experiment, however the values used for the high power microwave test are shown in Table. 2.2. These particular dimensions and also the machining tolerances that went into the structure design were chosen after numerous eigenmode simulations were performed to calculate the condition for beam-wave synchronism at S-Band frequencies, consideration was made

to align with other standard components purchased for the experiment, and after discussion with the MIT central machine shop where all structures were fabricated. The device can be easily scaled in order to be used at different frequencies.

Table 2.2: Dimensions of the MTM2 structure shown in Fig. 2-9 that were used in high power microwave testing.

Variable	Dimension (mm)
w	29
wg	63
d	43
b	37
g	4.45
bw	2.5
th	3.125
p	10

This metamaterial plate design makes use of single CSRRs. The resonant frequency of the CSRRs is designed to be below cutoff for TM modes in the empty waveguide ($f_c \approx 4.2$ GHz for 43 mm by 63 mm waveguide). The metamaterial plates are created by machining CSRRs with period $p = 10$ mm and width $b = 37$ mm along two metal plates of thickness $th = 3.125$ mm. The resonators have a slot width of $g = 4.45$ mm. These plates are then placed with a separation of $w = 29$ mm in a rectangular waveguide with inner dimensions $wg = 63$ mm by $d = 43$ mm.

The eigenmode solver of the High Frequency Structure Simulator (HFSS) code and CST Microwave Studio (MWS) were used to simulate the eigenmodes of one period of the total structure. There are again two general types of modes, antisymmetric ($E_{z,axis}=0$) and symmetric ($E_{y,axis}=0$). The dispersion curves of the four lowest order modes calculated by the eigenmode solver are shown in Fig. 2-10. Also shown is the beam line $2\pi f = k_z v_0$ for a 500 keV electron beam. It's immediately obvious that the two lower negative group velocity modes of the structure have disappeared. However, the positive group velocity mode and the upper negative group velocity modes still exist. The two negative group velocity modes are analogous to the negative group velocity mode that was discovered in the waveguide filled with a dielectric with a

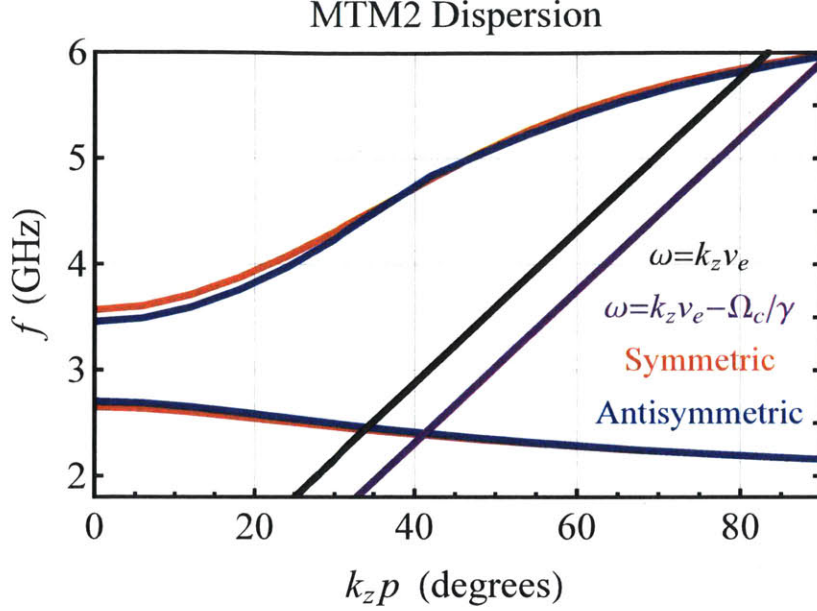


Figure 2-10: Dispersion relation for the four lowest order modes solved with the eigenmode solver of HFSS for one period of the MTM2 design described by Fig. 2-9 and Table 2.2. The antisymmetric modes are in blue and the symmetric modes in red. There are two negative group velocity modes and two positive group velocity modes shown. Also shown is the beam line for a 500 keV electron beam (black) and the beam line corresponding to the anomalous Doppler shift in a magnetic field of 400 G (purple).

Lorentzian response. Nevertheless, due to the symmetry of the waveguide which arises from the use of the two metamaterial plates the singular negative group velocity mode has become two different modes.

To understand the differences between these modes it is again instructive to look at the field profiles generated by the eigenmode solver. In Fig. 2-11 and Fig. 2-12 the field profiles of the two symmetric and two antisymmetric modes are shown, respectively. The fields are plotted for a phase advance of 34 (negative group velocity modes) and 82 (positive group velocity modes) degrees, which is the approximate phase advance of the modes corresponding to synchronism with a 500 keV beam. For each mode the vector field distribution within the CSRRs is shown on the far left. In the center the $|E_y|$ and $|E_z|$ fields are shown in the full structure on the plane of symmetry that intersects the CSRRs along the center of the waveguide (the x plane).

MTM2 Field Patterns - Symmetric Modes ($E_{\text{axis}} \sim E_y$)

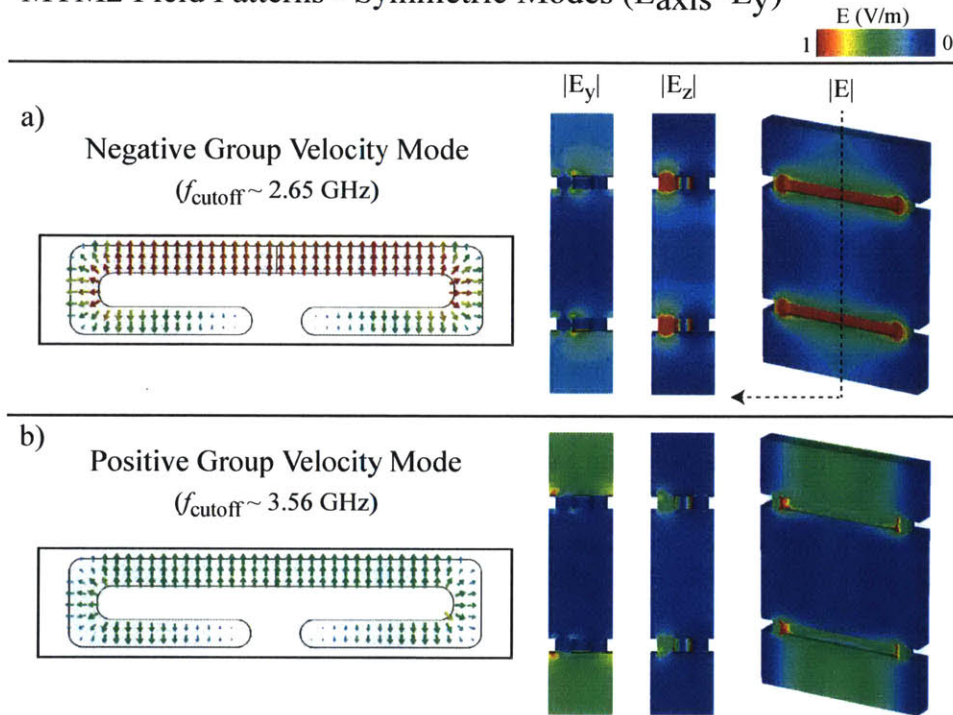


Figure 2-11: Field profiles of the three symmetric modes (red curves of Fig. 2-10) of MTM2. Shown are the vector field distributions within the CSRRs on the far left, the $|E_y|$ and $|E_z|$ fields on the symmetry plane that intersects the CSRRs along the center of the waveguide, and $|E|$ plotted on the plane that is normal to the electron beam direction. Note the difference between the difference between the $|E_y|$ and $|E_z|$ fields of these symmetric modes and antisymmetric modes of Fig. 2-12.

MTM2 Field Patterns - Antisymmetric Modes ($E_{\text{axis}} \sim E_y$)

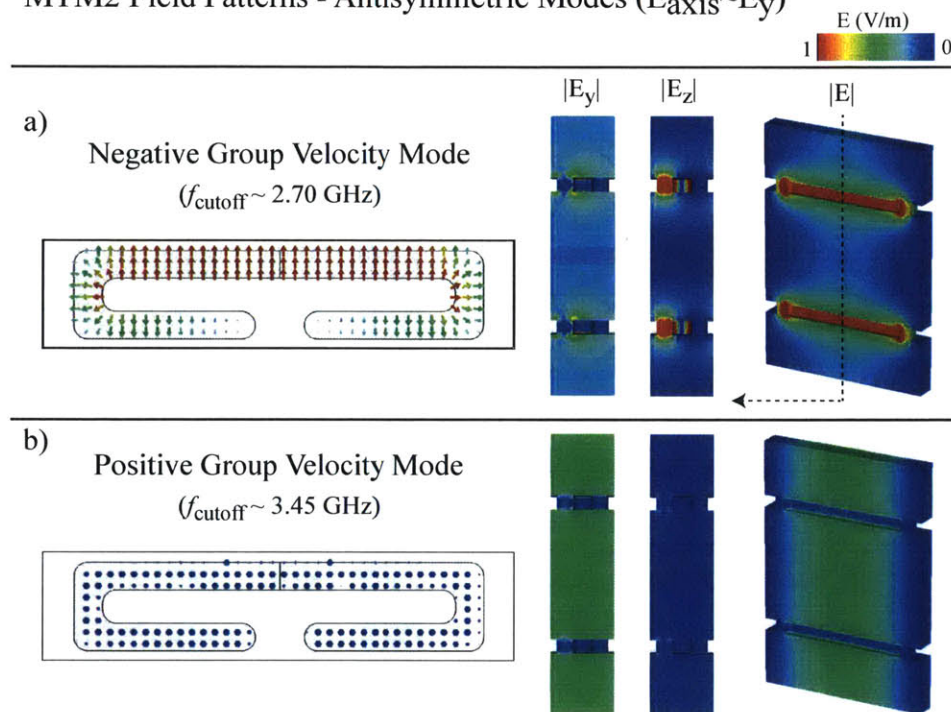


Figure 2-12: Field profiles of the three antisymmetric modes (blue curves of Fig. 2-10) of MTM2. Shown are the vector field distributions within the CSRs on the far left, the $|E_y|$ and $|E_z|$ fields on the symmetry plane that intersects the CSRs along the center of the waveguide, and $|E|$ plotted on the plane that is normal to the electron beam direction. Note the difference between the difference between the $|E_y|$ and $|E_z|$ fields of these antisymmetric modes and symmetric modes of Fig. 2-11.

The qualitative differences between the symmetric and antisymmetric modes is the same as what was discovered in the MTM1 structure. Looking at the $|E_y|$ and $|E_z|$ components for the electric field in Fig. 2-12 and Fig. 2-11, it's clear the fields that the electron beam sees are essentially that of a TE -like mode in the case of the antisymmetric mode and a TM -like mode in the case of the symmetric mode on the axis of the metamaterial device. The frequency of the negative group velocity antisymmetric mode is slightly higher than the frequency of the negative group velocity symmetric mode.

The main difference between this structure and the last is that it no longer has a lower negative group velocity mode due to the fact that the CSRR is singular and does not have two different resonances, which in the MTM1 structure depended on the phase difference of the fields in each of the individual CSRRs that comprise the dual CSRR unit cell.

2.2.4 MTM3 Design

The MTM3 structure is constructed by placing two periodic metamaterial plates into a rectangular waveguide. The MTM3 design is essentially identical to the MTM2 design, but is scaled to a higher frequency. A CAD rendering of the MTM3 structure and metamaterial plate it utilizes is shown in Fig. 2-13. In this figure the structure dimensions are labeled with corresponding variable names. Different values of the variables that describe the waveguide in Fig. 2-13 were investigated in simulation and experiment, however the values used for the high power microwave test are shown in Table. 2.3. These particular dimensions and also the machining tolerances that went into the structure design were chosen after numerous eigenmode simulations were performed to calculate the condition for beam-wave synchronism at S-Band frequencies, consideration was made to align with other standard components purchased for the experiment, and after discussion with the MIT central machine shop where all structures were fabricated.

This metamaterial plate design makes use of single CSRRs. The resonant frequency of the CSRRs is designed to be below cutoff for TM modes in the waveguide.

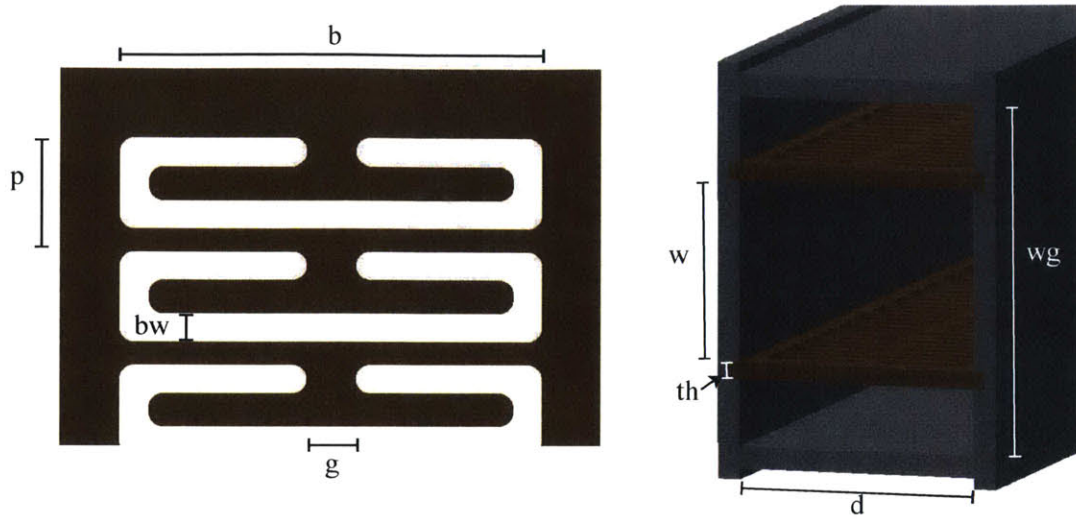


Figure 2-13: CAD rendering of the MTM3 structure on the right and one of the two identical metamaterial plates it uses on the left. Variable names for important dimensions are given, and values used for microwave testing are given in Table 2.3.

The metamaterial plates are created by machining CSRRs with period $p = 5$ mm and width $b = 24$ mm along two metal plates of thickness $th = 3.125$ mm. The resonators have a slot width of $g = 3.5$ mm. These plates are then placed with a separation of $w = 25$ mm in a rectangular waveguide with inner dimensions $wg = 60$ mm by $d = 29.6$ mm.

The eigenmode solver of the High Frequency Structure Simulator (HFSS) code and CST Microwave Studio (MWS) were used to simulate the eigenmodes of one period of the total structure. There are again two general types of modes, antisymmetric ($E_{z,axis}=0$) and symmetric ($E_{y,axis}=0$). The dispersion curves of the four lowest order modes calculated by the eigenmode solver are shown in Fig. 2-14. Also shown is the beam line $2\pi f = k_z v_0$ for a 500 keV electron beam. The two negative group velocity modes are analogous to the negative group velocity mode that was discovered in the waveguide filled with a dielectric with a Lorentzian response. Like the MTM2 structure, however, the singular negative group velocity mode has become two different modes.

The difference between these two modes was described for the MTM2 structure, and the explanation for the difference between these two types of modes in the MTM3

Table 2.3: Dimensions of the MTM3 structure shown in Fig. 2-9 that were used in high power microwave testing.

Variable	Dimension (mm)
w	25
wg	60
d	29.6
b	24
g	3.5
bw	1
th	3.125
p	5

structure is identical. In Fig. 2-15 and Fig. 2-16 the field profiles of the two symmetric and two antisymmetric modes are shown, respectively. The fields are plotted for a phase advance of 26 (negative group velocity modes) and 63 (positive group velocity modes) degrees, which is the approximate phase advance of the modes corresponding to synchronism with a 500 keV beam. For each mode the vector field distribution within the CSRRs is shown on the far left. In the center the $|E_y|$ and $|E_z|$ fields are shown in the full structure on the plane of symmetry that intersects the CSRRs along the center of the waveguide (the x plane).

Looking at the $|E_y|$ and $|E_z|$ components for the electric field in Fig. 2-16 and Fig. 2-15, it's clear the fields that the electron beam sees is essentially a *TE*-like mode in the case of the antisymmetric mode and a *TM*-like mode in the case of the symmetric. The frequency of the negative group velocity antisymmetric mode is slightly higher than the frequency of the negative group velocity symmetric mode.

2.3 Theory of an Electron Beam Interacting with a Metamaterial Waveguide

Of particular interest is the performance of the metamaterial devices when compared against more conventional BWOs such as rippled wall devices. In order to make a comparison we investigate some of the standard parameters used to describe com-

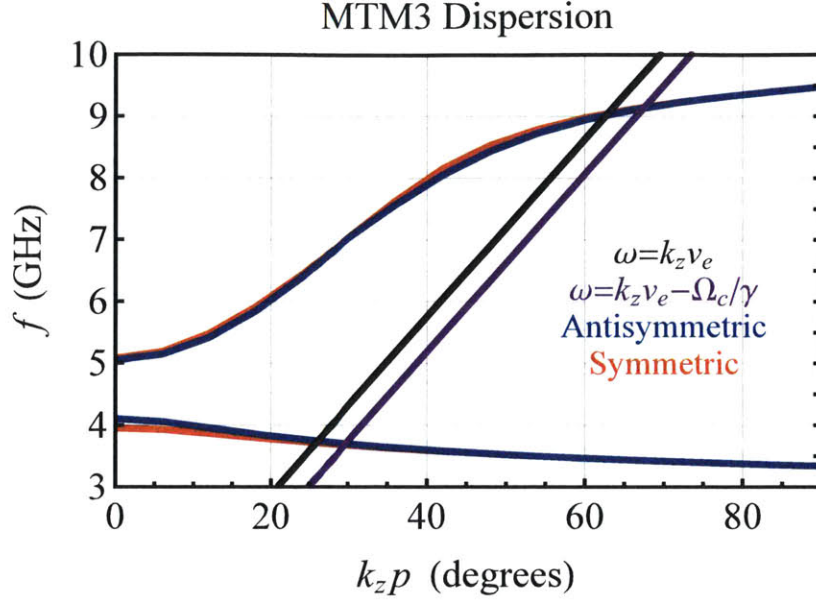


Figure 2-14: Dispersion relation for the four lowest order modes solved with the eigenmode solver of HFSS for one period of the MTM3 design described by Fig. 2-13 and Table 2.3. The antisymmetric modes are in blue and the symmetric modes in red. There are two negative group velocity modes and two positive group velocity modes shown. Also shown is the beam line for a 500 keV electron beam (black) and the beam line corresponding to the anomalous Doppler shift in a magnetic field of 400 G (purple).

monly used BWO tubes. The coupling impedance is a useful parameter that measures the beam-wave coupling of an electron beam and an electromagnetic wave. We define the coupling impedance for the symmetric modes by

$$K_z = \frac{E_{wz}^2}{2k_z^2 P} \quad (2.3.1)$$

and the coupling impedance for the antisymmetric modes by

$$K_y = \frac{E_{wy}^2}{2k_z^2 P} \quad (2.3.2)$$

where $|E_{wz}|$ and $|E_{wy}|$ are the components of the electric field parallel and perpendicular to the direction of and in phase with the electron beam, P is the power flux, and k_z is the wavenumber. $|E_{wz}|$ and $|E_{wy}|$ are calculated from the fields solved in

MTM3 Field Patterns - Symmetric Modes ($E_{\text{axis}} \sim E_y$)

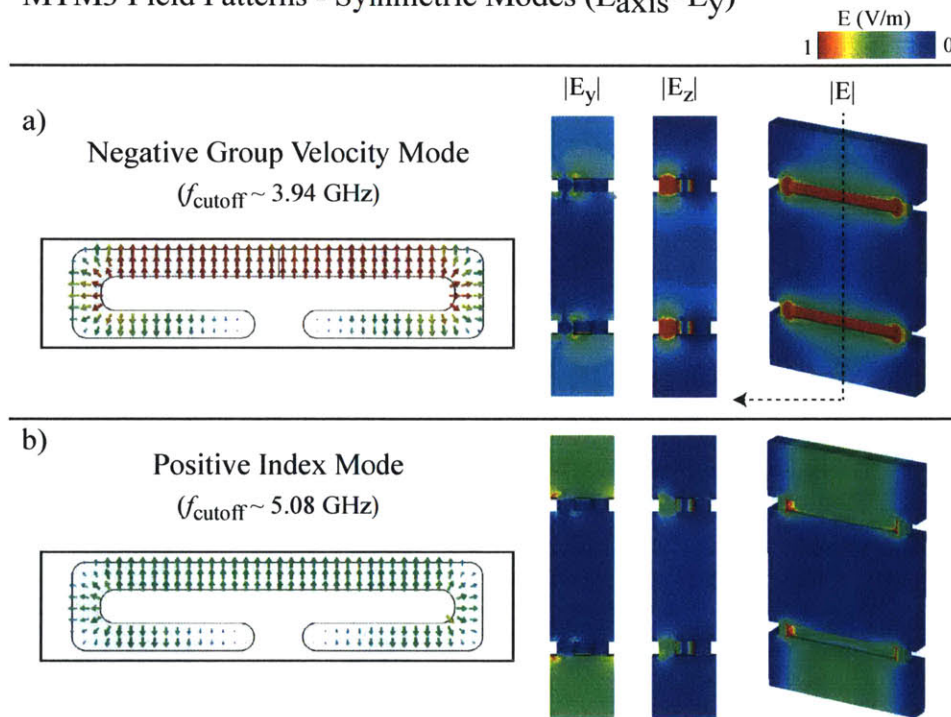


Figure 2-15: Field profiles of the three symmetric modes (red curves of Fig. 2-14) of MTM3. Shown are the vector field distributions within the CSRRs on the far left, the $|E_y|$ and $|E_z|$ fields on the symmetry plane that intersects the CSRRs along the center of the waveguide, and $|E|$ plotted on the plane that is normal to the electron beam direction. Note the difference between the difference between the $|E_y|$ and $|E_z|$ fields of these symmetric modes and antisymmetric modes of Fig. 2-16.

MTM3 Field Patterns - Antisymmetric Modes ($E_{\text{axis}} \sim E_y$)

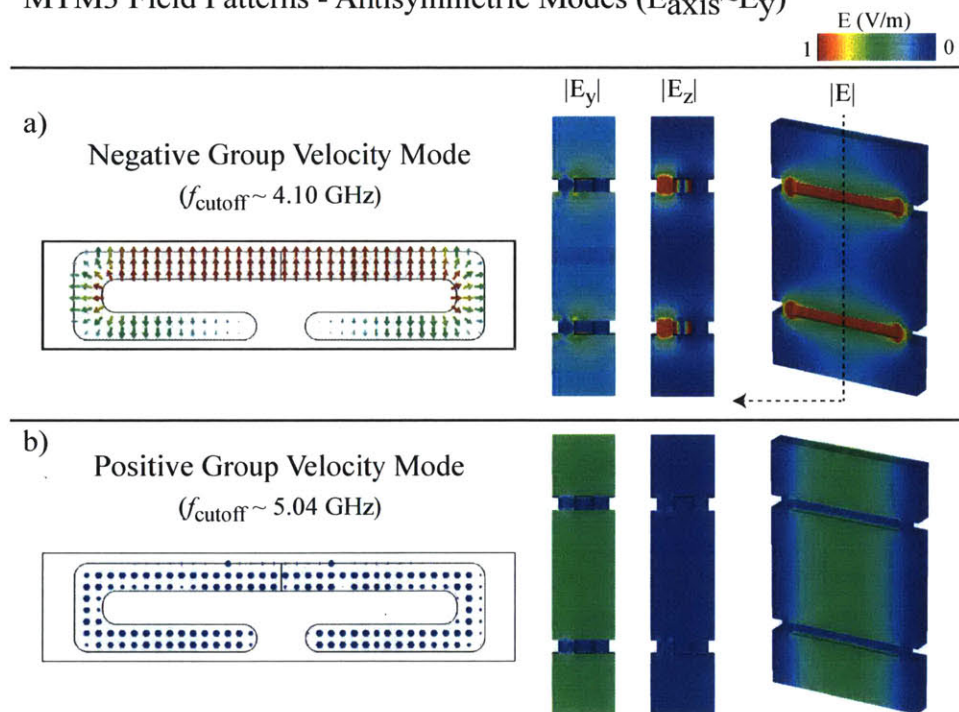


Figure 2-16: Field profiles of the three antisymmetric modes (blue curves of Fig. 2-14) of MTM3. Shown are the vector field distributions within the CSRs on the far left, the $|E_y|$ and $|E_z|$ fields on the symmetry plane that intersects the CSRs along the center of the waveguide, and $|E|$ plotted on the plane that is normal to the electron beam direction. Note the difference between the difference between the $|E_y|$ and $|E_z|$ fields of these antisymmetric modes and symmetric modes of Fig. 2-15.

the eigenmode simulations and are given by the following expressions

$$\begin{aligned} E_{wz} &= \frac{1}{p} \int E_z(z) e^{ik_z z} \\ E_{wy} &= \frac{1}{p} \int E_y(z) e^{ik_z z} \end{aligned} \quad (2.3.3)$$

P may be calculated from the fields from the following expression

$$P = \int_A \vec{E} \times \vec{H}^* \quad (2.3.4)$$

where A is the area of a plane of the unit cell perpendicular to the beam direction. P can also be estimated from the dispersion relation and eigenmode simulations from the following equation

$$P = U v_{gr} \frac{1}{p} \quad (2.3.5)$$

where U is the stored energy in one period of an eigenmode simulation (1 J in the CST Microwave Studio eigenmode solver), v_{gr} is the group velocity, and p is the structure period. The power flux near the point of synchronism can then be calculated from the dispersion curve via the relation

$$v_{gr} = \frac{\partial \omega}{\partial k} \quad (2.3.6)$$

The coupling impedances for the six modes of MTM1 that were solved with the eigenmode solver were calculated and are shown in Table 2.4.

The fields used to calculate the coupling impedances for each particular mode were taken from the eigenmode simulation corresponding to beam-wave synchronism (i.e. taken from the simulation corresponding to the phase advance where the beam line intersects the particular dispersion curve of each mode). In addition, the coupling impedances for the four modes of the MTM2 device that were solved with the eigenmode solver were calculated and are shown in Table 2.5 Finally, the coupling impedances for the four modes of the MTM3 device that were solved with the eigenmode solver were calculated and are shown in Table 2.6

Table 2.4: Coupling impedances and group velocities of the six lowest order modes of the MTM1 device. The coupling impedances and group velocities were calculated at the point of synchronism with a 500 keV beam.

MTM1 Structure and Mode	K (Ohms)	v_{gr}/c
Negative Group Velocity Antisymmetric-Lower	151	0.0073
Negative Group Velocity Antisymmetric-Upper	34	0.13
Positive Group Velocity Antisymmetric	25	0.18
Negative Group Velocity Symmetric-Lower	114	0.0053
Negative Group Velocity Symmetric-Upper	65	0.096
Positive Group Velocity Symmetric	11	0.20

Table 2.5: Coupling impedances and group velocities of the four lowest order modes of the MTM2 device. The coupling impedances and group velocities were calculated at the point of synchronism with a 500 keV beam.

MTM2 Structure and Mode	K (Ohms)	v_{gr}/c
Negative Group Velocity Antisymmetric	160	0.086
Positive Group Velocity Antisymmetric	9	0.11
Negative Group Velocity Symmetric	131	0.075
Positive Group Velocity Symmetric	6	0.10

Table 2.6: Coupling impedances and group velocities of the four lowest order modes of the MTM3 device. The coupling impedances and group velocities were calculated at the point of synchronism with a 500 keV beam.

MTM3 Structure and Mode	K (Ohms)	v_{gr}/c
Negative Group Velocity Antisymmetric	59	0.073
Positive Group Velocity Antisymmetric	4	0.16
Negative Group Velocity Symmetric	78	0.058
Positive Group Velocity Symmetric	3	0.15

The linear theory outlined in Ref. [59] calculates the start current for oscillation, I_{st} , of a traveling TM electromagnetic wave with a rectilinear electron beam and is an extension of the linear theory pioneered by John Pierce. When the beam current is above I_{st} the device will oscillate with zero input signal. The start current depends on the coupling impedance, device geometry, mode of interaction, and beam parameters. The theory developed by Pierce is only applicable to interaction with traveling TM

modes and so is unsuitable to calculate the start current for interaction with the antisymmetric modes. However, when the axial magnetic field is very strong, the beam is confined to the axis and one can expect an interaction only with the symmetric modes since the antisymmetric modes have no longitudinal electric field and the electrons are prevented from transverse deflections. In addition, Pierce's theory is not applicable to modes where the group velocity is very low, as is the case for the lower negative group velocity modes of the MTM1 design, so we only use it to estimate the start current of the upper negative group velocity symmetric mode of MTM1, the negative group velocity mode of MTM2, and the negative group velocity mode of MTM3. For the symmetric negative group velocity modes the start current is given by the formula

$$I_{st} = 4U_0 \frac{(CN)_{st}^3 \lambda_z^3}{KL^3} \quad (2.3.7)$$

where U_0 is the beam energy, $\lambda_z = \frac{2\pi}{k_z}$ is the longitudinal wavelength, L is the total length of the structure, $N = L/\lambda_z$ is the number of longitudinal wavelengths, and C is the Pierce parameter. The Pierce parameter is defined as

$$C^3 = \frac{I_0 K}{4U_0} \quad (2.3.8)$$

Here I_0 is the beam current. From Table 8.1 in Ref. [26] the start condition $(CN)_{st}$ is calculated to be 0.314 for zeroth order axial harmonic operation. From Eq. 2.3.7 the start current is plotted in Fig. 2-17 as a function of structure length for both the MTM1, MTM2, and MTM3 negative group velocity symmetric modes. Traditionally one operates a BWO at $\sim 3\times$ the start current. Increasing the current well beyond the start current ($> 7\times$) can result in auto-modulation of the output power as the device enters a stochastic regime. This type of behavior has been observed in both theory and experiment as shown, for example, in Ref. [27].

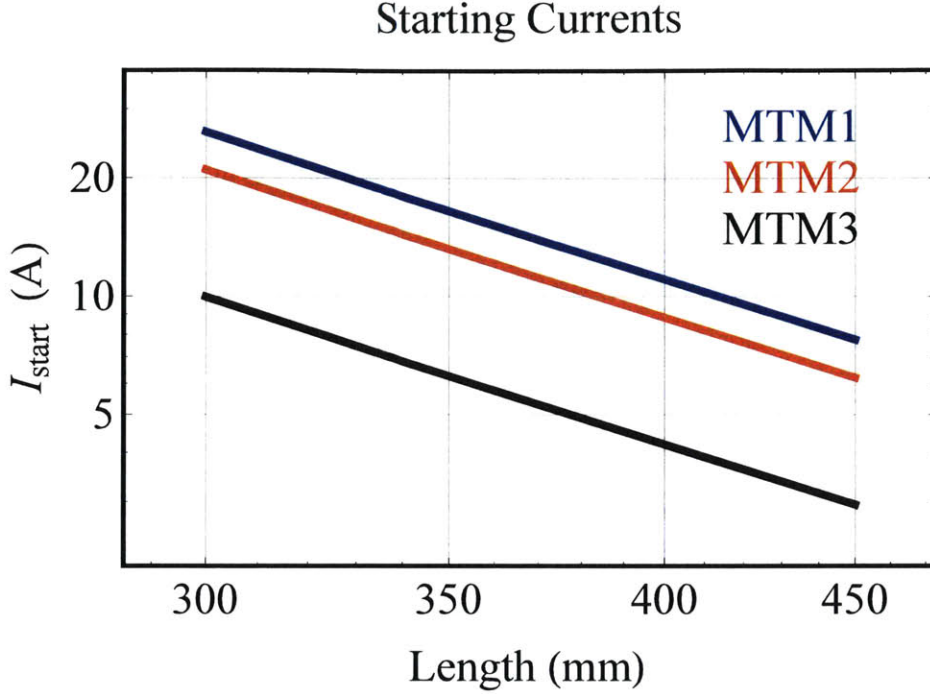


Figure 2-17: The start current as a function of length plotted for the symmetric upper negative group velocity mode of MTM1 (blue), the symmetric negative group velocity mode of MTM2 (red), and the symmetric negative group velocity mode of MTM3 (black) which is obtained from the linear theory of Pierce extended by Ref. [59].

2.4 PIC Simulations

We use the Particle in Cell (PIC) solver of CST Particle Studio to investigate the performance of the various metamaterial structures utilizing a relativistic electron beam [60]. Using a PIC code, we are able to calculate the self consistent solution for the mutual coupling between relativistic particles and electromagnetic fields. The code is able to simulate the qualitative behavior of a DC electron beam in the different metamaterial structures and take into account ohmic losses and reflections from the output coupler and the end of the waveguide. In addition, the PIC solver is also able to capture nonlinear effects that would be missed in a more basic (i.e. Pierce) treatment of the beam-wave interaction. We use the code to simulate the performance of the MTM1, MTM2, and MTM3 structures as well as an effective dielectric with a Lorentz response. The particular model of each of the structures simulated with the PIC solver

is shown in Fig. 2-18. Each structure has an identical outer waveguide and output

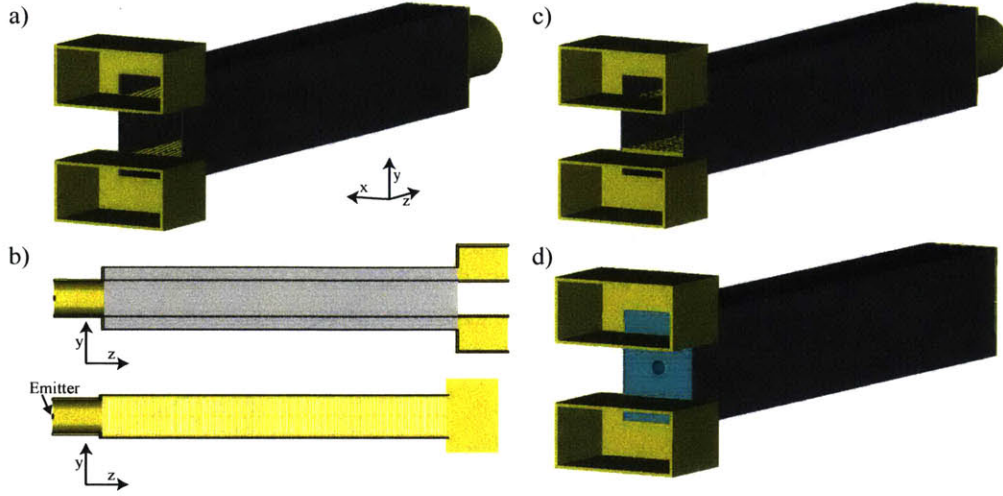


Figure 2-18: a) Perspective view of the 352 mm long MTM1 structure simulated in CST. b) Cross section views of the same MTM1 structure. c) Perspective view of the 370 mm long MTM2 structure simulated in CST d) Perspective view of the 352 mm long waveguide filled with a Lorentzian dielectric simulated in CST

coupler. All simulations assume a lossy steel outer waveguide with conductivity $6 * 10^6$ S/m and in the case of the MTM1, MTM2 and MTM3 designs, lossy copper metamaterial plates with conductivity $5 * 10^7$ S/m. For all of the PIC simulations performed, the beam size was determined (by changing the emitter radius) so that or a given magnetic field, the radius of the electron beam was picked to match that required for Brillouin flow to avoid scalloping of the beam. For a given axial magnetic field B , the radius of the beam used in the simulations is given by the formula [61]

$$r_b = 0.83 \frac{\sqrt{I_b}}{U_0^{1/4} B} \quad (2.4.1)$$

where r_b is the beam radius in mm, U_0 is the beam energy in eV, I_b is the beam current in A, and B is in Teslas. In Fig. 2-19 a plot of the beam radius used in the simulations performed for a 500 keV, 80 A electron beam for a magnetic field from 400 to 1800 G is shown. For more information on the details of the code setup, see Appendix A.

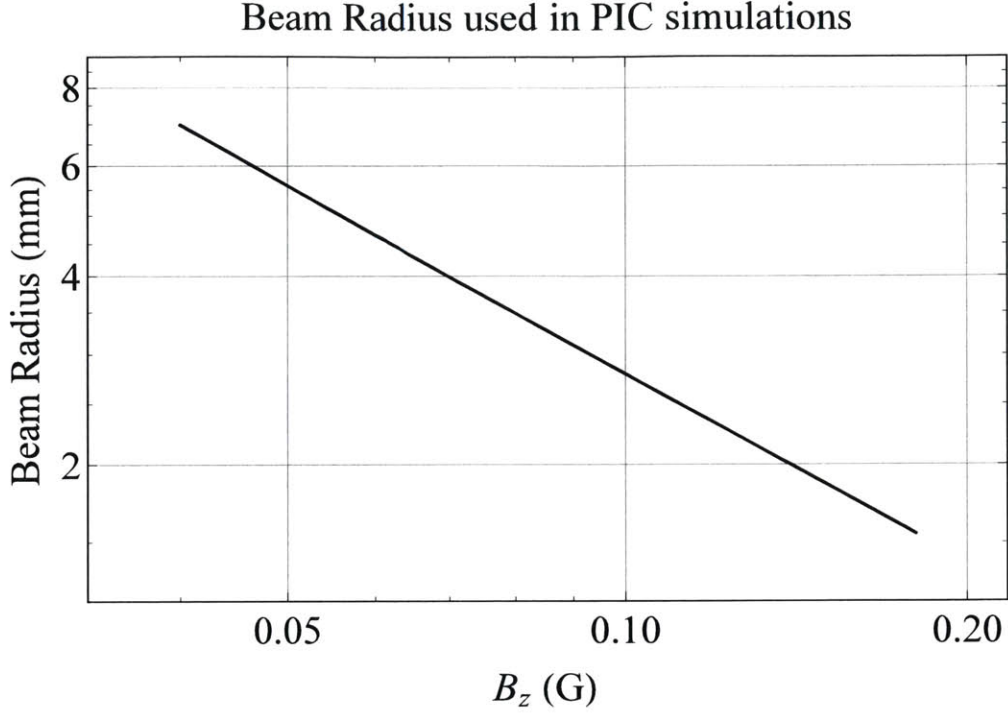


Figure 2-19: Beam radius used in each of the PIC simulations for different magnetic field values for a 500 keV, 80 A electron beam that avoided scalloping of the electron beam.

2.4.1 MTM1 PIC Simulations

A perspective view of the MTM1 metamaterial structure simulated with the PIC solver is shown in Fig. 2-18a, and two cross section views are shown in Fig. 2-18b. In Fig. 2-18b, the electron beam comes from the left. Output ports are shown in Fig. 2-18a and were used to record the power generated and coupled out of the structure. An 80 A, 500 keV ($v_0 = 0.86 c$) beam is used for the simulations. The electron beam simulated was a DC beam with a 10 ns rise time to reach full current from zero initial starting current. A variable, but uniform axial magnetic field was used to confine the beam. In Fig. 2-20 the output power and frequency is shown for a simulation with an axial magnetic field of 1.5 kG. See Table A.1 for a more detailed description of the inputs to the simulation. In the simulation, the device saturates at an output power of 5.75 MW after 280 ns. The output frequency is peaked at 2.82 GHz. The simulation used approximately 5 million mesh points and took approximately 5 days

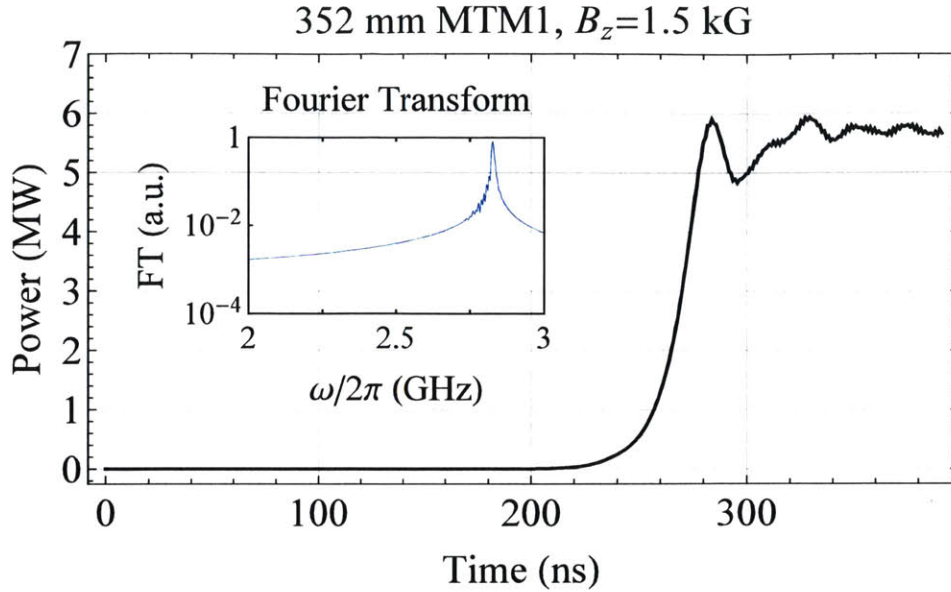


Figure 2-20: Output power of a 352 mm long metamaterial waveguide with the design of MTM1 calculated by the PIC simulation along with the Fourier Transform of the output signal. The simulation uses a 500 keV, 80 A electron beam with a 10 ns rise time and a longitudinal field of 1.5 kG. The output power saturates at about 5.5 MW and the radiation is peaked at 2.82 GHz.

to complete on a desktop with 128 GB of RAM and 64 processors. A simulation performed with 2 million mesh points predicted a nearly identical output power and saturation time (6 MW and 280 ns). See Table A.2 for a more detailed description of the inputs to the simulation.

For different values of B , the qualitative behavior of the electron beam is very different. In Fig. 2-21 the electric field profile and particle trajectories are shown for the case where $B = 1.5$ kG. See Table A.1 for a more detailed description of the inputs to the simulation. It is clear from the electric field plots that the beam excites the symmetric mode, and the particle orbits are roughly constrained to the axis. In addition to the qualitative snapshots of particle trajectories that CST is able to produce, it also is able to export the phase space of the particles at any particular time during the simulations. In Fig. 2-22 a snapshot of the electron energies is plotted along the full length of the simulation for an axial magnetic field of 1.5 kG. In addition, a histogram plot below the electron energy plot shows the electron density

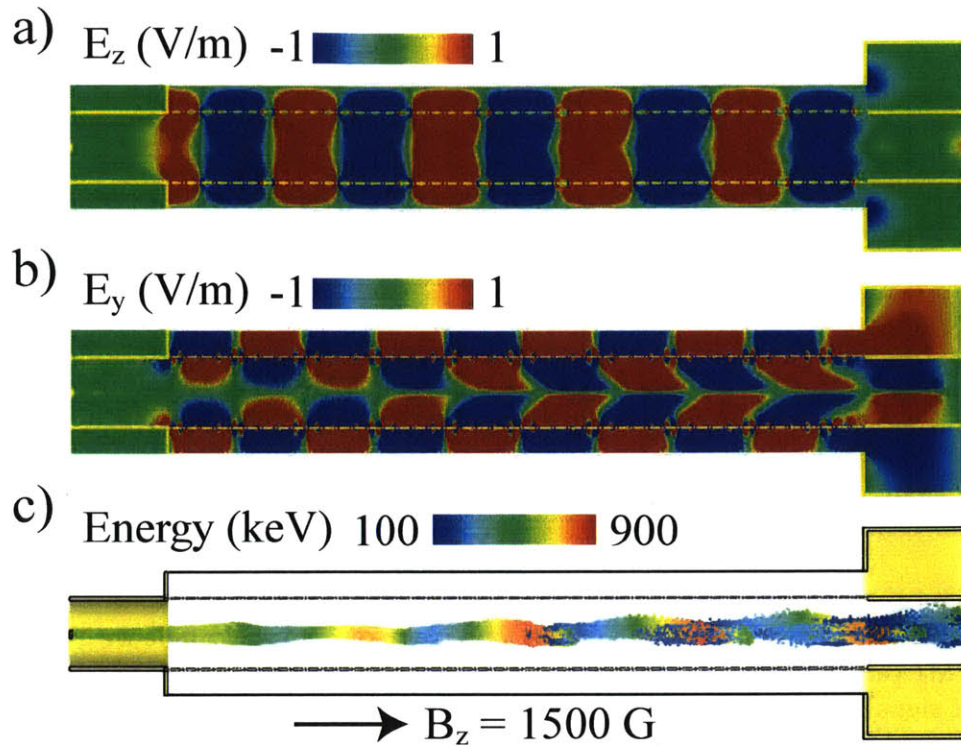


Figure 2-21: For the PIC simulation of the 352 mm long MTM1 structure, a) E_z component of the electric field b) E_y component of the electric field c) Electron trajectories. The electron beam is incident from the left and the color of each particle indicates it's energy. The arrow indicates the direction of the magnetic field which has a magnitude of 1.5 kG. The field distributions and particle trajectory plots were generated 300 ns after the injection of the electron beam.

(which is proportional to the current) along the axis of the device. Bunches are clearly evident and are spaced at approximately one wavelength apart.

In Fig. 2-23 the electric field profile and particle trajectories are shown for the case where $B = 700$ G. See Table A.3 for a more detailed description of the inputs to the simulation. It is clear from the electric field plots that the beam excites the antisymmetric mode, and the electron beam spirals around its initial center with an angular frequency nearly equal to that of the output microwave frequency ($2\pi * 2.813$ GHz) which was calculated in the CST PIC code by using a particle monitor to measure the position of the beam centroid at the end of the waveguide. This spiral frequency was also determined to be approximately the same for different of magnetic

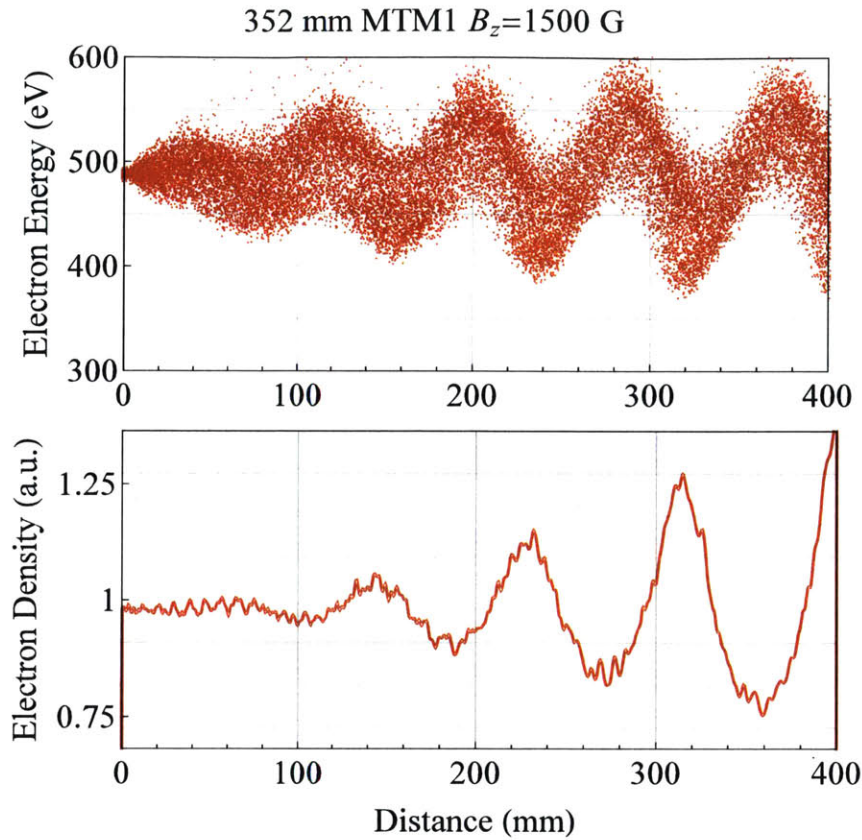


Figure 2-22: Snapshot of the electron energies at $t=200$ ns after injection of the 500 keV electron beam in the 352 mm MTM1 device when the magnetic field is 1.5 kG. The beam is incident from the left and bunches form at approximately the longitudinal wavelength corresponding to the condition for synchronism.

fields (± 0.05 GHz). In Fig. 2-24 a snapshot of the electron energies is plotted along the full length of the simulation. There is a major qualitative difference between the way electrons lose energy between the high B field (axial bunching) and low B field (spiral bunching) cases. The velocity modulation of the antisymmetric mode (700 G) is much less than that produced by the symmetric mode (1.5 kG). For the excitation of the antisymmetric waveguide mode, the energy loss rate by the electron beam is essentially constant along the length of the waveguide. Practically speaking, this could have significant benefits if operation in the antisymmetric mode were to be used in conjunction with a depressed collector in order to achieve high efficiency.

Besides the qualitative behavior of the beam, the magnetic field was also observed

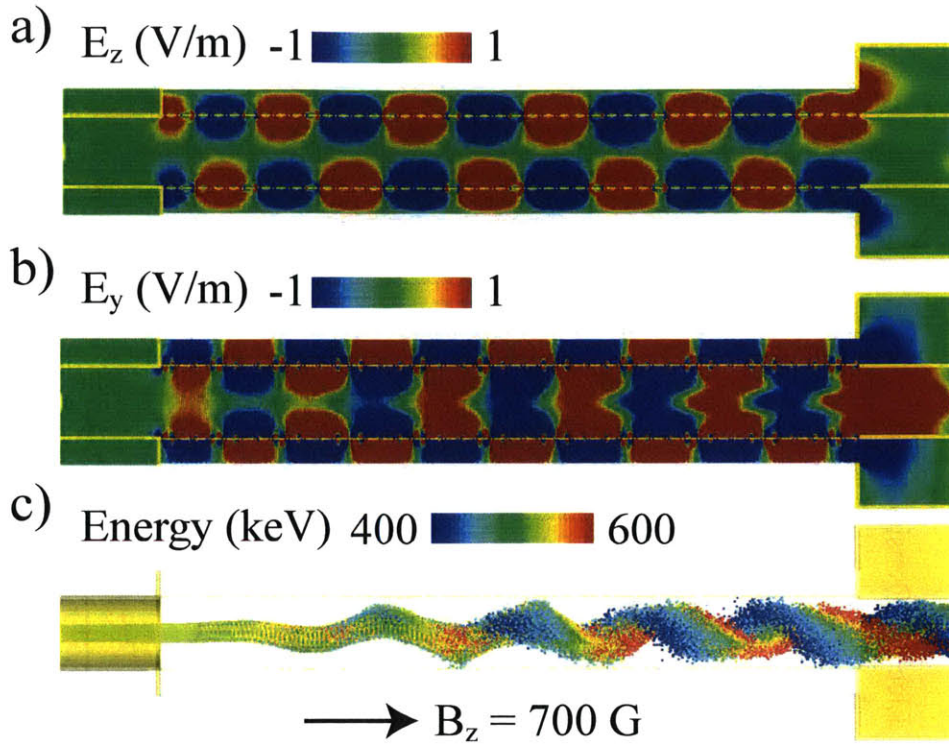


Figure 2-23: For the PIC simulation of the 352 mm long MTM1 structure, a) E_z component of the electric field b) E_y component of the electric field c) Electron trajectories. The electron beam is incident from the left and the particle color indicates it's energy. The beam is observed to spiral. The arrow indicates the direction of the magnetic field which has a magnitude of 700 G. The field distributions and particle trajectory plots were generated 300 ns after the injection of the electron beam.

to slightly tune the frequency and significantly affect the output power of the device. In Fig. 2-25 the output power, saturation time, output frequency and calculated beam interception are shown for different simulations performed at eight different B fields. The magnetic field is the only parameter varied in each of the simulations as well as the beam radius which is made to match the curve shown in Fig. 2-19 to avoid scalloping of the electron beam. See Table A.4 for a more detailed description of the inputs to the simulation. The beam interception is calculated by measuring the average current getting through the structure without being intercepted on any component (i.e. making it to the collector in the experiment). Particles that are intercepted are lost to the simulation; no secondary electron emission is included in

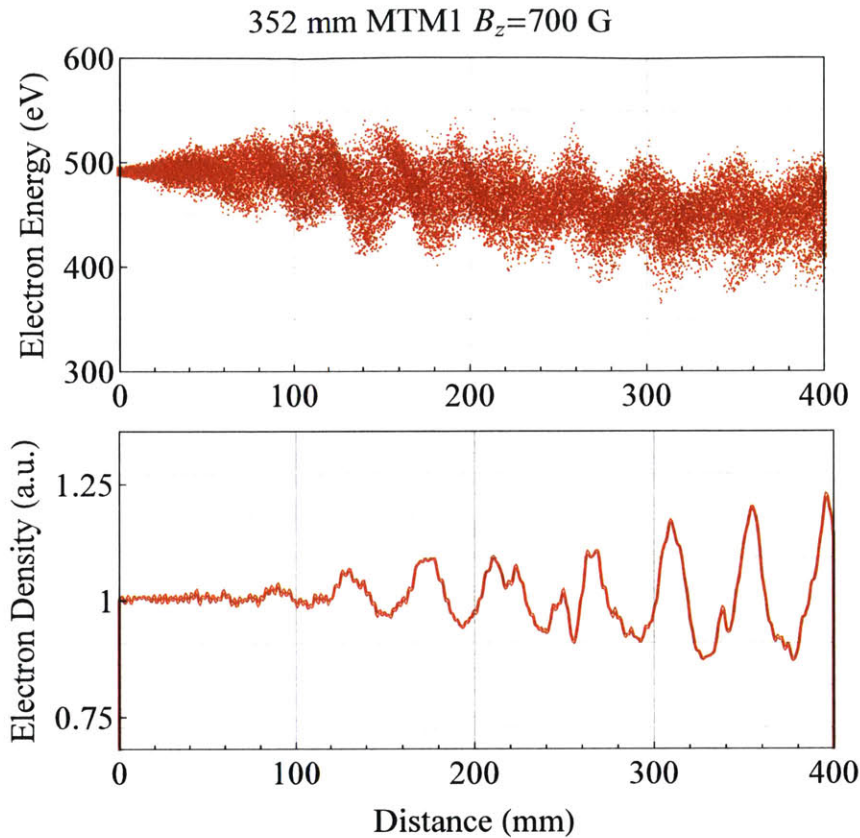


Figure 2-24: Snapshot of the electron energies at $t=200$ ns after injection of the 500 keV electron beam in the 352 mm MTM1 device when the magnetic field is 700 G. The beam is incident from the left and bunches form at approximately half the longitudinal wavelength.

the simulations. The highest output power occurs near the transition magnetic field between 700 and 900 G, which is the magnetic field in which the beam transitions from a spiraling trajectory to a linear one. Near this magnetic field value the saturation time is also very long. The red line in the plots indicates the magnetic field where the device transitions from excitation of the antisymmetric mode at low magnetic field to excitation of the symmetric mode at high magnetic field.

2.4.2 MTM2 PIC Simulations

A perspective view of the MTM2 metamaterial structure simulated with the PIC solver is shown in Fig. 2-18c. The structure is 37 periods and 370 mm long and the

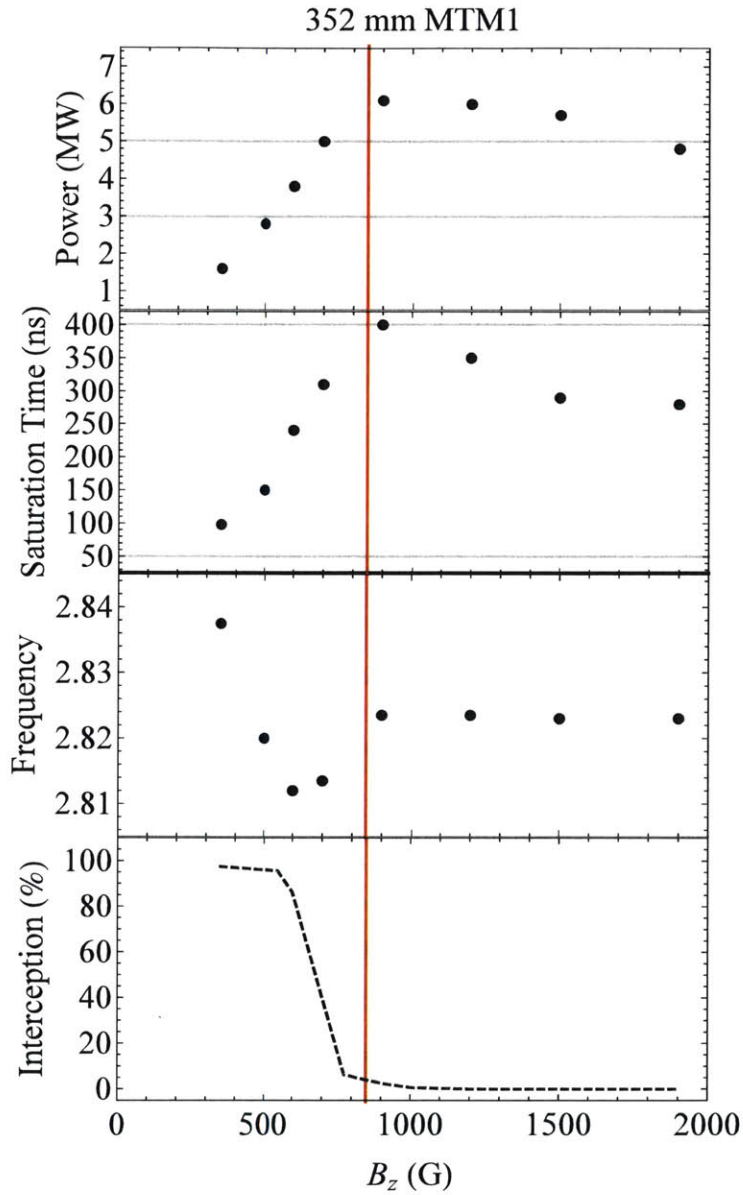


Figure 2-25: Output power, saturation time, output frequency, and beam interception calculated for the 352 mm MTM1 device for eight different simulations performed at different magnetic field values. The red line in each plot is drawn between the two simulations where the beam is observed to transition from purely axial bunching to bunching while spiraling between 800 and 900 G to indicate the transition between modes.

same type of electron beam is used in the simulations of this structure as was used in the simulations of the MTM1 structure. In Fig. 2-26 the output power and frequency are shown for a simulation with an axial magnetic field of 1.5 kG. See Table A.5 for a more detailed description of the inputs to the simulation. In the simulation, the

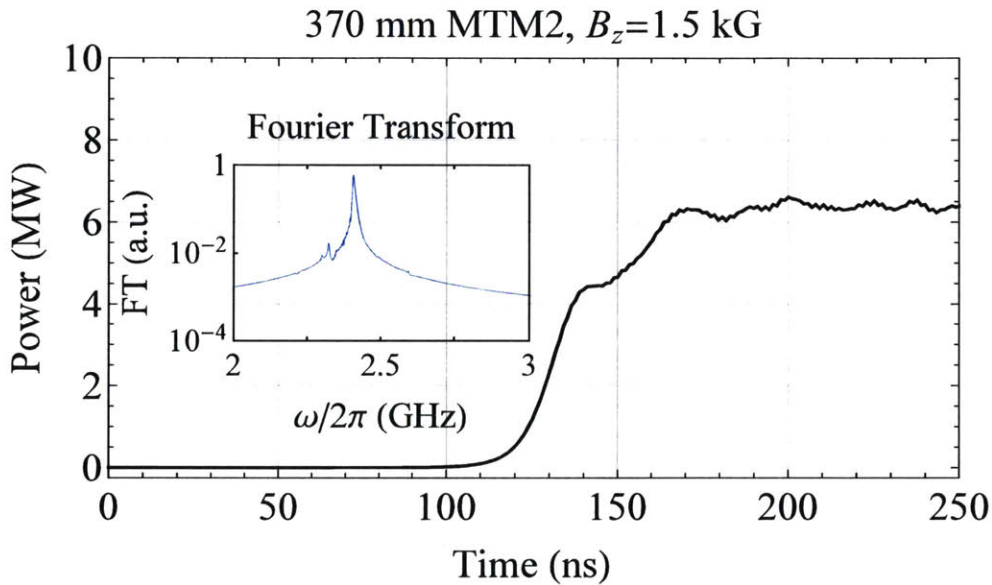


Figure 2-26: Output power of a 370 mm long metamaterial waveguide with the design of MTM2 calculated by the CST PIC simulation along with the Fourier Transform of the output signal. The simulation uses a 500 keV, 80 A electron beam with a 10 ns rise time and a longitudinal field of 1.5 kG. The output power saturates at about 6.2 MW and the radiation is peaked at 2.40 GHz.

device saturates at an output power of 6.2 MW after 175 ns. The output frequency is peaked at 2.40 GHz. Because of the simpler geometry in the metamaterial unit cell, the simulation used approximately 2 million mesh points and took approximately 1 day to complete on a desktop with 128 GB of RAM and 64 processors. A simulation performed with 0.8 million mesh cells showed a nearly identical saturation time and output power (170 ns and 6 MW). See Table A.6 for a more detailed description of the inputs to the simulation.

For different values of B , the qualitative behavior of the electron beam again mimics the behavior observed in the MTM1 design. In Fig. 2-27 the electric field profile and particle trajectories are shown for the case where $B = 1.5$ kG. It is clear

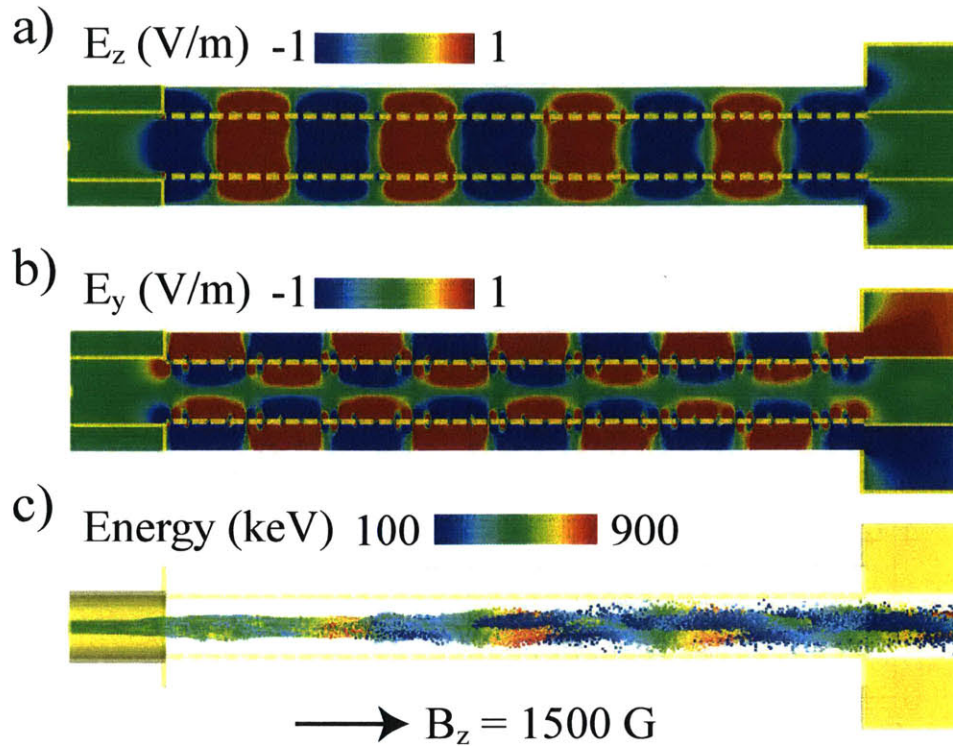


Figure 2-27: For the PIC simulation of the 370 mm long MTM2 structure, a) E_z component of the electric field b) E_y component of the electric field c) Electron trajectories. The electron beam is incident from the left and the color of each particle indicates it's energy. The arrow indicates the direction of the magnetic field which has a magnitude of 1500 G.

from the electric field plots that the beam excites the symmetric mode, and the particle orbits are roughly constrained to the axis.

In Fig. 2-28 the electric field profile and particle trajectories are shown for the case where $B = 700$ G. See Table A.7 for a more detailed description of the inputs to the simulation. It is evident from the electric field plots that the beam excites the antisymmetric mode, and the electron beam spirals around its initial center with an angular frequency nearly equal to that of the output microwave frequency ($2\pi * 2.357$ GHz) which was again calculated in CST by using a particle monitor to measure position of the beam centroid at the exit of the device.

Besides affecting the qualitative behavior of the beam, the magnetic field was also observed to slightly tune the frequency and significantly affect the output power of

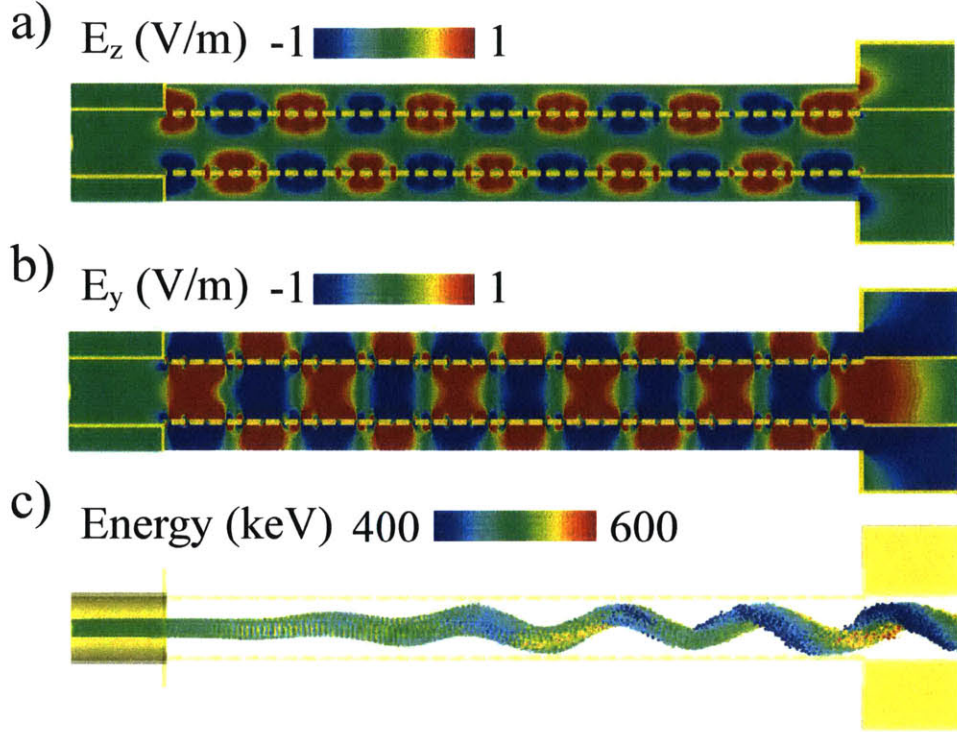


Figure 2-28: For the PIC simulation of the 370 mm long MTM2 structure, a) E_z component of the electric field b) E_y component of the electric field c) Electron trajectories. The electron beam is incident from the left and the particle color indicates it's energy. The beam is observed to spiral. The arrow indicates the direction of the magnetic field which has a magnitude of 700 G.

the device. In Fig. 2-29 the output power, saturation time, output frequency and calculated beam interception are shown for several different simulations with different B fields. The magnetic field is the only parameter varied in each of the simulations as well as the beam radius which is made to match the curve shown in Fig. 2-19 to avoid scalloping of the electron beam. See Table A.8 for a more detailed description of the inputs to the simulation. The highest output power occurs near the transition magnetic field at 800 G, which is near the magnetic field in which the beam transitions from a spiraling trajectory to a linear one. However, significant beam interception is observed when the antisymmetric mode is excited so that nearly all the electron beam is intercepted on the metamaterial structure.

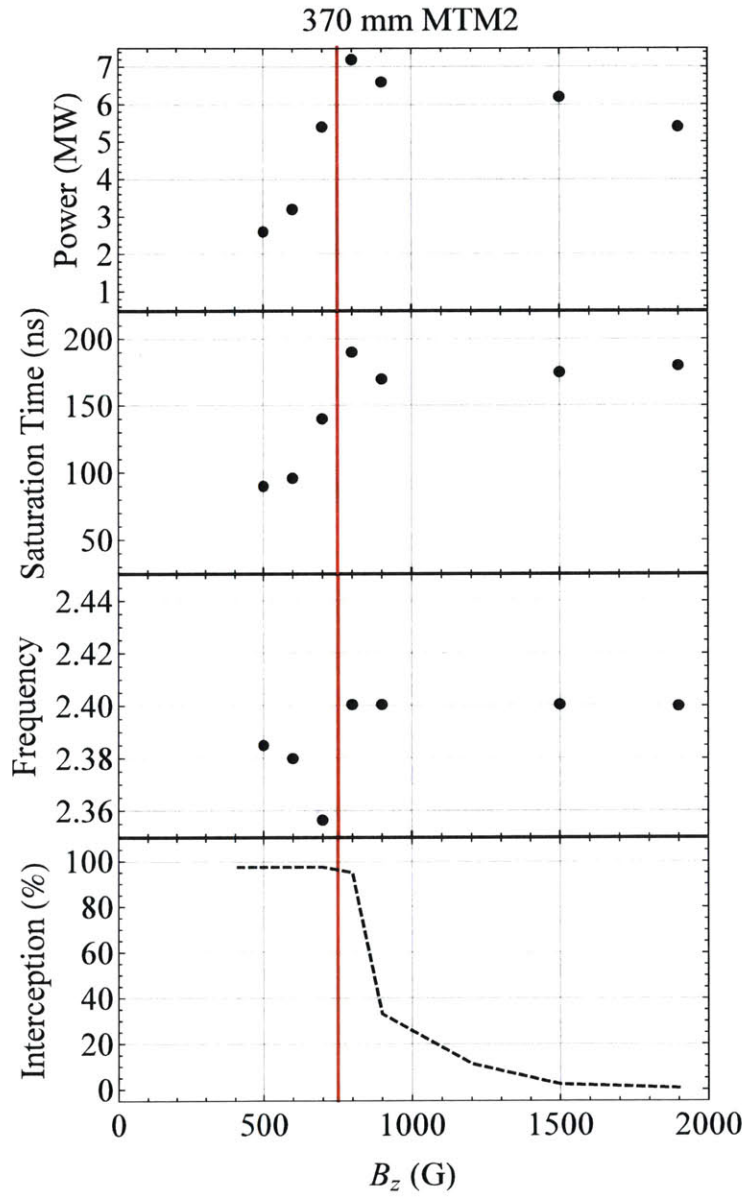


Figure 2-29: Output power, saturation time, output frequency, and beam interception calculated for the 370 mm MTM2 device for simulations performed at seven different magnetic field values. The red line in each plot is drawn between the two simulations where the beam is observed to transition from purely axial bunching to bunching while spiraling between 700 and 800 G.

2.4.3 MTM3 PIC Simulations

The MTM3 metamaterial structure simulated with the PIC solver structure was 84 periods and 420 mm long. The structure that was simulated looked similar to the MTM2 structure which is shown in Fig. 2-18c since it was a scaled version of the MTM2 design. The same type of electron beam was used in the simulations of this structure as were used in the simulations of the MTM1 and MTM2 structure. In Fig. 2-30 the output power and frequency is shown for a simulation with an axial magnetic field of 1.5 kG. See Table A.9 for a more detailed description of the inputs to the simulation. In the simulation, the device saturates at an output power of 1

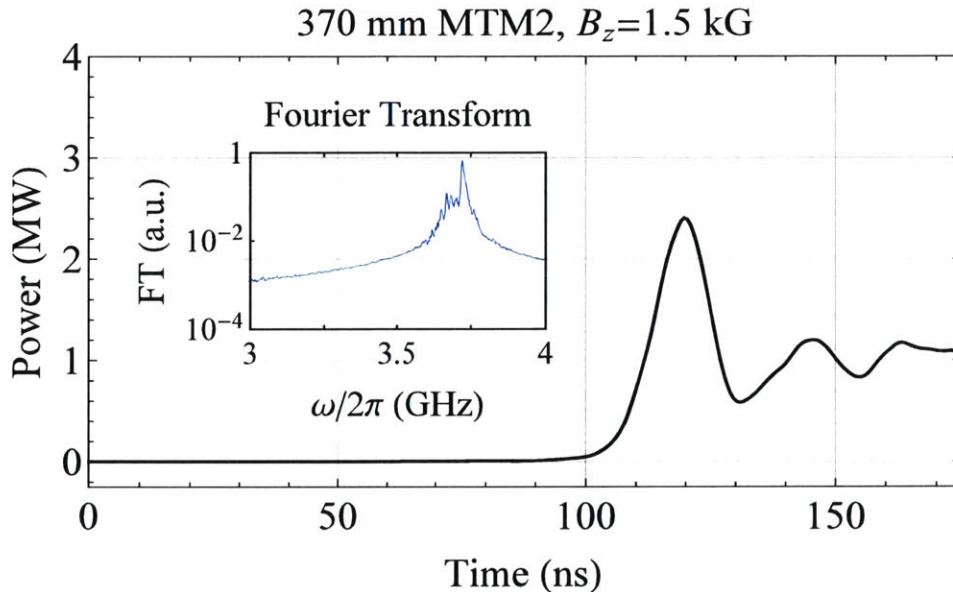


Figure 2-30: Output power of a 420 mm long metamaterial waveguide with the design of MTM3 calculated by the PIC simulation along with the Fourier Transform of the output signal. The simulation uses a 500 keV, 80 A electron beam with a 10 ns rise time and a longitudinal field of 1.5 kG. The output power saturates at about 1 MW and the radiation is peaked at 3.71 GHz.

MW after 120 ns. The output frequency is peaked at 3.71 GHz. The simulation used approximately 5 million mesh points and took approximately 2.5 days to complete on a desktop with 128 GB of RAM and 64 processors.

The qualitative behavior of the electron beam as the magnetic field was varied mimicked the behavior observed in the MTM2 and MTM1 designs. For low magnetic

field values (800 G or less) the antisymmetric mode was excited and the beam was observed to spiral, and for higher magnetic field values the beam bunched axially. Besides affecting the bunching of the beam, the magnetic field was also observed to slightly tune the frequency and significantly affect the output power of the device. In Fig. 2-31 the output power, saturation time, output frequency and calculated beam interception are shown for seven different simulations with different B fields. The magnetic field is the only parameter varied in each of the simulations as well as the beam radius which is made to match the curve shown in Fig. 2-19 to avoid scalloping of the electron beam. See Table A.10 for a more detailed description of the inputs to the simulation. The highest output power occurs near the transition magnetic field at 900 G, which is near the magnetic field in which the beam transitions from a spiraling trajectory to a linear one. Again a significant amount of beam interception is observed when the antisymmetric mode is excited so that nearly all the electron beam is intercepted on the metamaterial structure. In this structure, there is also beam interception when the symmetric mode is excited except at a very high magnetic field (1800 G).

2.4.4 Effective Medium PIC Simulations

In addition to the realizable metamaterial plates, we also simulate the interaction of an electron beam with the theoretical metamaterial composed of a Lorentz dielectric like the one investigated in Section 2.1 in order to show that the effective medium theory is valid for our metamaterial structure. A perspective view of the waveguide filled with a theoretical dielectric material that was simulated with the PIC solver is shown in Fig. 2-18d. The dielectric completely fills the waveguide except for a small beam tunnel of radius 5 mm through with the beam of radius 3 mm can pass and has a Lorentz response in the transverse direction. In order to avoid the beam hitting the dielectric and causing problems with dielectric charging, a nearly infinite magnetic field (4 T) was used to keep the particle orbits fixed to the z -axis. The permittivity of the dielectric in the directions transverse to the electron beam velocity is defined

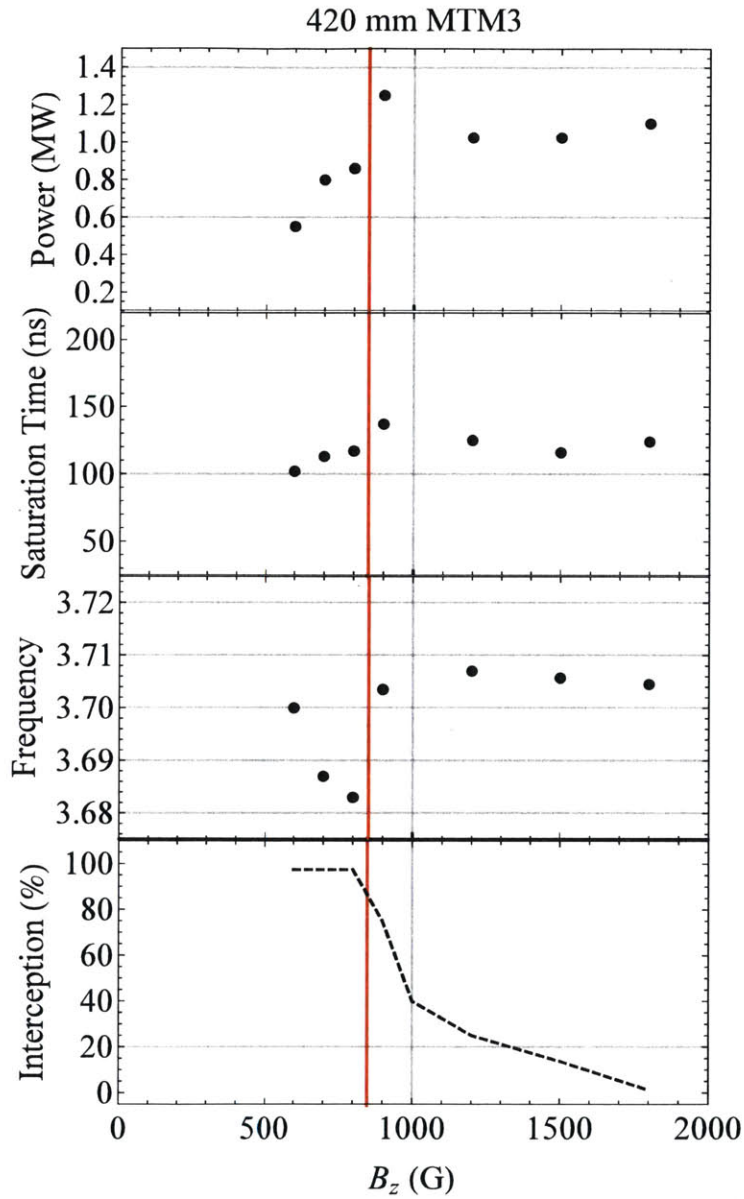


Figure 2-31: Output power, saturation time, output frequency, and beam interception calculated for the 420 mm MTM3 device for simulations performed at seven different magnetic field values. The red line in each plot is drawn between the two simulations where the beam is observed to transition from purely axial bunching to bunching while spiraling between 800 and 900 G.

to be

$$\epsilon_{eff} = 1 - \frac{\omega_p^2}{\omega^2 - \omega_0^2} \quad (2.4.2)$$

where ω_p is the plasma frequency and ω_0 is the resonant frequency. The particular numerical values of ω_0 and ω_p are chosen so that the dispersion of the waveguide matches the dispersion of the MTM1 metamaterial structure. Since the permittivity is given by $\epsilon = \frac{c^2 k^2}{\omega^2}$, the resonance and plasma frequencies in Eq. 2.4.2 are determined from the dispersion relation by letting $\epsilon \rightarrow \infty$ and $\epsilon \rightarrow 0$, which corresponds to letting $k_z p \rightarrow \infty$ and $k_z p \rightarrow 0$, respectively. To match this we set the resonance frequency at $\omega_0 = 2\pi \cdot 2.5 \text{ GHz}$ and the plasma frequency at $\omega_p = 2\pi \cdot 1.8 \text{ GHz}$. The dispersion relation predicted by the effective medium model vs. the dispersion of the upper negative group velocity mode of the MTM1 metamaterial structure that was found with the eigenmode solver is shown in Fig. 2-32. The model predicts a mode with negative group velocity at approximately the same frequency as the MTM1 structure, however the frequency of interaction is slightly higher for the model than for the MTM1 metamaterial structure (2.96 vs. 2.83 GHz).

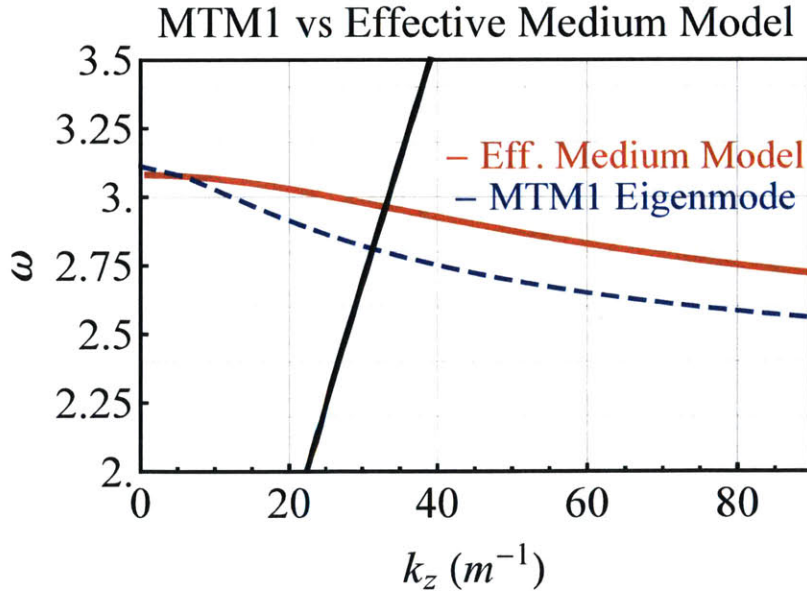


Figure 2-32: Dispersion relation for the upper negative group velocity mode of the MTM1 metamaterial structure (blue dashed) plotted against the dispersion of the effective medium structure (red). Also shown is the beam line for a 500 keV electron beam in black.

The simulation uses an identical beam to the previous PIC simulations at 500 keV, 80 A and with a 10 ns rise time. In Fig. 2-33 the output power and frequency are shown. See Table A.11 for a more detailed description of the inputs to the simulation. In the simulation, the device saturates at an output power of 1.2 MW after 450 ns.

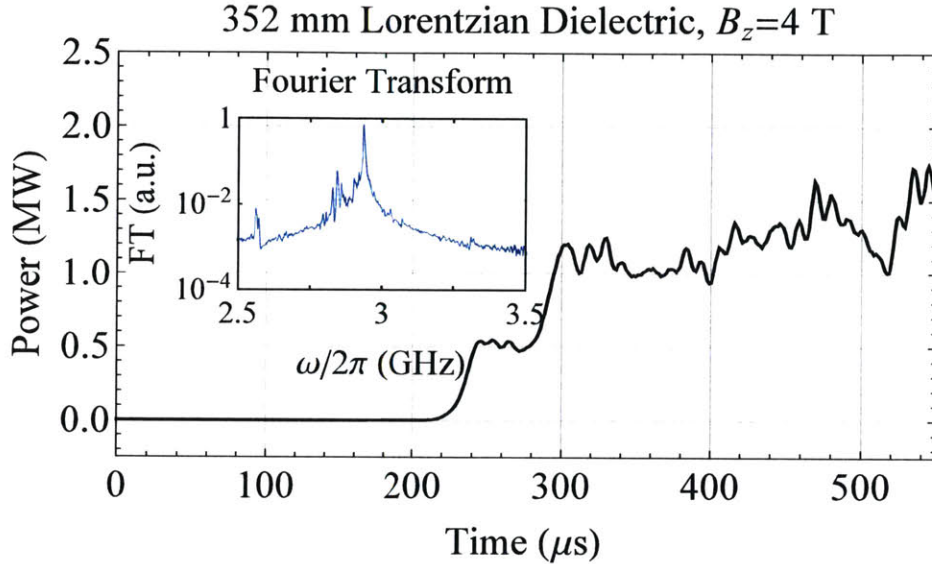


Figure 2-33: Output power of the Lorentz dielectric filled waveguide calculated by the PIC simulation along with the Fourier Transform of the output signal. The simulation uses a 500 keV, 80 A electron beam with a 10 ns rise time and a longitudinal field of 4 T. The output power saturates at about 1.2 MW and the radiation is peaked at 2.92 GHz.

The output frequency is peaked at 2.92 GHz. Because of simple geometry involved, the simulation used approximately 500 thousand mesh points and took approximately 4 hours to complete on a desktop with 128 GB of RAM and 64 processors, which was much faster than the full simulations of the MTM1, MTM2 and MTM3 devices.

In Fig. 2-34 the electric field profile and particle trajectories are shown. Because of the strong magnetic field the electrons are confined to the axis and excite a mode which qualitatively looks similar to the symmetric modes of the MTM1, MTM2 and MTM3 simulations. The mode has 3 variations along the y axis, one along the x axis, and has an electric field that is longitudinal on axis $E_y \approx 0$.

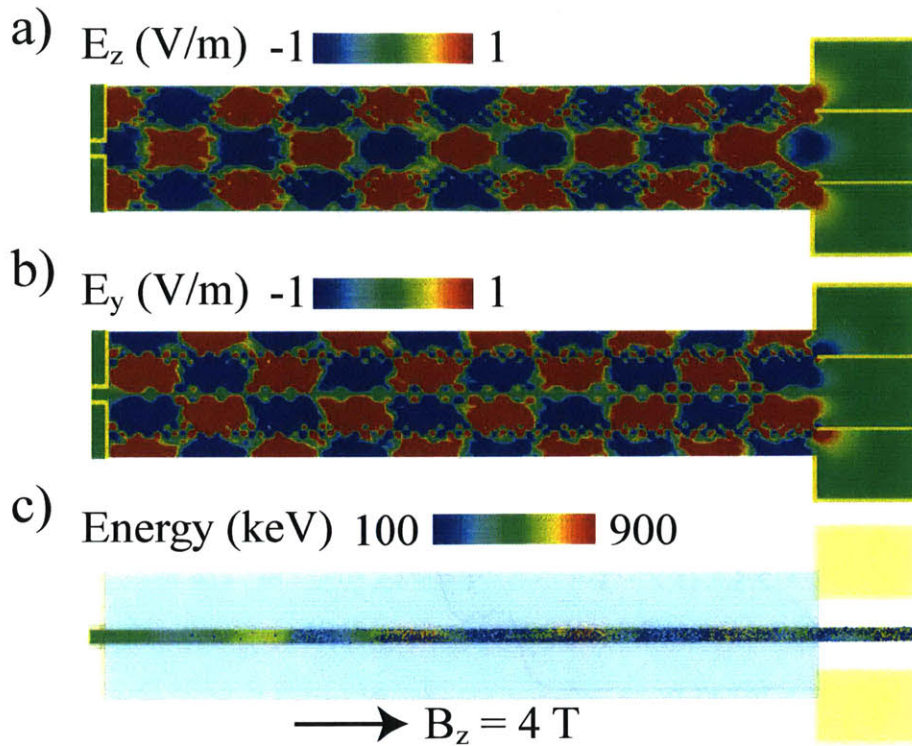


Figure 2-34: For the PIC simulation of the 352 mm long waveguide filled with a dielectric possessing a Lorentz electric response, a) E_z component of the electric field b) E_y component of the electric field c) Electron trajectories. The electron beam is incident from the left and the particle color indicates it's energy. The arrow indicates the direction of the magnetic field which has a magnitude of 4 T, which confines the beam to the small beam tunnel in the theoretical Lorentzian dielectric. The field distributions and particle trajectory plots were generated 400 ns after the injection of the electron beam.

2.5 Cold Tests

To validate the electromagnetic response of the metamaterial waveguide design, measurements of microwave transmission in several test structures with different overall designs were performed using a vector network analyzer (VNA model Agilent E8363B). These low power microwave measurements are meant to verify the results of section 2.2 and show the existence of below-cutoff modes supported by the metamaterial. They do not investigate the beam-wave coupling that was analyzed with the PIC simulations. In addition, different coupling schemes were examined in the test

structures in order to investigate any potential problems associated with coupler design. Coupling to metamaterial devices can be one of the main engineering challenges associated with using metamaterial structures since they generally have very complex field patterns that are unlike the field patterns of a standard rectangular or cylindrical waveguide [62, 63]. In the designs for the MTM1, MTM2 and MTM3 structures, coupling to the negative group velocity mode was non-trivial since the electric field topology of the negative group velocity mode in the metamaterial waveguide is unlike the fundamental waveguide mode of the standard WR284 rectangular waveguide that was planned to be used for output couplers and microwave loads in the high power experiment.

Two different test structures were designed based on the metamaterial plate design of MTM1, which for purposes of clarity are called MTM1a and MTM1b since they have slightly different designs than the MTM1 design. The first test structure, MTM1a, is shown in Fig. 2-35 along with a CAD rendering showing the general design of the structure. The structure is identical to that shown in Fig. 2-5 except with $p = 7$ mm, $w = 16$ mm, and $g = 2$ mm. The change in the dimensions of the structure shifted the operating frequency (simulated and experimental) slightly lower than the design in section 2.2 (synchronism with a 500 keV beam is now at 2.6 GHz instead of 2.856 GHz) but otherwise the mode pattern and dispersion were similar. The overall structure length was 20 periods (160 mm). The metamaterial plates were aligned in a brass WR340 waveguide (inner dimension $wg = 86$ mm by $d = 43$ mm) by end supporting plates, and the metamaterial resonators were created by machining out two brass plates.

In this test design, coupling was accomplished through WR284 waveguide mated to the sides of the test structure. This matched the polarization of the electric field in the fundamental TE mode of the WR284 waveguide and the polarization of the axial field in the symmetric negative group velocity modes of the test structure. This coupling scheme is different than that used in the PIC simulations of the metamaterial structures, and was originally chosen for the simplicity of using only one output coupler. However, this design was not used in high power testing due to space limita-

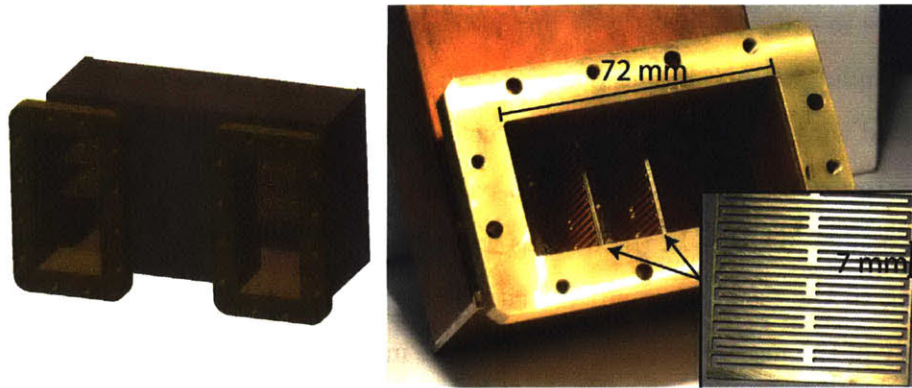


Figure 2-35: CAD rendering, photograph of the MTM1a metamaterial test structure based on a slightly modified version of the MTM1 design, and photograph of the CSRR loaded brass plate. The photo is taken looking into one of the identical WR284 input ports for coupling in/out of the structure. The negative group velocity mode in the test CSRR structure is excited by the fundamental mode of the input WR284 waveguide. The flange shown in the photograph mates to coax to WR284 waveguide adapters.

tion inside the bore of the solenoid where the high power test structure needed to fit. Additionally this coupling scheme only serves to excite the symmetric modes in the waveguide since the electric field in the WR284 waveguides has the wrong polarization to excite the antisymmetric modes. Therefore this design was not investigated in the PIC simulations since it was not possible to experimentally test it.

Coax to WR284 waveguide adapters are used to excite the fundamental TE mode in the WR284 waveguide. The transmission measurement is shown in Fig. 2-36 in blue, along with a simulation of the same setup using CST Microwave Studio in red. Excitation of the negative group velocity mode is demonstrated by non-zero transmission where the negative group velocity mode was predicted by HFSS eigenmode simulation. The simulation and measurement show excellent agreement. The simulation is able to predict all of the spatial modes of the structure (seen as resonances on the transmission plot) although there is a very small (<0.025 GHz) frequency shift. In addition, near the design frequency of 2.6 GHz, the experiment and simulation are in agreement to within 2 dB.

A second cold test structure, MTM1b, was built to test a different coupling method and to investigate the excitation of the antisymmetric vs. symmetric modes. A

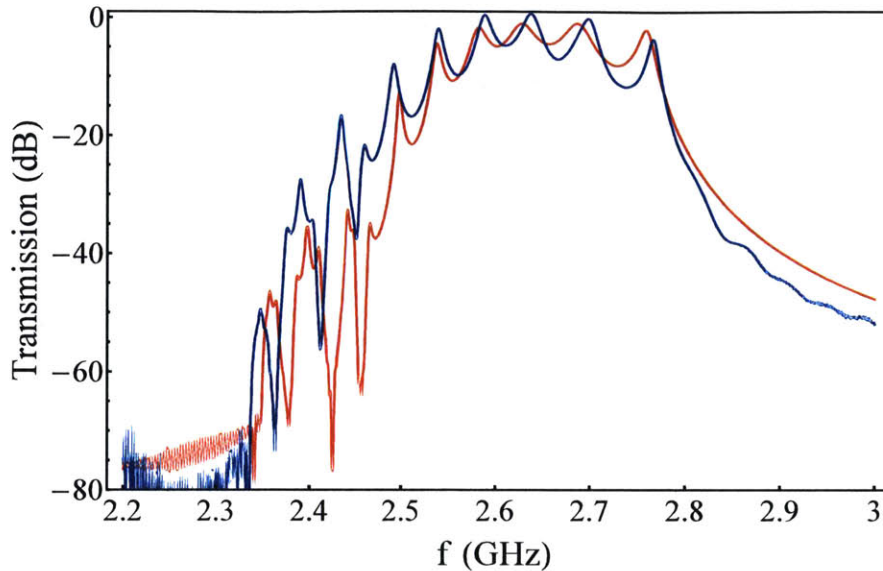


Figure 2-36: Transmission measurement of the test MTM1a structure (blue) compared with CST Microwave Studio simulation (red). Note that the design of MTM1a is slightly different than the design of MTM1. See surrounding text.

photograph of the test structure is shown in Fig. 2-37. The structure is identical to that shown in Fig. 2-5 except with $p = 8$ mm, and $g = 2$ mm, and $w = 36$ mm. By controlling the phase between the input ports the antisymmetric and symmetric modes could be independently excited. The test structure is 47 periods (376 mm) in length and terminates in two output ports which are identical to the input ports. The VNA was again used to measure the transmission through the test structure. Two phase matched power splitters were used to split the input power evenly between the two input waveguides and recombine the power at the output waveguides. Phase matched cables were used to take the power from the splitters to the coax to WR284 waveguide coupler heads. The orientation of one of the waveguide heads was flipped to change the phase of the input microwave signal by 180 degrees. This caused the 'surface waves' on each metamaterial plate to be in phase (symmetric waveguide mode) or 180 degrees out of phase (antisymmetric waveguide mode).

In Fig. 2-38 the experimental (blue) and simulated (red) transmission is shown for the symmetric waveguide mode (corresponding to 180 degree phase shift between the

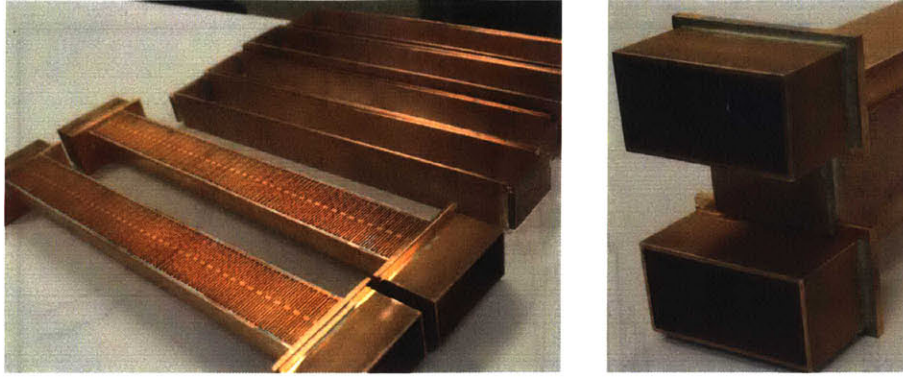


Figure 2-37: Photographs of the MTM1b metamaterial test structure based on a slightly modified version of the MTM1 design. The device has two input ports and two output ports. By controlling the phase between the input ports the antisymmetric and symmetric modes could be independently excited. Note that the design of MTM1b is slightly different than MTM1.

excitation) and the antisymmetric mode (corresponding to a 0 degree phase shift). The simulated transmission curves were calculated using the time domain solver of CST Microwave Studio. The slightly higher cutoff frequency of the antisymmetric mode calculated in the eigenmode dispersion and transmission simulations with CST and HFSS was also seen in the transmission measurement. Here the cutoff frequency is defined by letting $k_{zp} \rightarrow 0$ in Fig. 2-6, or in Fig. 2-38 is the maximum frequency where transmission of microwave power is observed. (For a positive group velocity mode, the cutoff frequency would be the minimum frequency where transmission of microwave power would be observed.) This shows that each mode could be excited independently from the other by choosing appropriate an appropriate phase difference between the metamaterial plates.

The simulation and measurement in both of the plots in Fig. 2-38 show good agreement. The cutoff frequency of both modes is correctly modeled to within 0.05 GHz, and nearly 20 spatial modes are resolved in both measurements. There is a disagreement in the transmission of about 10 dB near 2.7 GHz in both agreements. This disagreement may be due to poor contact between the top and bottom metamaterial waveguide and the central guide. Similar transmission error was see in the MTM1 structure presented in section 4.2.1.

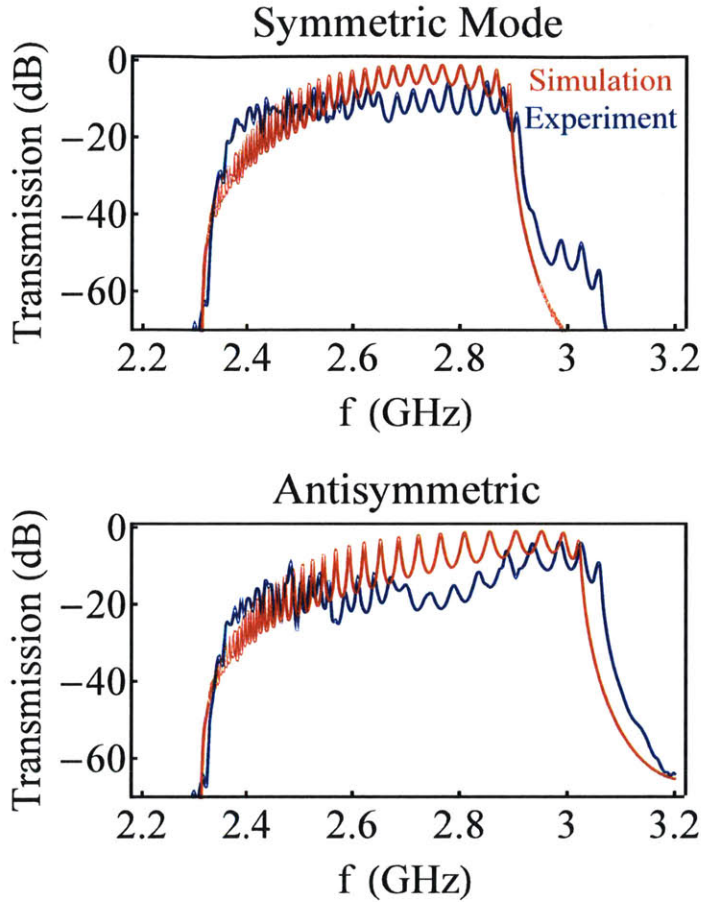


Figure 2-38: Transmission measurement of the test MTMBWO structure (blue) compared with CST Microwave Studio simulation (red).

2.6 Summary of Design

In this chapter we outline the general theory and specific simulation tools that went into the design of a beam-powered, metamaterial waveguide. Three different metamaterial structures were presented which are called MTM1, MTM2, and MTM3. Eigenmode simulations were presented for a linear analysis of the wave propagation in the metamaterial structures and in order to investigate the field structure of the modes supported in the waveguides. A simple linear theory was presented to show that for all three metamaterial structures oscillation should occur in the symmetric mode as long the length of the structure the structures is long enough (typically

greater than 300 mm). PIC simulations are discussed which were used to characterize the performance of the metamaterial BWO design. They show that multi-megawatt operation is predicted in all three structures for a 500 keV, 80 A electron beam. They also highlight the fact that the magnetic field controls whether the device oscillates in the antisymmetric mode or the symmetric mode. Finally low-power measurements are shown to benchmark the simulation tools vs. experiment and show good agreement between the two.

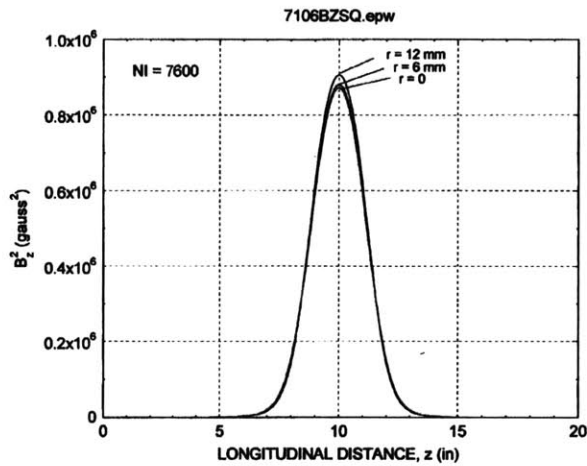
Chapter 3

High Power Test Experimental Setup

In this chapter the setup for the high power microwave test of the metamaterial structures, which used a 500 keV and 80 A electron beam, is introduced. The various RF components used to investigate the microwave signal are discussed. In addition, the transport of the 500 keV electron beam which was formed using an electrostatically focused electron gun and guided with a magnetic lens and solenoid is also examined.

3.1 Magnetic Lens and Solenoid

A water cooled, low aberration magnetic lens and a set of four large bore pancake magnets were used in the metamaterial experiment to confine the 500 keV electron beam. All magnets were designed by Haimson Research Corporation and their fabrication was also supervised by Jake Haimson. Knowing the magnetic field profiles of each of the magnetic components was important in understanding the transport of the electron beam through the experiment. The magnetic field profile of the magnetic lens was provided by Haimson Research Corporation and is shown below in Fig. 3-1. The lens was designed so that the squared magnetic field integrated along the axis at different radii is the same. This is so that electrons at different radial positions in the electron beam focus to the same axial location.



B_z^2 Radial Dependency of Lens Assembly.

LENS No. 1 ANALYSIS DATA
FOR NI = 7600 ampere-turns (I = 14 A)

RUN No.	Beam Radius r (mm)	Max B_z (gauss)	$\int B_z dz$ (gauss-cm)	$\int B_z^2 dz$ (gauss ² -cm)
601	0	933.8	9441.05	6.103×10^6
602	3	935.0	9441.13	6.113×10^6
603	6	938.4	9441.23	6.140×10^6
604	9	944.1	9441.28	6.187×10^6
605	12	952.1	9441.38	6.254×10^6

Comparison of $\int B_z^2 dz$ Values versus Radial Distance from Axis.

Figure 3-1: Magnetic field profile provided by Haimson Research Corporation measured at 3 different radial positions. Also shown is the longitudinal field integrated along the axis at different radial positions.

It was necessary to calculate the magnetic field profile of the solenoid since Haimson Research Corporation only provided the magnetic field profile for these magnets for a different experimental configuration. The solenoid was constructed from a stacked set of four pancake magnets which were sandwiched between two steel pole pieces. The inner diameter of the pancake magnets was specified at 7.97 in, and the two 0.55 in thick pole pieces had bore diameters equal to the pancake magnets. The 2D electrostatic field code Poisson was used to calculate the magnetic field profile [64]. The result for a current of 175 A in the solenoid coils is shown in Fig. 3-2. The magnetic field of the solenoid assembly was also measured at 3 axial locations (on the axis at both pole pieces and on the axis at the center of the solenoid) and agreed with the calculation to within $\pm 1.5\%$.

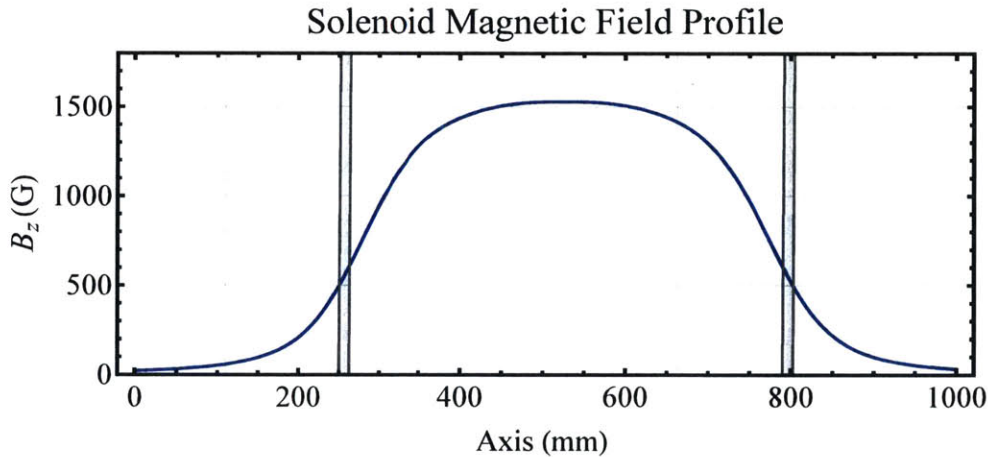


Figure 3-2: Magnetic field profile of the solenoid and steel pole pieces calculated with the code Poisson for a current of 175 A through each of the solenoid magnets. The field profile is shown in blue, and the location of the pole pieces is given in gray. The four pancake magnets are sandwiched between the pole pieces.

In the metamaterial experiment the two solenoid magnets closest to the gun and two solenoid magnets closest to the collector were run in series on different power supplies. This allowed the magnetic field in the metamaterial structure to be profiled which had an effect on the operation of the device.

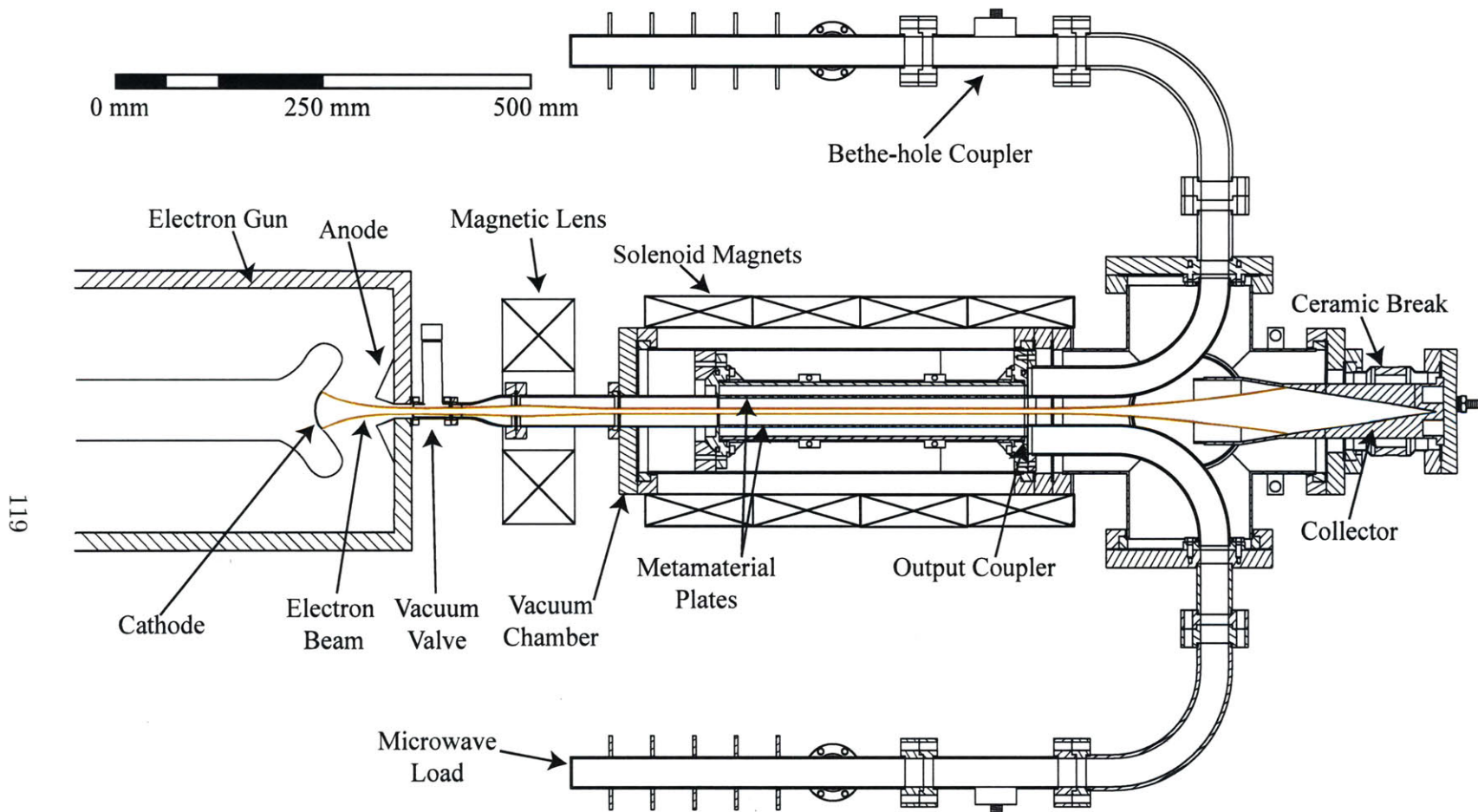
3.2 500 keV Electron Beam and Transport

The metamaterial experiment utilized a 500 keV electron beam. The electron gun used to generate this beam was designed and built by Haimson Research Corporation. The gun was initially designed for operation up to 550 kV and 92 A as part of a 17 GHz choppertron amplifier experiment. The gun was designed to create a low convergence, electrostatically focused, and space-charge limited beam. The beam is focused to a 7.5 mm waist diameter in the gun isolation vacuum valve. After traveling through a short, field free, adjustable drift region the beam was then focused by a water cooled, low aberration lens into a water-cooled solenoid assembly. The lens and solenoid systems were mounted on linear bearing supports that could be independently adjusted.

The metamaterial experiment was installed in place of the 17 GHz choppertron experiment and used the electron gun, magnetic lens, and solenoid support assembly designed by Haimson Research Corporation. Therefore, the metamaterial experiment had to mate to the components that were recycled from the 17 GHz experiment, and it was necessary to know the dimensions of the components used in this experiment. A block drawing of the 17 GHz choppertron experiment was provided by HRC for this purpose. A schematic of the metamaterial experiment that uses the Haimson Research electron gun is shown in Fig. 3-3 where all of the major components are labeled and an approximate scale is given for reference.

The Pierce-type gun uses a thermionic cathode. The emitter is made from a porous tungsten matrix that is impregnated with barium. Barium that travels to the surface of the emitter has a low work function which allow these types of cathodes to achieve high emission current densities and very long operation lives. A photograph of the original cathode installed before the 17 GHz choppertron amplifier experiments were performed is shown in Fig. 3-4.

In order to achieve the temperatures necessary for high electron emission, the cathode uses a molybdenum heater element which is embedded under the emitter in a ceramic matrix. The heater is then powered by an external power supply. Unfortunately, the heater element of the gun burned out during operation in June 2015, and



119

Figure 3-3: Simplified schematic of the high power metamaterial experiment. The structure shown in this schematic is the 370 mm MTM2 metamaterial structure. The electron beam (orange) is formed by an electrostatically focused Pierce electron gun. The beam generates microwaves in the metamaterial circuit and then is dumped into a high power beam collector. The microwaves are coupled out of the metamaterial structure and into Bethe-hole couplers, where the power and frequency of the microwaves can be measured. The scale shown in the figure is approximate.

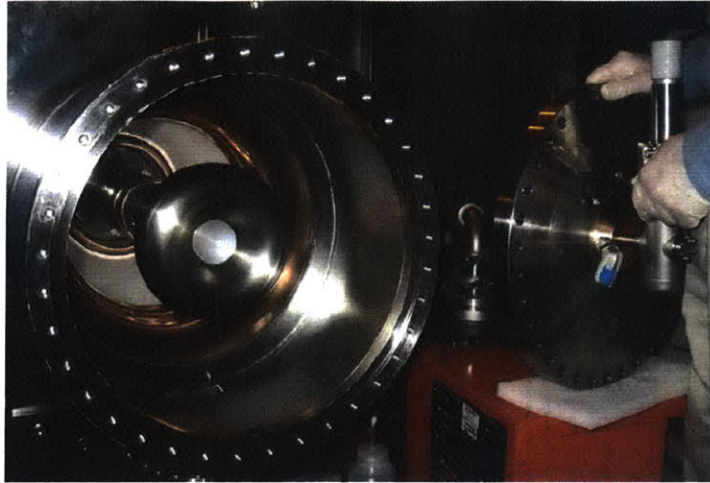


Figure 3-4: Photograph of the cathode opened up to air for installation. The anode is centered on the inside of the flange on the right. The gun vacuum isolation valve is also shown attached to the beam tunnel (not visible).

was replaced in July 2015. Because the heater element is embedded under the emitter, it was necessary to replace the whole cathode. The replacement of the cathode was observed to have a slight effect on the perveance (emitted current for a particular voltage) of the electron gun. The operational secondary heater current of 23 A, which is the new specification provided by Jake Haimson of Haimson Research Corporation in July of 2015, was exceeded in the original cathode and this was the likely reason for failure. In any case, all data taken prior to July 2015 has a slightly different voltage/current ratio than data taken after this date. Traces of the voltage and current measured at the collector for the same magnetic field taken with the old cathode on May 29, 2015 and with the new cathode on October 14, 2015 are shown in Fig. 3-5 and Fig. 3-6, respectively. After replacement of the cathode the emitted current of the gun was observed to be higher for the same gun voltage (for 490 keV and the same magnetic field settings the measured current was 81.5 A with the old cathode and 84.5 A with the replacement cathode).

After the cathode was replaced in July 2015 care was taken to characterize the operation of the heater of the new cathode for future reference. In Fig. 3-7 the variation of heater current with applied voltage is shown as the power to the heater filament is

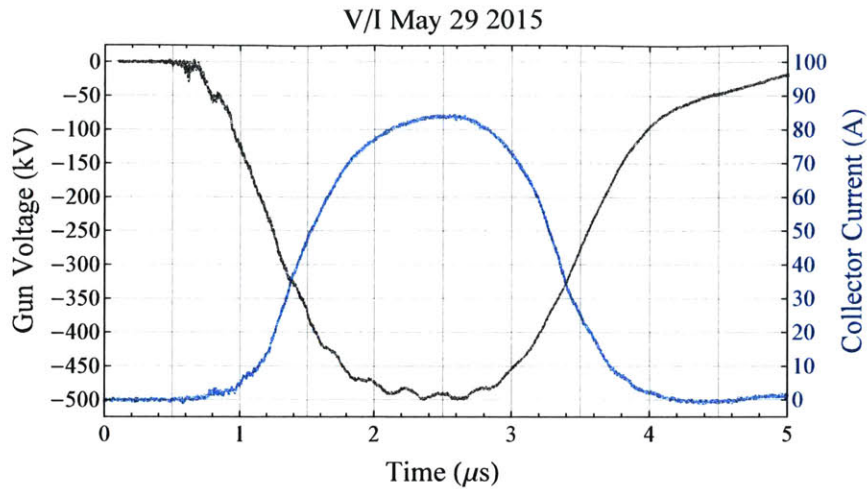


Figure 3-5: Gun voltage (black) and measured current at the collector (blue) of the electron gun before the cathode was replaced. The measurement was taken on May 28, 2015 for a solenoid current of 50 A and a lens current of 12 A. The heater was set to 84% on the variac.

slowly increased from 0 W to its full operational value of approximately 360 W. Measurements of the heater current were performed with a current clamp approximately 30 minutes after each increase in voltage in order to measure the current at the steady state value. The voltage measurements were made with a standard voltmeter. Note that as the temperature of the cathode changes the resistance also changes and so the V/I relationship is not a straight line.

It was already stated that the electron gun produces an electron beam electrostatically focused to a 7.5 mm waist diameter in the gun isolation vacuum valve. The exact location of the focus was specified by Haimson Research Corporation as well as the beam envelope (in the absence of any external magnetic fields) past the focal spot. The specification drawing for the gun focus that was provided is shown in Fig. 3-8.

From the beam focus location it was necessary to calculate the beam profile along the axis of the experiment to ensure that it safely made it to a high-power, water-cooled beam collector. To accomplish this two different approaches were used. A commercial 3D particle tracking code called MICHELLE was used to calculate the beam envelope [65]. The code has been used successfully to design other Pierce-type and MIG-type guns at MIT and has been benchmarked against guns built elsewhere.

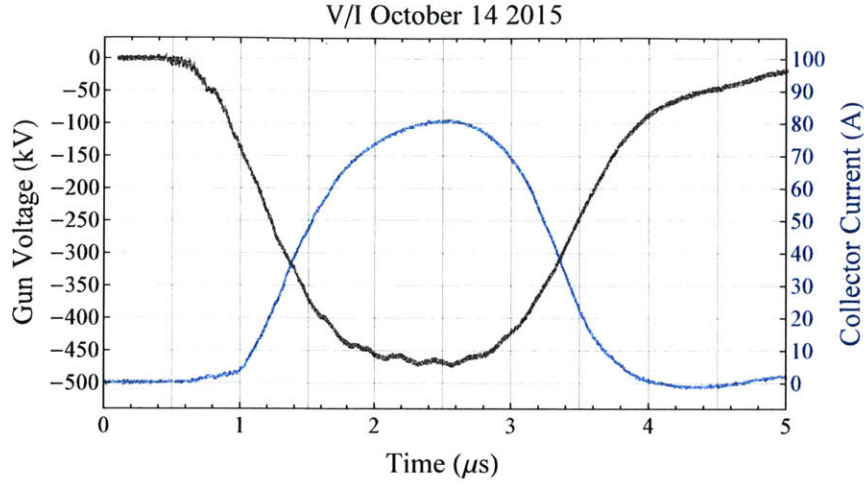


Figure 3-6: Gun voltage (black) and measured current at the collector (blue) of the electron gun after the cathode was replaced. The measurement was taken on October 14, 2015 for a solenoid current of 50 A and a lens current of 12 A. The heater was set to 74% on the variac.

In addition to this code, a 1D code was written to solve the beam envelope equation when given an input beam current, voltage, focus waist radius, and 1D axial magnetic field profile. The 1D code was much faster to use than the MICHELLE code both in simulation time and in simulation setup time, and therefore this was generally used to explore different magnetic field profiles once it was benchmarked against the much more powerful MICHELLE code for a few different magnetic field profiles.

The 1D code calculates the electron beam envelope from the envelope equation. For an electron beam traveling in a magnetic field that is parallel to the beam velocity the envelope equation is given by [66]

$$r'' + \frac{e^2 B_z^2}{2m_e \gamma \beta c} r - \kappa \frac{1}{r} - \frac{\epsilon_n^2}{\beta^2 \gamma^2 r^3} = 0 \quad (3.2.1)$$

where r is the beam envelope, B_z is the magnetic field, κ is the generalized perveance of the electron beam, ϵ_n is the normalized emittance, β is the electron velocity relative to the speed of light, and γ is the electron energy relative to the electron rest mass.

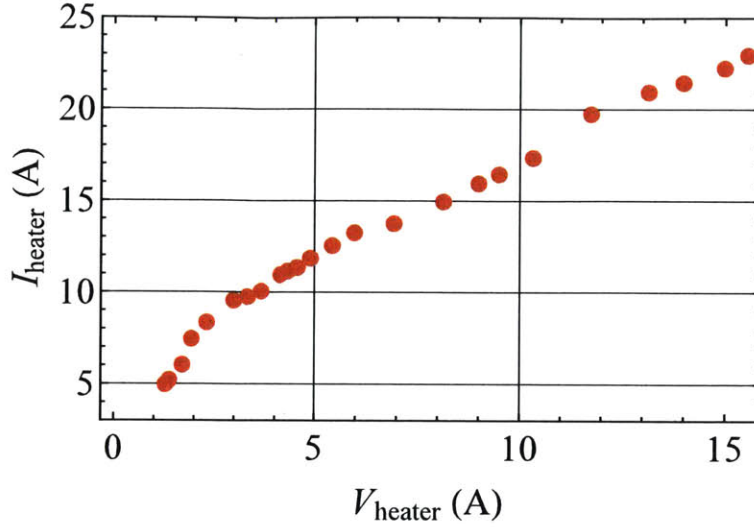


Figure 3-7: Measured secondary heater current and voltage applied to the heater element as the power in the primary power supply is increased from 0 to its full operational value. The nominal operating point of the gun is with a heater current of 23 A which was specified by Haimson Research Corporation.

The term κ , which is dimensionless, is given by the following equation

$$\kappa = \frac{eI}{2\pi\epsilon_0 m_e \beta^3 \gamma^3 c^3} \quad (3.2.2)$$

For $I = 80 \text{ A}$, $\gamma = 1.98$, and $\beta = 0.86c$ (which corresponds to a 500 keV beam), $\kappa = 0.00188$.

It can be shown that the beam used in the metamaterial experiment is space-charge dominated, and therefore the emittance term in Eq. 3.2.1 can be ignored. From Liouville's theorem we know that for a set of non-interacting particles, the normalized emittance $\epsilon_n = \beta\gamma\epsilon$ is conserved [66]. Therefore, we can estimate the emittance at the cathode from the following equation

$$\epsilon_n = 2a\sqrt{\frac{KT}{m_e c^2}} \quad (3.2.3)$$

where T is the temperature of the cathode and a is the radius of the cathode. For $T = 1000 \text{ C}$ and $a = 25 \text{ mm}$, $\epsilon_n = 23 \text{ mm mrad}$. Comparing the space charge term and

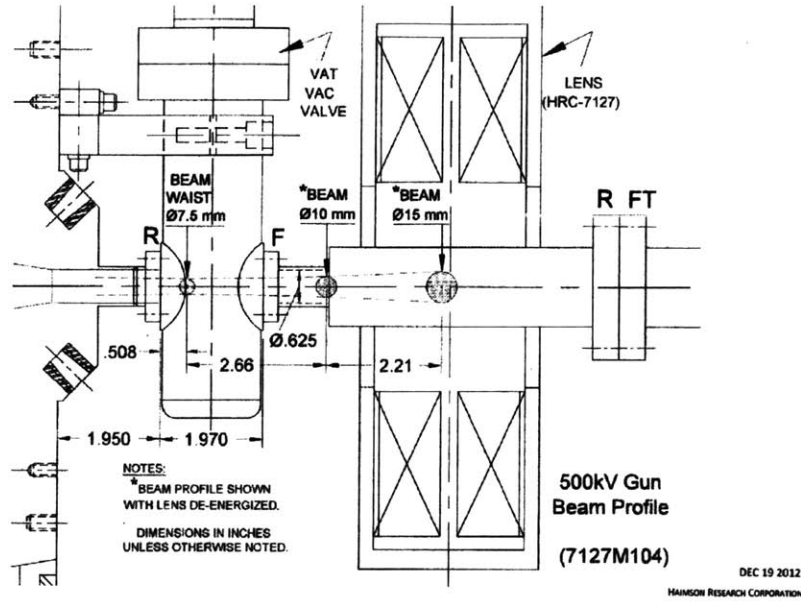


Figure 3-8: Beam envelope for the Haimson Research Corporation 500 keV gun. The beam is focused to a waist size of 7.5 mm in the gun vacuum isolation valve a distance of 12.5 mm from the face of the mini conflat flange where the vacuum valve is attached.

emittance terms in Eq. 3.2.1 for the focused beam (where $r=3.75$ mm) we find that

$$\frac{\epsilon_n^2}{\kappa\beta^2\gamma^2r^2} = 0.007 \tag{3.2.4}$$

and so ignoring the emittance term in Eq. 3.2.1 is a good approximation for the metamaterial experiment electron beam. The resulting envelope equation to be solved by the 1D beam envelope code is then given by the equation

$$r'' + \frac{e^2B_z^2}{2m_e\gamma\beta c}r - \frac{eI}{2\pi\epsilon_0m_e\beta^3\gamma^3c^3} \frac{1}{r} = 0 \tag{3.2.5}$$

The 1D beam envelope code takes the relevant beam parameters, the current in the lens, the current in the solenoid, the axial location of the lens, and the axial location of the solenoid and from that calculates the resulting total magnetic field profile from the simulated and provided magnetic field profiles given in the previous section. It

then uses this total magnetic field profile to calculate the beam envelope along the length of the experiment with an initial condition of $r'(0) = 0$ and $r(0) = 3.75\text{mm}$, corresponding to the focused beam spot specified by Haimson Research Corporation.

As an example the code was run for a typical operating point (12 A of current in the lens, 137.5 A of current in the solenoid, center of lens spaced 145 mm from the gun focus, and the edge of the solenoid pole plate spaced 90 mm from the edge of the lens) and compared with the code MICHELLE. The MICHELLE simulation was performed as a 2D axisymmetric emission of 186 particles from a flat emitter of the same size of the focused beam radius, and the beam was allowed to propagate down a straight metal pipe of radius 25 mm. The emission was fixed to 500 keV and 80 A and the beam envelope was recorded and compared with the 1D beam envelope code, which is shown below in Fig. 3-9.

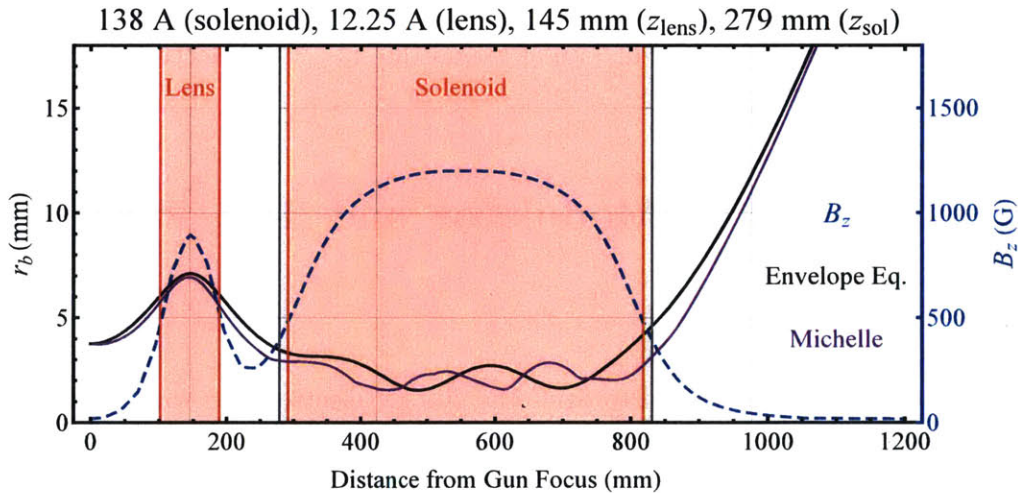


Figure 3-9: Beam envelope of a 500 keV, 80 A electron beam starting from a focused 7.5 mm width spot size calculated with MICHELLE (purple) and the 1D code developed at MIT (black) for the magnetic field shown as a dashed blue curve (magnetic scale on the right). The red shaded regions indicate the location of the magnets which produces the blue magnetic field curve shown. The beam is incident from the left and the metamaterial experiment is installed in the region where the solenoid magnet is.

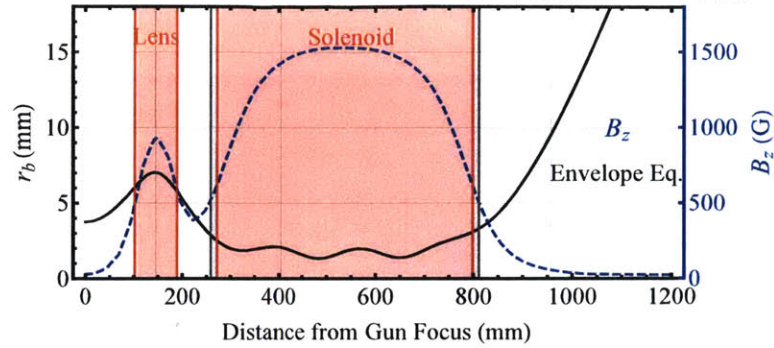
The 1D MIT code was then used to calculate the beam envelope for several different operating points. It was desired to create a variable size beam without much

scalloping (fairly flat radial profile) in the solenoid region where the metamaterial experiment fits. The reason the 1D MIT code was superior to the MICHELLE code was that it was much faster (less than 5 seconds to run vs. approximately 5 minutes to run) and the optimization of the radial profile in the solenoid region could be automated, where the MICHELLE code had to be rerun every time. In Fig. 3-10 three different operating conditions are shown which give flat beam profiles with waist diameters of approximately 4, 7, and 15 mm. The locations of and the currents in the lens and solenoid that were used in the code to produce the magnetic field profiles (shown as the blue curves in the figures) are given at the top of each plot. In the figure z_{lens} is the distance from the beam focus to the center of the magnetic lens and $z_{solenoid}$ is the distance from the beam focus to the edge of the solenoid pole piece. From the figure it is evident that as the solenoid field is decreased the beam size gets bigger for our flat profiled beam. Experimentally this means that beam size and magnetic field are not independent of each other and as the magnetic field of the experiment was varied this also had an affect on the size of the electron beam.

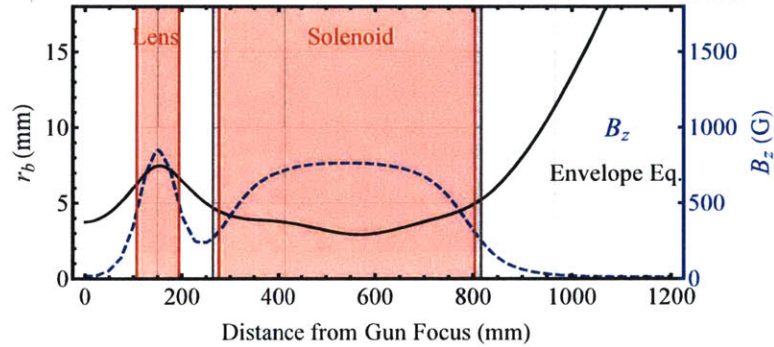
3.3 High Power Modulator and Test Facility in NW21

The high power modulator used to drive the 500 kV electron gun was designed and built by MIT and is used to power the gun of the metamaterial experiment, the gun of a 17 GHz klystron, and the gun of a 17 GHz linac accelerator which is driven by the klystron. The guns for the linac and klystron are installed on ports on the southeast side of the modulator tank which is opposite the port for the metamaterial experiment, which is located on the northwest side of the tank. The modulator has a nominal flat-top pulse of 1 μs and a rise and fall time of approximately 1 μs as well. A photograph showing the 500 kV electron gun installed on the northwest port of the modulator tank is shown in Fig. 3-11. The klystron and linac guns are installed on the opposite side of the modulator, and the edge of the klystron gun enclosure is just

175 A (solenoid), 12.25 A (lens), 145 mm (z_{lens}), 259 mm (z_{sol})



88 A (solenoid), 11.75 A (lens), 150 mm (z_{lens}), 264 mm (z_{sol})



42 A (solenoid), 10.3 A (lens), 200 mm (z_{lens}), 334 mm (z_{sol})

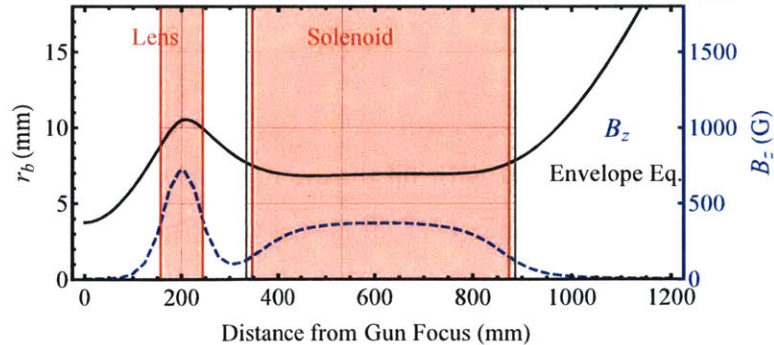


Figure 3-10: Beam envelopes of a 500 keV, 80 A electron beam starting from a focused 7.5 mm width spot size calculated by the 1D beam envelope code (black) for three different magnetic field profiles (blue dashed). The three beam profiles illustrate that a relatively flat beam profile could be created in the solenoid with different waist diameters. The red shaded regions indicate the location of the magnets which produced the magnetic field curve plotted in blue. The locations of and the currents in the lens and solenoid that were used to produce the magnetic field profiles are given at the top of each plot.

visible on the left side of the photograph.

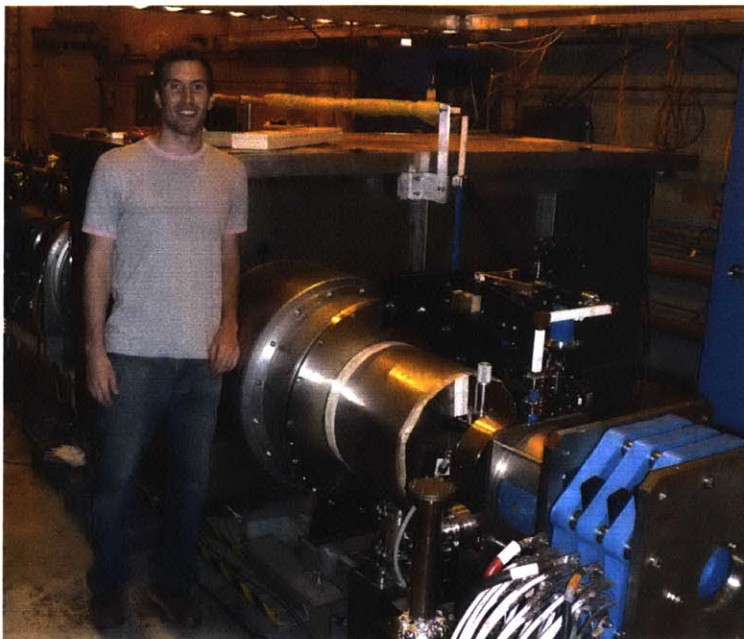


Figure 3-11: Photograph of the 500 kV electron gun mounted to the high power modulator. This photograph was taken before installation of the metamaterial experiment and magnets, and some of the magnets used in the choppertron experiment are visible on the lower right side of the picture.

The modulator tank was filled with oil during normal operation. A photograph looking into the tank with the tank cover off is shown in Fig. 3-12. The gun used to power the metamaterial experiment was connected to the copper tube labeled 'high voltage connection' on the right side of the photograph. The photograph was taken where the heater power supply was connected to power the heater of the metamaterial experiment gun only. To run either the klystron or klystron/linac guns in addition to the gun used for the metamaterial experiment, the red banana plugs shown in Fig. 3-12 must be plugged into the primary side of the klystron and/or linac heater supplies.

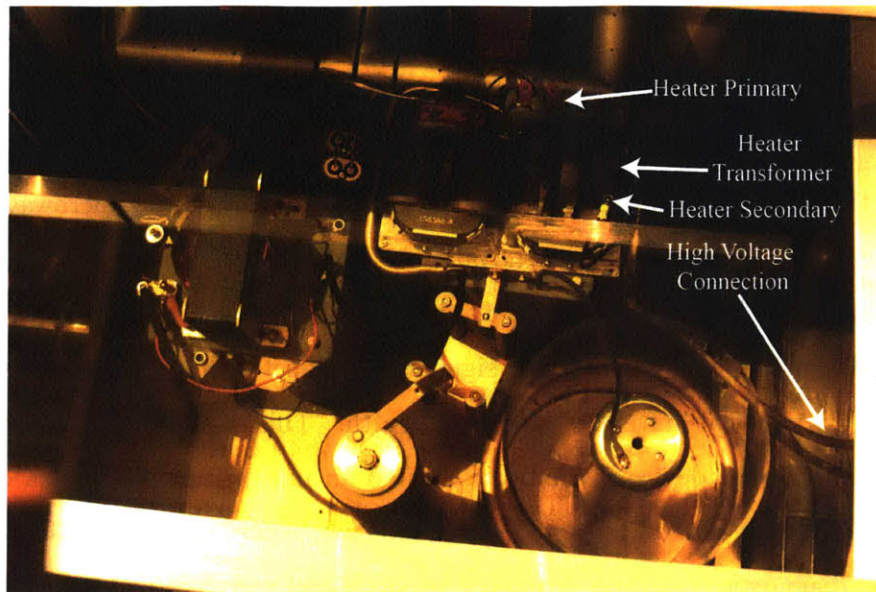


Figure 3-12: Photograph taken looking in to the modulator tank. The photo was taken just prior to operation of the metamaterial experiment gun. Because the klystron and linac use the same modulator, some of the connections in the tank are different when running those experiments.

3.4 Vacuum System

Because the electron gun (more specifically, the thermionic cathode) requires a high vacuum to operate, the structure needed to be designed inside of a vacuum chamber. This constrained the materials that were available for structure fabrication. All of the components were fabricated from either stainless steel or copper (except for the microwave absorbers in the RF loads which were a silicon carbide composite), and care was taken in the choice of materials for braze and solder joints that saw vacuum.

The vast majority of the vacuum seals were formed by commercially available conflat style flanges, which use a compression-type seal on a copper gasket between two flat flange faces that have a sharp knife edge. The use of these flanges placed a size constraint on the experiment because the vacuum chamber needed to slide into the solenoid magnet. The solenoid has an internal bore diameter of 7.97 in. and so the largest standard conflat flange that could fit in the solenoid was the 8 in. diameter conflat (after a small amount of machining was done to the edges of the flanges to

bring them below 7.97 in.) The 8 in. flanges mate to stainless steel cylindrical tubes with a maximum inner diameter of 6 in., so the metamaterial structure and coupler had to be designed to fit in a cylinder with a 6 in. diameter.

Since the experiment was built without the intention to use the microwave power for any particular application it was advantageous to build the entire system without RF windows. This feature had the benefit that operation at a different frequency other than the design frequency would not significantly affect the RF power diagnostics. Typically RF windows have a narrow bandwidth. This would limit the ability to fully characterize the device if the beam excited an unexpected mode at a different frequency. However, eliminating the RF windows also complicated the design of some of the RF diagnostics to some extent. The loads and couplers had to be designed using rectangular waveguide at high vacuum. In order to achieve this, all of the RF waveguide components were fabricated with SLAC-style WR284 vacuum flanges. The flanges are unlike the conflat flanges, which can be torqued very tightly because they use a compression-type seal on a copper gasket. Instead the SLAC-style flanges use a shear-type seal on a fully annealed copper gasket and must be tightened with a torque wrench to 15-20 ft.-lbs. Over tightening these flanges can damage them. SLAC provided drawings of the flanges and specified the torque limits for their use.

Three pumps were used on the metamaterial vacuum system. Because the silicon carbide composite of the RF loads can outgas when it absorbs microwaves, both of the RF loads were fabricated to have pump ports which mated to 20 L/s ion pumps. In addition, a 75 L/s ion pump was used to mate to the vacuum chamber near the collector since the collector would outgas significantly when struck by the high power electron beam. The gun has a 150 L/s ion pump attached to it before the gun vacuum isolation valve, which can be closed to isolate the gun from the rest of the metamaterial vacuum system. This valve made it much easier to test different metamaterial structures. Without it, it would have been necessary to bring the cathode up to air every time it was necessary to open the tube and do work on the experiment. After opening the metamaterial vacuum chamber (with the gun isolation valve closed) it was observed that typically the tube could reach a vacuum

of $5\text{-}9 \times 10^{-7}$ T within 3-6 hours of closing the vacuum and turning on the ion pumps and reach a baseline of $1\text{-}4 \times 10^{-9}$ T after it was left to sit for 2 weeks.

Care was taken to clean all components before installation in the tube with acetone and ethanol. All metamaterial structures were additionally put in the PSFC sonicator for 45 minutes in a bath of acetone and then a bath of ethanol. Before the first structure installation, the entire tube was baked out to ~ 150 °C to remove water vapor on component surfaces.

3.4.1 RF Components

The metamaterial experiment uses several microwave waveguide components that mate to the experiment for diagnostic purposes. Because of the symmetry of the output coupler there are two identical RF arms which are each comprised of an internal waveguide bend, a waveguide to conflat flange mating port, an external waveguide bend, a Bethe-Hole directional coupler, and a microwave load. Here the descriptors ‘external’ and ‘internal’ refer to whether the component was completely inside the vacuum chamber, or whether the component had to hold vacuum on one side and was exposed to atmosphere on the other. All the components that needed to hold vacuum had to be fabricated with copper gasket vacuum seals. A CAD drawing of one RF arm which labels each of these components is shown in Fig. 3-13. The internal waveguide bend was designed to bring power out of the structure by mating the output coupler of the structure to the conflat flange mating port. Because the waveguide bend was inside the vacuum, it was fabricated from standard thickness WR284 waveguide and did not need flanges with a vacuum seal. However, special waveguide flanges were designed on the coupler side to allow transport of the beam and on the mating port side to fit inside the vacuum chamber. The flanges were modified versions of standard CMR284 waveguide flanges which are commercially available. The internal waveguide bend and flanges were fabricated and brazed together by Penn Engineering.

The waveguide to conflat flange mating port was designed to mate to the standard WR284 waveguide inside the vacuum chamber. The design for the mating port

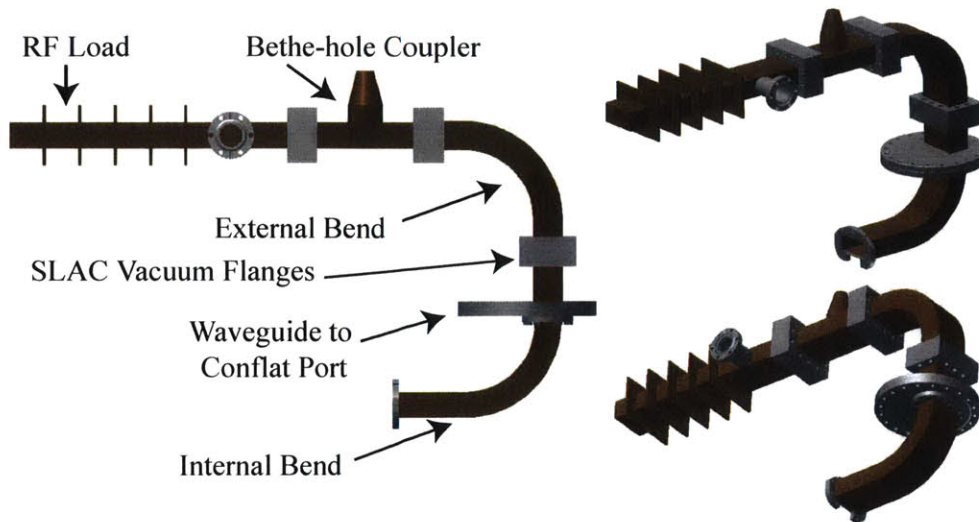


Figure 3-13: CAD rendering of one of the RF arms which labels the RF load, Bethe-hole coupler, external waveguide bend, waveguide to conflat mating port, and internal bend. Refer to Fig. 3-19 for how the RF arm fits to the rest of the metamaterial assembly.

and the external waveguide was sent to Haimson Research Corporation where they were fabricated because they required the use of a high-temperature Hydrogen braze in order to secure the steel SLAC-type vacuum flanges on the sections of copper waveguide.

The two waveguide bends and waveguide to conflat flange mating port were designed with large enough bend radii so that they operate over a wide frequency band. The simulated S_{11} and S_{12} of these components connected together as they are in the experiment are shown in Fig. 3-14.

Because the experiment generated a significant amount of microwave power it was necessary to pick off a very small amount of power for the sensitive microwave diagnostics. Bethe-hole style directional couplers were chosen because they have a very small coupling, and because the designs for these types of couplers that have SLAC-style vacuum flanges were made available from SLAC to outside vendors. Bethe-hole directional couplers are used at SLAC for their 60 MW 2.856 GHz klystrons. The couplers used in the experiment were built by CML Engineering. These couplers were then calibrated at MIT. The coupling for the two Bethe-hole directional couplers is

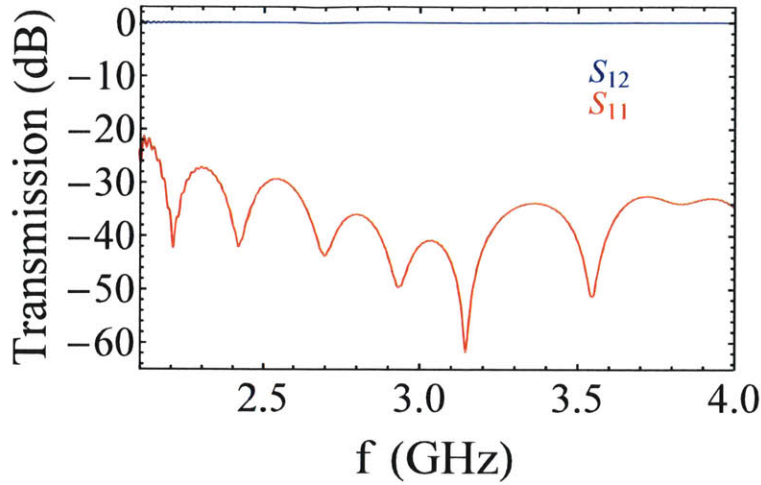


Figure 3-14: Simulated S_{11} and S_{21} of the internal waveguide bend, waveguide to conflat flange mating port, and external waveguide bend showing good transmission over a wide frequency range. The assembly connects the output coupler of the device to the Bethe-hole coupler.

shown in Fig. 3-15.

One of the experiments performed with the high power electron beam generated microwaves at approximately 5.95 GHz. Calibration of the couplers at this frequency required a different approach than simply measuring the transmission with the VNA. This is because the WR284 waveguide which is used to bring the microwaves out of the experiment ceases to be single-moded above 4.16 GHz. There are five supported modes at 5.95 GHz, and so the output coupling of the Bethe-hole couplers at this frequency depends not only on the frequency, but on the mode content of the microwaves in the waveguide.

However, using CST MWS we can calculate the mode content of the 5.95 GHz microwaves in the couplers that are produced from the metamaterial structure. Then CST can be used to calculate the coupling for each of the 5 different modes at 5.95 GHz. Since we can benchmark the CST model of the coupler over the frequency band where only the TE_{10} mode exists and the coupling was able to be measured to a high degree of accuracy (~ 0.1 dB), we have a way to benchmark this mode dependent calibration method.

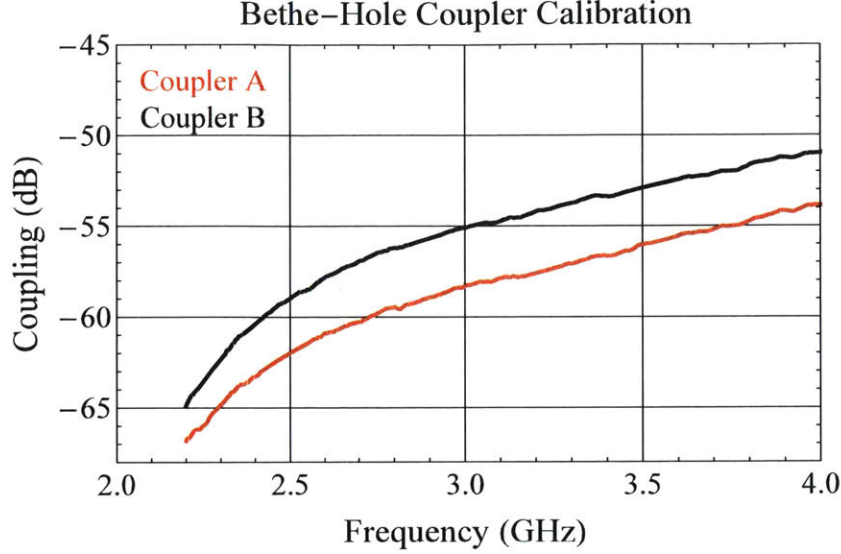


Figure 3-15: Measured coupling of the two Bethe-Hole couplers used in the experiment which was taken November 2015. Looking from the electron beam to the collector, coupler A was mounted on the right and coupler B on the left. The measured coupling at 2.35, 2.43, 2.85, and 3.70 GHz in coupler A was - 63.8 dB, -62.8 dB, -59.3 dB, and -55.2 dB, respectively, and the measured coupling at the same frequencies in coupler B was -61.2 dB, -59.8 dB, -56.0 dB, and -52.1 dB, respectively. The coupling could be adjusted by rotating the stripline detector in the head and recalibrating. Different coupling values were used for data prior to October 5, 2015.

The mode content of microwaves in the waveguide emitted by the metamaterial structure was solved with CST MWS and is shown in Fig. 3-16. In the simulation, the mode content of microwaves launched from the metamaterial structure was calculated in the waveguide before the Bethe-hole coupler. The microwaves were launched from a small antenna near the gun end of the metamaterial structure. At 5.95 GHz Approximately 99% of the microwave power was found to be in the TM_{11} (cutoff 4.87 GHz) and TE_{10} (cutoff 2.08 GHz) modes and the rest in the TE_{20} (cutoff 4.16 GHz), TE_{01} (cutoff 4.41 GHz), and TE_{11} (cutoff 4.87 GHz) modes.

The coupling of the five modes was calculated in CST MWS. The dimensions of the couplers were taken from drawings provided by CML Engineering or measured directly. The coupling values calculated with CST are shown in Fig. 3-17. The coupling of the TE_{20} , TE_{01} , and TE_{11} modes was found to be significantly (< -10 dB) lower than the TE_{10} and TM_{11} modes and so only the coupling for the TE_{10} and

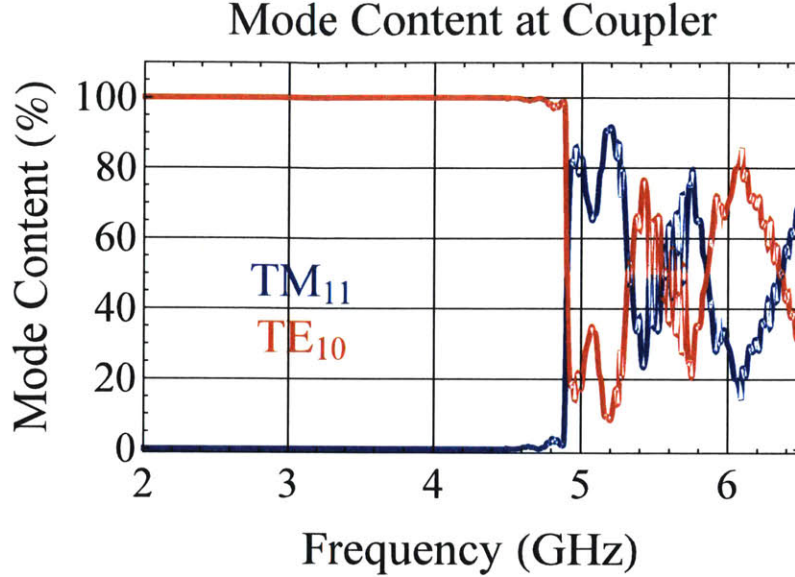


Figure 3-16: Mode content of microwaves entering the Bethe-hole coupler as launched from the metamaterial structure. Almost all of the power is in the TE_{10} and TM_{10} modes.

TM_{11} modes are shown.

Using the results of Fig. 3-16 and Fig. 3-17 it is straightforward to obtain the coupling, which is shown in Fig. 3-18. The coupling values of couplers A and B at 5.95 GHz are calculated to be -46.3 dB and -48.4 dB, respectively. However, where a direct comparison can be made there is obviously some disagreement between the measured and simulated coupling, (up to +/-0.5 dB) which is visible in the plot in Fig. 3-18. We can expect at least this much error in the end result and estimate that the total error in this method is +/-1 dB. A more accurate measurement of the power at 5.95 GHz would require a major redesign of the entire output coupler section.

The microwave loads used in the experiment were also built by CML Engineering. The loads use a cone shaped lossy ceramic disk made from a silicon carbide composite that has minimal outgassing in UHV. The microwave loads were calibrated at CML where the S_{11} of the loads over S-Band was measured with a VNA. The measured S_{11} was everywhere less than 30 dB over the frequency range from 2.5 to 4 GHz in both loads.

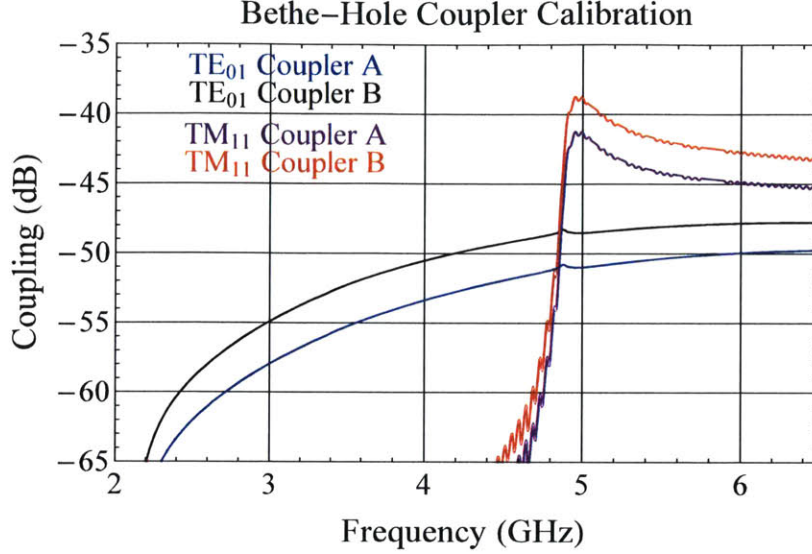


Figure 3-17: Plot of the simulated output coupling of microwaves in the TE_{10} mode in coupler A (blue solid) and coupler B (black solid), as well as the simulated coupling of microwaves in the TM_{11} mode in coupler A (purple solid) and coupler B (red solid).

3.4.2 Structure Assembly and Installation

The metamaterial structure assembly was fabricated in-house at the MIT Central Machine Shop. A CAD drawing of the experiment with labels of the major parts is shown in Fig. 3-19. A photograph of the unassembled collector assembly and ceramic standoff is shown in Fig. 3-20. The collector was designed as a two piece assembly that could be bolted together to decrease the size of the structure that needed to be put in the brazing oven. The components for the collector assembly were fabricated at the MIT Central Machine shop, but the copper collector piece was brazed to the collector flange by CPI in Beverly, Massachusetts. The braze required the use of a dry hydrogen furnace. A small channel was machined into the collector and N-type fittings machined into the collector flange to which it was brazed so that the collector could be water cooled. The collector flange was bolted to a ceramic standoff so that it was electrically isolated from the rest of the experiment. The current reaching the collector could be measured with a 10 to 1 current to voltage ratio rogowski coil.

Several metamaterial structures were tested in the high power experiment. All of the metamaterial structures were constructed from 6 individual plates (two side

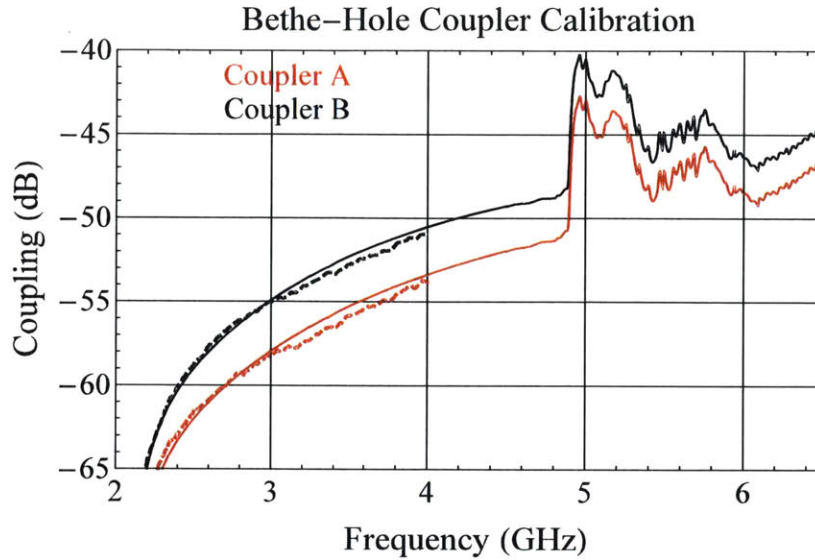


Figure 3-18: Plot of the calculated coupling for the metamaterial experiment for coupler A (red solid) and coupler B (black solid). Also shown is the measured transmission of the coupling of coupler A (blue dashed) and coupler B (black dashed) over the frequency range where the coupler is single-moded and the measurement can be performed with the VNA.

plates made from stainless steel, two top plates made from stainless steel, and two metamaterial plates made from copper) which were either bolted or brazed together and then bolted to stainless steel end flanges so that they could be secured in the vacuum chamber and bolted to the output RF arms. Photographs of two of the metamaterial structures that were tested are shown in Fig. 3-21. In Fig. 3-21a-c the structure shown uses the design of MTM1 discussed in the previous chapter and is 352 mm long (44 metamaterial periods). The structure in this photograph was held together by bolts. In Fig. 3-21d the structure uses the design of MTM2 and is 370 mm long (37 metamaterial periods). This structure was brazed together along the full length of each of the 6 plates. To accomplish this, the braze material was inserted into the slots where the top and metamaterial plates fit into the side plates.

A photograph of the fully assembled experiment after being baked out, but prior to installation on the electron gun is shown in Fig. 3-22. The tube could slide into the bore of the magnet without breaking the vacuum seal. Once the tube was in place in the magnet it could be slightly pressurized with dry nitrogen while the vacuum seal

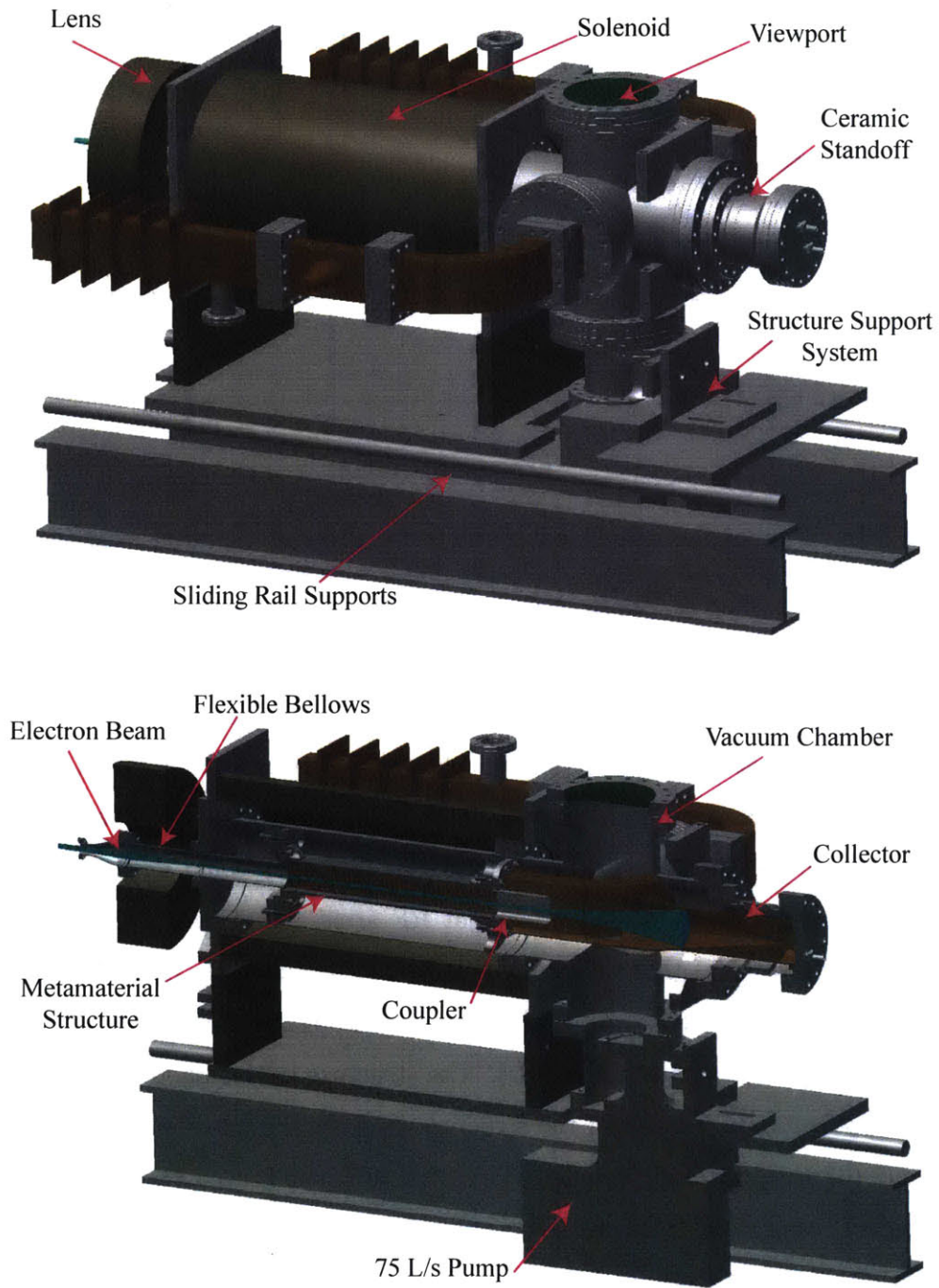


Figure 3-19: Perspective view and cut perspective view of the high power metamaterial experiment. All of the major components are labeled. The electron beam is generated on the left by the 500 kV gun (not shown).

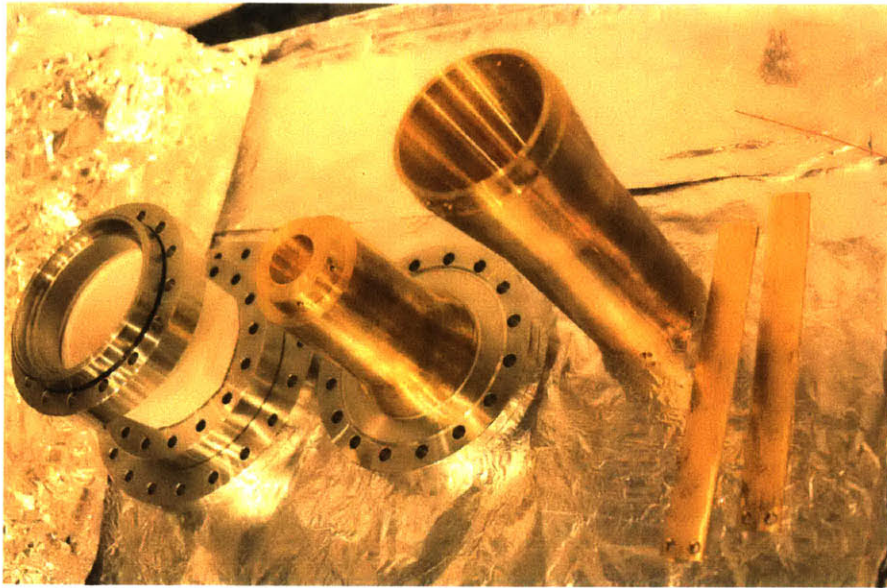


Figure 3-20: From left to right, ceramic standoff, collector piece 1 that bolts to the ceramic standoff, collector piece 2 that bolts on to the end of collector piece 1, collector fingers that bolt to the end of collector piece 2 that provide a ground plane for the beam after it exits the structure.

was broken and the tube was installed on the gun.

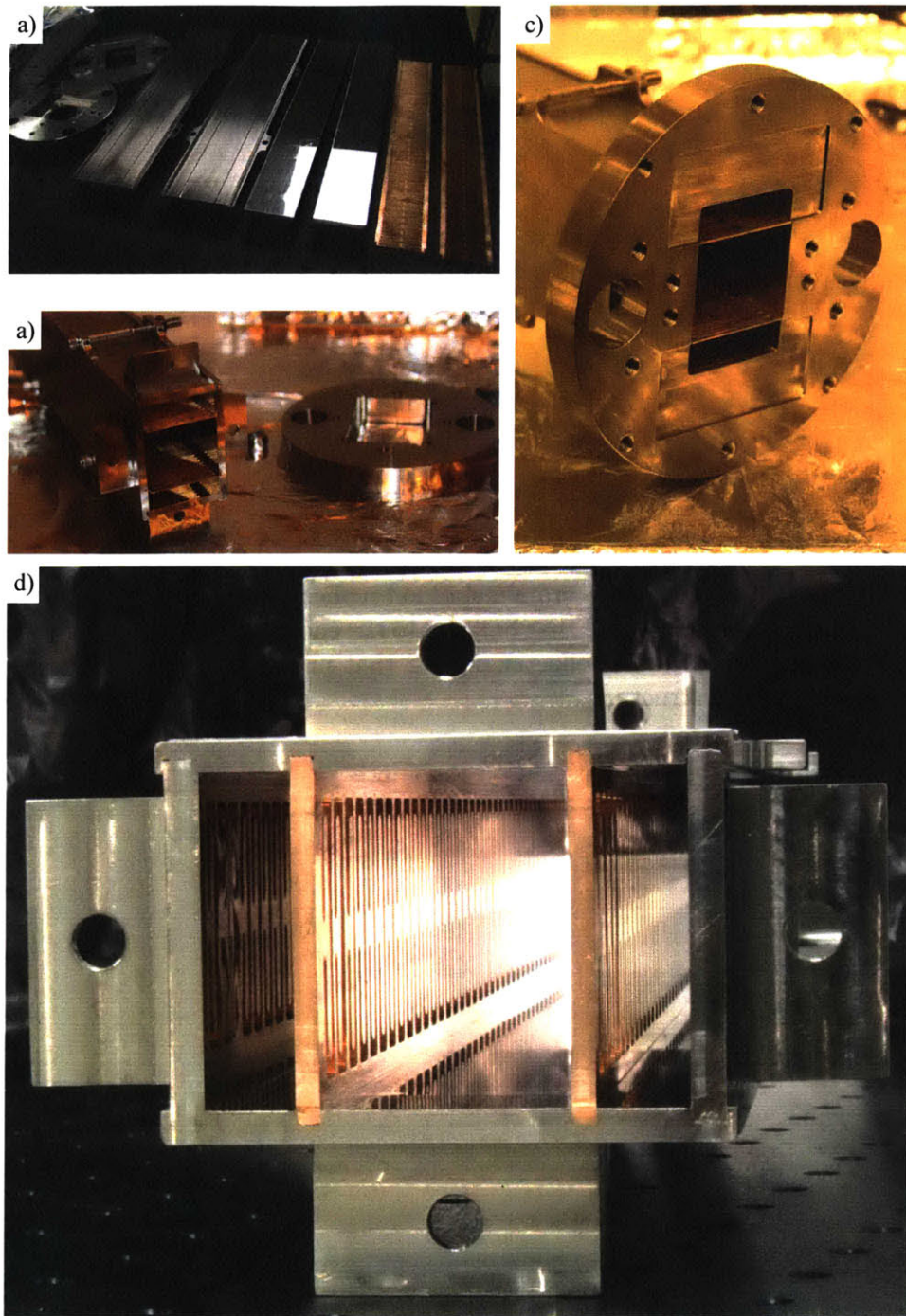


Figure 3-21: a) Photograph of the unassembled 352 mm MTM1 metamaterial structure which is composed of 6 plates that are bolted together and then bolted in between two unique end flanges. b) Photograph of the MTM1 metamaterial structure bolted together without end flanges and c) with end flanges showing the collector side of the structure (inner dimensions of the metamaterial waveguide are 63 mm x 43 mm for scale). d) Photograph of the 370 mm brazed MTM2 metamaterial structure (inner dimensions of the metamaterial waveguide are 63 mm x 43 mm for scale).

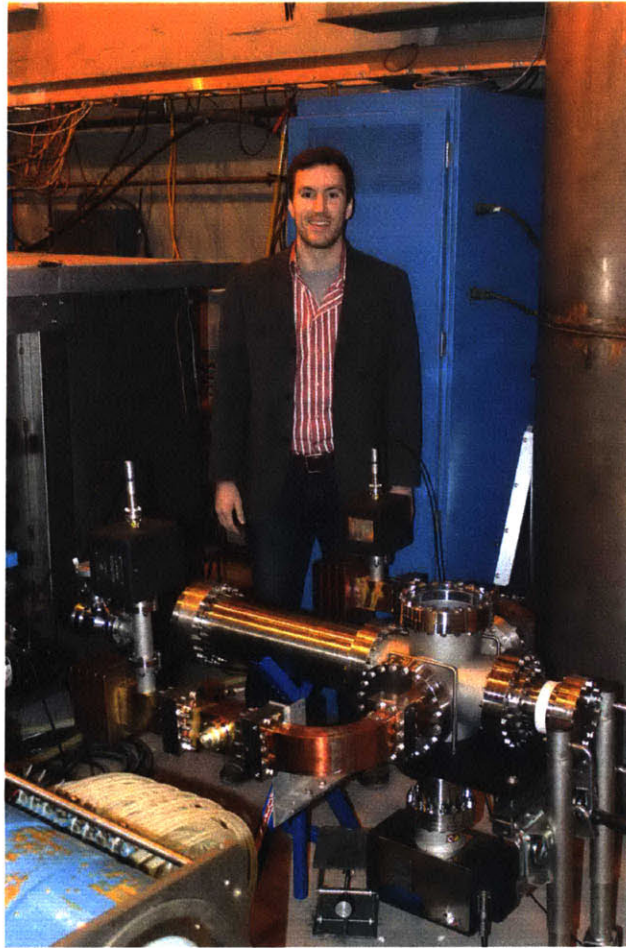


Figure 3-22: Photograph of the experiment under vacuum after bakeout. This photo was taken before the experiment was installed on the gun. To install on the gun, the tube was inserted into the magnet (just visible in the bottom left of the photo) and the vacuum was opened. Dry nitrogen could be pumped through the structure so that it never saw atmospheric air after bakeout.

Chapter 4

Experimental Results

Several experiments were performed testing different metamaterial structures using the high power electron beam. Since the method of assembly proved to be important to the performance of the different structures that were tested with the beam, the experimental results that are presented in the following chapter are characterized by their metamaterial design (MTM1, MTM2, and MTM3), length, and method of assembly. A summary of the different designs that were tested is presented in Fig. 4-1. Three different methods were used in the assembly of the various structures: bolting the structure together, bolting the structure together with indium foil filling the joints, and completely brazing the structure together.

4.1 Experimental Diagnostics

Two main diagnostics were used in order to characterize the microwave signals generated by the metamaterial device. A Keysight DS0-S 604A S-Series oscilloscope with the ability to measure signals of up to 6.2 GHz (if only two of its four channels were utilized, memory depth of 100 Mpts) or 4.2 GHz (if all 4 channels were utilized, memory depth of 50 Mpts) was used to measure the microwave signals. The scope can sample a maximum of 20 GSa/s and was useful for providing real time Fourier transforms of microwave signals measured in the lab.

In addition to the oscilloscope, a Keysight N1912A P-Series power meter was used

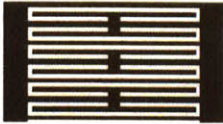


Mode	Design	Frequency of Negative Group Velocity Modes	Frequency of Positive Group Velocity Modes
MTM1		2.8 GHz	4.8 GHz
MTM2		2.4 GHz	5.9 GHz
MTM3		3.7 GHz	9.2 GHz

Figure 4-1: Summary of the MTM1, MTM2, and MTM3 designs which were tested in experiments. The approximate frequency of Cherenkov synchronism with a 500 keV electron beam for the negative group velocity modes and positive group velocity modes of each design is also shown.

to read the power signals detected from two N1922A detector heads. The heads are self-calibrating and can measure microwave power from 50 MHz to 40 GHz. The safe operating power range for the heads is -30 dBm to +23 dBm. The detector displays a calibrated power trace (similar to an oscilloscope) which is read by a Labview program that was created to save the power meter data with a time stamp. Additional fixed attenuation from commercially available attenuators was also necessary to avoid damaging the diodes in the sensitive detectors that the power meter used.

In addition to the oscilloscope and power meter, a vector network analyzer (VNA model Agilent E8363B) was used in order to measure the transmission of the meta-material structures. The VNA can measure the phase and amplitude of a low power microwave signal and so calculate the S-parameters of a microwave circuit.

Commercially available coaxial microwave bandpass filters purchased from Minicircuits (models VBFZ-2130+ and VBFZ-3590+) were used for some measurements to measure the power at one frequency when more than one frequency was present in the output signal. The insertion loss of the bandpass filters was specified by Minicir-

cuts.

4.2 Experiments Using the MTM1 Design

A 352 mm long structure based on the MTM1 design presented in Chapter 2 was tested. The structure was composed of 6 individual plates which fit together with interlocking joints. This structure was tested with all three assembly methods: bolting, bolting with indium, and brazing. The results of all three tests are presented below.

4.2.1 Unbrazed MTM1 Structure Results

A photograph of the 352 mm unbrazed structure based on the MTM1 design that was bolted together is shown in Fig. 4-2. The side plates have pockets which were

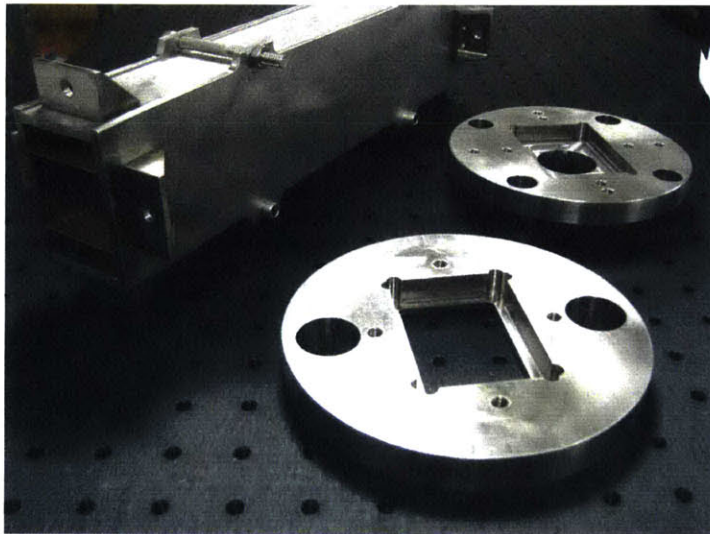


Figure 4-2: Photograph of the 352 mm unbrazed MTM1 structure taken on October 17, 2014 before high power testing. 3 of the 4 bolts that hold the two side plates are visible in the photograph. The top, bottom, and metamaterial plates are then sandwiched between these two side plates and sit in pockets which were machined into the side plates. The whole structure then slides into pockets in two end flanges to which it is then bolted and which are shown on the right hand side of the photo. For scale, the spacing of the holes on the optical table the structure rests on is 1 inch.

machined into them so the top, bottom, and metamaterial plates would be held together when bolted. Finally, the structure ends are bolted into two flanges which

are shown on the right. One of these flanges is secured to the vacuum chamber and the other is bolted to the output coupler.

This structure was tested over a range of magnetic field values from 1200 G to 1550 G and a wide range of voltage values. Initially there were concerns about testing structures at low magnetic field values because it was not certain if a catastrophic failure would result if the beam was somehow deflected. Major deflections were observed in the PIC simulations of the structure at magnetic fields less than 850 G, and so magnetic field values lower than 1200 G were not initially investigated for this structure, although later experiments performed at magnetic field values below 1200 G were performed with the same structure assembled with indium foil (section 4.2.2) and brazed (section 4.2.3).

Over the range of parameters investigated the output power was measured to be 20 ± 10 W (this error bar is only approximate and based on the shot-to-shot variation of power observed in the lab over wide range of operating voltages and magnetic field values). A characteristic plot of the power, collector current, and gun voltage is shown in Fig. 4-3. This power trace was taken with a solenoid field of 1500 G and a lens

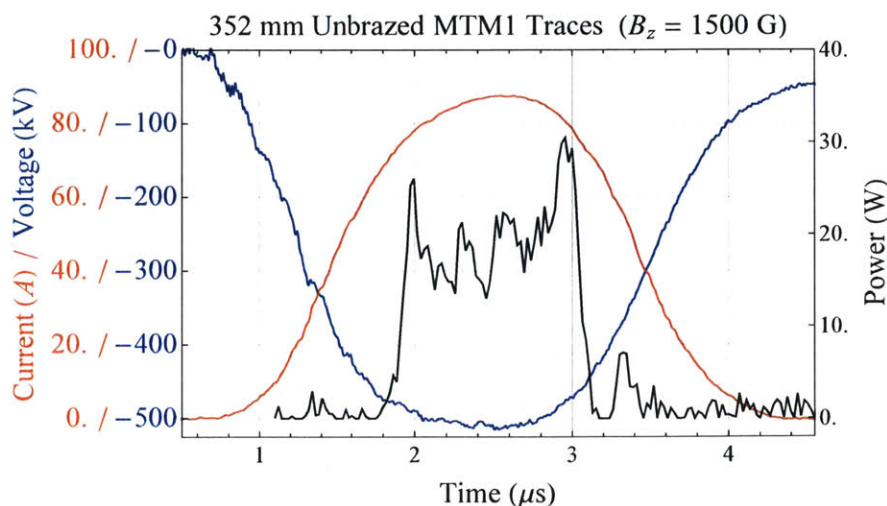


Figure 4-3: Electron gun voltage (blue curve) and measured collector current (red curve) for an applied magnetic field of 1500 G plotted with the measured microwave power (black). The scale for the current (voltage) is given on the left in red (blue) and the scale for the microwave power is given on the right in black.

current of 12 A (which corresponds to a peak magnetic field at the center of the lens of roughly 875 G). Averaged over the FWHM of the RF pulse, the metamaterial structure produced $20 \text{ W} \pm 5 \text{ W}$ for a voltage of 510 kV and beam current of 84 A. The predicted power from the CST PIC simulations for a similar operating condition (see Fig. 2-20) was over 5.5 MW at 2.82 GHz. The output power predicted by CST PIC simulations and the measured output power disagree by more than 5 orders of magnitude.

For the measurement in Fig. 4-3, the location of the magnetic lens was 140 mm away from the focal spot of the gun, and the edge of the steel solenoid pole plate was approximately 256 mm from the focus of the gun. Using the 1D beam envelope code for this configuration, the beam diameter is inversely proportional to the magnetic field and ranges from a diameter of 4.2 mm at 1200 G to 3.2 mm at 1550 G at 500 keV and 80 A. The beam size could be measured using a beam witness plate measurement, however this is a fairly complicated measurement for a 500 keV, 80 A electron beam and was not attempted for this experiment.

For the same magnetic field as Fig. 4-3, the frequency was also measured in both of the RF arms. In order to make this measurement, the output microwave signal was measured with the oscilloscope over a 50 ns window near the peak of the current and voltage pulse corresponding to the flat-top of the RF pulse. In Fig. 4-4 a plot of the measured microwave signal and the corresponding Fourier transformed signal is shown. The time duration on the x-axis of the microwave signal in Fig. 4-4 corresponds to the time of the current, voltage, and power traces of Fig. 4-3. The signal peak in the Fourier transformed signal is centered at 2.837 GHz, in very good agreement to 2.82 GHz which is the value predicted by CST PIC simulations (see Fig. 2-20). In the Fourier transform that is shown, the bandwidth of the central lobe is time-limited due to the fact that the Fourier transform was calculated from a time window of 50 ns, but this does not affect the value of the central frequency. Despite the low output power of the metamaterial structure, it is clear that the output microwave signal was coherent in Fig. 4-4. CST PIC simulations predict 5 MW of microwave power at a frequency of 2.830 GHz. While the frequency was in good

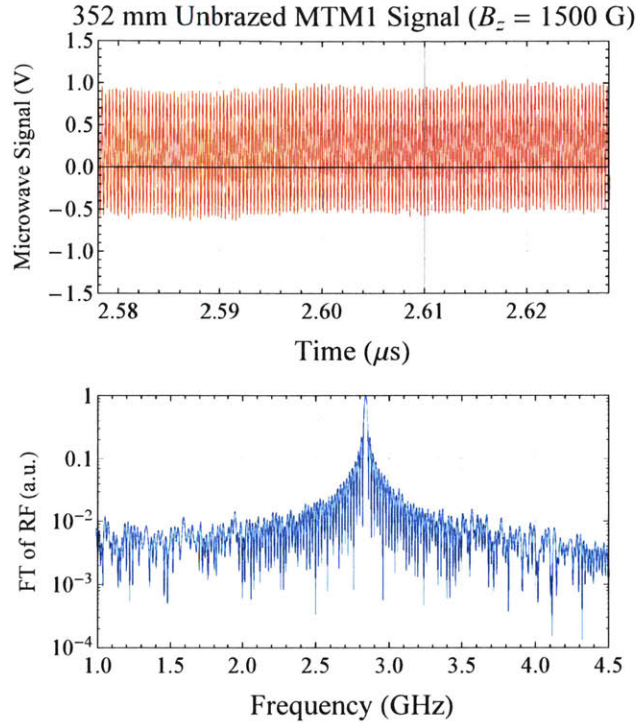


Figure 4-4: Top: Normalized microwave signal measured with the 6 GHz oscilloscope over a 50 ns time window. The time on the x-axis corresponds to the time of Fig. 4-3, though the signal was measured from a different shot with identical settings. Below: Fourier transform of the measured signal. The signal is peaked at 2.837 GHz, which is very close to the frequency of 2.820 GHz that was predicted by CST PIC simulations.

agreement, the output power was 10^5 times lower than simulated.

The frequency and power was measured at a few different magnetic field values at a fixed voltage and current of 500 kV and 81 A, respectively. This is shown in Fig. 4-5. The power was averaged over the FWHM of the signal and the frequency was measured over a 50 ns window in the flat top of the voltage pulse. Because the power was so low compared to the predicted value by the CST PIC simulation, no attempt was made to analyze the statistical variation of the output power and so no error bars are shown. The frequency measurements in Fig. 4-5 were very repeatable at each of the magnetic field values where the measurements were made.

In addition to the above measurements, the frequency was measured as the voltage of the gun was varied. The result of these measurements is shown in Fig. 4-6. The

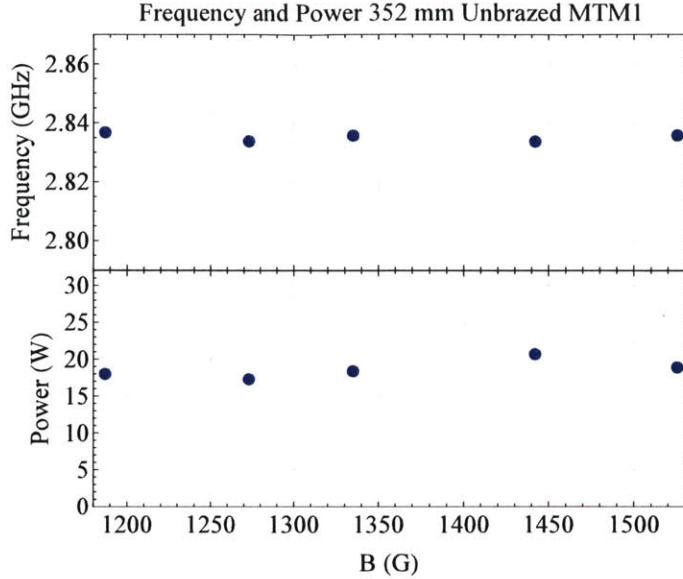


Figure 4-5: Microwave frequency and output power of the 352 mm unbraided MTM1 structure at different magnetic field values taken from 1200 G to 1550 G.

frequency of operation as a function of voltage can be estimated by using the cold dispersion relation that was solved with the eigenmode solvers of HFSS and CST and shown in Fig. 2-6, and by using the theory of a cold interacting electron beam with the resonance condition $\omega = k_z v_z$. As the gun voltage is varied so is the energy of the electron beam, and this affects the slope of the beam line and therefore changes the frequency where the beam line intersects the cold dispersion curve. The red curve in Fig. 4-6 corresponds to the frequency predicted by the cold dispersion relation downshifted by 50 MHz. Qualitatively the measured dispersion, or slope of the frequency vs. voltage curve, agrees quite well with simulation. The shift may be due to fabrication errors or possibly due to the effect of the space charge of the beam. Because the electron beam is formed by a Pierce gun it is impossible to independently vary the voltage from the current, and near the design point of 500 kV the gun current varies as $V^{3/2}$. Thus care should be taken in ascribing the frequency tuning as purely due to the dispersion of the waveguide or as a combination of dispersion and the changing space charge of the beam.

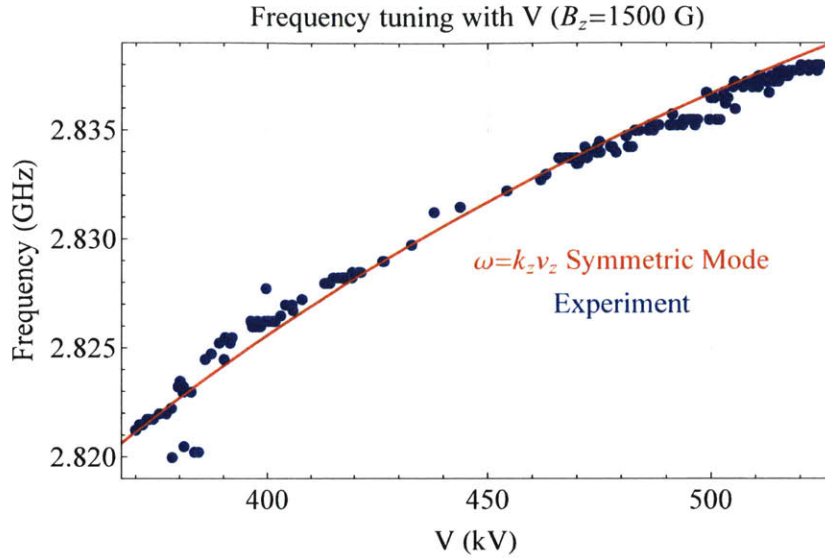


Figure 4-6: Frequency tuning of the 352 mm unbrazed MTM1 structure as the voltage (and current) of the electron beam is varied from 520 kV to 380 kV. The voltage shown on the x-axis is the average voltage over the 50 ns window that the microwave signal is taken, which is approximately equal to the peak gun voltage.

4.2.2 Unbrazed MTM1 Structure with Indium Foil Results

The 352 mm unbrazed MTM1 structure produced much less power than what was predicted with PIC simulations (see section 4.2.1). It was hypothesized that the way that the structure was assembled had a negative impact on its performance. The structure was bolted together from six individual plates which allowed for small gaps in the joints of the structure where the plates fit together. When the structure was removed from vacuum, it was cold tested with the VNA and then also tested with indium foil put into the structure joints before bolting together. The transmission from these two measurements is shown in Fig. 4-7.

In both transmission measurements two straight probes were inserted into the axis of the structure in order to selectively excite the symmetric mode of the structure. It is clear from the figure that the transmission in the upper negative group velocity mode (the high power design mode which theoretically spans from approximately 2.6 GHz to 3.2 GHz and is shown in Chapter 2 in Fig. 2-6) is significantly enhanced when the indium foil is used. In addition, the transmission in the lower negative

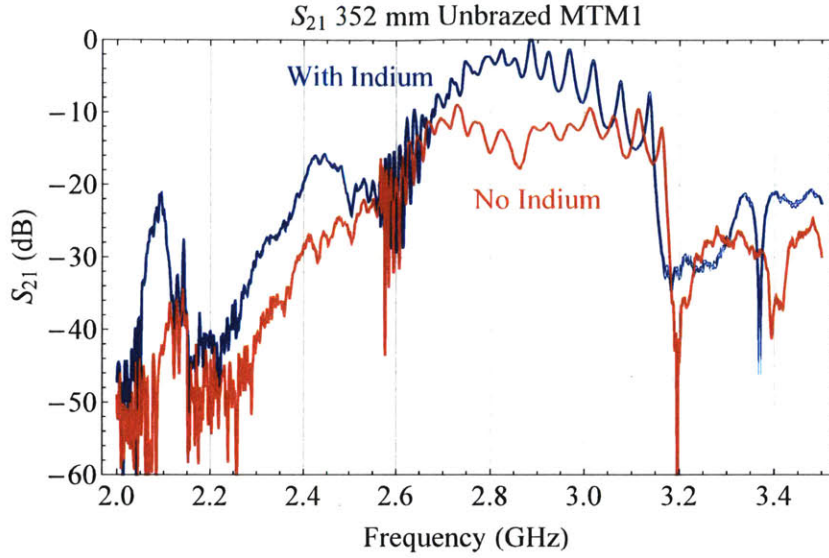


Figure 4-7: Transmission of the 352 mm metamaterial structure with (blue) and without (red) indium foil put into the structure joints before the structure was bolted together. The measurement was made using two straight probes at either end of the metamaterial structure inserted parallel to the direction of the beam in order to selectively excite the symmetric mode.

group velocity mode (at approximately 2.1 GHz) is also significantly enhanced. One interesting feature of the measurement, however, is that there seems to be a mode between the two known modes which is also enhanced (frequency from approximately 2.25 GHz to 2.6 GHz), but was not found with the eigenmode solver.

The reason indium foil was used in the joints was to seal the gaps in the structure joints since it is a good conductor and has some similar qualities to a liquid at room temperature. In addition to this, indium foil had been used previously as a good electrical seal in other experiments in our group.

The indium structure was then returned to vacuum and tested with the electron beam. For high magnetic fields the structure was observed to behave approximately the same as without the indium foil (power $\sim 10\text{-}100$ W, $f \sim 2.83$ GHz). However, it was decided to test the structure at lower magnetic fields as well and risk any problems with beam interception. It was discovered that at low magnetic field (< 400 G) the structure produced megawatts of output power at 2.35 GHz. A characteristic plot of a high power trace, collector current, and gun voltage taken at 294 G is shown in

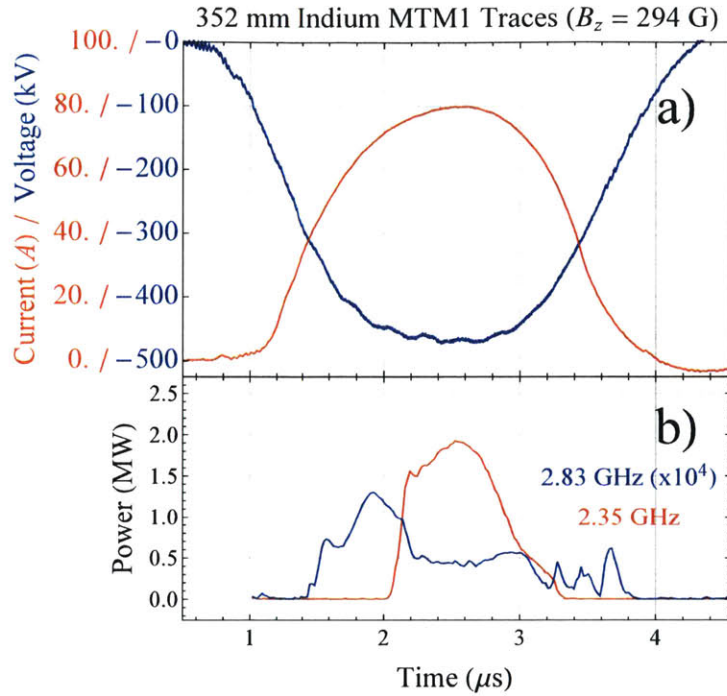


Figure 4-8: a) Electron gun voltage (blue curve) and measured collector current (red curve) for an applied magnetic field of 294 G. The scale for the current (voltage) is given on the left in red (blue). b) Using microwave filters it was determined that nearly all of the microwave power was measured at 2.35 GHz, as evidenced by the two power traces showing the 2.35 GHz power (red) and 2.83 GHz power (blue) below the voltage and current traces. The 2.83 GHz power trace is blown up by a factor of 10^4 so that it is visible. The scale for the microwave power is given on the left in black.

Fig. 4-8.

Averaged over the FWHM of the RF pulse, the metamaterial structure produced approximately 1.5 MW for a voltage of 465 kV and beam current of 78 A. In the figure the power at 2.35 GHz and 2.83 GHz was independently measured by using commercially available coaxial microwave bandpass filters purchased from Minicircuits (models VBFZ-2130+ and VBFZ-3590+). The power in the 2.83 GHz mode produces 120 W of peak power, but the 2.35 GHz mode produces 2 MW of peak power. The measured microwave power at 2.35 GHz was observed to be fairly sensitive to the structure alignment. Care was taken to align the structure by sliding the position of the magnet assembly so that it produced both a maximum of output

power and so that the power in both RF arms was approximately equal. Using the 1D beam envelope code, at the operating conditions shown in Fig. 4-8 the beam diameter was approximately 19 mm.

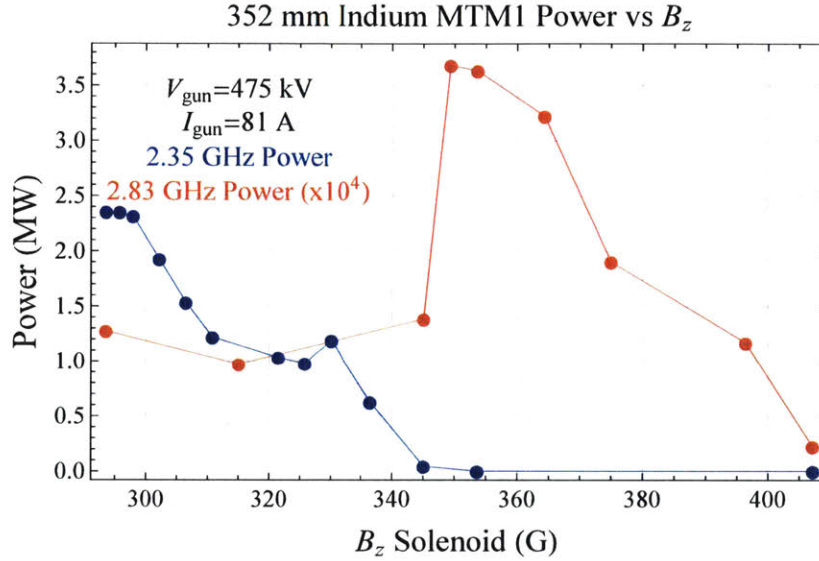


Figure 4-9: Microwave power measured at 2.83 GHz (red) and 2.35 GHz (blue) as the solenoid field is varied from 300 to 400 G. The microwave power at each particular frequency was measured using band pass filters between the coupler and power meter. The gun voltage and current were fixed at 475 kV and 81 A and the magnetic lens current is held fixed at 11 A. The 2.83 GHz microwave power trace is blown up by a factor of 10^4 so that it is visible when compared to the 2.35 GHz.

The variation of the microwave power in each mode was measured as a function of the applied solenoid field. This is shown in Fig. 4-9 where the gun voltage and current were fixed at 475 kV and 81 A and the magnetic lens current was held fixed at 11 A. High power microwave generation in the 2.35 GHz mode is observed below 350 G. At 400 G and above no microwaves are detected at 2.35 GHz. The 2.83 GHz microwave signal remains roughly constant at ~ 20 W for higher magnetic field values, and then quickly rises to about 300 W at approximately the same magnetic field the 2.35 GHz microwaves start.

In Fig. 4-10 the measured frequency of the 2.35 GHz microwave signal is shown as the gun voltage is varied. The dispersion of the measured frequency data at 2.35 GHz is opposite that of the 2.83 GHz mode. No microwaves at 2.35 GHz were observed

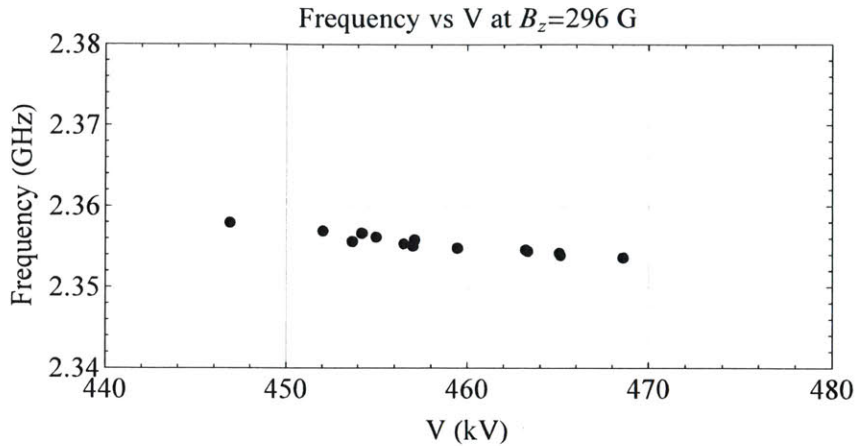


Figure 4-10: Frequency tuning of the 2.35 GHz microwave signal as the voltage (and current) of the electron beam is varied from 520 kV to 380 kV. The voltage shown on the x-axis is the average voltage over the 100 ns window centered at 2.5 μ s and the frequency is also measured at 2.5 μ s over a 250 ns window.

below 445 kV. In addition to the data already presented, the microwave signal at 2.35 GHz was not observed to tune significantly with magnetic field. The excitation of the 2.35 GHz mode was observed to be very sensitive to alignment, which made repeatability of the measurements difficult if the structure was moved.

One interpretation of the above measurements and the origin of the 2.35 GHz microwaves was that the introduction of the indium foil served to create the gaps in the slots of the structure to the extent that a long enough section of the structure supported slot modes which could then be excited by the electron beam. Inspection of the cold transmission data presented in Fig. 4-7 seems to confirm the hypothesis that the addition of indium improved the transmission of a mode there. In Fig. 4-11 a photograph is shown of the metamaterial structure assembled with indium foil taken after high power testing. Unfortunately, it was nearly impossible to cut the strips to a consistent thickness and uniformly put them in the slots along the length of the structure. This was especially the case in the small 1 mm thick slots that the metamaterial plates fit in, which are incidentally the most critical.

To investigate this idea further, additional eigenmode simulations were performed with small gaps around the edges of the metamaterial plates to model the gaps that

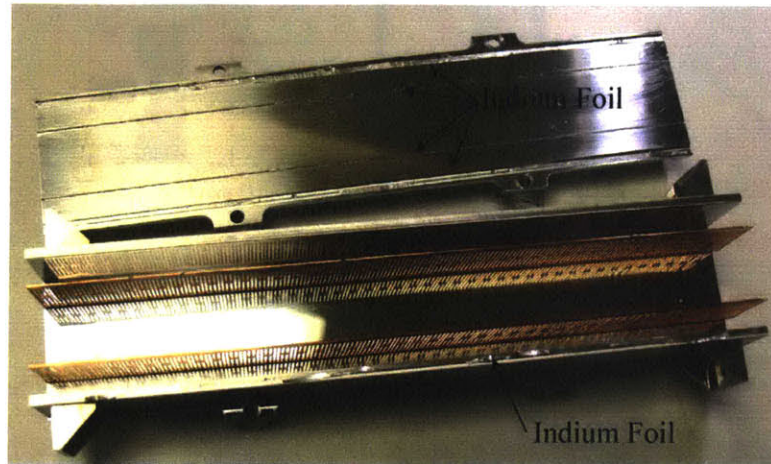


Figure 4-11: Photograph of the partially unassembled 352 mm unbrazed MTM1 structure that had indium foil put in structure joints before the structure was clamped together. The photograph was taken on October 6, 2015 after high power testing.

might be present in the actual experiment. Modes that are present due to any gaps in the structure joints are called 'slot modes.' In Fig. 4-12 the electric field profile and dispersion of the four lowest order slot modes is shown. In the simulation gaps of 0.5 mm were used around the metamaterial plates. All of the four slot modes have positive group velocities near the beam line. The structure supports an anti-symmetric and symmetric mode with positive group velocities that have no cutoff and an antisymmetric and symmetric mode that have positive group velocities and cutoff frequencies at 2.06 GHz. The dispersion curves of the symmetric and antisymmetric modes are nearly identical in this structure and so they overlap on the plot. Different gap variations (from 0.2 to 2 mm) and geometries were investigated in the eigenmode simulations, but all seemed to produce a qualitatively similar dispersion relation and a cold beam-wave interaction frequency of 2.2 to 2.4 GHz. Finally, a CST PIC simulation was run of a 352 mm long structure with the same design as shown in Fig. 4-12 that produced 700 kW of microwave power at 2.40 GHz. Not all of the same gap geometries and gap widths could be investigated with the PIC solver as were investigated with the eigenmode simulations due to constraints on computation

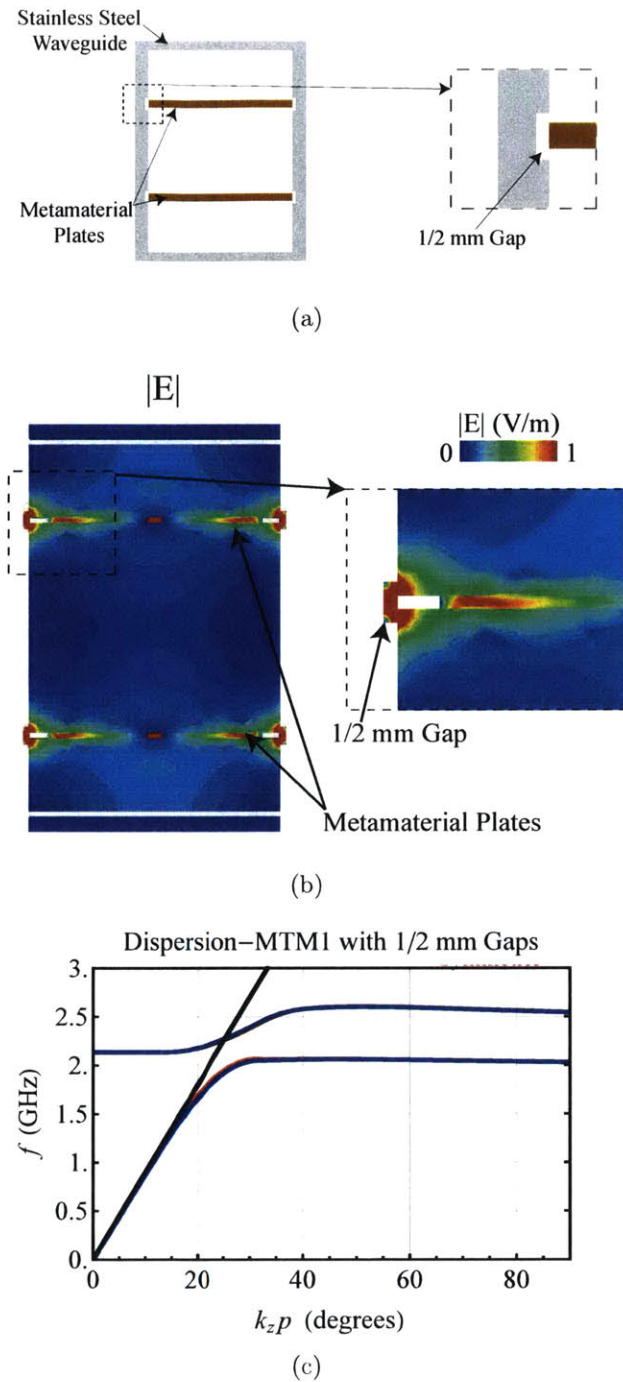


Figure 4-12: a) Simplified schematic of the MTM1 metamaterial structure with a 0.5 mm gap around the metamaterial plate. b) Electric field amplitude generated by an eigenmode simulation in CST MWS in the MTM1 metamaterial structure with a gap. The field corresponds to the antisymmetric mode that intersects the beam line at 2.30 GHz. c) Dispersion relation for the four lowest order modes of the above structure and for a 500 keV electron beam (black). There are two antisymmetric (red) modes and two symmetric (blue) modes.

time.

It is unlikely that the structure had uniform slots along the full length of the structure, or that the gaps were 0.5 mm. The tolerance of the slots around the metamaterial plates was specified at 1 mil, and the thickness of the plates was specified at 2 mils, so any gaps that were present in the structure were very small (and impossible to simulate with the current simulation capabilities). The results of the above discussion are merely included to illustrate the fact that poor electrical contact around the metamaterial plates could support a mode which has a) positive group velocity ($\frac{\partial\omega}{\partial k} > 0$ and b) a frequency of approximately 2.35 GHz, which is close to what was measured in the high power experiments.

4.2.3 Brazed MTM1 Structure Results

In order to verify that gaps in the structure were causing the high power excitation observed when the structure was assembled using indium foil, the structure was tested after being completely brazed together. The structure was first tested with the VNA to measure the transmission, which is shown in Fig. 4-13. This measurement was performed using SMA coax to WR284 couplers to excite the antisymmetric mode of the structure. Comparing Fig. 4-13 to Fig. 4-7 it is clear that there is a drastic difference in the transmission below 2.6 GHz, and especially at 2.35 GHz where high power operation was observed with the structure assembled with indium foil.

The power detected at higher magnetic field values remained unchanged from the measurements made when the structure was bolted both with and without indium foil, as is illustrated in the power, collector current, and gun voltage traces shown in Fig. 4-14 which were taken at a magnetic field of 1285 G. The beam diameter at this operating condition was approximately 4.2 mm. Averaged over the FWHM of the RF pulse, the metamaterial structure produced 30 W of power at 2.83 GHz for a voltage of 465 kV and beam current of 78 A. When the structure was put under vacuum and tested with the high power electron beam, no power at 2.35 GHz was detected and all of the microwave power came from the 2.83 GHz mode.

The power from the 2.83 GHz mode at low magnetic field (< 400 G) was also

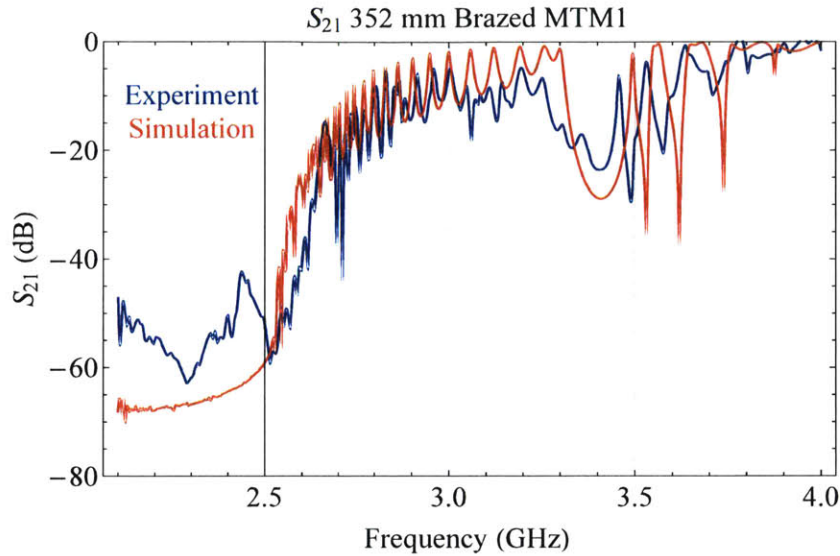


Figure 4-13: Transmission of the brazed 352 mm metamaterial structure (blue) compared with a CST MWS simulation of the transmission (red). The measurement (and associated simulation) were performed using SMA coax to WR284 couplers to excite the antisymmetric mode of the structure. Note that the transmission below 2.6 GHz is significantly reduced from when it was assembled with and without indium in the joints and bolted together.

approximately the same as the structure assembled with indium, though without competition from the 2.35 GHz mode the power trace did have a qualitatively different profile. This is illustrated in the power, collector current, and gun voltage traces shown in Fig. 4-15 which was taken at a magnetic field of 265 G. The beam diameter at this operating condition was approximately 25 mm. Averaged over the FWHM of the RF pulse, the metamaterial structure produced 275 W at 2.83 GHz for a voltage of 460 kV and beam current of 75 A.

Finally in Fig. 4-16, the microwave power is shown as a function of the applied solenoid field at a few different magnetic field values. Uniform current interception of ~ 5 A prevented measurements at lower magnetic values. Since the power is so low compared to the predicted output power, it is difficult to draw any conclusions on the variation of the power from low magnetic field to high magnetic field.

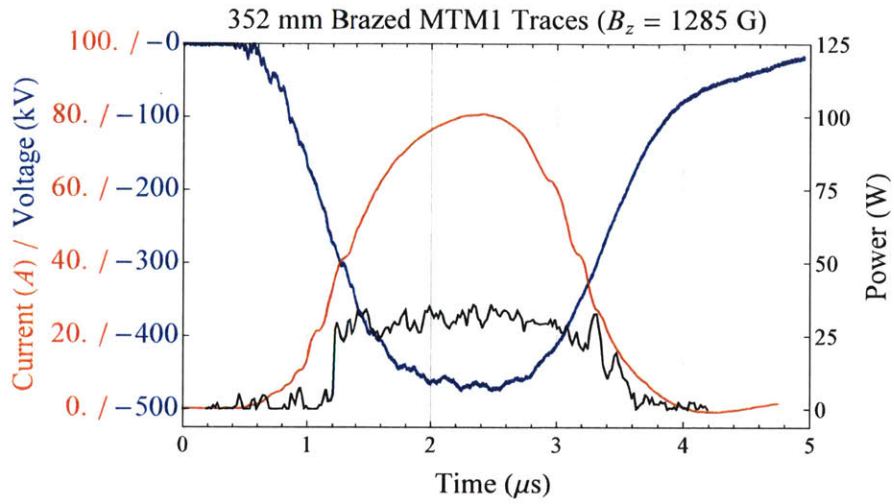


Figure 4-14: Microwave power (black curve), electron gun voltage (blue curve) and measured collector current (red curve) for an applied magnetic field of 1285 G. The scale for the current (voltage) is given on the left in red (blue) and the scale for the microwave power is given on the right in black.

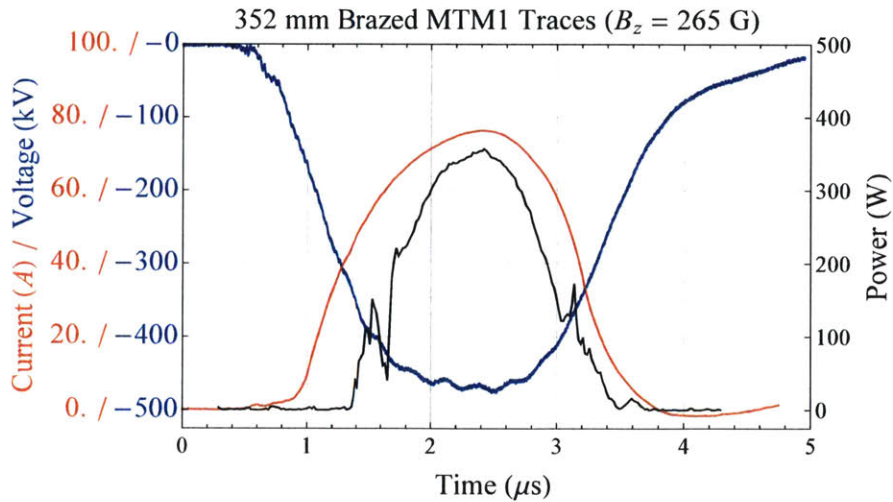


Figure 4-15: Microwave power (black curve), electron gun voltage (blue curve) and measured collector current (red curve) for an applied magnetic field of 265 G. The scale for the current (voltage) is given on the left in red (blue) and the scale for the microwave power is given on the right in black.

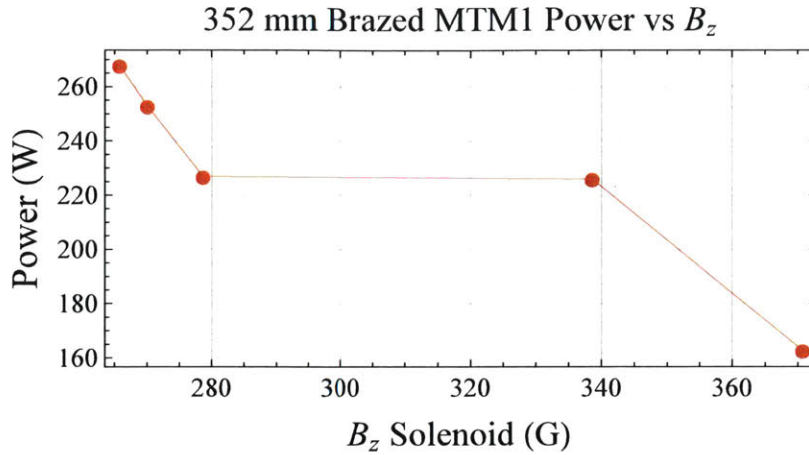


Figure 4-16: Microwave power measured at 2.83 GHz as the solenoid field is varied from 260 to 350 G. The microwave power at each particular frequency was measured using a 2.83 GHz band pass filter between the coupler and power meter. The gun voltage and current were fixed at 460 kV and 76 A and the magnetic lens current was held fixed at 10.8 A.

4.3 Experiments Using the MTM2 Design

4.3.1 370 mm Unbrazed MTM2 Structure Results

A photograph of the 370 mm structure based on the MTM2 design is shown in Fig. 4-17. The unbrazed structure was first tested with the VNA to measure the transmission, which is shown in Fig. 4-18. This measurement was performed using SMA coax to WR284 couplers to excite the antisymmetric mode of the structure. The simulated and measured transmission agree fairly well, however the measured transmission at the operating frequency (2.4 GHz) is about 5 dB below the simulated transmission. The 370 mm unbrazed MTM2 structure was tested right after the 352 mm unbrazed MTM1 structure and before the 352 mm MTM1 structure assembled with indium foil. The structure was tested over the same parameter space as the 352 mm unbrazed MTM1 structure because there were still concerns about testing structures at low magnetic field values which were anticipated to cause major beam deflections. Therefore this structure was tested over a range of magnetic field values from 1200 G to 1700 G and a wide range of voltage values. Lower magnetic field values were not investigated for this structure and the output power was not observed to

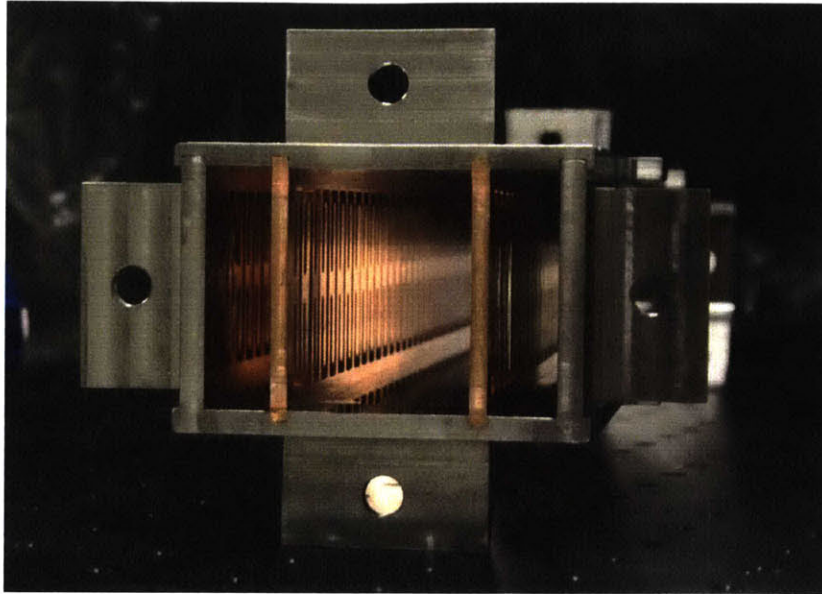


Figure 4-17: Photograph of the brazed 370 mm metamaterial MTM2 structure taken on January 1, 2015 after high power testing. This photo was taken after the structure was brazed together, however, the bolted structure looks identical. The braze material is not visible, but was put into the slots that were machined into the side plates prior to being put into a dry hydrogen furnace. For scale reference, the inner dimensions of the rectangular waveguide are 63 mm by 43 mm.

vary more than ± 10 W over the range of parameters investigated. A characteristic plot of the power, collector current, and gun voltage is shown in Fig. 4-19. Averaged over the FWHM of the RF pulse, the metamaterial structure produced 25 W for a voltage of approximately 510 kV and beam current of 84 A. The measured frequency for these same voltage, current, and magnetic field settings was 2.431 GHz. This agreed fairly well with the CST PIC simulation which predicted a frequency of 2.401 GHz. However, the power predicted by CST PIC simulations (6.4 MW) was again 10^5 higher than what was measured in the experiment.

4.3.2 370 mm Brazed MTM2 Structure Results

The 370 mm structure was then sent out to be brazed. It was then tested with the VNA to measure the transmission, which is shown in Fig. 4-20. This measurement was performed using SMA coax to WR284 couplers to excite the antisymmetric mode

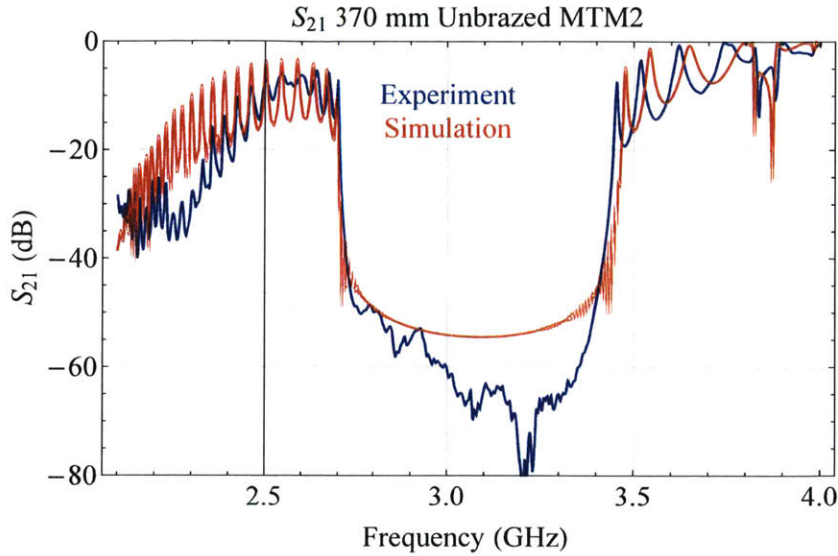


Figure 4-18: Transmission of the 370 mm unbrazed metamaterial structure (blue) compared with a CST MWS simulation of the transmission (red). The measurement (and associated simulation) were performed using SMA coax to WR284 couplers to excite the antisymmetric mode of the structure.

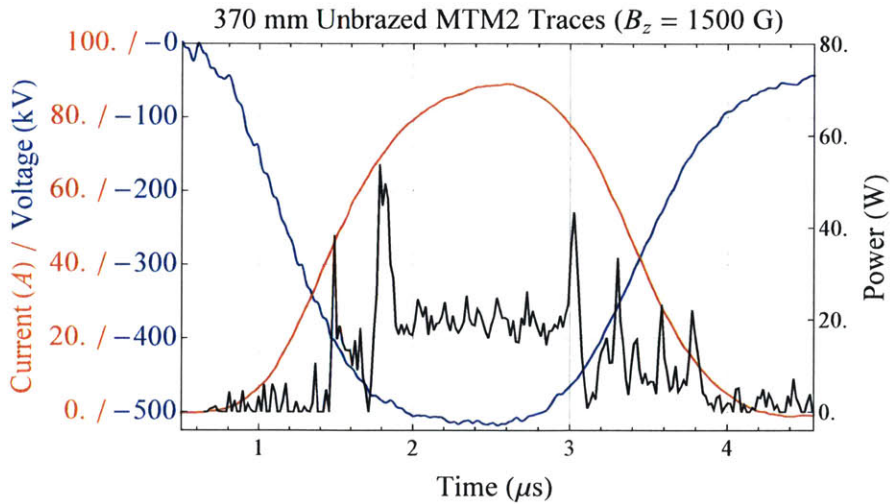


Figure 4-19: Microwave power (black curve), electron gun voltage (blue curve) and measured collector current (red curve) for an applied magnetic field of 1500 G. The scale for the current (voltage) is given on the left in red (blue) and the scale for the microwave power is given on the right in black.

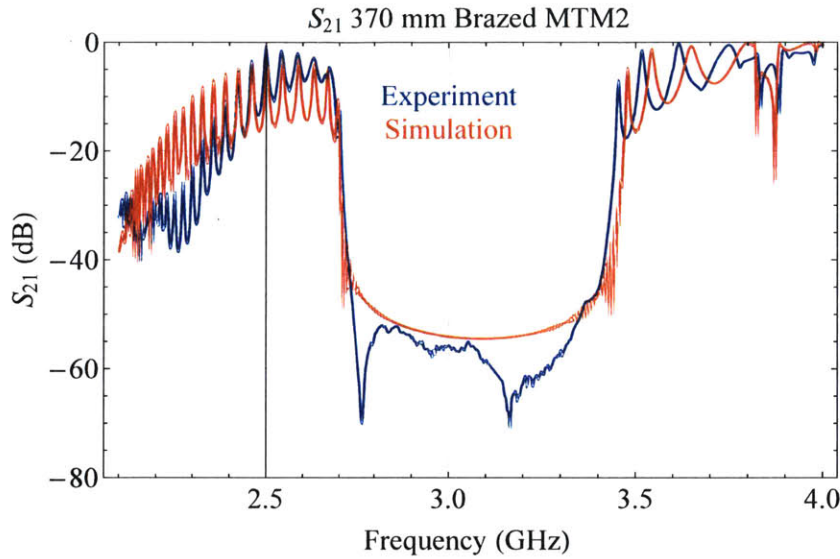


Figure 4-20: Transmission of the 370 mm brazed MTM2 metamaterial structure (blue) compared with a CST MWS simulation of the transmission (red). The measurement (and associated simulation) were performed using SMA coax to WR284 couplers to excite the antisymmetric mode of the structure.

of the structure. The simulated and measured transmission agree fairly well, and comparing these results to Fig. 4-18 it is apparent that brazing helped to improve the transmission of the design mode. The measured transmission at the operating point near 2.4 GHz agrees almost exactly with the simulation.

The structure was then returned to vacuum and tested with the electron beam. For all of the data presented for the 370 mm brazed MTM2 structure on the following pages, the location of the magnetic lens was 145 mm away from the focus spot of the gun, and the edge of the steel solenoid pole plate was approximately 260 mm from the focus of the gun. Different lens and solenoid positions were investigated, but were not observed to significantly impact the results. A plot of a high power trace, collector current, and gun voltage for an applied magnetic field of 375 G is shown in Fig. 4-21. The beam diameter at this operating condition was approximately 17 mm. Averaged over the FWHM of the RF pulse, the metamaterial structure produced 2.3 MW at 2.380 GHz for a voltage of 400 kV and beam current of 62 A. For high magnetic fields (700 G and above) the structure was observed to behave

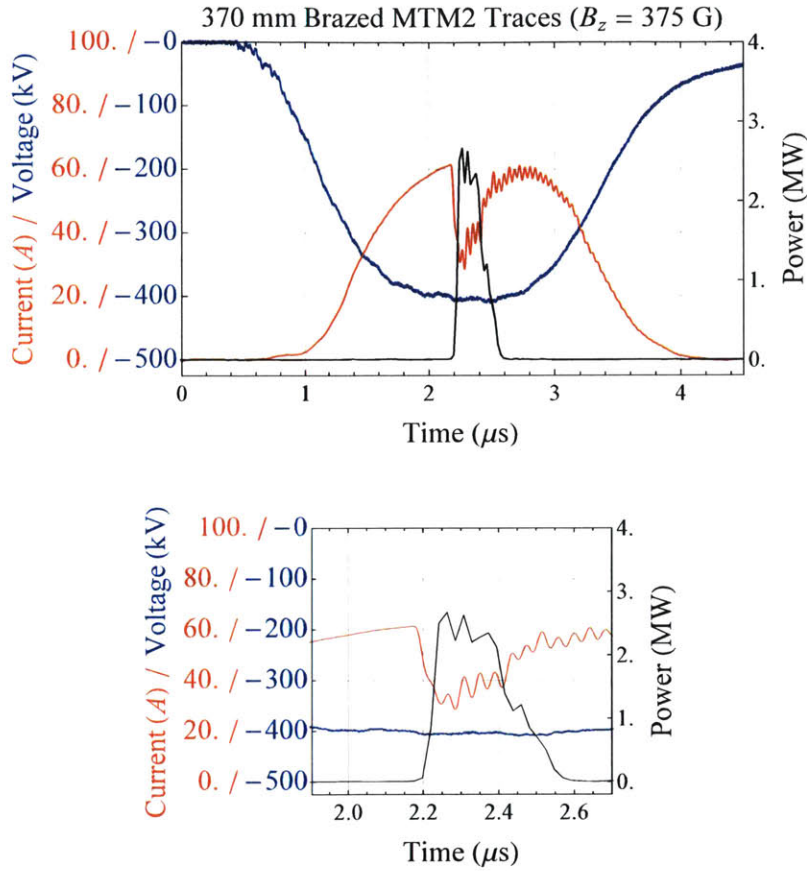


Figure 4-21: Microwave power (black curve), electron gun voltage (blue curve) and measured collector current (red curve) for an applied magnetic field of 375 G. The scale for the current (voltage) is given on the left in red (blue) and the scale for the microwave power is given on the right in black. The lens current was set at 10.1 A. A blow up of the high power trace is also shown below.

approximately the same as the bolted structure (microwave power ~ 10 - 100 W, $f \sim 2.44$ GHz). However, below a certain magnetic field value the structure produced megawatts of output power at approximately 2.4 GHz, provided that the voltage and current were above a particular threshold. In all instances of high power generation, a significant amount of beam interception was also observed as evidenced by a missing portion of the collector current. While the beam interception was significant, in PIC simulations performed at the same magnetic field approximately 98% of all the current was intercepted on the metamaterial structure (beam interception in the PIC

simulations was presented in Chapter 2, for the comparison of this measurement with simulation see section 2.4.2). It should be further noted that the PIC simulations do not have any model of re-emission, flashover, or gas generation from associated beam interception, which likely have a major impact on the operation of the device. If any of these effects are responsible for terminating the RF pulse, the PIC simulations would be unable to predict the pulse shortening. A camera was used to monitor the quartz window on top of the experiment for light emission from inside the chamber and none was observed. However, it should be noted that there is not a direct line of sight from the window to the metamaterial structure and so only very bright flashes of light would have been detected on the camera.

Fig. 4-21 is an example of a high power trace where there is an RF ‘flat-top,’ or a period of a few hundred nanoseconds of continuous power. However, many of the shots where high power was observed had very high peak power pulses (> 5 MW) with shorter time durations (100 ns). A plot of such a power trace along with the gun voltage and collector current is shown in Fig. 4-22. The trace was taken with an applied magnetic field of 431 G. The beam diameter at this operating condition was approximately 14 mm. The peak power observed exceeds 5 MW at 2.386 GHz for a

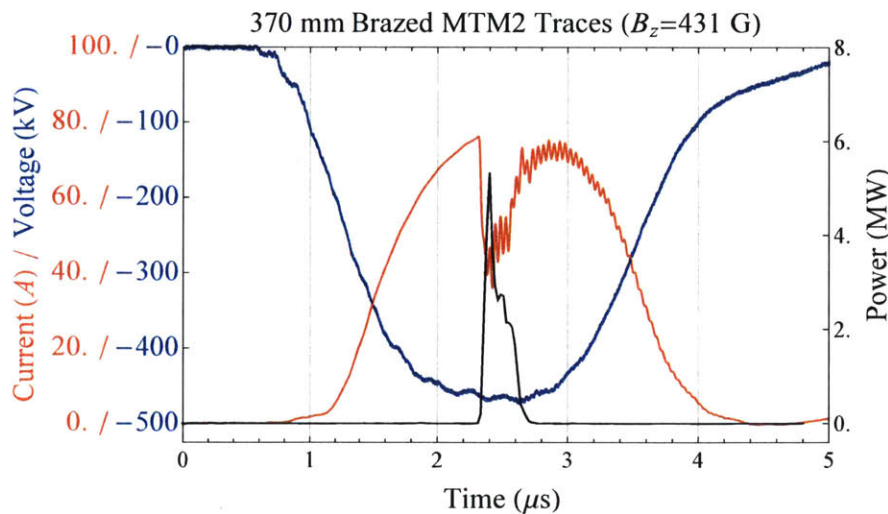


Figure 4-22: Microwave power (black curve), electron gun voltage (blue curve) and measured collector current (red curve) for an applied magnetic field of 431 G. The scale for the current (voltage) is given on the left in red (blue) and the scale for the microwave power is given on the right in black. The lens current was set at 10.8 A.

voltage of approximately 460 kV and beam current of 75 A. The measured microwave power did have a certain degree of shot-to-shot variation in both the measured RF power ($\pm 50\%$) and the RF pulse duration (the pulse length defined by the FWHM power value) at any given voltage or magnetic field. Despite the shot-to-shot variation in pulse duration, over all of the parameters investigated the pulse length was greater than 100 ns and less than 400 ns, and the mean duration was approximately 300 ns.

The structure was found to have a starting voltage (or current) at which high power microwave generation would occur for a particular magnetic field value. The high power turn-on condition was defined by the minimum voltage where over a megawatt of power was generated. Because the change in the output power of the device was very abrupt (i.e. the device produced a peak power of at least 2 MW or only a few hundred watts of power) the turn-on condition or starting voltage was easily defined by this abrupt transition. Typically one defines a starting current for operation. However, since the gun that was used in the experiment is a Pierce gun the current follows the voltage. Therefore, since it is actually the voltage that is varied in the experiment, this is the value that is recorded. The current roughly varies as $V^{3/2}$. The starting voltage was very repeatable and was found to depend on the applied solenoid field. The starting voltages for the 370 mm brazed MTM2 structure are shown in Fig. 4-23. The lens current was set at 10.8 A for this measurement. The starting voltage was observed to be very slightly influenced by magnetic field of the lens, however this had only a small effect on the value. The approximate beam size in Fig. 4-23 ranged from 12 mm at 450 G to 15 mm at 410 G.

The microwave frequency was observed to tune with the gun voltage for a fixed magnetic field of 410 G. In Fig. 4-24, the frequency of the microwave signal is shown as the gun voltage was varied from 450 to 490 kV. The beam diameter is approximately 15 mm over these voltages. All of the data points in Fig. 4-24 were taken above the starting voltage and produced a high power microwave pulse with peak power exceeding 2 MW. The solid red curve represents the frequencies predicted by the cold dispersion relation of the antisymmetric mode governed by the resonance condition $\omega = k_z v_z$, and the solid black curve corresponds to the anomalous Doppler resonance

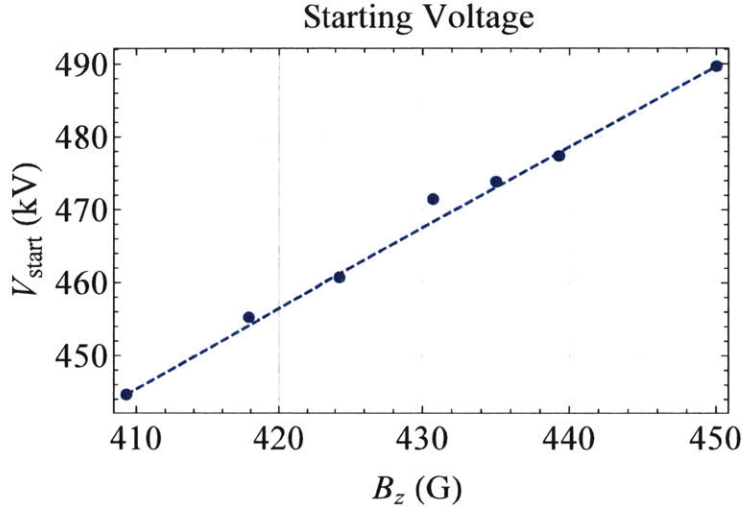


Figure 4-23: Measured starting voltage (related to the starting current) of the 370 mm brazed MTM2 structure. For voltages above the dashed curve (which is drawn to guide the eye) the structure produced more than 1 MW of power, and below the curve the structure produced about 1 kW or less.

condition $\omega = k_z v_z - \Omega_c / \gamma$. In addition to the predicted eigenmode frequencies, the frequency predicted by CST PIC simulations for the same operating conditions are also shown in this figure. Very good agreement between the CST PIC simulations, anomalous Doppler shifted antisymmetric mode, and experiment was found. The frequency of these high power shots is lower than low power shots at higher magnetic field values (i.e. 1500 G) where the frequency was closer to 2.44 GHz due to the Cherenkov synchronism ($\omega = k_z v_z$) with the symmetric mode.

To illustrate this fact, the frequencies of the low power microwave signals were measured at higher magnetic field values and above the starting voltage. This is shown in comparison to PIC simulations in Fig. 4-25. In addition to this plot, the measured and predicted phase difference between the microwave signals in RF arm 1 and arm 2 is also shown. The measurements were made for a fixed gun voltage and current of 489 kV and 84 A with the lens current set at 10.8 A, and the beam diameter varies from 20 mm at 350 G to 3 mm at 1800 G. These are compared with CST PIC simulations (green stars) performed at the same voltage and current values. See Table A.12 for

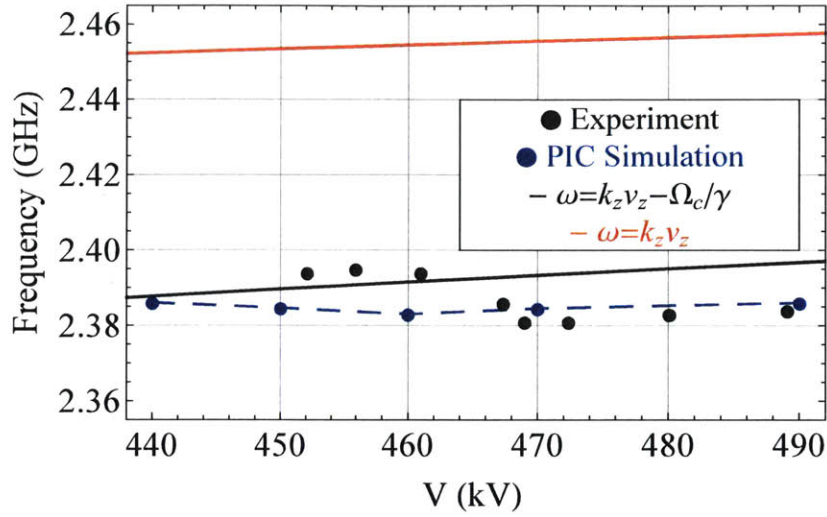


Figure 4-24: Variation of the frequency of the high power microwave pulses with the gun voltage for the 370 mm brazed MTM2 structure at a fixed magnetic field of 410 G with the lens current set at 10.8 A. The frequencies of the antisymmetric mode predicted by the eigenmode simulation corresponding to the normal (Cherenkov) resonance condition and the anomalous Doppler resonance condition is displayed as the solid red curve and black curve, respectively. Frequencies predicted by CST PIC simulations are also shown (blue).

a more detailed description of the inputs to the simulation. From the plot, there are two different transitions that the device makes which depend on the magnetic field and are important to point out. First, there is a transition from the antisymmetric to the symmetric mode around 750 G which is highlighted by the different shaded blue (antisymmetric) and red (symmetric) regions. The transition between these two modes is determined by the change in phase that is measured between the output signals of the RF arms and shown in Fig. 4-25c. The PIC simulations accurately predict the magnetic field where this transition occurs. At this transition there is also a change in the frequency tuning, which is highlighted in Fig. 4-25b. Above 700 G the frequency of the device is approximately constant, while below this value the frequency changes with the magnetic field. To compare this with the cold dispersion model for the MTM2 structure that was solved with the eigenmode solver, there are three different curves shown in Fig. 4-25b. These curves correspond to the frequencies predicted by the cold dispersion relation for the resonance condition $\omega = k_z v_z$ with

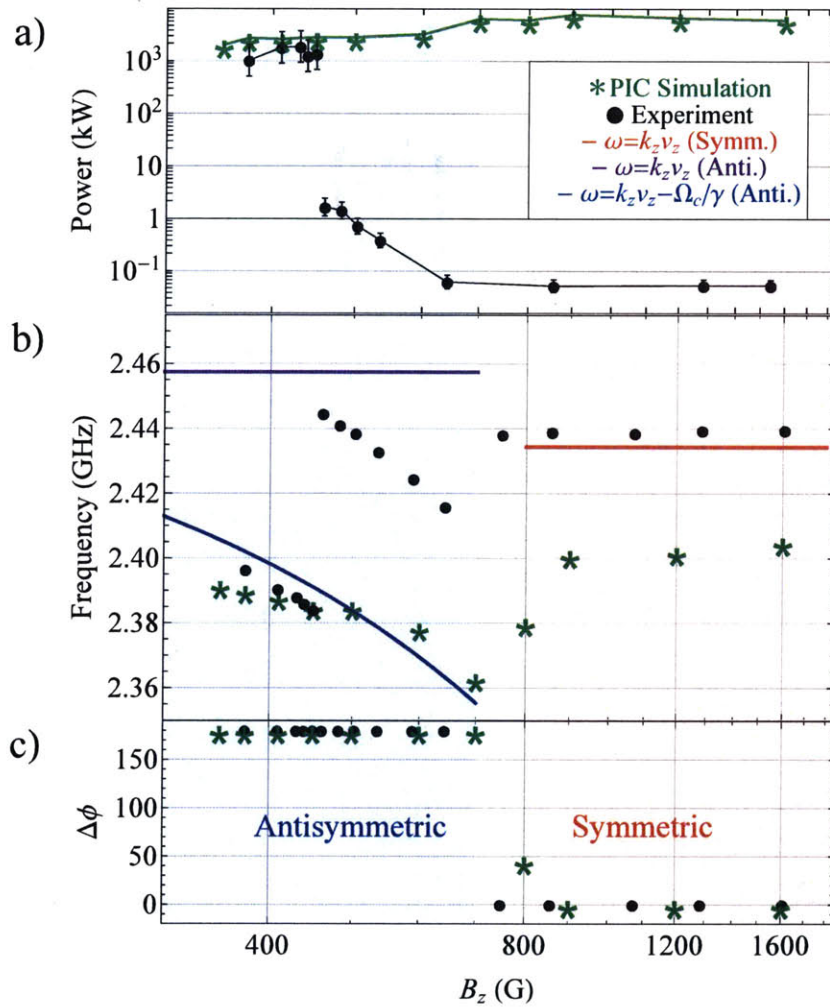


Figure 4-25: Stacked plot of the a) average microwave power (top), b) frequency (middle), and c) phase difference between the two RF arms (bottom). All of the green star data points are those obtained from PIC simulations, and the black data points are the experimentally measured values. The power plot shows a distinct transition at about 430 G where the device starts to produce high power in the antisymmetric mode, and a transition at about 750 G where the device switches from antisymmetric to symmetric mode excitation.

the symmetric mode (red), $\omega = k_z v_z$ with the antisymmetric mode (purple), and $\omega = k_z v_z - \Omega_c/\gamma$ with the antisymmetric mode (blue). Qualitatively, these predicted frequencies do agree with both the simulations and the measured values; however, in the range of magnetic field values from 450 to 700 G, the measured frequencies are higher than the predicted values by CST. In addition, the frequencies lie in between the frequency curves predicted by the $\omega = k_z v_z$ and $\omega = k_z v_z - \Omega_c/\gamma$ resonance conditions of the antisymmetric mode.

Second, there is a transition between high power operation which also likely affects the frequency where the device operates. This transition occurs at approximately 435 G where the average output power jumps from just over 1 kW to over 1 MW. While this transition was measured in the experiment, it was not predicted by the CST PIC simulations. In fact, the PIC simulations predicted high power microwave generation for all of the magnetic field values shown at the voltage and current values that were investigated in Fig. 4-25a. Quantitatively, the CST PIC simulations do a better job at predicting the frequency of high power operation (as is shown in Fig. 4-25) than they do of the low power operation. Understanding the low power frequency is difficult because the device has not reached saturation and is in a pre-oscillation state. For high power operation there is likely a nonlinear shift in the frequency as the device locks in to a particular frequency value.

4.3.3 420 mm Brazed MTM2 Structure Results

A structure fabricated with the MTM2 design, but 420 mm long instead of 370 mm, was tested with the high power electron beam. This structure was only high power tested after being brazed. It was first tested with the VNA to measure the transmission, which is shown in Fig. 4-26. This measurement was performed using SMA coax to WR284 couplers to excite the antisymmetric mode of the structure. The measured transmission near the operating point at 2.4 GHz agrees almost exactly with the simulation.

The 420 mm brazed MTM2 structure was then put under vacuum and tested with the high power electron beam. For all of the data presented for this structure, the

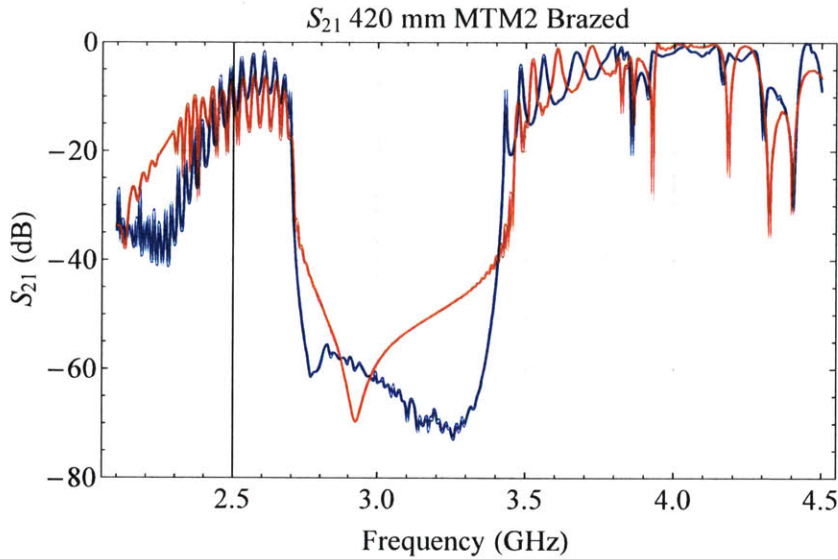


Figure 4-26: Transmission of the 420 mm brazed MTM2 metamaterial structure (blue) compared with a CST MWS simulation of the transmission (red). The measurement (and associated simulation) were performed using SMA coax to WR284 couplers to excite the antisymmetric mode of the structure.

location of the magnetic lens was 145 mm away from the focus spot of the gun, and the edge of the steel solenoid pole plate was approximately 260 mm from the focus of the gun. When the structure was tested with the electron beam it produced over 100 kW over a wide range of magnetic field values. However, the frequency of oscillation was measured with the oscilloscope and verified with microwave band-pass filters to be approximately 5.95 GHz. This corresponds to the intersection of the beam line with the positive group velocity modes shown in Fig. 2-10. Unfortunately, the higher frequency of operation was problematic for the power measurement because the WR284 waveguide which is used to bring the microwaves out of the experiment ceases to be single-moded above 4.16 GHz. In fact there are five supported modes at 5.95 GHz, and so the output coupling of the Bethe-hole couplers at this frequency depends not only on the frequency, but on the mode content of the microwaves in the waveguide. It was shown in Chapter 3 that nearly all of the power exists in the TM_{11} and TE_{10} modes of the waveguide (see Fig. 3-16 and surrounding discussion), and the coupling values of couplers A and B at 5.95 GHz are estimated to be -46.3 dB and

-48.4 dB, respectively. However, it was estimated that an error of approximately ± 1 dB exists for these coupling values so this uncertainty should be reiterated before drawing conclusions about the device performance.

A plot of the 5.95 GHz microwave power trace, collector current, and gun voltage for an applied magnetic field of 1550 G is shown in Fig. 4-27. Averaged over the

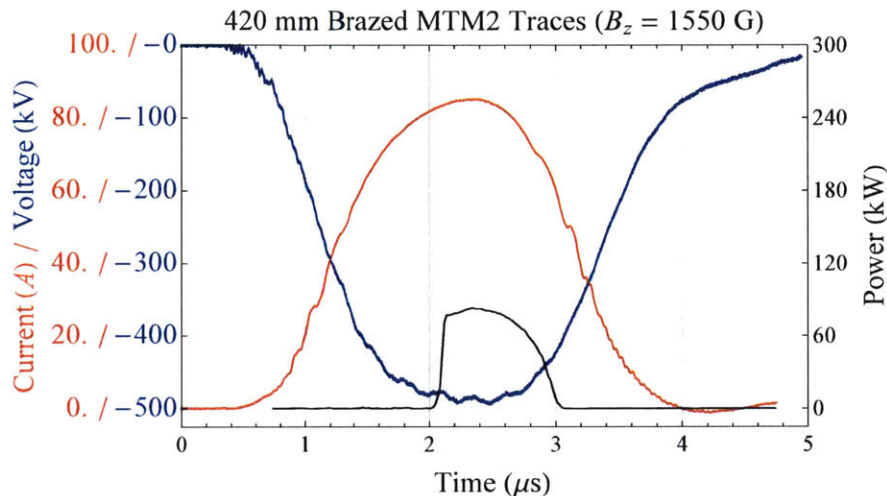


Figure 4-27: Microwave power (black curve), electron gun voltage (blue curve) and measured collector current (red curve) for an applied magnetic field of 1550 G. The scale for the current (voltage) is given on the left in red (blue) and the scale for the microwave power is given on the right in black. The lens current was set at 11 A.

FWHM of the RF pulse, the metamaterial structure produced approximately an average of 85 ± 20 kW (black curve) at 5.95 GHz for a voltage of approximately 485 kV and beam current of 83 A. For all of the different parameters investigated the device was only observed to operate in the symmetric positive group velocity mode determined by the phase difference between the microwave signals. Plots of microwave traces taken at 790 G and 640 G are shown in Fig. 4-28 and Fig. 4-29, respectively. Averaged over the FWHM of the RF pulse, the metamaterial structure produced approximately 170 ± 45 kW at 5.95 GHz for a voltage of 485 kV, beam current of 83 A, and a magnetic field of 790 G. In addition, the structure produced 140 ± 35 kW for a magnetic field of 640 G and the same voltage and current. In all three traces, the microwave signal is observed to start only when the voltage is near its maximal, flat-top value. In Fig. 4-30 the variation of the microwave power and

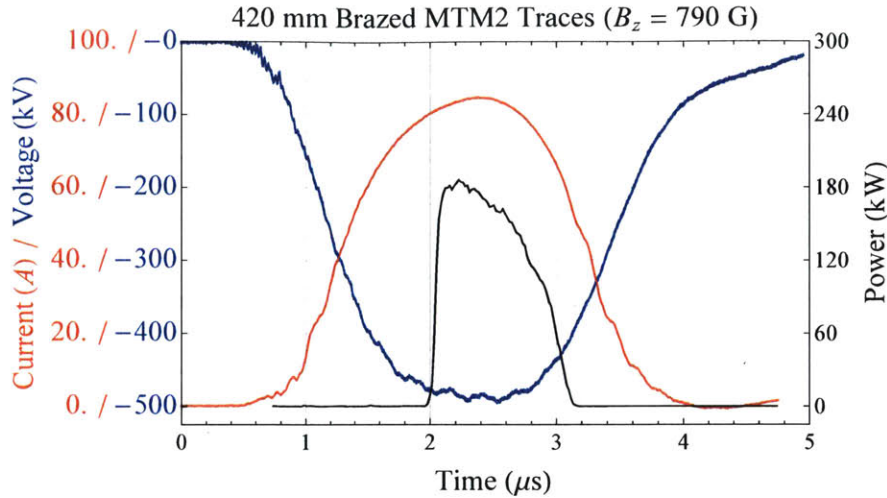


Figure 4-28: Microwave power (black curve), electron gun voltage (blue curve) and measured collector current (red curve) for an applied magnetic field of 790 G. The scale for the current (voltage) is given on the left in red (blue) and the scale for the microwave power is given on the right in black. The lens current was set at 11 A.

tuning of the frequency as the magnetic field is varied is shown. In the figure, the gun voltage and current are held fixed at 480 kV and 81 A. The microwave power is averaged over the FWHM of the microwave pulse, corresponding to 2.05 to 2.95 μs in Fig. 4-27. The peak power occurs at approximately 700 G.

The microwave frequency was observed to tune with the gun voltage for a fixed magnetic field. In Fig. 4-31, the frequency of the microwave signal is shown as the gun voltage is varied from 440 to 490 kV and the magnetic field is kept fixed at 1550 G. The frequency tuning of the device with voltage does not match what was predicted by the eigenmode simulations. This discrepancy may be due to strong end reflections which can affect the frequency of operation. In addition, the dispersive effect of the beam current can also affect the output frequency.

Additionally, the power at 5.95 GHz was measured at fixed values of the solenoid field while the gun voltage was varied. This is shown in Fig. 4-32 for a solenoid field of 640, 790, and 1550 G. The microwave power is averaged over the FWHM of the microwave pulse. The dashed trendlines are drawn to guide the eye.

Lower magnetic field values were also investigated for the 420 mm structure. Similar to the experiments performed with the 370 mm brazed MTM2 structure, it was

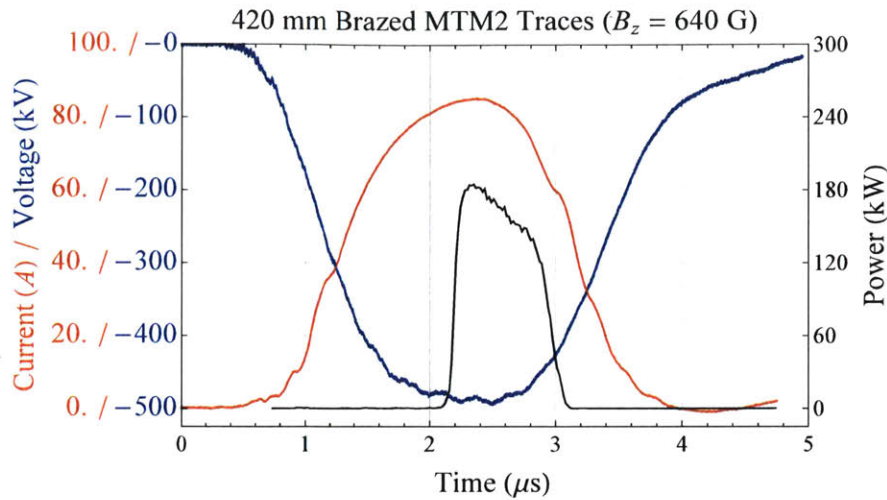


Figure 4-29: Microwave power (black curve), electron gun voltage (blue curve) and measured collector current (red curve) for an applied magnetic field of 640 G. The scale for the current (voltage) is given on the left in red (blue) and the scale for the microwave power is given on the right in black. The lens current was set at 11 A.

discovered that for some lower magnetic field values the structure produced high power microwave pulses at approximately 2.4 GHz. Because there was also microwave generation at 5.95 GHz, it was necessary to use the band pass microwave filters to measure the power generated at 2.4 GHz only.

In the measurements, it was observed that for the same voltage, the magnetic field value at which the device was observed to turn-on at 2.4 GHz was higher in the 420 mm structure than in the 370 mm structure. In all instances of high power generation, a significant amount of beam interception was also observed. A plot of a high power trace, collector current, and gun voltage for an applied magnetic field of 514 G is shown in Fig. 4-33. The peak power is approximately 400 kW for a voltage of 465 kV and beam current of 78 A. It is obvious from Fig. 4-33 that the device does not produce microwaves at the peak of the voltage and current, but rather on the voltage rise and well below the flat-top value. This behavior was actually consistent over all magnetic field, magnetic lens, alignment, and voltage values investigated. The microwave pulse always started at approximately $1.7 \mu\text{s} \pm 100 \text{ ns}$ (in reference to Fig. 4-33).

A plot of a high power trace, collector current, and gun voltage for an applied

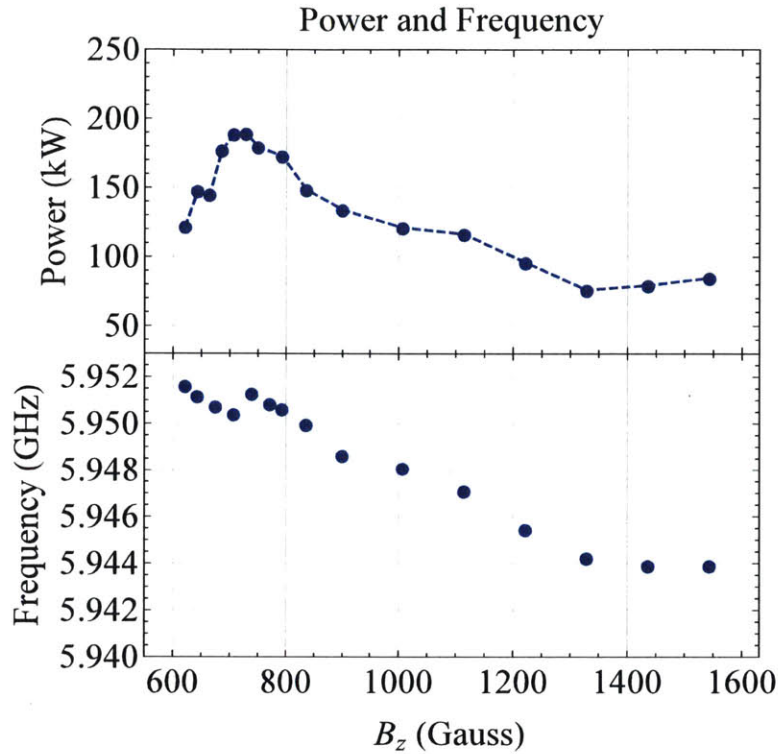


Figure 4-30: Variation of the frequency and microwave power of the positive group velocity mode of the 420 mm MTM2 structure as a function of the magnetic field. The power is averaged over FWHM of the RF pulse. The gun voltage and current were fixed at 480 kV and 81 A. The lens current was 10.8 A.

magnetic field of 470 G is shown in Fig. 4-34. The peak power is approximately 150 kW for a voltage of approximately 430 kV and beam current of 69 A.

It is not clear why the device would turn on at a fraction of the maximal voltage and current values or why it was never observed to turn on during the fall of the voltage trace. One very likely possibility is that competition with the 5.95 GHz mode would keep the 2.4 GHz mode from starting again during the fall of the voltage pulse. In addition, during the voltage and current flat-top the 5.95 GHz would compete with the 2.4 GHz mode and so the 2.4 GHz mode was short lived.

It is also possible that since the electron beam is focused differently at different voltage/current ratios, the coupling of the beam to the mode is not at its peak at the

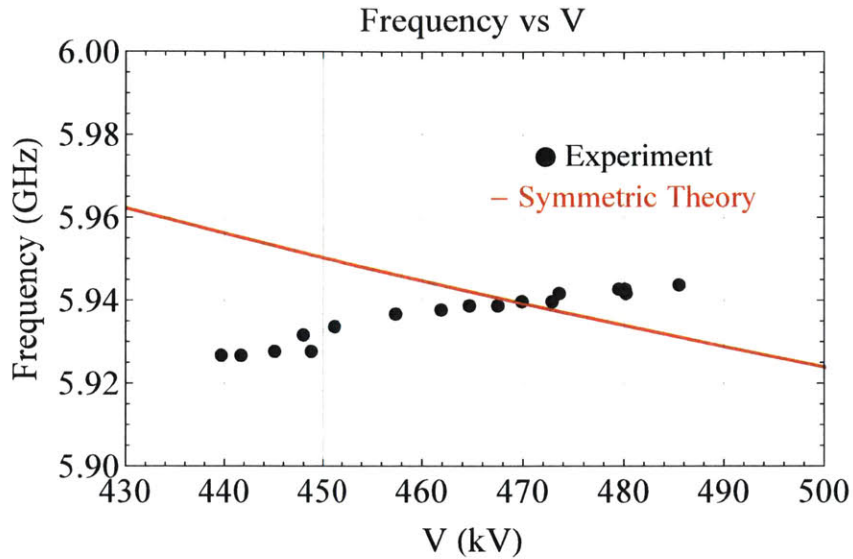


Figure 4-31: Variation of the frequency of the symmetric positive group velocity mode with the gun voltage for the 420 mm brazed MTM2 structure at a fixed magnetic field of 1550 G, with the lens current set at 12 A. The frequency of the symmetric mode predicted by the eigenmode simulations is displayed as the solid red curve (which is shifted up in frequency by 65 MHz).

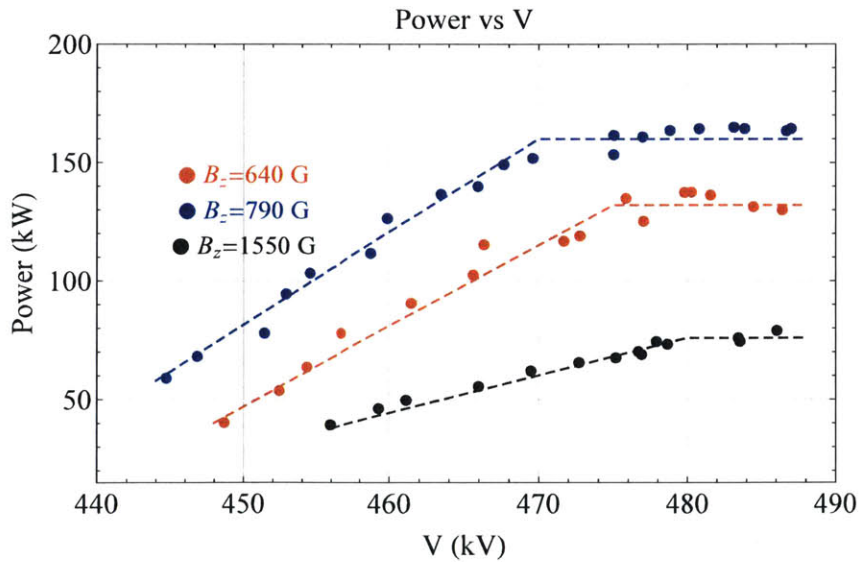


Figure 4-32: Variation of the 5.95 GHz microwave power as a function of the gun voltage for 640 G (red), 790 G (blue) and 1550 G (black). The power is averaged over the FWHM of the RF pulse.

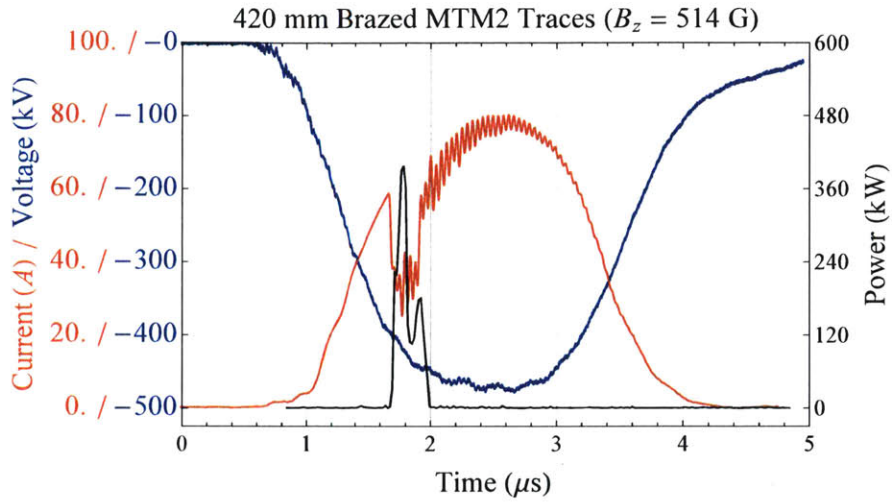


Figure 4-33: Microwave power in the 2.4 GHz mode (black curve), electron gun voltage (blue curve), and measured collector current (red curve) for an applied magnetic field of 514 G. The scale for the current (voltage) is given on the left in red (blue) and the scale for the microwave power is given on the right in black. The lens current was set at 10.1 A.

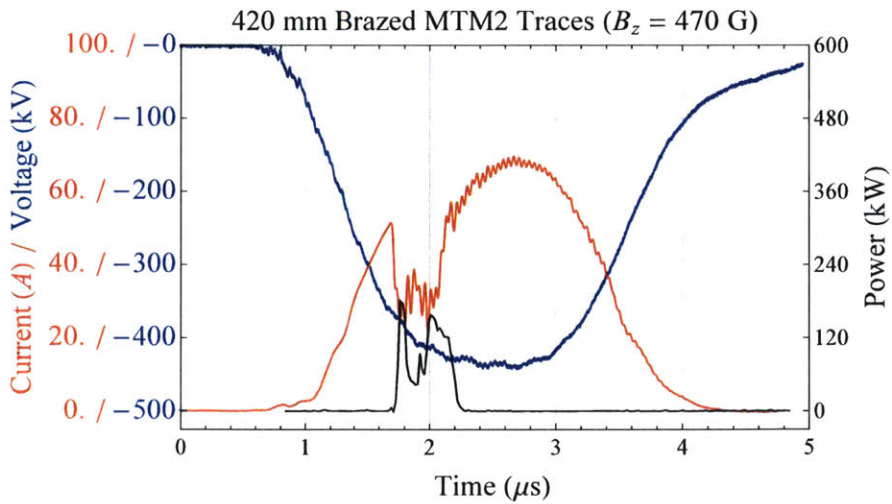


Figure 4-34: Microwave power (black curve), electron gun voltage (blue curve) and measured collector current (red curve) for an applied magnetic field of 470 G. The scale for the current (voltage) is given on the left in red (blue) and the scale for the microwave power is given on the right in black. The lens current was set at 10.1 A.

voltage maximum but during the rise and fall of the pulse. In other words, the rise and fall of the voltage has an effect on the beam location in the structure which thus has a significant impact on the beam-wave coupling. If the beam was focused very close to the metamaterial plates during the voltage rise, which could be the case if there is significant scalloping of the beam, this could cause the structure to start to oscillate at 2.4 GHz.

4.4 Experiments Using the MTM3 Design

A fully brazed 420 mm long structure fabricated with the MTM3 design was tested with the high power electron beam. The period of the MTM3 design is 5 mm, so the total number of periods in the structure was 84. The structure was designed in order to minimize the start current of the negative group velocity mode while still working with the system that was fabricated to test the MTM1 and MTM2 structures. Practically, this meant that the structure had a smaller spacing between the metamaterial plates (25 mm for MTM3 vs. 29 for MTM2 and 36 for MTM1), was built to the maximum length that could be tested in the setup (420 mm), and operated in the negative group velocity mode at a higher frequency than the MTM2 and MTM1 structures, but still under the frequency where the waveguides became overmoded (at 4.16 GHz). The brazed MTM3 structure was first tested with the VNA to measure the transmission, which is shown in Fig. 4-35. This measurement was performed using SMA coax to WR284 couplers to excite the antisymmetric mode of the structure. The measured transmission near the operating point of 3.7 GHz agrees almost exactly with the simulation.

The 420 mm brazed MTM3 was tested with the high power electron beam. For all of the data presented for this structure, the location of the magnetic lens was 145 mm away from the focus spot of the gun, and the edge of the steel solenoid pole plate was approximately 260 mm from the focus of the gun. A plot of the microwave power trace, collector current, and gun voltage for an applied magnetic field of 1550 G is shown in Fig. 4-36. The beam diameter at this operating condition was approximately

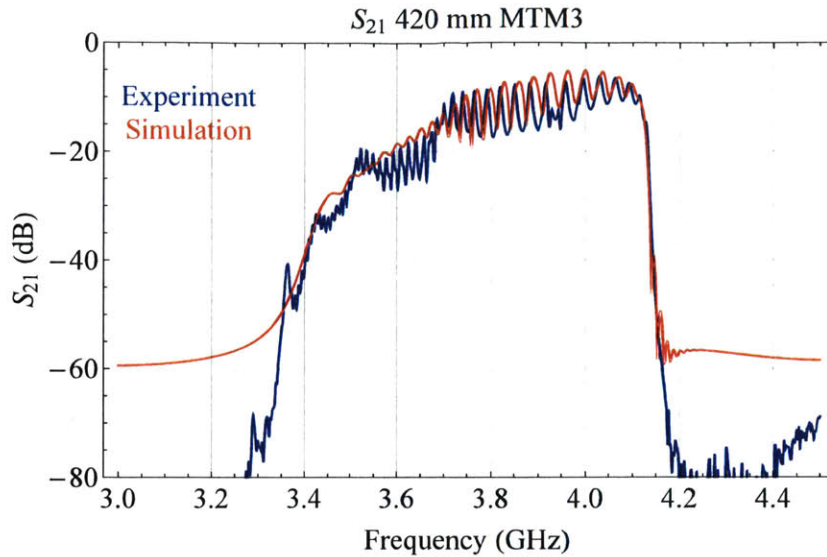


Figure 4-35: Transmission of the 420 mm brazed MTM3 metamaterial structure (blue) compared with a CST MWS simulation of the transmission (red). The measurement (and associated simulation) were performed using SMA coax to WR284 couplers to excite the antisymmetric mode of the structure.

3.4 mm. The structure produced approximately 80 W of power at 3.74 GHz for a voltage of 475 kV and beam current of 80 A.

The output power of the structure was approximately constant with magnetic field, however for magnetic field values between 420 and 450 G the structure produced very short pulses of microwaves (pulse length ~ 100 ns) that were up to 2 kW in peak power. To illustrate this, a plot of the microwave power trace, collector current, and gun voltage for an applied magnetic field of 450 G is shown in Fig. 4-37. The beam diameter at this operating condition was approximately 13 mm. The structure produced a peak power of 2 kW at 3.74 GHz for a voltage of 475 kV and beam current of 81 A, but the pulse was only about 100 ns long. Below 400 G a significant amount of beam interception was observed (greater than 15 A) so that the device wasn't run below this magnetic field value. The interception was uniform in time, unlike the interception observed with the high power operation of both MTM2 structures which occurred only while the device produced high power microwaves.

The frequency was measured as the voltage of the gun was varied at a fixed

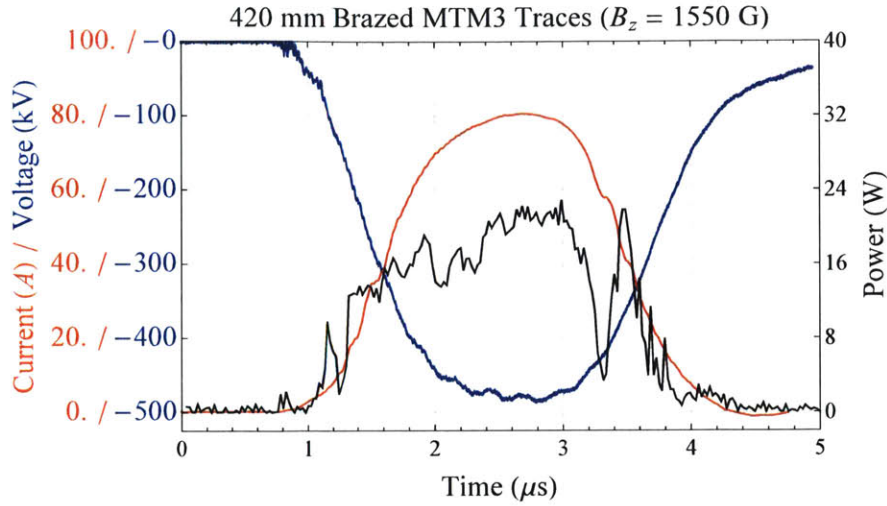


Figure 4-36: Microwave power (black curve), electron gun voltage (blue curve) and measured collector current (red curve) for an applied magnetic field of 1550 G. The scale for the current (voltage) is given on the left in red (blue) and the scale for the microwave power is given on the right in black. The lens current was set at 12 A.

magnetic field. This is shown in Fig. 4-38. The magnetic field was fixed at 1550 G, and the voltage corresponds to the average value over the 1 μ s flat-top of the gun. The dashed curve corresponds to the symmetric mode cold dispersion that was solved with the eigenmode solver. The eigenmode simulation curve was downshifted by 30 MHz. A shift of this magnitude may be due to fabrication errors or possibly due to the effect of the space charge of the beam.

Finally, the power, microwave frequency, and phase difference between the microwave signals in the two RF arms ($\Delta\phi$) were measured at a fixed voltage and current as the magnetic field was varied. The results of these measurements are shown in Fig. 4-39 along with the results of PIC simulations that were performed at the same operating conditions. See Table A.13 for a more detailed description of the inputs to the simulation. The measurements and simulations were all done at a fixed voltage and current of 465 kV and 78 A. The switch in $\Delta\phi$ between the RF arms at approximately 850 G indicates the magnetic field value where the device transitions from antisymmetric to symmetric mode excitation. When the phase difference measured at the Bethe-hole couplers was 0, the structure was oscillating in the symmetric mode

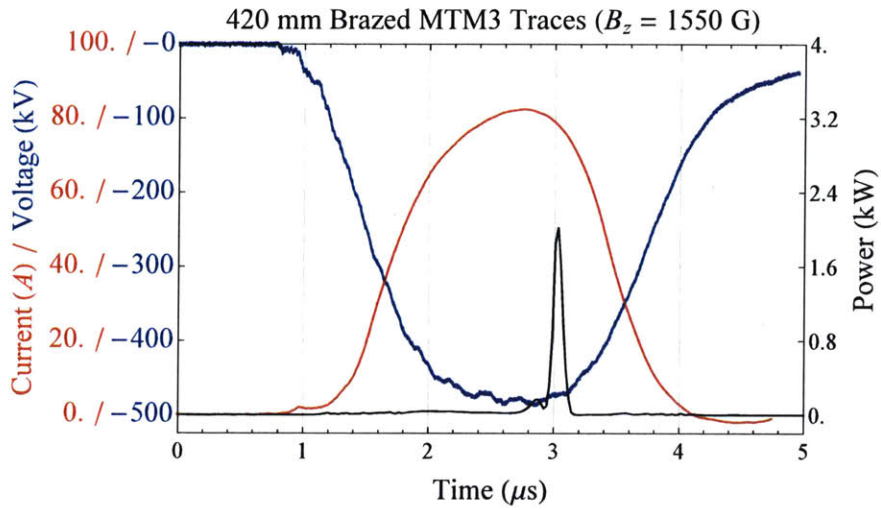


Figure 4-37: Microwave power (black curve), electron gun voltage (blue curve) and measured collector current (red curve) for an applied magnetic field of 450 G. The scale for the current (voltage) is given on the left in red (blue) and the scale for the microwave power is given on the right in black. The lens current was set at 11.3 A.

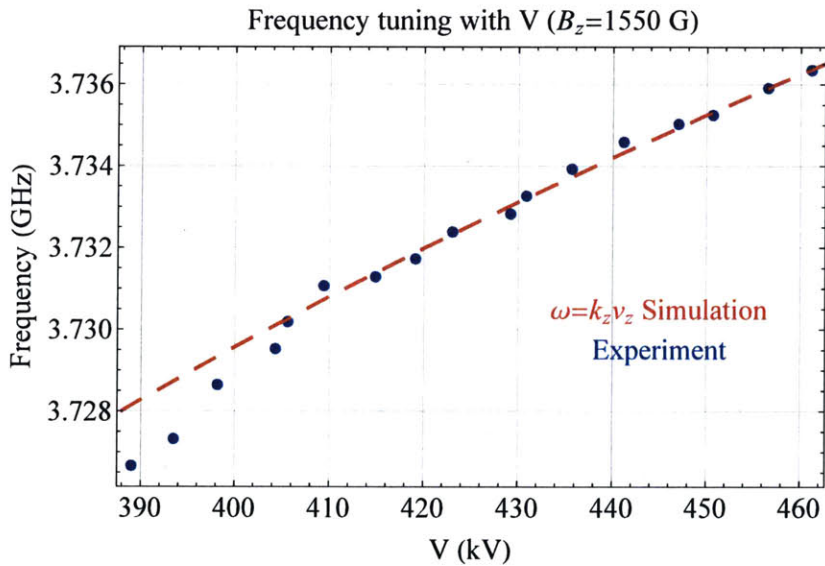


Figure 4-38: Frequency tuning of the structure as the voltage (and current) of the electron beam is varied from 390 kV to 365 kV.

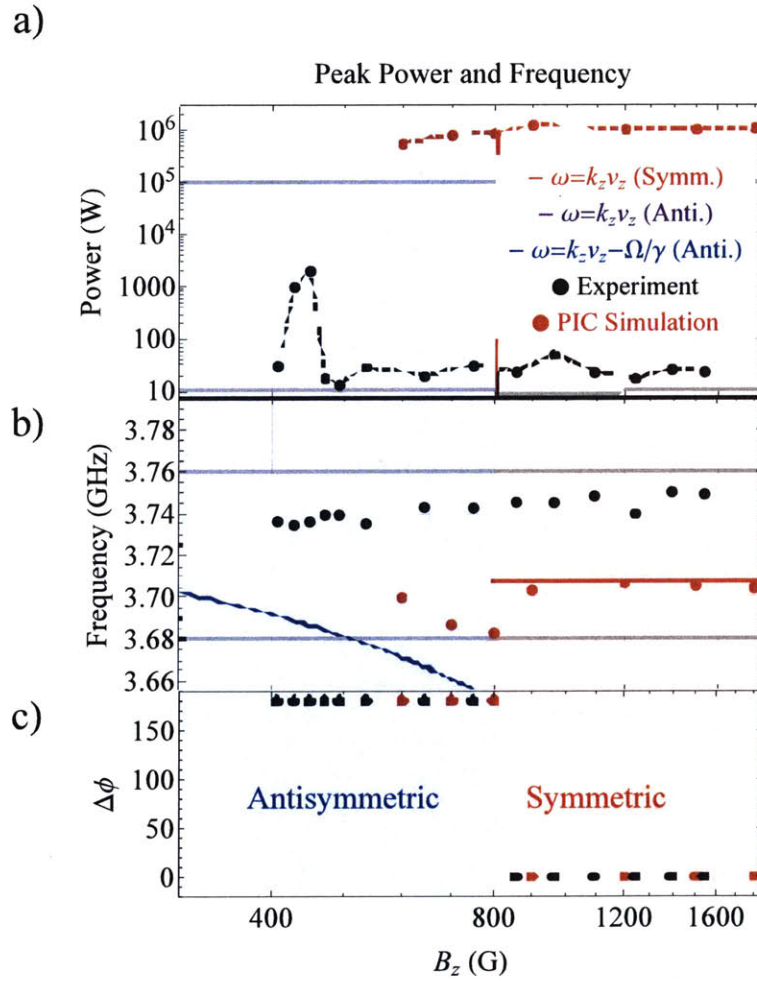


Figure 4-37: Stacked plot of the a) average microwave power (top), b) frequency (middle), and c) phase difference between the two RF arms (bottom). All of the red data points are those obtained from PIC simulations, and the black data points are the experimentally measured values. The power plot shows a distinct transition at 800 G where the device switches from antisymmetric to symmetric mode excitation.

and when the phase difference was π , the device was operating in the antisymmetric mode. In the figure, the power shown is the peak microwave power observed. Where the device produced one kilowatt or more of peak power near 450 G, the pulse width was approximately 100 ns. The device produces very little power (<100 W) for higher magnetic field, when the symmetric mode is excited. At the transition between the antisymmetric and symmetric mode, the qualitative tuning of the frequency does not change, unlike the tuning that was measured and predicted with PIC simulations for the MTM2 structure.

4.5 Summary of Results

This thesis presents the first experimental demonstration of coherent, high power microwave generation from a metamaterial interacting with an electron beam. Three different metamaterial designs are presented: MTM1, MTM2, and MTM3 with design frequencies of 2.8, 2.4, and 3.7 GHz, respectively. A summary of the three different metamaterial designs that were tested is presented in Fig. 4-40.

The most significant results came from a structure that was built with the MTM2 design (see section 2.2.3 and 4.3.2) that was 370 mm long. Multi-megawatt output power levels were achieved at a frequency near 2.39 GHz using a 490 keV, 84 A electron beam. In addition, an important discovery of this thesis was that multi-megawatt operation was observed with the anomalous Doppler interaction and not the Cherenkov interaction. This was significant because all of the previous theoretical work focused on the Cherenkov instability [39, 40, 41, 42, 43, 45, 46, 47], and to the author's knowledge, there is no previous discussion of an electron beam interacting with cyclotron modes that are supported by a metamaterial waveguide.

Despite the good agreement between theory, simulation, and experiment for the anomalous Doppler interaction with the antisymmetric mode, poor agreement between simulation and experiment was achieved with regard to the output power of the metamaterial structure for the Cherenkov interaction with the symmetric mode (see section 4.3.2). Nevertheless, the radiation observed from the Cherenkov interaction

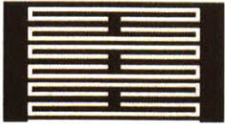


Mode	Design	Frequency of Negative Group Velocity Modes	Frequency of Positive Group Velocity Modes
MTM1		2.8 GHz	4.8 GHz
MTM2		2.4 GHz	5.9 GHz
MTM3		3.7 GHz	9.2 GHz

Figure 4-40: Summary of the MTM1, MTM2, and MTM3 designs which were tested in experiments. The approximate frequency of Cherenkov synchronism with a 500 keV electron beam for the negative group velocity modes and positive group velocity modes of each design is also shown.

was coherent, and this suggests that the BWO was in a pre-oscillation state, but still below threshold for full oscillation. Attempts to achieve high power in the Cherenkov interaction with the other two designs (MTM1 and MTM3) were unsuccessful. The discrepancy found between experiment and simulation highlights an important area for future research to develop a better theory and/or simulations that match the experimental results obtained in this thesis. A summary of the experimental results obtained for the brazed metamaterial structures is presented in Table 4.1.

Table 4.1: Summary of the experimental results obtained for all four brazed meta-material structure tests. P_{max} is the maximum power observed at any magnetic field or voltage value, and f_0 is the frequency for the corresponding maximum power measurement. The 352 mm MTM1 simulation inputs are shown in Table A.1- A.4, the 370 mm MTM2 simulation inputs are shown in Table A.5- A.8, and the 420 mm MTM3 simulation inputs are shown in Table A.9- A.11.

		MTM1	MTM2		MTM3
Length		352 mm	370 mm	420 mm	420 mm
P_{max}	Experimental Symmetric $v_g < 0$ Mode	30 W	30 W	No Power	40 W
	<i>PIC Simulation</i>	6 MW	7 MW	3 MW	1 MW
	Antisymmetric $v_g < 0$ Mode	350 W	5 MW	400 kW	2 kW
	<i>PIC Simulation</i>	5 MW	5 MW	6 MW	1 MW
	Symmetric $v_g > 0$ Mode	No Power	No Power	200 kW	No Power
	<i>PIC Simulation</i>	No Power	No Power	No Power	No Power
	Antisymmetric $v_g > 0$ Mode	No Power	No Power	No Power	No Power
	<i>PIC Simulation</i>	No Power	No Power	No Power	No Power
f_0	Symmetric $v_g < 0$ Mode	2.83 GHz	2.44 GHz	No Power	3.74 GHz
	<i>PIC Simulation</i>	2.82 GHz	2.40 GHz	2.42 GHz	3.70 GHz
	Antisymmetric $v_g < 0$ Mode	2.83 GHz	2.39 GHz	2.40 GHz	3.73 GHz
	<i>PIC Simulation</i>	2.83 GHz	2.38 GHz	2.41 GHz	3.69 GHz
	Symmetric $v_g > 0$ Mode	No Power	No Power	5.95 GHz	No Power
	<i>PIC Simulation</i>	No Power	No Power	No Power	No Power
	Antisymmetric $v_g > 0$ Mode	No Power	No Power	No Power	No Power
	<i>PIC Simulation</i>	No Power	No Power	No Power	No Power

Chapter 5

Conclusions

5.1 Summary of Accomplishments and Relevance

The theoretical investigation, design, and experimental test of a novel microwave generator that uses metamaterials and an electron beam in order to produce high-power coherent microwave radiation was presented in this thesis. This work is important in the two broader fields of vacuum electronics and metamaterial physics/engineering. While vacuum electronics and high power microwaves are a nearly century old field of study, applications of vacuum electronic devices span many disciplines and present an important part of our national defense and world economy. High power microwaves have applications in radar, communications, particle accelerators, plasma heating, industry, and materials processing. Therefore, development of new microwave sources is an important and relevant scientific challenge. In contrast, the metamaterial community is only about a decade old, and the importance of the applications it may have are not yet well defined. However, this field is growing rapidly and as new ideas are developed many novel areas of application in optics and microwave engineering are developing, including optical and microwave cloaks, perfect lenses, advanced antennas, and advanced microwave sources. This thesis presents several different meaningful contributions to both of these fields.

The most important contribution of this thesis is that, to the author's knowledge, this is the first experimental demonstration of coherent microwave generation from a

metamaterial using an electron beam, and this accomplishment opens the door to new types of microwave sources and active metamaterials. More than 5 MW of microwave power at 2.4 GHz was observed from the 370 mm metamaterial structure using the MTM2 design and a using 490 keV, 84 A electron beam with a one microsecond pulse. High power microwaves were generated in the negative group velocity antisymmetric mode for magnetic field values in the range of 375 to 450 G (see section 4.3.2). The high power interaction (> 1 MW of power) was determined to be consistent with that predicted by an anomalous Doppler shifted resonance. This caused the microwave frequency and phase to be controlled by the magnetic field.

In addition, up to 0.2 MW of power was generated in the positive group velocity symmetric mode at 5.95 GHz in the 420 mm metamaterial structure using the MTM2 design (see section 4.3.3). This same structure also produced up to 0.4 MW in the negative group velocity antisymmetric mode at 2.4 GHz for magnetic field values below 600 G.

Finally, up to 3 MW of output power were produced in the 352 mm metamaterial structure using the MTM1 design assembled with indium foil and a 490 keV, 84 A electron beam (see section 4.2.2). It was determined that gaps in the joints where the metamaterial plates bolted to the waveguide were responsible for a slot mode with a positive group velocity that produced the high power observed. The microwave frequency of the slot mode was 2.35 GHz.

A summary of the high power experimental results from each of the structures tested is presented in Table 5.1.

Table 5.1: High power experimental results from the metamaterial structures that were tested.

Structure	Mode	Interaction	P_{max}/f_0
352 mm MTM1 (Indium Unbrazed)	$v_g > 0$ Slot	Cherenkov	3 MW/2.35 GHz
370 mm Brazed MTM2	$v_g < 0$ Anti.	Anom. Doppler	5 MW/2.39 GHz
420 mm Brazed MTM2	$v_g < 0$ Anti.	Anom. Doppler	0.4 MW/2.40 GHz
420 mm Brazed MTM2	$v_g > 0$ Symm.	Cherenkov	0.2 MW/5.95 GHz
420 mm Brazed MTM3	$v_g < 0$ Anti.	Anom. Doppler	2 kW/3.73 GHz

This thesis has increased the physical understanding and computational modeling of metamaterials. Very good agreement was obtained in cold test and measurements made with a vector network analyzer. In addition, excellent agreement between PIC simulations, eigenmode simulations and the high power experiment was obtained for the predicted frequency, phase, and mode switching of different metamaterial devices, in particular the MTM2 device. Furthermore, this work has made advancements in the design of new types of metamaterial structures for vacuum and/or high power environments. The specific design constraints placed on the device, namely to operate at high vacuum and high power, resulted in the design of a new type of metamaterial loaded waveguide that is fairly simple to fabricate. Other applications with similar design constraints will be able to use and build on the designs presented in this thesis.

5.2 Discussion of Discrepancies Between the Results and Simulation/Theory

While the PIC and eigenmode simulations were able to accurately predict many of the operating conditions observed such as the peak power, frequency of operation, and the transition between the antisymmetric and symmetric mode, the theory and codes did not do a good job of predicting the starting condition of the structures for the original design modes (the negative group velocity symmetric modes) at 2.8, 2.4, and 3.7 GHz for the MTM1, MTM2, and MTM3 structures, respectively. (We limit our discussion here to the design modes of each structure which were the negative group velocity symmetric/antisymmetric modes, and leave out the performance of the slot mode in the case of the unbrazed MTM1 structure and the positive group velocity mode in the case of the 420 mm MTM2 structure.) In each iteration of the brazed structures the coupling impedance and/or length of structure tested was increased. This was motivated by the fact that in the analytical theory of the starting current presented in Chapter 2, the starting condition depends on the coupling impedance times the length of the interaction circuit cubed. However, for all of the structures tested the

simple linear theory predicted a starting current that was several times below the 80 A that was available from the electron gun. Nevertheless, it was hypothesized that the linear theory might be quantitatively inaccurate for the metamaterial structures because of their very flat dispersion, but it could still be useful in describing the qualitative behavior of the starting conditions.

This hypothesis turned out to be false. In fact, the structure with the best performance was the 370 mm MTM2 structure which did not have the lowest start current predicted by the linear theory. The 420 mm MTM2 structure was also able to produce high power in the negative group velocity mode, but the results were complicated by competition with the positive index mode. In this regard, the design of MTM2 was superior to MTM1 and MTM3. However, the PIC simulations and the theory were unable to predict this result.

The discrepancy between the PIC simulations/theory and the experiment can potentially be explained by some of the following issues which were not investigated in this thesis, but are highlighted here for future reference.

5.2.1 Structure Fabrication Errors

Any unintentional differences between the experimental and simulated structures could have affected the startup condition. It has already been discussed in Chapter 4 that the slots in the MTM1 bolted structure produced unexpected modes. However, these modes were also seen in the cold test and were eliminated by brazing the structure, whereas all of the brazed structures had good agreement between cold test and CST MWS simulations. This indicates that the cold wave propagation in the brazed metamaterial structures was correctly modeled. Therefore, it is unlikely that fabrication errors had much of an effect on the device startup. However, it is possible that an optimized output coupler design could improve the device performance. The current output coupler (which was designed for space limitations and simplicity) does have a significant amount of reflection and this could negatively affect the performance of the device.

5.2.2 Numerical Issues

The author did encounter discrepancies with the tracking solver of CST and the MICHELLE code when dealing with relativistic particles which were unable to be resolved. In private discussions with other groups, similar problems were discovered with high space charge, relativistic DC beams. It is possible that there are some problems in the way CST handles the calculation of fields from relativistic particles in the PIC solver. There is some concern regarding resolution of the code and convergence criteria/whether convergence was met, since the CST code had an internal algorithm to determine the time step and the number of particles to be used in the simulation. See Appendix A for more details about the PIC simulations.

5.2.3 Voltage and Current Pulse

There are some very important limitations on what can be simulated in the PIC simulations that could affect their accuracy. In particular, the voltage pulse from the modulator had a certain amount of time variation, whereas the simulations all used an electron beam with a constant energy. Over the 1 μ s ‘flat top’ of the experimental modulator pulse, there is $\pm 4\%$ variation in the voltage and $\pm 9\%$ variation in the current. In the simulations it is not possible to simulate a changing voltage, however the simulations are able to simulate the current ramping up from 0 A to a final DC value (i.e. 80 A). In simulations performed with very long ramp-up times (250 ns) it was observed that the interaction did not start (i.e. no microwaves generated and no electron bunches formed) until the current reached the final DC value. This is instructive as it shows that the metamaterial device may be sensitive to time variations in the beam current and voltage. This is also consistent with the observation that the only device to produce high power was the brazed 370 mm and 420 mm MTM2 structures when excited in the antisymmetric mode. These structures, when excited in the antisymmetric mode at 400 G, were observed to have the fastest saturation time in the PIC simulations, ~ 90 ns. This was faster than the MTM1 or MTM3 designs and almost twice as fast as the start up of the symmetric mode in the MTM2

design. The startup of the antisymmetric mode for the MTM2 design may have been fast enough to overcome any variation in the voltage and current that would have killed oscillations in the symmetric mode or the other designs. This is potentially a limitation of metamaterial based oscillator designs, as the very low group velocity and long filling time may mean that these devices are more sensitive to the current and voltage waveforms.

5.3 Potential Future Work

New structures could be tested which build on the successes of this thesis, and several recommendations can be made from the results presented. First, since the MTM2 structures were the most successful and the 420 mm and 370 mm long structure did have fairly different results, an additional structure with the MTM2 design but of a different length could be built and tested in the existing setup fairly easily. This would give valuable information about the performance of the device with length. In addition, a tapered structure (dispersion and beam channel dimensions) could possibly optimize the interaction as well as reduce beam interception. Reduced beam interception may result in longer and flatter RF pulses, and this could be investigated experimentally.

Along similar lines, the MTM2 structure operated at a lower frequency and had the longest period of all the structures tested and it is possible that these parameters had an effect on its performance that were not captured by the PIC simulations or the linear theory. Variations of these parameters in the MTM2 design could be studied with future tests. One should note that the PIC simulations did predict that the MTM2 design had the fastest saturation time of all three structures and this is possibly a clue to the success of this design over the others. Future design work could investigate the importance of the saturation time in the start up of the desired mode, especially taking into consideration the finite duration and flatness of the voltage/current pulse. In addition, it may be possible to tune the high power modulator to improve the flatness of the voltage pulse.

While the oscillator is an interesting device to study, amplifiers find much more use in various microwave applications due to their stability and phase control. In addition, an amplifier based metamaterial may not suffer from the negative effects associated with the long filling/saturation time found with the oscillator since there is a microwave input into the device. One of the structures (i.e. the MTM2) presented in this thesis could be tested as a backward-wave amplifier (BWA) if a small resonant cavity is placed in between the metamaterial structure and the gun. The MIT test stand does have room to put a small cavity in between the magnetic lens and before the solenoid pole plate. Testing the structure with input RF will help to better characterize the metamaterial structure. A test like the one described could potentially be used to estimate the starting condition of the structure at different magnetic field values (particularly for the symmetric mode), which is of interest to the oscillator experiment. In addition, to the author's knowledge this would be the first test of a metamaterial based microwave amplifier.

It will be important for future experiments to have a better understanding of the beam-wave interaction in metamaterial structures. An emphasis should be placed on deriving the starting conditions of metamaterial based microwave devices like the ones shown in this thesis. The linear theory presented in this thesis (see section 2.3) could be extended to a fully-relativistic electron beam for structures with very low group velocity and high space-charge. This would most likely modify the starting condition that was estimated analytically and presented in Chapter 2.

More advanced PIC simulations (or simulations performed with alternative PIC codes besides CST) could potentially get rid of some of the issues encountered with numerical Cherenkov oscillations and other observed effects (MAGIC, ICEPIC, etc.) [67]. In addition, they could provide a benchmark against the PIC simulations done in CST Particle Studio. Since there is a very large disagreement between the CST PIC code and the experiment over the starting condition of the symmetric mode, a different PIC simulation could provide valuable information about any discrepancy that is observed between the two codes. Ideally, a PIC code should be chosen that has a history of correctly modeling the starting conditions of high space-charge, relativistic

devices with low group velocity.

Appendix A

CST PIC Code Documentation

The CST PIC code uses a self-consistent method for the transient simulation of particle dynamics and can calculate space charge and self-magnetic as well as relativistic effects when propagating particles through static or HF electromagnetic fields. For more information on the CST PIC code, see Ref. [60].

In the design environment, there are several important steps and parameters which are necessary to run the code. All of the important design parameters are highlighted in the following description of the code setup in **bold**, and these parameters are then given in the sections that follow for the different simulations performed.

- *Structure Design*: The design environment for the code is similar to most CAD software packages. In the modeling tab, various 3D shapes can be created, and boolean operations on shapes can be performed in order to build a structure with the desired shape. The material properties can then be specified or loaded from an internal database. For the simulations in this thesis, the properties stored for copper and stainless steel were used for the metamaterial plates and rectangular waveguide, respectively (see Fig. 2-18).
- *Particle Source*: CST has several different particle source models, but only the DC emission model was used. Before the simulation, the user specifies the **beam energy** and **beam current**. There are also the options to specify an energy and angular spread (not investigated in this thesis). A rise time also

must be specified. For all the simulations in this thesis the rise time was 10 ns, except for some simulations presented in the discussion of discrepancy in Chapter 5 in which a rise time of 250 ns was used. The particle sources must be specified on the face of a metal surface, so in all of the simulations in this thesis a small disk was used as the emitter. The radius of the disk could be changed to change the **beam radius**. The beam radius was chosen for all simulations to match the condition for Brillouin flow (see Fig. 2-19).

The beam itself is composed of individual beamlets, and the number of beamlets is specified by the user. For all of the simulations presented in the thesis 185 beamlets were used. Additional simulations were performed with as many as 3000 beamlets, but this did not affect the simulation results. The time step and the number of particles emitted per unit time, or the total **number of particles** in the simulation at any given time, was automatically calculated by CST for a stable simulation.

- *Mesh*: CST automatically calculates the **mesh points** based on a **frequency range** of interest which must be specified by the user. The mesh size also depends on the geometry of the device being simulated. CST's perfect boundary approximation (PBA) allows complex geometries to be simulated with fewer mesh points than a traditional PIC simulation with a rectangular grid. The code also allows the user to specify a **minimum axial mesh size** (in the direction of the electron beam) and a **minimum mesh cells per wavelength** parameter for increased mesh control.
- *Output Ports*: For all simulations, two output ports were specified which were mated to the output waveguide sections of the device (see Fig. 2-18). The relevant impedance of the port is automatically calculated by CST. The CST code calculates the power exiting the simulation at the port and this is displayed during the simulation.
- *Monitors*: Electric field and particle monitors could be set up to produce a snapshot of the fields or particles in the simulation at a given time. These did

not affect the simulation, but were used to provide pictures of these quantities used in this thesis.

- *Magnetic Field*: A uniform axial magnetic field, B_z was used in all simulations.
- *Background Material*: Vacuum was set as the background material in all simulations.
- *Boundaries*: E-walls were specified on the two faces perpendicular to the direction of the electron beam for all simulations. Open boundaries were specified on the other wall faces.

Table A.1: Simulations presented in Fig. 2-20, pg. 93; Fig. 2-21, pg. 94; Fig. 2-22, pg. 95

Design	MTM1
Length	352 mm
Beam Energy	500 keV
Beam Current	80 A
Beam Radius	1.9 mm
Frequency Range	2.6 to 3.5 GHz
Mesh Points	5.4 Million
minimum mesh axial mesh size	0.15 mm
minimum mesh cells per wavelength	10
Number of Particles	800k
B_z	1500 G

Table A.2: Simulations presented on pg. 93

Design	MTM1
Length	352 mm
Beam Energy	500 keV
Beam Current	80 A
Beam Radius	1.9 mm
Frequency Range	2.6 to 3.5 GHz
Mesh Points	2 Million
minimum mesh axial mesh size	0.6 mm
minimum mesh cells per wavelength	10
Number of Particles	126k
B_z	1500 G

Table A.3: Simulations presented in Fig. 2-23, pg. 96; Fig. 2-24, pg. 97

Design	MTM1
Length	352 mm
Beam Energy	500 keV
Beam Current	80 A
Beam Radius	4.0 mm
Frequency Range	2.6 to 3.5 GHz
Mesh Points	5.4 Million
minimum mesh axial mesh size	0.15 mm
minimum mesh cells per wavelength	10
Number of Particles	800k
B_z	700 G

Table A.4: Simulations presented in Fig. 2-25, pg. 98

Design	MTM1
Length	352 mm
Beam Energy	500 keV
Beam Current	80 A
Beam Radius	8.0 to 1.5 mm
Frequency Range	2.6 to 3.5 GHz
Mesh Points	5.4 Million
minimum mesh axial mesh size	0.15 mm
minimum mesh cells per wavelength	10
Number of Particles	800k
B_z	350 to 1900 G

Table A.5: Simulations presented in Fig. 2-26, pg. 99; Fig. 2-27, pg. 100

Design	MTM2
Length	370 mm
Beam Energy	500 keV
Beam Current	80 A
Beam Radius	1.9 mm
Frequency Range	2.0 to 3.5 GHz
Mesh Points	1.6 Million
minimum mesh axial mesh size	1 mm
minimum mesh cells per wavelength	10
Number of Particles	300k
B_z	1500 G

Table A.6: Simulations presented on pg. 99

Design	MTM2
Length	370 mm
Beam Energy	500 keV
Beam Current	80 A
Beam Radius	1.9 mm
Frequency Range	2.0 to 3.5 GHz
Mesh Points	0.8 Million
minimum mesh axial mesh size	N/A
minimum mesh cells per wavelength	10
Number of Particles	230k
B_z	1500 G

Table A.7: Simulations presented in Fig. 2-28, pg. 101

Design	MTM2
Length	370 mm
Beam Energy	500 keV
Beam Current	80 A
Beam Radius	4.0 mm
Frequency Range	2.0 to 3.5 GHz
Mesh Points	1.6 Million
minimum mesh axial mesh size	1 mm
minimum mesh cells per wavelength	10
Number of Particles	300k
B_z	700 G

Table A.8: Simulations presented in Fig. 2-28, pg. 101

Design	MTM2
Length	370 mm
Beam Energy	500 keV
Beam Current	80 A
Beam Radius	5.6 mm to 1.5 mm
Frequency Range	2.0 to 3.5 GHz
Mesh Points	1.6 Million
minimum mesh axial mesh size	1 mm
minimum mesh cells per wavelength	10
Number of Particles	300k
B_z	500 to 1900 G

Table A.9: Simulations presented in Fig. 2-30, pg. 103

Design	MTM3
Length	420 mm
Beam Energy	500 keV
Beam Current	80 A
Beam Radius	1.9 mm
Frequency Range	2.0 to 6 GHz
Mesh Points	5.5 Million
minimum mesh axial mesh size	0.35 mm
minimum mesh cells per wavelength	10
Number of Particles	600k
B_z	1500 G

Table A.10: Simulations presented in Fig. 2-31, pg. 105

Design	MTM3
Length	420 mm
Beam Energy	500 keV
Beam Current	80 A
Beam Radius	4.6 to 1.6 mm
Frequency Range	2.0 to 6 GHz
Mesh Points	5.5 Million
minimum mesh axial mesh size	0.35 mm
minimum mesh cells per wavelength	10
Number of Particles	600k
B_z	600 to 1800 G

Table A.11: Simulations presented in Fig. 2-33, pg. 107

Design	Effective Medium
Length	352 mm
Beam Energy	500 keV
Beam Current	80 A
Beam Radius	1.9 mm
Frequency Range	2.0 to 3.5 GHz
Mesh Points	0.5 Million
minimum mesh axial mesh size	0.35 mm
minimum mesh cells per wavelength	10
Number of Particles	160k
B_z	1500 G

Table A.12: Simulations presented in Fig. 4-25, pg. 169

Design	MTM2
Length	370 mm
Beam Energy	489 keV
Beam Current	84 A
Beam Radius	1.7 to 8.0 mm
Frequency Range	2.0 to 3.5 GHz
Mesh Points	1.6 Million
minimum mesh axial mesh size	1 mm
minimum mesh cells per wavelength	10
Number of Particles	300k
B_z	350 to 1600 G

Table A.13: Simulations presented in Fig. 4-39, pg. 182

Design	MTM3
Length	420 mm
Beam Energy	465 keV
Beam Current	78 A
Beam Radius	4.7 to 1.6 mm
Frequency Range	2.0 to 6 GHz
Mesh Points	5.5 Million
minimum mesh axial mesh size	0.35 mm
minimum mesh cells per wavelength	10
Number of Particles	600k
B_z	600 to 1800 G

Bibliography

- [1] V. L. Granatstein, R. K. Parker, and C. M. Armstrong. Vacuum electronics at the dawn of the twenty-first century. *Proceedings of the IEEE*, 87:702–716, 1999.
- [2] J. Benford, J. A. Swegle, and E. Schamiloglu. *High Power Microwaves*. Taylor and Francis Group, LLC, Baltimore, Maryland, 2nd edition, 2007.
- [3] Ea-18g growler. URL <http://www.airforce.gov.au/Technology/Aircraft/EA18G-Growler/?RAAF-wWtm2RqFW2KOPyup3hIJncFVFKb020LN>.
- [4] Air force wants new energy weapons to cause non-lethal bioeffects. URL <http://www.wired.com/2013/04/air-force-directed-energy/>.
- [5] C. L. Holloway, E. F. Kuester, J. A. Gordon, J. O'Hara, J. Booth, and D. R. Smith. An overview of the theory and application of metasurfaces: The two-dimensional equivalents of metamaterials. *IEEE Antennas Propag. Mag.*, 54: 10–31, 2012.
- [6] J. D. Jackson. *Classical Electrodynamics*. John Wiley and Sons, Hoboken, New Jersey, 1st edition, 1999.
- [7] V. G. Veselago. The electrodynamics of substances with simultaneously negative values of ϵ and μ . *Sov. Phys. Usp.*, 47:509–514, 1968.
- [8] R. Marques, F. Martin, and M. Sorolla. *Metamaterials with Negative Parameters: Theory, Design and Microwave Applications*. John Wiley and Sons, Hoboken, N. J., 2008.
- [9] L. Solymar and E. Shamonina. *Waves in Metamaterials*. Oxford University Press, New York, N. Y., 2009.
- [10] I. M. Ehrenberg, S. E. Sarma, and B. Wu. A three-dimensional self-supporting low loss microwave lens with a negative refractive index. *J. Appl. Phys.*, 112: 073114, 2012.
- [11] X. Zhang and Z. Liu. Superlenses to overcome the diffraction limit. *Nature Materials*, 7:435–441, 2008.
- [12] N. Seddon and Bearpark T. Observation of the inverse doppler effect. *Science*, 28:1537–1540, 2003.

- [13] J. Chen, Y. Wang, B. Jia, T. Geng, X. Li, L. Feng, W. Qian, B. Liang, X. Zhang, M. Gu, and S. Zhuang. Observation of the inverse doppler effect in negative-index materials at optical frequencies. *Nature Photonics*, 5:239245, 2011.
- [14] A. Grbic and G. V. Eleftheriades. Experimental verification of backward-wave radiation from a negative refractive index metamaterial. *J. Appl. Phys.*, 92(10): 5930–5935, 2002.
- [15] W. Rotman. Plasma simulation by artificial dielectrics and parallel-plate media. *IRE Trans. Antennas Propag.*, 10:82–95, 1962.
- [16] J. B. Pendry, A. J. Holden, W. J. Stewart, and I. Youngs. Extremely low frequency plasmons in metallic microstructures. *Phys. Rev. Lett.*, 76:4773–4776, 1996.
- [17] J. B. Pendry, A. J. Holden, D. J. Robbins, and W. J. Stewart. Magnetism from Conductors and Enhanced Nonlinear Phenomena. *IEEE Trans. Microwave Theory Tech.*, 47:2075–2084, 1999.
- [18] D. R. Smith, W. J. Padilla, D. C. Vier, S. C. Nemat-Nasser, and S. Schultz. Composite medium with simultaneously negative permeability and permittivity. *Phys. Rev. Lett.*, 84:4184–4187, 2000.
- [19] D. R. Smith and N. Kroll. Negative refractive index in left-handed materials. *Phys. Rev. Lett.*, 85:2933–2936, 2000.
- [20] S. H. Gold and G. S. Nusinovich. Review of high-power microwave source research. *Rev. Sci. Instrum.*, 68:3945–3974, 1997.
- [21] V. L. Ginzburg. Radiation by uniformly moving sources (Vavilov-Cherenkov effect, transition radiation, and other phenomena. *DPhysics-Uspekhi*, 39:973–982, 1996.
- [22] S. J. Smith and E. M. Purcell. Visible light from localized surface charges moving across a grating. *Phys. Rev. Lett.*, 39:1069, 1953.
- [23] R. Kompfner. *The Invention of the Travelling-Wave Tube*. San Francisco Press, San Francisco, CA, 1964.
- [24] J. R. Pierce. *Travelling Wave Tubes*. Van Nostrand, New York, New York, 1950.
- [25] G. Zorpette. With a little help from our friends. URL <http://spectrum.ieee.org/geeklife/profiles/withalittlehelp-from-ourfriends>.
- [26] S. E. Tsimring. *Electron Beams and Microwave Vacuum Electronics*. John Wiley and Sons, Hoboken, New Jersey, 2007.

- [27] N. S. Ginzburg, N. I. Zaitsev, E. V. Ilyakov, I. S. Kulagin, Yu. V. Novozhilova, R. M. Rozenhal, and A. S. Sergeev. Observation of Chaotic Dynamics in a Powerful Backward-Wave Oscillator. *Phys. Rev. Lett.*, 89(108304), 2002.
- [28] R. H. Varian and S. F. Varian. A high frequency oscillator and amplifier. *J. Appl. Phys.*, 10:321–327, 1939.
- [29] A. Zangwill. *Modern Electrodynamics*. Cambridge University Press, New York, New York, 2013.
- [30] G. S. Nusinovich. *Introduction to the Physics of Gyrotrons*. The John Hopkins University Press, Baltimore, Maryland, 1st edition, 2004.
- [31] G. S. Nusinovich, M. Korol, and E. Jerby. Theory of the Anomalous Doppler Cyclotron-Resonance-Maser Amplifier with Tapered Parameters. *Phys. Rev. E*, 59:2311, 1999.
- [32] N. S. Ginzburg. Nonlinear Theory of Electromagnetic Wave Generation and Amplification Based on the Anomalous Doppler Effect. *Radiophysics and Quantum Electronics*, 22:323–330, 1979.
- [33] S. P. Kuznetsov and A. P. Chetverikov. Transient Nonlinear Theory of an Ultrarelativistic Backward-Wave Tube with an Anomalous Doppler Effect. *Radiophysics and Quantum Electronics*, 24:78–84, 1981.
- [34] K. Ogura, M. R. Amin, K. Minami, X. D. Zheng, Y. Suzuki, W. S. Kim, T. Watanabe, Y. Carmel, and V. L. Granatstein. Experimental demonstration of a high-power slow-wave electron cyclotron maser based on a combined resonance of Cherenkov and anomalous Doppler interactions. *Phys. Rev. E*, 53: 2726–2729, 1996.
- [35] T. Maly, G. T. Debelouchina, V. S. Bajaj, K. Hu, C. Joo, M. L. Mak-Jurkauskas, J. R. Sirigiri, P. CA. van der Wel, J. Herzfeld, R. J. Temkin, and R. G. Griffin. Dynamic nuclear polarization at high magnetic fields. *The Journal of chemical physics*, 128(5):052211, 2008.
- [36] Vgt-8110 gyrotron oscillator. URL "http://img.directindustry.com/pdf/repository_di/33711/gyrotrons-116013-1b.jpg".
- [37] T. Jiang, K. Chang, Li-Ming Si, L. Ran, and H. Xin. Active Microwave Negative-Index Metamaterial Transmission Line with Gain. *Phys. Rev. Lett.*, 107(205503), 2011.
- [38] A. R. Katko, J. P. Barrett, B. Popa, G. Shvets, and S. A. Cummer. Active Microwave Negative-Index Metamaterial Transmission Line with Gain. *Phys. Rev. Lett.*, 105(123905), 2010.

- [39] M. A. Shapiro, S. Trendafilov, Y. Urzhumov, A. Alu, R. J. Temkin, and G. Shvets. Active negative-index metamaterial powered by an electron beam. *Phys. Rev. B*, 86(085132), 2012.
- [40] Y. P. Bliokh, S. Savel'ev, and F. Nori. Electron Beam Instability in Left-Handed Media. *Phys. Rev. Lett.*, 100(244803), 2008.
- [41] D. Shiffler, J. Luginsland, D. M. French, and J. Watrous. A Cerenkov-like Maser Based on a Metamaterial Structure. *IEEE Trans. Plasma Sci.*, 38:1462, 2010.
- [42] D. M. French, D. Shiffler, and K. Cartwright. Electron beam coupling to a metamaterial structure. *Phys. Plasmas*, 20(083116), 2013.
- [43] J. S. Hummelt, S. M. Lewis, M. A. Shapiro, and R. J. Temkin. Design of a Metamaterial-Based Backward-Wave Oscillator. *IEEE Trans. Plasma Sci.*, 42: 930–936, 2014.
- [44] C. Luo, M. Ibanescu, E. Reed, S. Johnson, and J. Joannopoulos. Doppler radiation emitted by an oscillating dipole moving inside a photonic band-gap crystal. *Phys. Rev. Lett.*, 96:043903, 2006.
- [45] Z. Duan, J. S. Hummelt, M. A. Shapiro, and R. J. Temkin. Sub-wavelength waveguide loaded by a complementary electric metamaterial for vacuum electron devices. *Phys. Plasmas*, 21:103301, 2014.
- [46] X. Lu, M. A. Shapiro, and R. J. Temkin. Modeling of the interaction of a volumetric metallic metamaterial structure with a relativistic electron beam. *Phys. Rev. ST Accel. Beams*, 18:081303, 2015.
- [47] A. Antipov, L. Spentzouris, W. Gai, M. Conde, F. Franchini, R. Konecny, W. Liu, J. G. Power, Z. Usuf, and C. Jing. Observation of wakefield generation in left-handed band of metamaterial-loaded waveguide. *J. Appl. Phys.*, 104(014901), 2008.
- [48] D. M. Pozar. *Microwave Engineering*. John Wiley and Sons, Hoboken, New Jersey, 3rd edition, 2005.
- [49] A. W. Trivelpiece and R. W. Gould. Space Charge Waves in Cylindrical Plasma Columns. *J. Appl. Phys.*, 30:1784–1793, 1959.
- [50] V. N. Shevchik, G. N. Shvedov, and A. V. Soboleva. *Wave and oscillatory phenomena in electron beams at microwave frequencies*. Pergamon Press, Oxford, U.K., 1966.
- [51] Y. Carmel, K. Minami, R. A. Kebs, W. W. Destler, V. L. Granatstein, D. Abe, and W. L. Lou. Demonstration of Efficiency Enhancement in a High-Power Backward-Wave Oscillator by Plasma Injection. *Phys. Rev. Lett.*, 62:2389–2392, 1989.

- [52] A. T. Lin and L. Chen. Plasma-Induced Efficiency Enhancement in a Backward-Wave Oscillator. *Phys. Rev. Lett.*, 63:2808–2811, 1989.
- [53] A. G. Shkvarunets, S. Kobayashi, Y. Carmel, J. Rodgers, T. M. Antonsen, L. Duan, and V. L. Granatstein. Operation of a Relativistic Backward-Wave Oscillator Filled with a Preionized High-Density Radially Inhomogenous Plasma. *IEEE Trans. Plasma Sci.*, 26:646–652, 1998.
- [54] C. Grabowski, J. M. Gahl, and E. Schamiloglu. Initial Plasma-Filled Backward-Wave Oscillator Experiments Using a Cathode-Mounted Plasma Prefill Source. *IEEE Trans. Plasma Sci.*, 26:653–668, 1998.
- [55] F. Falcone, T. Lopetegi, M. A. G. Laso, J. D. Baena, J. Bonache, M. Beruete, R. Marques, F. Martin, and M. Sorolla. Babinet Principle Applied to the Design of Metasurfaces and Metamaterials. *Phys. Rev. Lett.*, 93(197401), 2004.
- [56] G. Shvets. Photonic approach to making a material with a negative index of refraction. *Phys. Rev. B*, 67(035109), 2003.
- [57] ANSYS. High frequency structure simulator. URL <http://www.ansys.com/Products/Electronics/ANSYS-HFSS>.
- [58] Computer Simulation Technology. Microwave studio, . URL <https://www.cst.com/products/CSTMWS>.
- [59] H. Heffner. Analysis of the backward-wave traveling wave tube. *Proc. IRE*, 42: 930, 1954.
- [60] Computer Simulation Technology. Particle studio, . URL <https://www.cst.com/Products/CSTPS>.
- [61] A. S. Gilmour. *Klystrons, Traveling Wave Tubes, Magnetrons, Crossed-Field Amplifiers, and Gyrotrons*. Artech House, Norwood, MA, 2011.
- [62] R. Liu, Q. Cheng, T. Hand, J. J. Mock, T. J. Cui, S. A. Cummer, and D. R. Smith. Experimental Demonstration of Electromagnetic Tunneling Through an Epsilon-Near-Zero Metamaterial at Microwave Frequencies. *Phys. Rev. Lett.*, 100(023903), 2008.
- [63] B. Edwards, A. Alu, M. E. Young, M. Silveirinha, and N. Engheta. Experimental Verification of Epsilon-Near-Zero Metamaterial Coupling and Energy Squeezing Using a Microwave Waveguide. *Phys. Rev. Lett.*, 100(033903), 2008.
- [64] J. H. Billen and L. M. Young. Poisson/Superfish on PC Compatibles. *IEEE Proceedings of the Particle Accelerator Conference (PAC)*, 4:790–792, 1993.
- [65] J. Petillo, P. Blanchard, A. Mondelli, K. Eppley, W. Krueger, T. McClure, D. Panagos, B. Levush, J. Burdette, and M. Cattelino. The MICHELLE electron gun and collector modeling tool. *IEEE Proceedings of the Particle Accelerator Conference (PAC)*, pages 3054–3056, 2001.

[66] M. Reiser. *Theory and Design of Charged Particle Beams*. John Wiley and Sons, New York, New York, 1st edition, 1994.

[67] Orbital ATK. Magic. URL <http://www.mrcwdc.com/magic/description.html>.